The Modelling of Biological Growth: a Pattern Theoretic Approach

by

Nataliya Portman

A thesis
presented to the University of Waterloo
in fulfillment of the
thesis requirement for the degree of
Doctor of Philosophy
in
Applied Mathematics

Waterloo, Ontario, Canada, 2009

I hereby declare that I am the sole author of this thesis. This is a true copy of the thesis, including any required final revisions, as accepted by my examiners.

I understand that my thesis may be made electronically available to the public.

Abstract

Mathematical and statistical modeling and analysis of biological growth using images collected over time are important for understanding of normal and abnormal development. In computational anatomy, changes in the shape of a growing anatomical structure have been modeled by means of diffeomorphic transformations in the background coordinate space. Various image and landmark matching algorithms have been developed for inference of large transformations that perform image registration consistent with the material properties of brain anatomy under study. However, from a biological perspective, it is not material constants that regulate growth, it is the genetic control system. A pattern theoretic model called the Growth as Random Iterated Diffeomorphisims (GRID) introduced by Ulf Grenander (Brown University) constructs growth-induced transformations according to fundamental biological principles of growth. They are governed by an underlying genetic control that is expressed in terms of probability laws governing the spatial-temporal patterns of elementary cell decisions (e.g., cell division/death).

This thesis addresses computational and stochastic aspects of the GRID model and develops its application to image analysis of growth. The first part of the thesis introduces the original GRID view of growth-induced deformation on a fine time scale as a composition of several, elementary, local deformations each resulting from a random cell decision, a highly localized event in space-time called a *seed*. A formalization of the proposed model using theory of stochastic processes is presented, namely, an approximation of the GRID model by the diffusion process and the Fokker-Planck equation describing the evolution of the probability density of seed trajectories in space-time. Its time-dependent and stationary numerical solutions reveal bimodal distribution of a random seed trajectory in space-time.

The second part of the thesis considers the growth pattern on a coarse time scale which underlies visible shape changes seen in images. It is shown that such a “macroscopic” growth pattern is a solution to a deterministic integro-differential equation in the form of a diffeomorphic flow dependent on the GRID growth variables such as the probability density of cell decisions and the rate of contraction/expansion. Since the GRID variables are unobserved, they have to be estimated from image data. Using the GRID macroscopic growth equation such an estimation problem is formulated as an optimal control problem. The estimated GRID variables are optimal controls that force the image of an initial organism to be continuously transformed into the image of a grown organism. The GRID-based inference method is implemented for inference of growth properties of the *Drosophila* wing disc directly from confocal micrographs of Wingless gene expression patterns.

Acknowledgements

I would like to thank my supervisors Prof. Ulf Grenander for guidance and encouragement during my intellectual journey and Prof. Edward Vrscay for support in dissemination of research findings and writing this thesis.

Prof. Ulf Grenander has had a large influence on my professional development. His long-distance supervision via most insightful questions, comments, suggestions and encouragement sent electronically has been a valuable resource.

Prof. Edward Vrscay has provided me with freedom of mathematical thought, wonderful working conditions for thought development and support in promotion of my research.

In the beginning of my journey Johan Gielis introduced mathematical models of plant growth, and in the end Prof. Matthew Scott provided important insights into the connection of the inference problem formulation with the biology of growth. They have always been open for discussion and comments.

I have been lucky to work with such intelligent and friendly collaborators, and I express my deep gratitude for their generous support.

This research was supported in part by the Natural Sciences and Engineering Research Council of Canada (NSERC) in the form of a Postgraduate Scholarship, by the Ontario Ministry of Training, Colleges and Universities in the form of an Ontario Graduate Scholarship. I also received financial aid in the form of President's Scholarships from the University of Waterloo and teaching assistant and instructor positions from the Department of Applied Mathematics. For this I am very grateful.

I also would like to thank my husband James Portman for his patience and support. Some meant-to-be family weekends were lost in my studies and thesis typing and I am deeply appreciative of his understanding.

Finally, I am thankful to my sons Andrei and Alexander who have made life in Waterloo enjoyable filling it with family fun.

Dedication

This is dedicated to
Ulf Grenander,
whose Growth as Random Iterated Diffeomorphisms model paves the way to a
new universal mathematical language of biological growth.

Contents

List of Tables

List of Figures

Nomenclature

$\lambda(\xi)$	The instantaneous average rate of seed activation per unit area $d\xi \in \Xi$
$\Lambda(\xi, t)$	The Poisson intensity parameter $\Lambda(\xi, t) = \lambda_t \times \lambda(\xi)$
λ_t	The instantaneous average rate of seed activation at time t
λ_x	The intensity of seed activations per unit area dx in the absolute space
μ	The Poisson measure counting a number of activated seeds in Darcyan space-time $\Xi \times [t_0, T]$
$\Omega(t)$	A growing organism at time t occupying a compact region in $\Re^n,\ n = 1, 2, 3$, that is a subset of imaged coordinates expressed in a Cartesian system
$\phi^{\xi_{seed}, t}$	The elementary deformation resulting from a single seed activation $\xi_{seed} \in \Xi$ at time t
$\Re^n$	The n-dimensional space of real numbers with $n = 1, 2, 3$
Ξ	The Darcyan space that can be continuous, defined by $\Xi = \{0 \leq \xi_1 \leq 2\pi,\ 0 \leq \xi_2 \leq \infty\}$, or countable, defined by $\Xi = \{1 \leq \xi_1 \leq m,\ 1 \leq \xi_2 \leq n\}$, where ξ_1, ξ_2 are integers
ξ	The biological coordinates $\xi = (\xi_1, \xi_2)$, where ξ_1 and ξ_2 enumerate radial and angular coordinate curves of the Darcyan grid
$f(x, t)$	The probability density of a random seed trajectory in space-time
$J(x(\xi))$	The Jacobian matrix of the transformation $x = (x_1(\xi_1, \xi_2), x_2(\xi_1, \xi_2))$
$k(\tau)$	The anisotropic rate of expansion/contraction in the local polar coordinate system centered at an activated seed point
$k(\xi_{seed}, t)$	The isotropic relative rate of expansion/contraction
$s(x(\xi_{seed}, t))$	The radius of influence of the seed $x(\xi_{seed})$ activated at time t
X	The closed, simply connected set, representing the domain of an organism
$x(\xi)$	The Darcyan coordinates of an organism
$x(\xi_{seed})$	The activated seed in the X-field representing a single cell event

Part I

GRID Growth Patterns in Experiments and Theory of Stochastic Processes

Chapter 1

Introduction

1.1 Motivation

This thesis is concerned with the development of a particular mathematical model, the so-called "Growth as Random Iterated Diffeomorphisms" or "GRID". We show that the GRID approach is well-suited to accomplish three major and necessary tasks in the modelling of biological growth. First, however, we outline some biologically-based motivations for the development of such a model.

1.1.1 Advances in imaging technologies, MRI, fMRI, microscopy

Recent advances in imaging technologies have enabled biomedical researchers to access the inner biological processes of a living organism. Two main techniques, fluorescence microscopy and laser scanning confocal microscopy, are used to view the dynamics of gene expression patterns[1] in a cell cluster. Micrographs of gene expression patterns shed light on the their role in positioning and shaping of future adult structures of a developing embryo.

Other imaging techniques, notably magnetic resonance imaging (MRI), are used to visualize structure and function of suborganisms in vivo. In regards to biological growth, this technique allows detection of qualitative changes in tissue morphology and biochemistry as well as stages of a malignant tumor development.

The availability of various imaging modalities such as computer tomography (CT), functional magnetic resonance imaging (fMRI), and positron emission tomography (PET) provides an opportunity to conduct growth experiments by monitoring developmental stages of an organism in the form of images. One of the clinical purposes of such experiments is to classify the development of the organism into normal and abnormal classes based on its morphological features. A pathology

---

[1] gene expression patterns are distributions of gene product or protein concentrations in the cellular field of an embryo that guide its development

in observed development usually manifests itself as a drastic change in a topological structure (creation of a new biological material such as a tumor, for instance).

Another opportunity is to study the effects of a particular gene on normal development of anatomical structures in mouse embryos. Using MRI technology we can examine what is happening in an *in vivo* “knockout” mouse embryo with the gene of interest replaced by an inactive or mutated allele. In this way we are able to determine how this gene spatially controls embryonic development or how it contributes to a particular genetic disease.

It is difficult to detect pathology from a simple visual inspection of anatomical structure especially if it exists on the fine scale. Therefore, a quantitative framework for growth characterization is needed. A possibility of creating a database of biomedical images of individual growth patterns in healthy and disease groups naturally leads to the statistical modeling of growth and further study of normal and abnormal shape variations. Only then we are able to estimate the likelihood of the normal development for an observed growth phenomenon using statistical hypothesis testing for abnormality.

For the reasons stated above what is needed is to develop a useful mathematical model of a biological growth that

1. captures shape and structural changes of a growing organism at each observed stage of development using shape transformations,
2. reflects variability of growth patterns of an organism,
3. reveals a link between genetic activity and shape transformations of a growing multicellular structure.

The requirement (1) allows to obtain quantitative characteristics of a growth-induced deformation such as the Jacobian of transformation, for example. In order to capture interior anatomical changes shape transformations have to be defined over the compact continuum region occupied by the organism in $\Re^2$ or $\Re^3$. The requirement (2) provides randomness of growth patterns by imposing a statistical model on the deformation field resulting from growth. The requirement (3) means that shape transformations have to be biologically motivated and defined as deformation effects of gene actions. Otherwise, the growth model will provide just a mathematical quantitative description of the changing geometry of a growing organism.

The experimental support for the genetically controlled growth model comes from medical imaging. There is a possibility for medical researchers to conduct animal experiments with genetic modification and study the resulting anatomical changes. Then an experimentally tested growth model will contribute to understanding growth processes in living organisms.

1.1.2 Mathematical models in developmental biology

The subjects of growth and development have been studied for several decades. A traditional approach to representing laws of biological development is given in a continuum mechanics format: a developing multicellular organism is viewed as a continuum and its morphological changes are described by an evolution law of a density of a particular substance $c(\vec{r},t)$ in time. The density distribution or the concentration pattern is established through local interactions of substances over infinitesimal neighborhoods.

A chemical model for a biological pattern formation was introduced by Turing [67] in 1952 and further developed by Newman and Frisch [47] and Murray [45] where local interactions are captured by a reaction-diffusion differential equation. Two distinct types of molecules associated with genetic codes that are signals for structural change and development (morphogens) react and diffuse to produce steady spatially heterogeneous patterns of morphogen concentrations $A(\vec{r},t)$, $B(\vec{r},t)$

$$\frac{\partial \vec{c}}{\partial t} = \vec{f}(\vec{c}) + D\Delta\vec{c}, \tag{1.1.1}$$

where $\vec{c} = (A(\vec{r},t), B(\vec{r},t))$ is a vector of morphogen concentrations, $\vec{f}(\vec{c})$ is the vector source term and D is the diagonal matrix of positive diffusion coefficients. This model suggests a reaction-diffusion mechanism of generation of typical patterns (e.g., stripes and spots) observed on animal coats. It does not explain generation of shape associated with cell proliferation and cell enlargement.

Processes such as cell proliferation and enlargement play a major role in plant development. According to the mechanical model for generation of the plant morphology proposed by Yu-Xiang [71] the growth and form of the organism are viewed as a mass accumulation process in a potential field associated with the turgor pressure. The growing organism is considered to be a fluid described by the density function $\rho(\vec{r}(t),t)$ in a time derivative form

$$\frac{d\rho}{dt} = \nabla\rho \cdot \vec{\nu} + \frac{\partial \rho}{\partial t}, \tag{1.1.2}$$

where $\nabla\rho$ is the density gradient and $\vec{\nu}$ is the mass transfer rate. A relation between the mass accumulation and the turgor pressure field is defined by Maxwell's formula [71]

$$\rho(\vec{r},t) = \frac{1}{4\pi}\nabla^2\Psi, \tag{1.1.3}$$

where Ψ is a turgor pressure potential. By taking the time derivative of (1.1.3) and substituting it into (1.1.2) we obtain a second order differential equation of a general evolution of a biological system in the potential field. This model considers a role of the turgor pressure in shaping the organism. The solutions present dependence on certain hypotheses regarding the values of morphological parameters (such as the number of petals, the width of a petal) that are supposed to be predetermined by the natural selection rule. These hypotheses have not been confirmed experimentally.

A similar view of plant growth, particularly leaf growth, as a mass accumulation process can be found in a joint work on simulation of plant leaf growth by Wang, Wan and Baranovski [68]. They have employed the modified Navier-Stokes and continuity equations to accommodate the mass increase due to growth. According to their model the dynamics of growth of a biological tissue is analogous to the dynamics of a viscous fluid characterized by the fluid velocity vector $\vec{u}$, pressure p exerted by the the growing cells, surface forces expressed by the stress tensor σ and the divergence of the velocity field $\nabla \cdot \vec{u}$ being equal to the spatial-temporal growth rate $L(\vec{r}, t)$.

The behavior of the growing plant tissue is described by the following modified momentum equation

$$\vec{u}_t + (\vec{u} \cdot \nabla)\,\vec{u} + \vec{u} \cdot (\nabla \cdot \vec{u}) = \nabla \cdot \sigma \tag{1.1.4}$$

and the modified continuity equation

$$\nabla \cdot \vec{u} = L(\vec{r}, t). \tag{1.1.5}$$

This model appears applicable to isotropic leaf growth. How to extend it to the anisotropic case when such morphological parameters as anisotropy (the degree to which growth occurs preferentially in any direction), directions (the angles of orientation of the principal directions of growth) and rotation rate per unit time (the angle through which each region turns relative to other regions) have to be incorporated remains an open question.

Another approach that considers the role of mechanical forces in morphogenesis, known as “Mechanical Theory for Generating Pattern and Form in Development”, was developed by Murray and Oster [49], Maini [46], Bentil [2] and Cruywagen [17]. According to their theory mechanical shaping of form occurs in early embryogenesis where cell movement and interactions between the cells and a tissue made up of a fibrous extra cellular matrix (ECM) as well as cell proliferation contribute to changes in the shape of a developing embryo. The model consists of three major equations:

(i) The conservation law for the cell population density

$$\frac{\partial n}{\partial t} = -\nabla \cdot \vec{J} + M, \tag{1.1.6}$$

where $n(\vec{r}, t)$ is the cell density, $\vec{J}$ is the flux of cells and M is the cell proliferation rate,

(ii) The mechanical balance of forces generated by the cells, the ECM and the external forces,

$$\nabla \cdot \vec{\sigma} + \rho \vec{F} = 0, \tag{1.1.7}$$

where $\sigma(\vec{r}, t) = \vec{\sigma}_{ECM} + \vec{\sigma}_{cell}$ represents the stress tensor and $\vec{F}$ the external force acting on the ECM,

(iii) The conservation equation for the matrix density

$$\frac{\partial \rho}{\partial t} + \nabla \cdot (\rho \vec{u}_t) = S(n, \rho, t), \tag{1.1.8}$$

where $\rho(\vec{r}, t)$ is the ECM density, $\vec{v}(t)$ is the displacement vector of the ECM and $S(n, \rho, t)$ is the rate of secretion of matrix by the cells.

This model is based on the exact physical laws and biological facts on the cell types, their movement properties and their role in embryogenesis. It provides a realistic description of the cell pattern formation subjected mainly to cell traction forces. The Mechanical Theory for Generating Pattern and Form underestimates the role of the genetic control system in the development of an embryo viewing morphogenesis as a purely mechanical event.

There is an alternative, energy-based approach in the study of plant growth that considers the role of biophysical signals such as growth forces on the tip of a plant shoot (apical meristem) in a large-scale plant pattern formation. The large-scale plant pattern means the tiling of the plant surface into irregular polygons such as ribs for a cactus, for instance, or plant phyllotaxis, i.e. spiral or whorled arrangement of phylla on the plant surface. According to the biophysical model introduced by Green [25] and further developed by Shipman and Newell [60] the generative region (a meristem area containing localized subregions of active cell divisions where phylla form as bumps) of a growing plant is modeled as a thin elastic shell (the tunica) attached to a thin elastic foundation under the compressive stress. There is experimental evidence [64] that the compressive stresses reach their critical values in the generative region causing buckling of the tunica and thus setting the plant pattern. Grown plant patterns approximate the patterns that minimize the elastic energy of the generative region, i.e. configurations with the lowest critical stress values.

The elastic energy is a functional of in-plane stresses and the normal displacements of the shell. The energy minimizing configurations in the form of deformations of the elastic shell have been derived via analytical study of the Euler-Lagrange equations for the elastic energy functional. The biophysical model provides a connection between the material properties of a plant and its pattern formation and the compressive stresses leading to the buckling of the tunica as a mechanism of shape generation.

The models considered above and their experimental validation indicate that mechanics of biological development plays a significant role in generation of shape. The mechanical models are useful as descriptions but of limited use for analysis and prediction.

There is also experimental evidence due to Reinhardt, Pesce and others [55] and Coen, Rolland-Lagan [15] that chemical signals such as growth hormones (auxin) are linked to biological shape formation. These signals are transported to certain sites in the tissue specifying an activated formative region with boundaries (see Fig.1.1.1). The spatial-temporal distribution of the growth hormone suggests pattern controlled growth of a biological organism causing structural changes such as

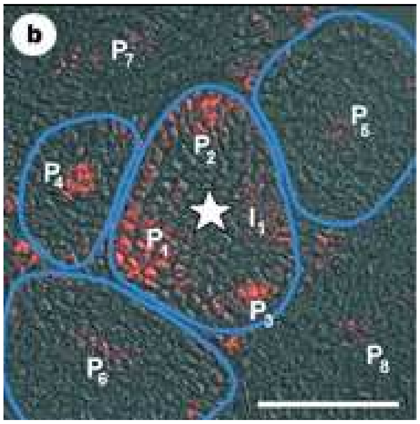

Figure 1.1.1: Polar transport of a growth hormone auxin in the cross-section of the shoot vegetative apex. $P_1,\ P_2,\ P_3$ are young leaf primordia, $P_4 - P_8$ are older leaf primordia.

{Courtesy of D. Reinhardt and E. R. Pesce, University of Bern [55] }

new organ formation.

It has also been well understood how regions with different gene activities or gene expression patterns are established during development [70], [14]. The question is: How are these gene expression patterns linked to generation of shape? How do growth and morphological change both influence and respond to the gene activity? How to model the genetically controlled growth explaining this link? Different strategies of modeling growth controlled by gene expression patterns have been discussed in papers by Coen, Rolland-Lagan and others [15] and by Green [25]. However, they have not been cast into a precise mathematical form. Perhaps, we should follow Green's advice, "To relate wide range of phenotypical activity to gene expression, schemes are needed where the input comprises reasonable gene products and the output embodies both the geometrical specifics and the various biological modes of implementation".

1.2 Why a pattern theoretic approach?

A sequence of images collected over time provides empirical knowledge about growth of an organism. In order to study and recognize the observed growth pattern as normal or abnormal mathematical representation of such knowledge is required. For this purpose a pattern theoretic framework is particularly well-suited since it appears to be a natural formal language of biological development.

In the view of Pattern Theory [27], the growth of an organism is a complex structure composed of simpler ones and regulated with appropriate probability laws. Indeed, there is order and logic to biological shape generation. For example, the development of a chicken limb begins from a small bud and proceeds in order through upper limb, forelimb, wrist to the digits. These modular units are simple building blocks of the chicken limb. Each modular unit evolves with some variations in size and shape. Variability of the modular structure of the chicken limb is captured by the similarity group of transformations with probability measures, a typical pattern theoretic tool for modeling.

Considering the phenomenon of a biological growth in general, the following elementary cell events contribute to generation of shape of a growing organism:

1. cell division or mitosis,
2. cell death, local arrest of growth,
3. cell enlargement,
4. cell movement typical for motile cells,

with time and locations of single cell events being controlled by the genes. We can then interpret elementary cell events in space-time as “atoms” or “generators” of growth using “atomistic” or elementary concepts of pattern theory. Mathematically, generators are represented by subsets of the full continuum of coordinates of organism’s domain.

Each elementary cell decision results in a local deformation of the cellular field of the organism such as expansion or contraction, for instance. Following a transformational concept of a pattern theoretic modeling, we can define a group of bijective transformations operating on atoms.

Given that a biological process of growth is a sequence of elementary cell decisions a growth pattern can be represented by subsequent local transformations of the coordinates of the initial cellular field into the coordinates of the grown cellular field. In pattern theoretic language, such a growth pattern is a composition of elementary transformations that is a configuration of generators with an architecture type called “chain” (a chain connector graph).

In the populations of specimens under study, growth patterns exhibit variability from specimen to specimen. It follows that elementary deformations should be random with probability distributions that can be explicitly induced by the underlying probability laws controlling occurrences of biological events in space-time. Using the pattern theoretic tool of probabilistic transformations, we can associate probabilities with growth configurations and thus capture the range of possible growth patterns.

One of the main purposes of a pattern theoretic model is to infer the source of an observed pattern. The source is the deep regular structure incorporated into the model and hidden via the sensing channel (positron emission (PET), computed tomography (CT), magnetic resonance imaging (MRI), confocal microscopy). Therefore, it has to be estimated. In the case of biological growth, gene actions governing a spatial-temporal process of elementary biological events are the source of observed shape changes. Representing the source by intensity of cell decisions per unit time and per unit volume and imposing a meaningful *a priori* probabilistic model we can develop an optimization algorithm for its *maximum a posteriori* estimation from images. In this way, we hope to gain a new insight into the growth-induced shape generation process as controlled by the genes. In particular, we expect that an analysis of the dynamics of growth seen in micrographs of a developing embryo will reveal the role of gene expression patterns in morphogenesis.

Representation of shape dissimilarities seen in images by probabilistic transformations of the underlying coordinate systems has been used in *computational anatomy* [32]. Computation of growth of brain structures based on the dynamical model of growth as a sequence of the genetically controlled transformations is a new direction of computational anatomy. With the development of the genetically-based model of growth using pattern theoretic concepts we hope to contribute to further advancements in this field.

We shall now have a look at a relevant pattern theoretic *Global Shape Model* [26] of brain structures in computational anatomy.

1.3 Pattern theoretic models in computational anatomy

The recently developed discipline of computational anatomy has emerged from a study of normal and abnormal variation of brain anatomies in humans and primate monkeys for the purpose of detection of pathological pattern behavior. Here, biological patterns are brain anatomies (gyri and sulci, sulcal folds, brain surface) that exhibit high variability in size and configuration. Therefore, the Global Shape Model to be described below appears to be appropriate since it captures a considerable biological variability around the typical or mean shape.

According to this model, differences in the population of some anatomical structure are studied in a biologically and quantitatively meaningful manner, namely, through diffeomorphic transformations

$$\vec{h} : \vec{x} \in \Omega \leftrightarrows \vec{h}(\vec{x}) = \vec{x} - \vec{u}(\vec{x}) \in \Omega, \tag{1.3.1}$$

where $\vec{u}(\vec{x})$ is the displacement field and Ω is a collection of 1D, 2D and 3D brain anatomies. Since brain anatomies reside in a continuum, it is natural to describe the relationships between brain structures within a given anatomic population with the diffeomorphisms (one-to-one, onto, differentiable with differentiable inverse).

The diffeomorphic behavior is especially important in the case of large deformations $\vec{u}(\vec{x})$ since we want topological features such as, for example, the adjacency or connectivity of the triangular mesh elements of the cortical surface to be preserved under the mapping of one brain surface to another. Quantitatively, the diffeomorphisms maintain the geometric features of the individual brain anatomies such as Riemannian length, Gaussian curvature and surface area that play a significant role in disease diagnosis. Also, the empirical statistics building towards one brain or the other are not biased. Thus, the emphasis is transferred from the image ensemble, coming in the form of rectangular arrays, to the diffeomorphic transformations that generate them. Formally, given any two elements $I_n,\ I_m \in I$, where I is the ideal medical imagery and $I_k = \{I_k(\vec{x}), \vec{x} \in \Omega\}$ is a contrast function taking the color intensity values from some imaging modality, we would like to compute diffeomorphisms h with their inverses $h^{-1} = \phi$ such that

$$I_n \underset{\phi_{mn}=h_{nm}^{-1}}{\overset{h_{nm}}{\rightleftarrows}} I_m. \tag{1.3.2}$$

In the case that h is a large deformation map it is assumed that it evolves in time as a flow given by the solution to the transport ordinary differential equation [32] with the boundary condition on $t \in [0, T]$ [10], [11], [13], [12],

$$I_n(h(\vec{x}, 0)) = I_n,\ \ I_n(h(\vec{x}, T)) = I_m, \tag{1.3.3}$$

$$\frac{d\phi(\vec{x}, t)}{dt} = \vec{v}(\phi(\vec{x}, t), t).\ \phi(\vec{x}, 0) = \vec{x}, \tag{1.3.4}$$

$$\frac{\partial h(\vec{x}, t)}{\partial t} = -\nabla_x^t h(\vec{x}, t)\vec{v}(\vec{x}, t),\ \ \vec{h}(\vec{x}, 0) = \vec{x}, \tag{1.3.5}$$

where $\vec{v}(\vec{x}, t) : \Omega \times [0, T] \to \Re^3$ is the space-time velocity field. The optimal estimate of h matching observation I_m to I_n is given by

$$\hat{h}(\vec{x}, T) = \int_0^T -\nabla_x^t \hat{h}(\vec{x}, t)\hat{\vec{v}}(\vec{x}, t)dt + \vec{x},\ \ \vec{x} \in \Omega, \tag{1.3.6}$$

where the velocity field estimate satisfies

$$\hat{\vec{v}}(\vec{x}, t) = \arg\min_{v \in V} \|v\|_V^2 + \|I_n(h(\vec{x}, T)) - I_m(\vec{x})\|^2. \tag{1.3.7}$$

On the right-hand side of (1.3.7) we have

(i) $\|v\|_V^2 = \int_0^T \int_\Omega \|L\vec{v}(\vec{x}, t)\|^2 d\vec{x}dt$ subject to $I_n(h(\vec{x}, 0)) = I_n,\ \ I_n(h(\vec{x}, T)) = I_m$. V is a Sobolev space with a norm induced by a linear differential operator L (the Navier operator [10], [11], [12] or the Laplacian [1], for instance). The choice of the differential operator is usually driven by the material properties of the considered template brain anatomy. If the template represents an elastic cortical surface then the differential operator L is derived from the linear shell theory of elasticity in order to realistically model bending of the elastic brain surface [18].

(ii) $\|I_n(h(\vec{x}, T)) - I_m(\vec{x})\|^2$ is a quadratic distance function defining the cost for landmark and image matching. Denoting $\|I_n(h(\vec{x}, T)) - I_m(\vec{x})\|^2 = d(\vec{x})$, we have

$$d(\vec{x}) = \begin{cases} \sum_{l=1}^L [\vec{y}_l - h(\vec{x}_l, T)]^t \Sigma_l^{-1} [\vec{y}_l - h(\vec{x}_l, T)] & \text{landmark matching,} \\ \frac{1}{\sigma^2} \int_\Omega |I_n(h(\vec{x}, T)) - I_m(\vec{x})|^2 dx & \text{image matching.} \end{cases} \tag{1.3.8}$$

Here, $\{x_l \in \Omega, l = 1, 2, \ldots, L\}$ and $\{y_l \in \Omega, l = 1, 2, \ldots, L\}$ are given landmarks in images I_n and I_m, respectively, to be matched.

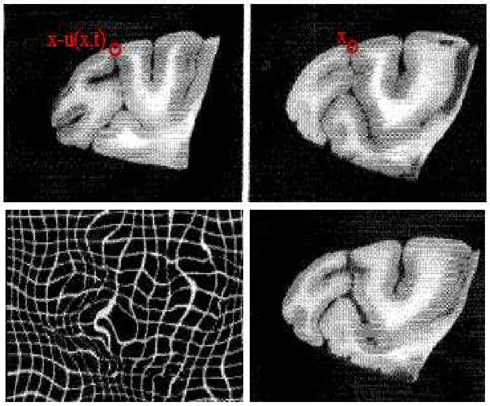

Figure 1.3.1: Top panel: The monkey cortex cryosection, I_{temp}, and the second monkey slice, I_{study}. Bottom panel: The fluid transformation applied to the Cartesian grid and the result of fluidly deforming $I_{template}$ into I_{study}.
{Courtesy of G. E. Christensen, R. D. Rabbitt, M. I. Miller [12]}

To build the Global Shape Model we need one or several templates containing typical structures of complex anatomy and the prior probability measure on the space of $\Re^n$- valued diffeomorphic transformations H with $n = 2, 3$. The template is empirically estimated from the image ensemble of brain anatomies as the average of the family of maps to the population of N anatomical shapes providing the minimum mean-squared distance template I_{temp} [31]. The other members of the population are viewed as *deformable templates* $I_i = I_{temp}(h_i(\vec{x})), \vec{x} \in \Omega$ that is $I_i(\vec{x}) = I_{temp}(\vec{x} - \vec{u}(\vec{x}))$. Figure 1.3.1 illustrates a 2D template of the monkey cortex cryosection I_{temp}, the second monkey slice I_{study}, the estimated fluid transformation h applied to the Cartesian coordinates of I_{temp} and the result of fluidly deforming $I_{template}$ into I_{study} [12]. As we can see, the diffeomorphic transformations are the non-linear displacement fields $u_1(\vec{x}), \ldots, u_n(\vec{x})$, with $n = 2$ or 3.

Now, we would like to associate a probability measure p with each field realization that explicitly induces the probability distribution on the space of images I. The general approach to construct the prior probability measure on the ideal imagery I or equivalently on the submanifolds $M_\alpha \in \Re^3$ (representing 0, 1, 2, 3-dimensional brain substructures) is to view the set of anatomical maps $h^i(\vec{x}) = \vec{x} - \vec{u}^i(\vec{x})$, $i = 1, \ldots, N$ as the set of samples from a Gaussian random field specified by the covariance matrix field $K : M_\alpha \times M_\alpha \to \Re^n \times \Re^n$ and a complete $\Re^n$-valued orthonormal basis $\{\vec{\psi}_k, k = 0, 1, 2, ...\}$ defined on the template submanifold M_α. The random Gaussian field becomes

$$\vec{u}(\vec{x}) = \left(\sum_{k_1=0}^{\infty} u_{k_1} \psi_{k_1}, \ldots, \sum_{k_n=0}^{\infty} u_{k_n} \psi_{k_n} \right), \tag{1.3.9}$$

where $n = 2,\ 3$ and $\vec{u}_k$ are independent Gaussian random variables with the maximum-likelihood estimates for the mean μ_k and variances σ_k^2 obtained from the population of N submanifolds M_α^i.

Overall, we conclude that the Global Shape Model represents anatomies as probabilistically deformable templates. The deformable template is an anatomical ensemble $(\Omega,\ H,\ I,\ P)$, where

1. $\Omega = \cup_\alpha M_\alpha$ is a collection of 0, 1, 2, 3-dimensional manifolds,
2. H is the set of diffeomorphic maps of high dimension defined as $\Re^n$-valued displacement fields, $n = 2,\ 3$,
3. $I = \cup_\alpha H_\alpha I_{temp} = \cup_\alpha I_\alpha$ is the set of ideal imagery where all elements $I_i \in I_\alpha$ are topologically equivalent,
4. $p \in P$ are prior probability measures on H representing the biological variability based on the observed population.

A given knowledge representation of the biological variability of brain anatomies in the form of prior probability measures on the deformable template can be used for the study of the neuropsychiatric disease (schizophrenia, for instance) and associated morphological changes. Populations of patients with neuropsychiatric diseases are characterized by subtle and distributed abnormalities of brain structure and shape. These populations can be compared to normal populations through the prior measure reflecting normal and abnormal variation of the component structures of the brain.

We are led to a Bayesian hypothesis testing for disease where the null hypothesis is formulated as the base measure representing normal anatomical variation: the random deformations h under the null hypothesis H_0 have densities $p_0(h)$. Disease or abnormality is understood in the sense of quantitative measure of anatomical variation relative to the base measure, that refers to

(i) local or regional alterations in the size and shape of brain structures representing large deviation from normal,

(ii) presence or absence of substructures corresponding to a fundamental change in topology.

Hence, the random deformations characterizing the disease have probability densities $p_1(h)$ constituting the disease hypothesis H_1.

Computational anatomy provides us with the rules of volumeric transformations given as the transport equations of continuum mechanics and probability measures constructed on the group of transformations in the way consistent with the physical properties of a deformable elastic solid. The probability laws (the Gaussian random fields) predict how this tissue can bend or change in reality based on a sample of observations. All in all, the Global Shape Model of brain anatomies generates very realistic structures and has a potential to reveal normal and diseased brain structures.

1.4 A link between anatomical models and the proposed GRID model

In computational anatomy, diffeomorphic transformations are determined by changes in pixel values of the brain images under study. These transformations are hidden in the background space of coordinates and are inferred from images as producing the shortest paths between a template image I_{temp} and an image under study I_α. A smooth mapping of anatomical and geometric landmarks onto their homologues from specimen to specimen was pioneered by F. Bookstein [3], [4], [5]. Such a transformation is modeled as a thin plate spline that interpolates the distances between the corresponding landmarks and minimizes the bending energy of any such interpolating function. Other image and landmark matching algorithms have been developed for inference of optimal large transformations that perform image registration consistent with the material properties of the considered template brain anatomy [43], [10], [11], [13], [12], [21], [35], [36], [41], [9].

These algorithms have been applied to estimation of deformation fields induced by growth. Clearly, the dynamic growth model is given by the continuum mechanics equation of motion (1.3.5) with the velocity field satisfying the optimality criterion (1.3.7). It describes growth as a diffeomorphic space-time flow applied to the Cartesian coordinates of anatomical structure at some initial age. Given a sequence of images collected over time $\{I_i\}_{i=1}^m$, the geometric flow carries the given initial brain anatomy through all ages i of the growth period $[1, m]$.

Figure 1.4.1 illustrates the dynamic growth model where the source of observations $I_t^D \in I^D$ is given by the set of all growth flows $I(h(\vec{x}, t)),\ t \in [0, T]$. Here, I's are ideal images and I^D are observed images obtained via some noisy sensing channel (MRI, CT, PET). The likelihood density function $P_{I_t^D|h(\vec{x},t)}$ models the image under study I_α^D as a sample from a Gaussian process with the mean given by the template image under transformation $I_{temp}^D(h(\vec{x}, t))$. P_h is a prior probability measure on the set of all flows H favoring a certain type of transformation (viscous, visco-elastic, elastic) at each time instant t. It is given in Gibbs form with the Gibbs potential usually defined as the Lagrangian energy density in the form $\|v\|_V^2 = \int_0^T \int_\Omega \|L\vec{v}(\vec{x}, t)\|^2 d\vec{x}dt$. The "inference engine" is an image and landmark matching algorithm that returns a *maximum a posteriori* estimate of the growth flow.

It is tempting to implement this model for image analysis of normal and abnormal patterns of growth. However, from a biological perspective, it is not material constants that regulate growth, it is the genetic control system. These random transformations are biologically motivated with the underlying genetic control expressed by probability laws governing the spatial-temporal patterns of elementary cell decisions. This fundamental biological fact hints at the presence of a hidden source of the growth-related transformation that controls it so that the template image is continuously deformed into the study image. Mathematically, such a transformation can be represented by a parameter-dependent diffeomorphic flow $h(\lambda(\vec{x}, t), \vec{x}, t)$, where λ is referred to the unknown growth parameter (or parame-

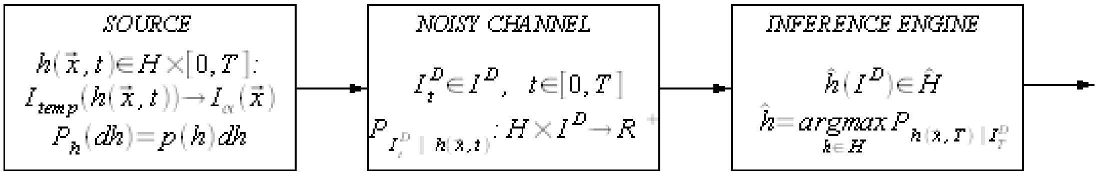

Figure 1.4.1: Illustration of the dynamic growth model in computational anatomy. The source of observations is the set of all growth flows $I(h(\vec{x},t)),\ t\in[0,T]$ with the prior probability measure P_h, I^D are observed noisy images, $\hat{h}(\vec{x},T)$ is an optimal estimate of the growth flow.

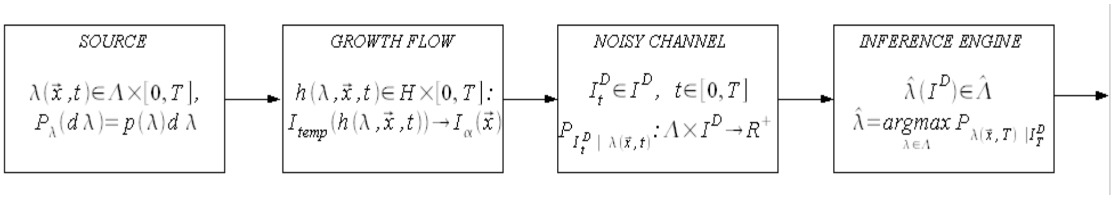

Figure 1.4.2: Illustration of the dynamic GRID growth model. The source of observations is the set of all growth parameters $\lambda(\vec{x},t)\in\Lambda\times[0,T]$ with the prior probability measure P_{λ}, $h(\lambda(\vec{x},t),\vec{x},t)$ are growth flows generated by the GRID equation of growth, I^D are observed noisy images, $\hat{\lambda}(\vec{x},T)$ is an optimal control of the growth flow.

ters) such as intensity of cell decisions, for instance. It seems natural to define a smaller, more structured subset of H appropriate to modeling biological deformations $h(\lambda(\vec{x},\cdot),\vec{x},\cdot)$ at each time t. We are led to a pattern theoretic model called *the Growth as Random Iterated Diffeomorphisms* (GRID) [62], [63], [29], that is schematically illustrated in Figure 1.4.2.

Thus, we are looking for unknown structures hidden deeper in given observations of growth. Figure 1.4.2 suggests that the growth properties can be estimated directly from images using a methodology in computational anatomy of constructing a flow with the least squares property.

1.5 Thesis organization

The Growth as Random Iterated Diffeomorphisms (GRID) model introduced by Grenander constructs complete shape transformations according to fundamental biological principles of growth. The GRID model offers a characterization of growth seen in images in terms of biologically meaningful growth parameters such as locations of elementary cell decisions (e.g. cell division, cell enlargement, cell death, etc.) called *seeds*, local deformation patterns and Poisson intensities underlying seed placements.

Growth deformation on the fine time scale is a composition of several, elementary, local deformations each resulting from a primitive cell decision. The locations of elementary biological events are the focal points of growth or *seeds* around which deformations are concentrated. At each time instant a seed is placed randomly on a time-varying biological coordinate system of the organism called the *Darcyan* system (in honor of D'Arcy Thompson [65]). In Part I of this thesis we study growth patterns on the fine time scale through 2D GRID growth experiments and apply theory of stochastic processes to develop its stochastic formulation and the corresponding statistical properties.

In Chapter 2 we introduce a new concept of a biological Darcyan coordinate system. Its purpose is to carry the genetic code of development and to reflect anatomical changes of the growing organism including its interior and boundary. Mathematically, this is a curvilinear coordinate system, and we develop novel computational methods to generate it based on potential theory and the Level Set Method.

The seed can act as a sink or a source of material, or a combination of both. A local deformation effect is defined by the nature of the seed and can represent a decay or growth in a preferential direction or mixed development. It is modeled with an angular deformation function to capture a variety of biological growth modes. An important consequence of this general model is that it allows a catalog of typical biological deformations to be created, the subject of Chapter 3 of the manuscript. Here, we simulate specific 2D growth patterns (growth of a fish fin, for instance) using certain types of local deformations represented by their corresponding angle-dependent functions.

Randomness incorporated into the model invites the theory of stochastic processes for characterization of the growth pattern in terms of probability distribution functions. Chapter 4 is dedicated to the study of stochastic aspects of the proposed model. In particular, we derive a continuous space-time approximation of the GRID model that is a stochastic differential equation of growth on the fine time scale. The one-dimensional case of the GRID model is considered here for which we derive the Fokker-Planck equation describing the evolution of the probability density of seed trajectories. Through its time-dependent and stationary numerical solutions we find that a random seed trajectory is bimodally distributed in time-space.

Since there is a large number of random biological events contributing to a visible growth pattern as seen in images, the Law of Large Numbers can be used to obtain a deterministic model of growth on a large time scale. In Part II we derive a deterministic integro-differential equation of growth known as a "thermodynamic limit" equation [29] and then develop a novel systematic approach that employs the 2D version of this equation to infer growth properties of the organism directly from micrographs of its gene expression patterns. We demonstrate this approach using confocal micrographs of gene expression patterns associated with larval development of the Drosophila wing disc.

The derivation of the deterministic equation of macroscopic growth is given in Chapter 5. The macrostructure is represented by a diffeomorphic flow evolving as a collective deformation effect of a multitude of cell decisions. According to the macroscopic growth equation the flow depends on such GRID parameters as the

Poisson intensity of cell decisions and the relative rate of expansion/contraction. One of the important properties discussed here is its consistency with the principle of biological invariance. That is, the inference of Poisson intensity parameter is invariant with respect to the Euclidean group of transformations of the Darcyan coordinate system of the organism.

In Chapter 6 we study a specific example from developmental biology, namely, the larval growth of the Drosophila wing disc given as a sequence of micrographs of the Wingless expression pattern. For direct inference of its growth properties expressed in GRID parameters we follow a methodology in computational anatomy of constructing a flow as a shortest path from one wing disc to another. Using the 2D GRID macroscopic growth law we formulate a discrete optimal control problem where the cost function is given in the form of a Gibbs potential that is the sum of observation (or likelihood) and prior energies. Thus, the proposed estimation algorithm is based on the optimal control problem formulation and further application of Polak-Ribière conjugate gradient routine.

In Chapter 7 we implement the inference algorithm for GRID characterization of the Drosophila wing disc growth. Two cases of growth are considered here. In the first case, the assumption is that the unknown Poisson intensity of cell decisions is time-independent and uniform probability density function in the organism's domain. We find an estimate of the relative rate of expansion/contraction. In the second case, the assumption is that the relative rate of expansion/contraction is constant and the Poisson intensity parameter is time-dependent and spatially non-uniform probability density, allowing the Poisson intensity of biological events to be estimated.

In the latter case, a major challenge is to design an appropriate cost function that measures not only a mismatch in image functions of the initial and grown organisms but also cell activities driving observed growth deformations. We investigate such prior models for the unobserved intensity function as a Gaussian random field and as a random field governing a spatial Poisson point process. We show that the latter choice is biologically motivated and consistent with the discretized version of the macroscopic growth law. From the Bayesian point of view, the optimal value of the Poisson intensity is a *maximum a posteriori* estimate, the mode of a posterior probability measure of a random intensity field given observations in the form of images.

Overall, the most exciting result of this thesis is the GRID-based inference "engine" that finds new potential application in the analysis of micrographs of gene expression patterns in embryos. If there is experimental evidence that the observed dynamics of levels of gene expression is correlated with an underlying biological process of cell decisions, then this hidden connection can be established at least in principle via *maximum a posteriori* estimation of the intensity of cell decisions and the growth-related transformation.

Chapter 2

Biological "Darcyan" coordinate system

In this chapter we introduce a new concept of a biologically meaningful coordinate system that (i) carries information about the spatial distribution of gene activity regions and (ii) captures its effect on the internal structure and shape of an organism during its growth. We develop a novel algorithm that uses image processing tools for the extraction of the boundary, from which is produced the interior Darcyan coordinate system by means of level set evolution.

2.1 A new concept of a biological "Darcyan" coordinate system

The motivation for the design of a biologically meaningful coordinate system within a multicellular organism comes from computational anatomy [32] and developmental biology. In computational anatomy [32], diffeomorphic transformations have been used for quantitative description of morphological changes in an anatomical structure caused by growth. These are one-to-one, onto, differentiable with differentiable inverse mappings defined on the compact background space of Cartesian coordinates defined by the displacement field $\vec{u}(\vec{x})$

$$\vec{x} \to \vec{h}(\vec{x}) = \vec{x} - \vec{u}(\vec{x}) \in \Omega, \tag{2.1.1}$$

where $\Omega \subset \Re^n, n = 2, 3$ represents some component of a human brain (e.g., gyri and sulci in 2D brain slice images, cortical surfaces).

During growth, a biological structure undergoes internal changes in the form of local expansions or contractions. Growth then can be described by subsequent transformations of a grid representing anatomical structures at different ages. Since biological growth exhibits significant variability among organisms in a given population, such deformations are assumed to be probabilistic. This leads to the modeling

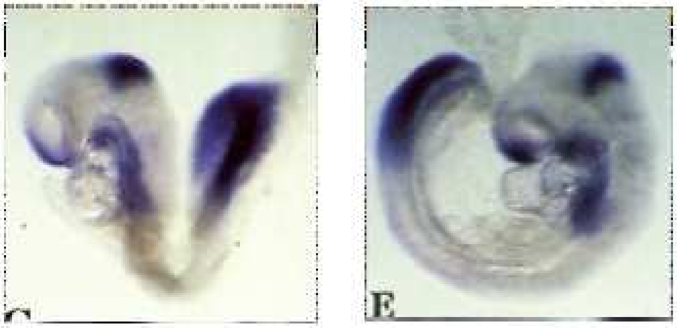

(a) (b)

Figure 2.1.1: Photomicrosopic images of stained mouse embryos corresponding to the gestation periods of approximately 8 and 9 days. {Reproduced with permission of the Company of Biologists}

of biological growth as a sequence of random transformations [29]. The following example from developmental biology suggests that such transformations should be biologically motivated with an underlying genetic control.

From a biological point of view, the complete shape of a growing organism evolves under the patterned control of a multitude of genes. For example, mouse embryonic development is controlled by 308 genes. The gene expression pattern manifests itself in the form of a spatio-temporal distribution of densities of gene products. Figure 2.1.1 shows the regional expression of gene `Fgf8`, called the fibroblast growth factor [39], in the developing mouse embryo observed at different phases of development. Regions with different gene activities designate formative areas where elementary structural changes such as cell division are expected.

With respect to modeling growth-induced deformations, it is desirable to develop biologically plausible coordinate representations that would result in analysis of full images of complete biological shapes including interiors and boundaries. Instead of a fixed Cartesian coordinate system, it seems natural to construct a time-evolving coordinate system within an organism for the spatial distribution of gene activity regions and for capturing changing anatomy of the growing organism as controlled by the active genes.

Ulf Grenander [29] introduced the "Darcyan" coordinate system, named in honour of D'Arcy Thompson [65], so that an elementary biological event such as cell division or cell death is expressed as a point or "seed" in the organism. The "seed" is a signal for a structural change. Given an arbitrary organism occupying a region $\Omega(t_0) \in \Re^2$ at initial time t_0 (see Fig.2.1.2), we shall denote its intrinsic coordinate system as $x(\xi) = (x_1(\xi_1, \xi_2), x_2(\xi_1, \xi_2))$, where $\xi \in \Xi = \{0 \leq \xi_1 \leq 2\pi, 0 \leq \xi_2 \leq \infty\}$. We refer to Ξ as the Darcyan space. All biological decisions will be made inside $\Omega(t)$ for $t \geq t_0$ in terms of the biological coordinates $\xi = (\xi_1, \xi_2)$. As seen in Figure 2.1.2, $x(\xi)$ is a curvilinear coordinate system with ξ_1 and ξ_2 representing radial and angular level sets, respectively. Points in $\Omega(t)$ are given in absolute space coordinates $\vec{x}(\xi_1, \xi_2)$.

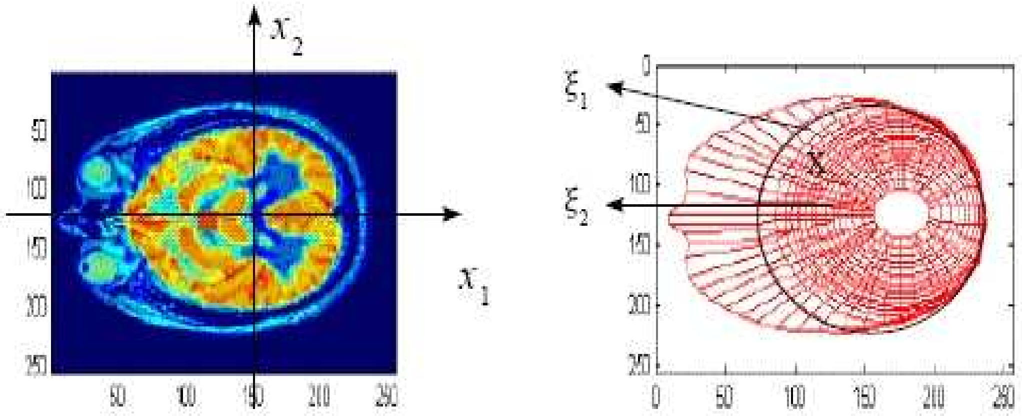

(a) (b)

Figure 2.1.2: A given organism $\Omega(t_0)$ and its biological coordinate system $x(\xi)$. X represents a "seed," i.e., a location of an elementary biological event.

The gene expression patterns are described in biological coordinates $\xi = (\xi_1, \xi_2)$ and the gene actions understood as elementary biological events are expressed as functions of $\xi = (\xi_1, \xi_2)$ and time t (seeds). Overall, the biological coordinate system of the organism consists of the Cartesian coordinate system $(x_1, x_2) \in \Omega(t)$ which reflects its gross anatomy along with its boundary, and the curvilinear coordinate system $(\xi_1, \xi_2) \in \Xi$ which carries the genetic program of its development.

Mathematically, the Darcyan coordinate system

$$\vec{x} : (\xi_1, \xi_2) \in \Xi \to (x_1, x_2) \in \Omega(t) \tag{2.1.2}$$

is a Lagrangian coordinate system: the Lagrangian coordinates $\xi = (\xi_1, \xi_2)$ follow structural changes of the organism as it develops in time. We express the Darcyan metrics through Riemannian metrics with the metric tensor $g = \{g_{ij}\}$ relative to the biological coordinates (ξ_1, ξ_2) as

$$(ds)^2 = \sum_{1 \le i,j \le 2} g_{ij} d\xi_i d\xi_j.$$

2.2 Construction of the Darcyan coordinate system

In this section, we explore two computational methods of constructing the Darcyan coordinate system, one based on potential theory (Poisson equation) and the other based on level set methods. Particular emphasis will be placed on the latter.

2.2.1 The elliptic technique

In order to design a biological coordinate system within an organism $\Omega(t) \in \Re^2$ we impose the following requirements:

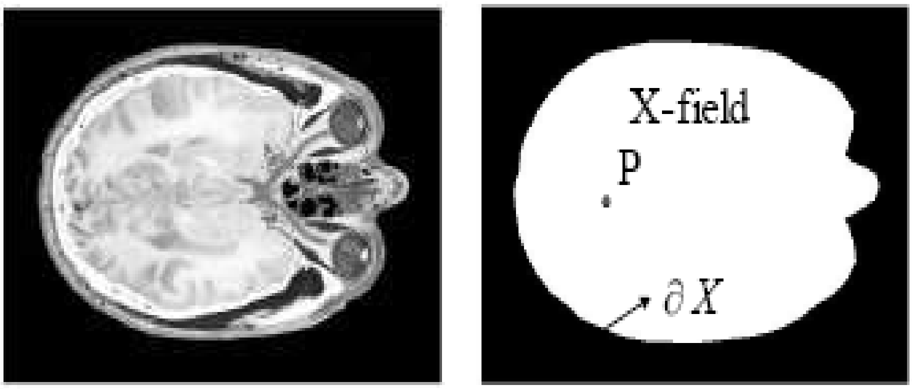

(a) (b)

Figure 2.2.1: An image I of a brain slice (left) and its interior (right) as a selected region of interest. P is a pole which serves as the origin of the biological coordinate system.

1. the distribution of grid cells within $\Omega(t)$ is uniform,
2. the coordinate curves are relatively orthogonal,
3. the coordinate curves are smooth.

Ulf Grenander [29] proposed to construct the biological coordinate system by solving Poisson's equation with Dirichlet boundary conditions in $\Omega(t_0)$ by placing a unit charge – modeled by a Dirac delta function – at an arbitrary interior point $P \subset \Omega(t_0)$, i.e.

$$\Delta u = \delta_P, \quad u|_{\partial\Omega(t_0)} = 0. \tag{2.2.1}$$

This method is known in grid generation literature as a modification of the *inhomogeneous Thomas-Thames-Mastin elliptic grid generator* [37]. Given an image I in the form of an $m \times n$ matrix of greyscale intensity values, we select a region of interest using the Matlab Image Processing Toolbox command `roipoly` to obtain a binary image of the same size with zeros outside the region $\Omega(t_0)$ and ones inside it (see Fig.2.2.1.b).

The numerical solution of (2.2.1) will produce equipotential contours of u within the X-field. We solve this boundary value by discretizing the Laplacian on an $m \times n$ lattice with integer nodal values and lattice cell size $\Delta x = \Delta y = 1$. We apply a simple numerical method known as the *method of successive overrelaxation* [54], with relaxation parameter $0 < w < 2$, as follows. Starting with the initial guess for the solution, $u_{ij}^{(0)} = u^{(0)}(x_i, y_j) = 0$, $1 \le i \le m$, $1 \le j \le n$, we update its values according to the iteration scheme

$$u_{ij}^{(n)} = (1-w)u_{ij}^{(n-1)} + w\frac{1}{4}\left(u_{i+1,j}^{(n-1)} + u_{i-1,j}^{(n)} + u_{i,j-1}^{(n)} + u_{i,j+1}^{(n-1)} - \delta_{Pij}\right), \tag{2.2.2}$$

where $\delta_{P_{ij}} = 1$ if $(x_i, y_j) = P$ and $\delta_{P_{ij}} = 0$ otherwise. A result obtained by 2000 such iterations with the relaxation parameter $w = 0.8$ is shown in Figure 2.2.2.a.

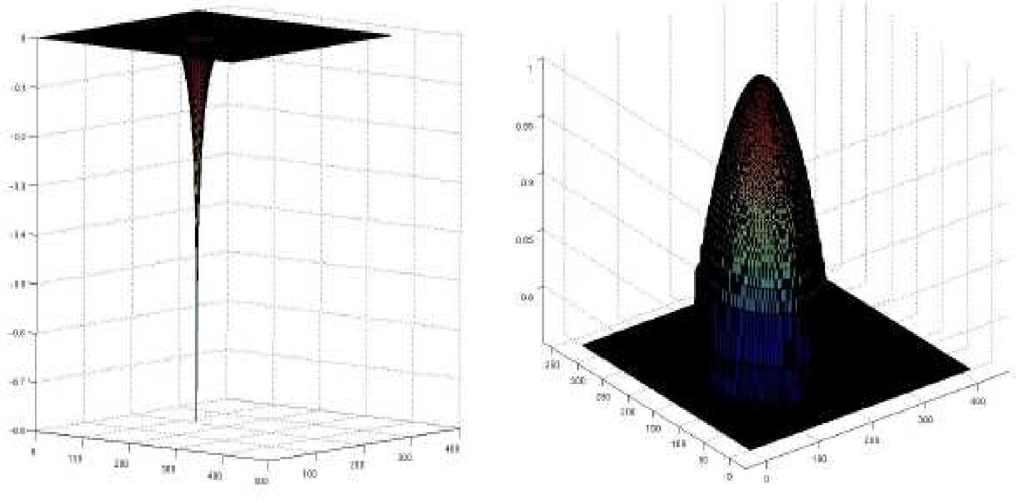

(a) (b)

Figure 2.2.2: (a) Graph of the potential function $u(x)$, a solution to the Dirichlet boundary value problem in (2.2.1) along with level sets. (b) Graphs of the normalized potential function $Lu(x)$, as given by (2.2.3), along with level sets.

Note how the equipotential contours $u(x_1, x_2) = C$, i.e., radial level sets, appear concentrated in the neighbourhood of the pole P. In order that the level sets be more evenly distributed, we consider the application of a nonlinear transformation to the solution of (2.2.1). For example, in Figure 2.2.2.b is presented a graph of the normalized potential v given by

$$v(x_i, y_j) = (Lu)(x_i, y_j) = \frac{1}{\max_{i,j} u(x_i, y_j)} \left[1 - e^{u(x_i, y_j)}\right] \tag{2.2.3}$$

after application of the Matlab histogram equalization procedure `(histeq,250)`, where 250 is the number of discrete greyscale values in the image.

In order to find the orthogonal angular coordinate curves, we parameterize the boundary $\partial\Omega$ by the arclength as $x(s),\ 0 \leq s \leq L$. Then let $\xi_2 = s$ and solve, for fixed ξ, the following ODE, given in vector form,

$$\frac{dx(t, \xi_2)}{dt} = \frac{\nabla v}{\parallel \nabla v \parallel}. \tag{2.2.4}$$

Here, v is the modified potential function obtained by means of some nonlinear transformation applied to the potential solution u of (2.2.1) and ∇v denotes the gradient of v at a point $x \in X \cup \partial X$ outside a neighbourhood of pole P.

The system of N discretized ODEs in (2.2.4) describes the advection of N initially equidistant points on the boundary ∂X of the organism in the direction of ∇v, which is initially normal to ∂X at a boundary point x. When each of these trajectories reaches the first nonzero radial level set $u(x(t_1, \xi_2)) = C_1$ or, equivalently, $\xi_1 = t_1$, we set $\xi_1 = t_1$ on each of the N solution curves. In this fashion,

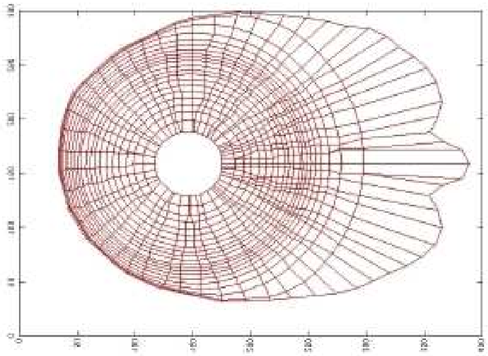

Figure 2.2.3: The Darcyan coordinate system constructed for the interior of the brain slice of Fig.2.2.1.

we generate N angular coordinate curves that cross $N-1$ radial coordinate curves by moving the points $x(\xi_1 = t, \xi_2 = s_j)$, $1 \leq j \leq N$, in a normal direction for $\xi_1 = t_i$, $t_1 < t_2 < \cdots < t_{N-1}$. The procedure of radial and angular coordinate curve construction presented above is realized in Matlab code “darcyan4.m” (see Appendix C). Examples of such Darcyan coordinate systems constructed by this elliptic technique are shown in the right panel of Figure 2.1.2.b and in Figure 2.2.3.

The computation of the radial and angular level sets was performed on a rectangular grid of 333 × 418 points. For $N = 60$, the total CPU time required was 67.38 seconds. Since the positions of boundary points as computed by (2.2.4) were restricted to integer values on the grid, the trajectories of some neighbouring points, as they moved closer to the origin and therefore to one another, merged into one trajectory. One way to overcome this difficulty is to redistribute the points along the non-zero radial level sets. Also, the grid cells appeared non-uniform in size. This is not usually an issue when one is interested in tracking localized growth away from the boundary.

All in all, the resulting Darcyan grid can be improved, if needed, depending upon the user’s intentions. For example, the accuracy in the approximation of the potential function solution of (2.2.1) could be increased, or the pole relocated or the refinement of the Cartesian grid increased. Unfortunately, there is an issue regarding the Poisson method for 3D coordinate grid generation: it is not guaranteed that a trajectory passing through an interior point is unique [29].

2.2.2 The Level Set Method

The level set method, introduced by Osher and Sethian [48] and described in [59], provides an alternative technique for the generation of Darcyan coordinate systems in 2D and 3D. In [58], it was shown that the level set method of the body-fitted grid generation method provides an efficient and flexible way of constructing evenly distributed, smooth exterior or interior grid lines around some closed, simply connected set X with an arbitrary boundary ∂X. However, the particular examples treated in [58] were limited to convex and nonconvex axisymmetric sets for which the radial coordinate curves tend toward a circle that smoothly collapses to a point that determines the origin of the coordinate system (Grayson-Hamilton Theorem [24]). Below, we propose a level set technique [52] that constructs a grid within an arbitrary set X.

The basic idea of this method is to view the boundary (or surface in the 3D case) of an organism as a propagating front. This front propagates inward and normal to itself with a speed law F that ensures the smooth evolution of the coordinate curves. Since a front that moves at a speed F which depends upon its curvature k and normal direction remains smooth for all times [59], the function $F(k)$ given by [58]

$$F(k) = \min(-k, F_{threshold}), \tag{2.2.5}$$

is an adequate model for our purposes. $F_{threshold}$ is needed to ensure that points with high negative curvature (i.e., belonging to nonconvex parts of the propagating boundary) do not move against the inward flow. We stress the fact that the front evolution under the speed law (2.2.5) is a geometric curve flow. The theory of front evolution [57] views the front as an interface separating two regions, and the Eulerian level set formulation of front motion [59] is usually chosen to construct a physically meaningful solution. Since the speed is determined by the intrinsic geometric properties of the front, it is natural to formulate the equations of front evolution in the following Lagrangian form,

$$x_t = F(k)\frac{y_s}{\sqrt{x_s^2 + y_s^2}}, \quad y_t = -F(k)\frac{x_s}{\sqrt{x_s^2 + y_s^2}}, \tag{2.2.6}$$

with $x(s, 0) = \alpha(s)$ and $y(s, 0) = \beta(s)$, $s \in [0, S]$, $t \in [0, T]$. Here $\vec{X} = (x(s, t), y(s, t))$ is the position vector of the curve at time t, parameterized by $s \in [0, S]$. The unit normal $\vec{n}$ to the evolving front and the mean curvature k are given by

$$\vec{n} = \left(\frac{y_s}{\sqrt{x_s^2 + y_s^2}}, -\frac{x_s}{\sqrt{x_s^2 + y_s^2}}\right), \qquad k = \frac{y_{ss}x_s - x_{ss}y_s}{(x_s^2 + y_s^2)^{3/2}}. \tag{2.2.7}$$

The problem of front motion in (2.2.6) is idealized when $\alpha(s)$ and $\beta(s)$ are given as smooth functions of s. In medical images, the boundaries of anatomical structures may exhibit a complex behaviour such as significant oscillations or sharp corners. Hence the initial data for the equations of motion in (2.2.6) are given in the form of an array of coordinates of boundary pixels. We are faced with two problems:

1. Extraction of the initial boundary information,
2. Numerical solution of the equations of motion (2.2.6) using discrete parametrization of the front.

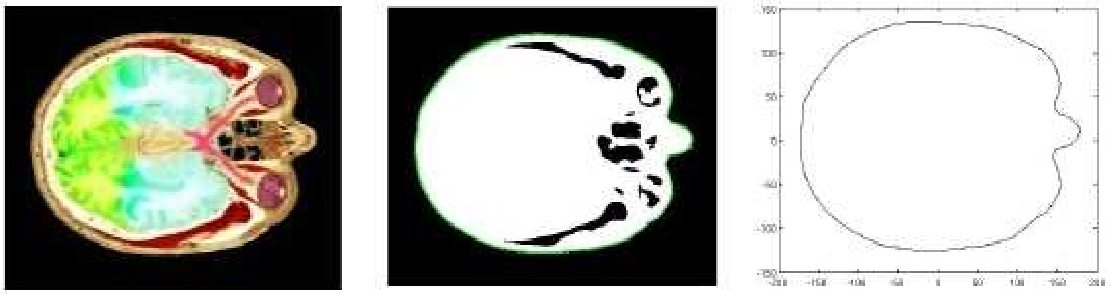

(a) (b) (c)

Figure 2.2.4: (a) Given image, (b) automatic boundary detection, (c) extracted boundary in absolute space.

In order to solve these problems, we propose the following algorithm.

Algorithm for interior coordinate system generation

1. Apply an averaging filter to a given image to remove small noise (e.g., small notches, oscillations) from the boundary.
2. Convert the intensity image to a binary image using the computed global image threshold intensity level.
3. Trace an object in the binary image by specifying the coordinates of the starting boundary pixel (its value is 1) and the initial direction for the search of the neighbouring boundary pixel. The Matlab image processing procedure `bwtraceboundary` identifies boundary pixel coordinates (see Fig.2.2.4.b).
4. Apply a linear transformation to the pixel coordinate system to shift the origin to the middle of the image domain and plot the extracted boundary (see Fig.2.2.4.c).
5. Reparametrize the boundary by the arclength α – note that, by definition, $d\alpha = \sqrt{(x_s^2 + y_s^2)}ds$ – and place N nodes $\vec{X}(\alpha_1), \vec{X}(\alpha_2), \cdots, \vec{X}(\alpha_N)$ uniformly in arclength over the boundary curve (see Fig.2.2.5.a).
6. Initialize the time step Δt so that the ratio $\Delta t/\Delta\alpha$, the arclength spacing between neighbouring boundary nodes, satisfies the *Courant-Friedrichs-Levy condition* [7] for stability of the numerical algorithm.
7. Discretize the equations of motion (2.2.6) using central difference schemes to approximate parameter derivatives at each node. Then solve the system of N unlinked ordinary differential equations with unknowns $\{\vec{X}(\alpha_i(\Delta t), \Delta t)\}_{j=1}^{N}$ using a second-order *Heun's method* [42].
8. Redistribute the nodes along a new radial curve to maintain their equal arclength spacing and thus to avoid the merging of trajectories of nodal points.

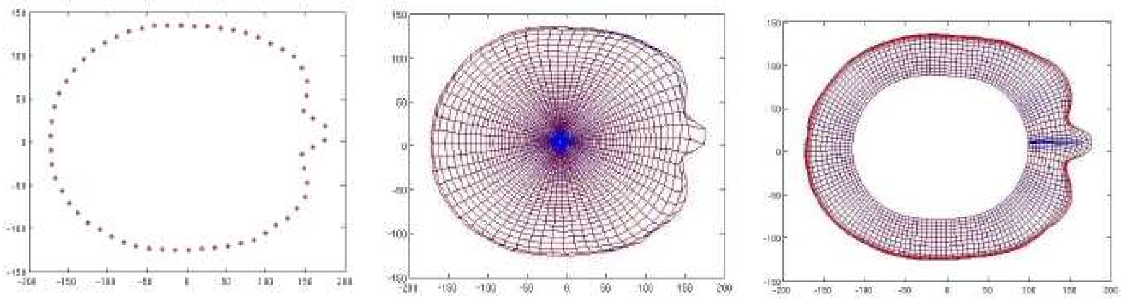

(a) (b) (c)

Figure 2.2.5: (a) Nodal distribution along the initial boundary, $N = 60$. (b) Interior grid of size 77×60. (c) Generation of interior grid without transversal adjustment.

9. Update the values for the time step and the arclength spacing, Δt and $\Delta \alpha$, respectively.
10. Repeat steps (7), (8) and (9) until the average length of trajectories of nodal points leaving the initial boundary becomes greater or equal to the initial arclength spacing multiplied by the parameter $coef \leq 1$, which controls the uniformity of grid cell size and depends upon the user's preference. Record and display the position of obtained radial lines as well as nodal trajectories (since they are angular curves).
11. Reinitialize the radial line obtained and apply steps (7)-(10) to the new initial curve until it is possible to control the stability of the numerical scheme (see Fig.2.2.5.b).

Steps 1-5 are realized in a Matlab code "get_init_boundary_f.m" (see Appendix C). Step 7 of derivative and curvature computation is performed by a Matlab routine "get_rhs.m" (see Appendix C), and Step 8 of nodal redistribution is carried out by a script "redistr.m" (see Appendix C). These subroutines are repeatedly called by a Matlab program "get_darcyan.m" (see Appendix C) that realizes the Level Set Method of Darcyan grid generation described above.

Some comments on the results of the algorithm.

1. The interior coordinate system appears well-structured at a cost of loss of orthogonality of coordinate curves. For initially nonconvex shapes, it is not always possible to compute the advection of N nodes of radial lines in their normal direction (Step 7) without nodal redistribution (Step 8) as time progresses. The transverse lines (nodal trajectories) can come together as shown in Figure 2.2.5.c and cause computational problems (division by zero). In order to avoid this difficulty, we have performed transversal adjustment according to the length of an obtained radial line. Other techniques of nodal redistribution are discussed in [58].

2. As an initially nonconvex closed curve propagates inward under the curvature flow defined by (2.2.5) and (2.2.6), it will not necessarily collapse to a convex

shape (see Fig.2.2.6.a). Moreover, the arclength spacing between neighbouring nodes decreases with time, causing the time step to decrease, thereby making further computations very expensive.

3. In particular, small variations in the computed curvature will grow unconditionally when the arclength spacing becomes on the order of 10^{-2}. To prevent the development of oscillations in the moving curve, some boundary smoothing techniques can be used. A simpler solution to this computational problem would be to terminate the propagation of the boundary as soon as its length starts to grow, followed by a smooth patching of the resultant curvilinear coordinate curves with polar coordinate curves (see Fig.2.2.6.b).

To achieve a transition to the polar grid, we apply an angle-preserving transformation to the terminating radial curve that changes the length of the radius-vector tracing its N nodes $\vec{R} = \vec{X}(\alpha) - \vec{X}_{origin}$ to the radius of a disk while preserving its angle with respect to the abscissa axis x_1. Thus, the angular lines will "flow" to the origin of the Darcyan coordinate system, $\vec{X}_{origin}$ that can easily be computed as the middle point of the terminating radial curve diameter (the maximum Euclidean distance between points of the curve).

In general, this transition cannot guarantee the smoothness of angular coordinate curves since they may enter the terminating radial curve at angles that are different from the ones formed by the radius-vector R and the x_1-axis. It may not be necessary to "close off" the constructed interior grid with the polar grid when one is interested in overall effects of growth on structural and shape changes. However, if it is a localized growth in the neighbourhood of the origin that causes shape changes then the *complete* interior coordinate system is needed.

All in all, the level set-based algorithm provides the most natural way to generate an intrinsic coordinate system within the organism together with its boundary since it allows the coordinate curves to align with its shape curves. It is a biologically meaningful coordinate system in the sense that the genetic program of the organism's development, expressed in terms of the Darcyan ξ_1 and ξ_2 coordinates, which in turn designate the locations of biological decisions (active genes) are independent of the absolute or physical space.

The constructed Darcyan coordinate system provides a computational grid

$$\vec{X}(\xi_{1_i}, \xi_{2_j}),\ 1 \leq i \leq M,\ 1 \leq j \leq N,$$

that deforms in time as the organism develops, thus reflecting its gross anatomical changes.

Remark 2.2.1. *The algorithm for 2D Darcyan coordinate system generation presented here requires further exploration in the case of significantly oscillating shapes (e.g. a "dumbbell" region). In such cases, the propagating front may not collapse to a single radial curve, requiring that the initial organism domain be segmented into two or more disjoint subdomains.*

Remark 2.2.2. *The flexibility and robustness of the level set approach for Darcyan grid generation is an asset when constructing 3D grids. The control of the distances*

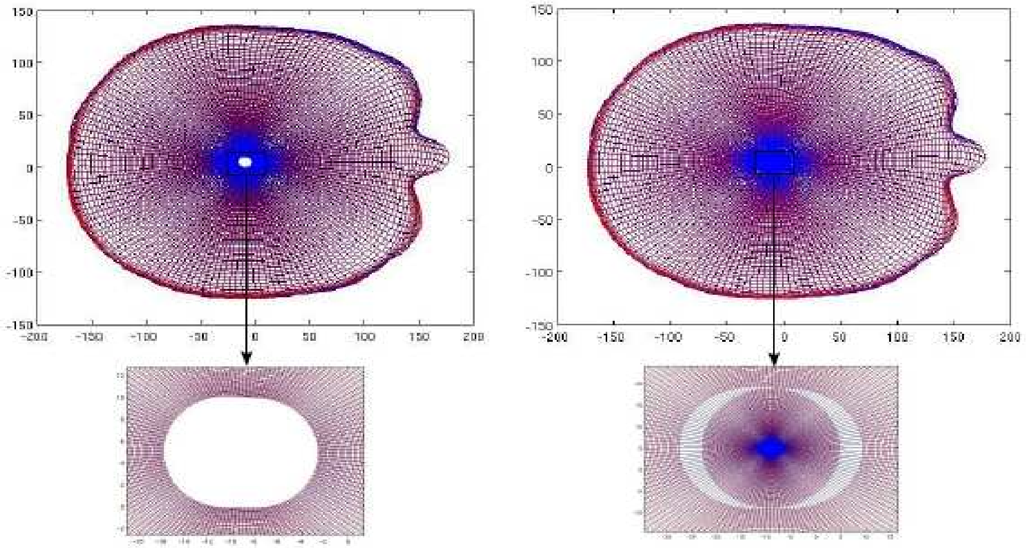

(a) (b)

Figure 2.2.6: (a) Curvilinear coordinate system and a close-up view of the neighbourhood of the terminating radial line. (b) Patching of the curvilinear system with a polar coordinate system. Image size: 150 × 211.

between transversal trajectories can be devised automatically, thus ensuring their separation at each time increment. According to [58], the level set technique of 2D grid generation extends in a straightforward manner to 3D. In the volumetric case, the Eulerian formulation of the equations of front motion is preferable. According to the Eulerian approach, the zero level set surface of a four-dimensional moving surface defines the position of the front. The Lagrangian method based on discrete parameterization of the moving surface would be extremely expensive to realize, requiring a redistribution of surface nodes, tracking nodal trajectories and a small time step for the stability of the numerical solution.

2.3 2D Darcyan coordinate representation of some organisms

We have tested our level-set algorithm for Darcyan coordinate system generation, described above, on other biological shapes. In Figure 2.3.1.a is shown a snapshot of a growing snapdragon petal lobe [56]. The coordinate system within the petal lobe (see Fig.2.3.1.b) was obtained with the grid parameters $F_{threshold} = -|\bar{k}(t)|$, where $\bar{k}(t) = (1/N)\sum_{i=1}^{N} k(\delta\alpha_i, t)$ is the mean curvature of the propagating boundary, $N = 150$ is the number of angular coordinate curves, $coef = 0.6$ is the grid cell size control parameter, and the ratio $\Delta t/\Delta\alpha = 0.8$ ensures the stability of the numerical scheme. Note that with this value of the parameter $coef$ we achieve a relatively uniform grid with only 37 radial lines. The value of $coef$ controls the density of

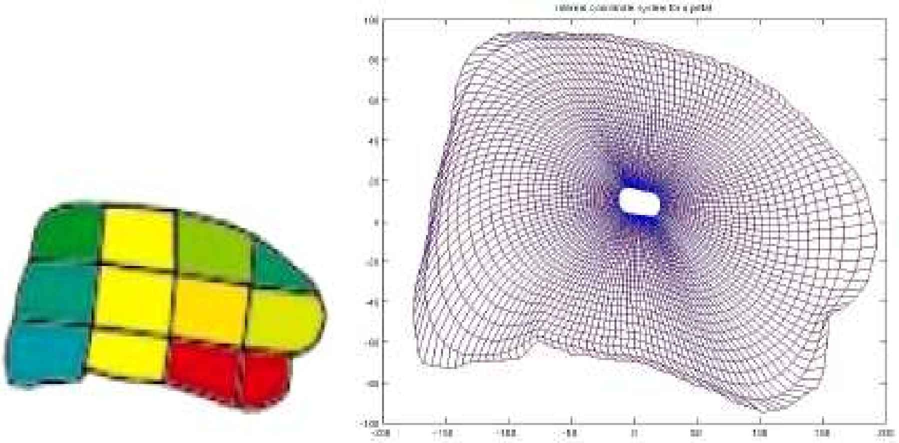

(a) (b)

Figure 2.3.1: (a) Snapdragon petal lobe.
{Courtesy of A.-G. Rolland-Lagan, J.A. Bangham, E. Coen [56]}
(b) The associated Darcyan coordinate system as an interior grid of size 150 × 37.

the field lines: the smaller it is, the denser the field lines are. Computation of the grid required about 1 min of CPU time.

For a more complex shape of a mouse embryo [19] given in Figure 2.3.2.a, we chose the number of angular lines to be $N = 300$, $coef = 1.0$ and $\Delta t/\Delta\alpha = 0.3$. The pointy mouse tail creates a localized high curvature variation in the embryo shape, presenting a major difficulty in handling nodal trajectories near the initial boundary. According to our algorithm, radial curves are recorded at time $\Delta T = \sum_{i=1}^{M} \Delta t_i$, when the average length of these trajectories reaches the arclength spacing of the previous radial curves. However, if we connect them with line segments, then these line segments will intersect.

Therefore, unlike the cases for the brain slice and the snapdragon petal, we record and display nodal trajectories at each time step $\Delta t = 0.3\Delta\alpha$ until the total variation of the moving radial line has significantly decreased. In this way, we obtain a more accurate behaviour of angular curves near the initial boundary. Representing the initial boundary with $N = 300$ nodes yields a finer grid (see Fig.2.3.2.b), thus allowing us to capture the geometry at a finer scale, such as the shapes of developing toes.

The examples presented above demonstrate the flexibility of the level set-based algorithm in grid design and its ability to handle corners and cusps in the initial boundary. It is also an efficient tool for interior grid generation. The CPU time for the 60 × 77 grid computation inside the brain slice (Fig.2.2.5.b) was 55.29 sec, as compared to the 67.38 sec required for the 60 × 60 grid (Fig.2.2.3) using the elliptic technique.

Having constructed the Darcyan coordinate system of an organism under study seen in micrographs, we can also represent its gene expression patterns in Darcyan coordinates. We can extract these biological coordinates by simply demarcating

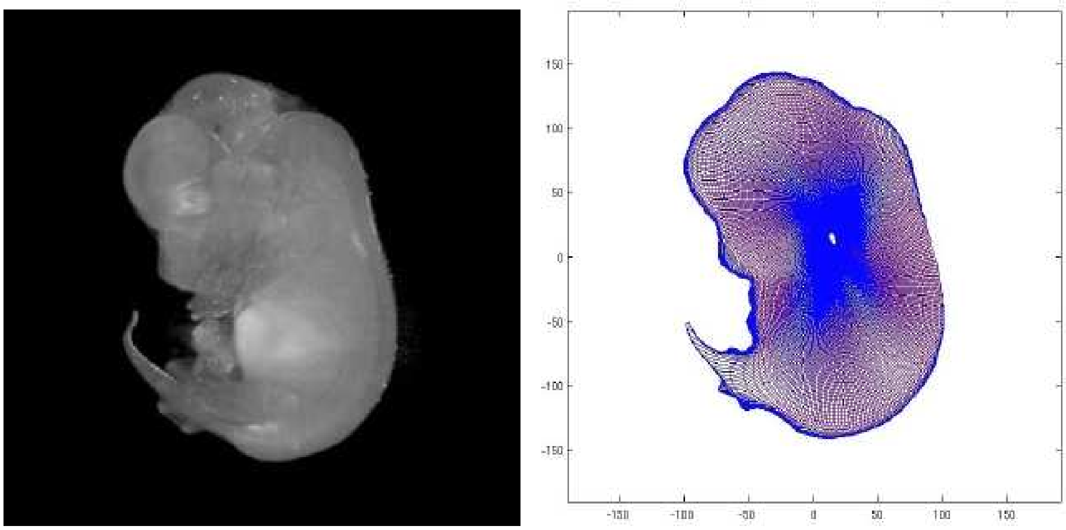

(a)

(b)

Figure 2.3.2: (a) A mouse embryo from the online mouse development atlas at `http://genex.hgu.mrc.ac.uk/Atlas/intro.html`. (b) Darcyan coordinate system of this embryo as an interior grid of size 300 × 125.

the subregions with high levels of expression using Matlab commands `ginput` and `inpolygon`. For example, given micrographs of limb development and cartilage formation revealed by expression of the *Sox9* gene (see Fig.2.3.2)[8] we generate Darcyan coordinate systems for the chick limb bud and then manually outline regions of active *Sox9* gene cites (see Fig.2.3.3). Darcyan coordinates of gene expression patterns marked by red stars in Figure 2.3.4 are visualized using a Matlab code "display_gs.m" (see Appendix C).

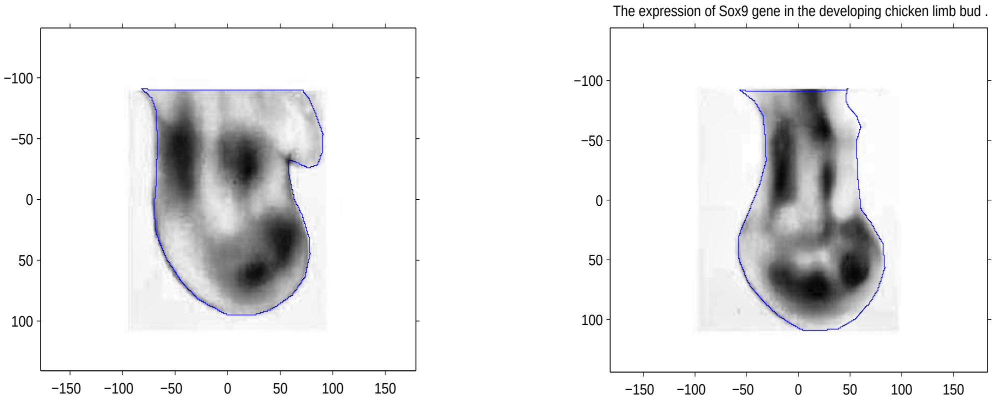

(a)

(b)

Figure 2.3.3: Expression of *Sox9* genes in the chicken limb bud at stages of (a) 24 hours and (b) 26 hours.

{Courtesy of Dr. Juan Hurle, Universidad de Cantabria, Santander, Spain [8]}

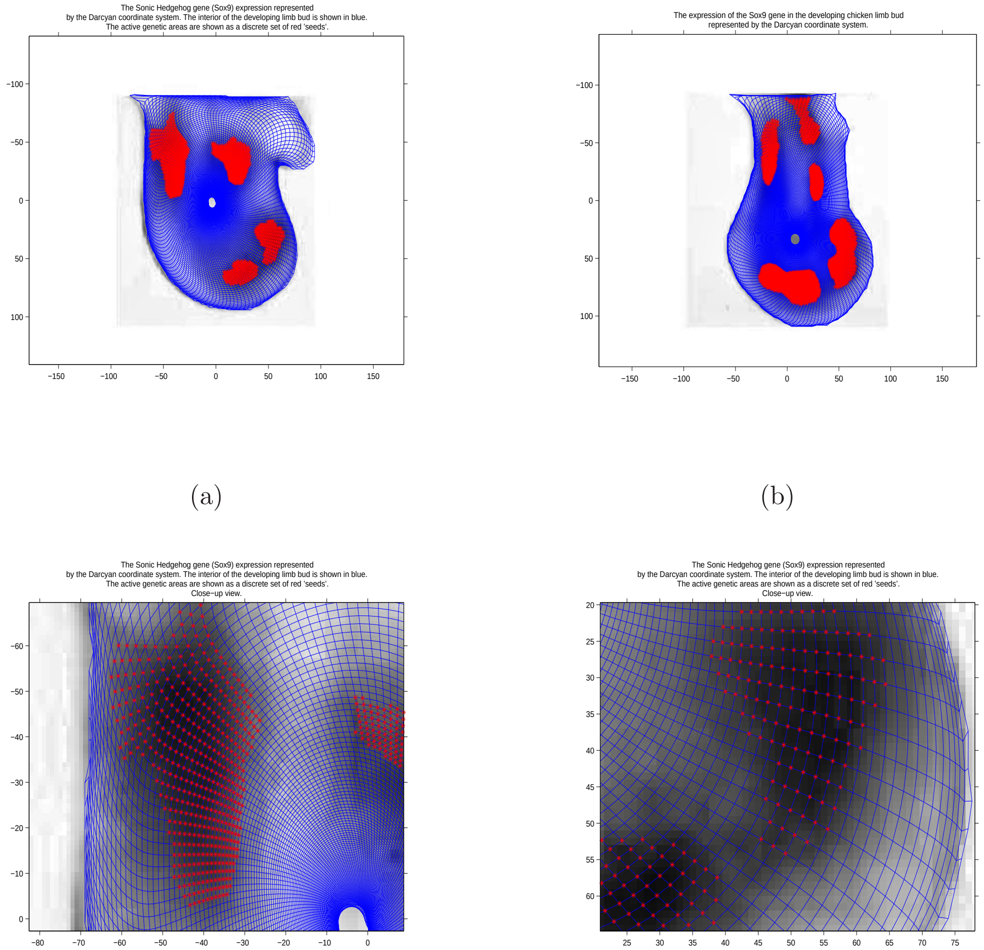

(a) (b)

(c) (d)

Figure 2.3.4: (a), (b) Darcyan coordinate systems of the chicken limb bud at stages of 24 and 26 hours; (c), (d) Close-up views of the seeds representing active *Sox9* gene sites.

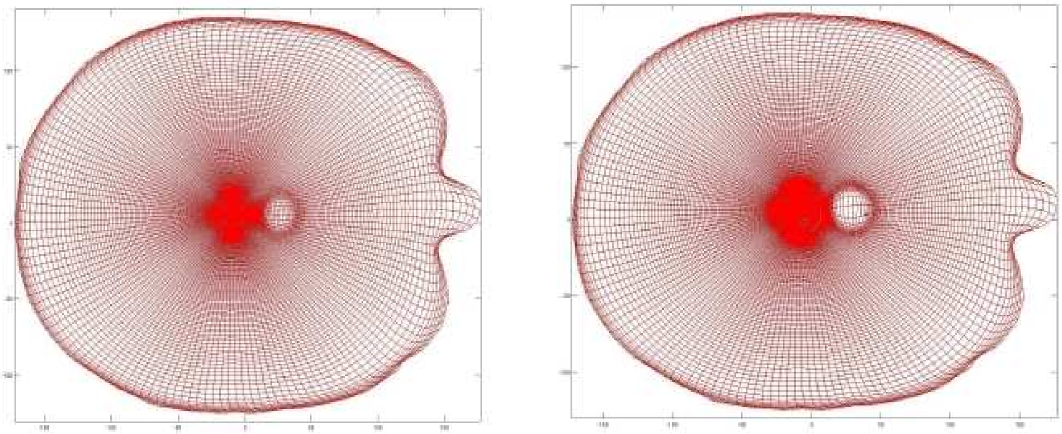

Figure 2.4.1: Deformed Darcyan coordinate system of Fig.2.2.4.a reflecting localized radial growth effect on the internal structure.

2.4 Application of Darcyan computational grids

The construction of a Darcyan coordinate system representing the domain of a biological system allows us to simulate the growth of the system. This can be accomplished provided that the growth properties (e.g., growth rate in space and time) are known. In Figure 2.4.1 is presented a synthetic example of a localized radial growth within the brain slice of Figure 2.2.4.a. There is local expansion in the active gene zone and the deformation effects decays away from the zone. As a result, there is no visible change to the boundary. With the development of the organism, its Darcyan coordinate system/grid deforms and captures the nature of localized growth. It is easily seen from Figure 2.4.1 that the amplitude of localized growth is independent of direction.

The Darcyan grid provides a computational domain for the application of diffeomorphic transformations that are defined by biological parameters such as amplitude of growth (possibly direction-dependent) and space- and time-dependent growth rates. As such, biological growth is modeled as a diffeomorphic flow. The deformed interior grid of the developing brain shown in Figure 2.4.1 is a realization of a diffeomorphic flow in time applied to the initial Darcyan coordinate system of the brain slice in Figure 2.2.6.b. This is one result of our experimental studies of the Growth as Random Iterated Diffeomorphisms (GRID) model of biological growth introduced by Grenander [29], further discussion of which will follow in Chapter 3.

Chapter 3

Introduction to the 2D GRID Model

Having built the Darcyan coordinate system of an organism we seek a dynamical growth model that relates anatomical changes of the organism with the gene activities expressed as functions of the biological Darcyan coordinates. Such a model should be capable of analysis of growth patterns in a variety of anatomical parts. In this chapter, we introduce a pattern-theoretic model called Growth as Random Iterated Diffeomorphisms (GRID) originally devised by U. Grenander [29], [33], that constructs complete growth-induced shape transformations according to fundamental biological principles of growth. The proposed model satisfies the following requirements.

(a) Developing organisms in embryology do not know absolute space: embryos develop in the absence of external forces.

(b) Changes in the anatomy of a developing embryo are driven by such biological events as mitosis, cell enlargement, cell movement and cell death.

(c) The equations of growth shall be formulated in terms of biological Darcyan coordinate system related to the anatomy of the organism.

(d) The transformations induced by growth must be diffeomorphic in order to prevent local overlaps of the organism with itself.

(e) Organisms under study consist of a large number of macroscopically small biological units, namely, cells.

(f) Single biological events occur randomly and cause local deformations.

3.1 Main "ingredients" of the 2D GRID model

We shall start developing the GRID model assuming, for simplicity, that growth takes place in $\Re^2$. We shall consider a 2D growing organism taking up the compact region denoted by $\Omega(t) \subseteq \Re^2$ at time t. $\Omega(t)$ is a subset of imaged coordinates expressed in a Cartesian system. We will refer to the Darcyan coordinate system of the imaged organism as $X(\xi)$.

3.1.1 Seeds as locations of cell decisions

According to the GRID model, a biological transformation of an organism is highly determined by cell decisions controlling elementary events like cell divisions, cell death, etc.. This view is consistent with the results of observations of biological growth as discussed, for example, in the classic work by S. Carroll [6]. Since elementary cell decisions are unobserved highly localized random events they are naturally modeled by points of the space-time stochastic Poisson process (see Appendix A) referred to as *seeds*. In relation to embryonic development, seeds represent locations of active gene sites in the cellular field of an embryo, where some structural changes are expected. Different genes may activate at different times, and the nature of resulting deformations may differ as well. This means that seeds turn on and off executing the genetic program of development, and each seed acts as a sink or a source of material, or a combination of both.

Gene activity regions often appear as simple geometric shapes – stripes, lines, spots, dots, or curves–that constitute gene expression patterns. They can be visualized using a powerful confocal microscopy imaging technique as illustrated by an example of the *Sox9* gene expression pattern in the developing chick limb bud [8] in Figure 3.1.1. High levels of concentration of this gene product mark the regions where cartilage growth will take place.

For simplicity of illustration of the GRID model we shall consider an initial organism in the form of a unit disk described by polar coordinates $(\xi_1, \xi_2) = (\rho, \theta)$. In this case, the initial Darcyan coordinate system coincides with the polar grid. Its active gene sets or seeds can be given in various simple geometric shapes or their combinations. Shown in Figure 3.1.2 is an example of spatial seed distribution within the circular organism given as a combination of a line segment, dots and a spot. During growth of the organism, seeds are activated one at each time instant of an elementary cell decision according to the spatial-temporal Poisson point process presented below.

3.1.2 Poisson intensity parameter

The spatial distribution of seeds given in Figure 3.1.2 can, in fact, be dependent on time. For example, single gene cites may be activated in the first stage of development, say, $[t_0, t_1]$, and seeds comprising a line segment and an area may be activated only in the second and third stages of development, $[t_1, t_2]$ and $[t_2, t_3]$, respectively, with times $t_0 \leq t_1 \leq t_2 \leq t_3$. Also, at each stage of development, the seeds turn on at random obeying some spatial probability distribution. The probability distribution may be uniform, for example, giving each seed an equal

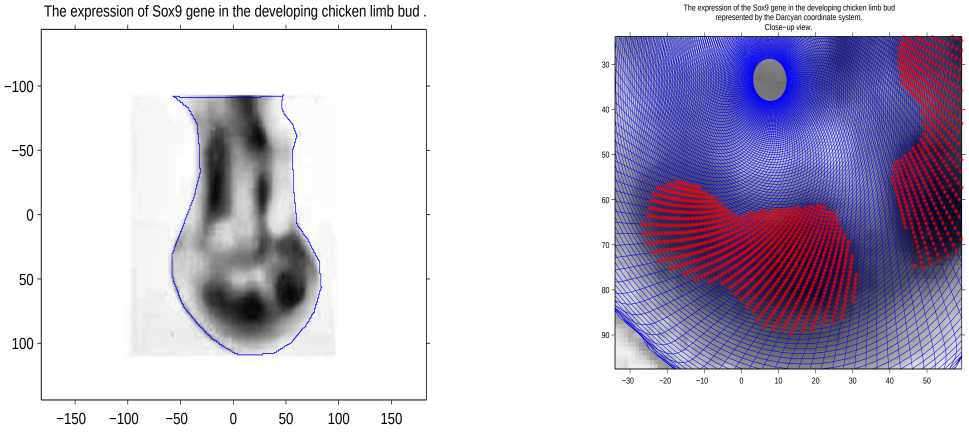

(a) (b)

Figure 3.1.1: (a) Cartilage formation in the chick limb bud revealed by expression of *Sox9* gene [8], (b) Seeds of future cartilage shown as subsets of the Darcyan coordinate system or red spots at stage of 26 hours.

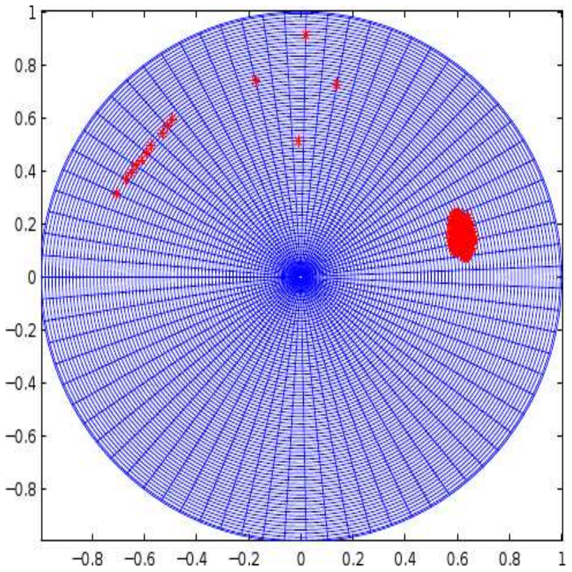

Figure 3.1.2: Example of a spatial seed distribution within an organism in the form of a unit disc. Seeds marked by red stars represent gene activity sites in Darcyan coordinates $(\xi_1, \xi_2) = (\rho, \theta)$.

chance to be activated. It may also be non-uniform, favoring activations of certain seeds over the others in the specified active gene set. We then expect these signals to be realized in anatomical changes of the developing organism in the absolute space-time $X \times [t_0, t_3]$.

Natural spatial-temporal heterogeneity of a biological process of cell decisions underlying shape changes leads to an inhomogeneous space-time Poisson point process. According to the Poisson model, the underlying biological process is a sequence of discrete events occurring as points in Darcyan space-time $\Xi \times [t_0, T]$ with the Poisson intensity parameter $\lambda(\xi, t)$. We assume the simplest form of the inhomogeneous Poisson process without space-time interaction, where the intensity is given by

$$\Lambda(\xi, t) = \lambda_t \times \lambda(\xi). \tag{3.1.1}$$

Here, $\lambda(\xi)$ represents the average genetically-controlled rate of seed activation per unit area $d\xi \in \Xi$ and λ_t is the instantaneous average rate of seed activation at a time t. The Poisson process induces a seed $x(\xi_1, \xi_2)$ in the absolute space X

(a) with intensity of events λ_t per unit time δt (e.g., a second, a minute) so that the expected value of the number of events $\mu(\Xi, T)$ in given time interval $[0, T]$ and anywhere in Ξ is

$$E(\mu(\Xi, T)) = \int_0^T \lambda_t dt$$

(b) with intensity of events λ_x per unit area dx (expressed in the absolute Cartesian coordinates!), so that the expected value of the number of events in some subregion $A \subset \Omega(t)$ and at any time $t \in [0, T]$ is

$$E(\mu(A, t)) = \int_A \lambda_x dx \overset{x=x(\xi)}{=} \int_{\Delta\Xi = x^{-1}(A)} \lambda(\xi) d\xi,$$

where $\lambda_x = \frac{\lambda(\xi)}{J(x(\xi))}$ with the Jacobian of transformation $J(x(\xi)) = \left|\frac{\partial(x_1,x_2)}{\partial(\xi_1,\xi_2)}\right|$ measures the intensity of seed activations in the absolute space expressed through the intrinsic intensity parameter $\lambda(\xi)$, $\xi = \xi(x)$.

The Poisson parameters λ_t and $\lambda(\xi)$ appear to be growth rate characteristics of a developing organism. The Jacobian $J(x(\xi)) = \left|\frac{\partial(x_1,x_2)}{\partial(\xi_1,\xi_2)}\right|$ is related to the density of seeds ξ in the X-field of the organism's domain that is clearly non-uniform (by construction of the Darcyan coordinate system). λ_t is an increasing function of time expressing the fact that as an organism grows there will be many elementary events. The intensity parameter λ_x can be interpreted as the speed of gene switching per dx area expressing the fact that the density of events, or the cell concentration is described in the Cartesian coordinates. All in all, the shape transformations of a growing organism are governed by the underlying Poisson process of discrete decisions of cells or seed placements in space-time with the intensity parameter

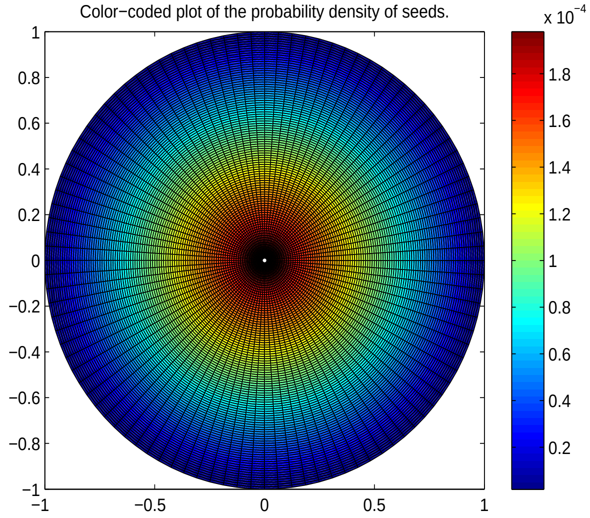

Figure 3.1.3: Color-coded plot of the normalized Poisson intensity $\lambda(\xi)$ of seed placements within an organism in the form of a unit disc. Seeds occupy all the nodes of the Darcyan grid of size 100 × 100.

$\Lambda(\xi, t)$ (3.1.1).

In practice, we usually normalize the intensity per unit area $\lambda(\xi)$ over a finite Darcyan space Ξ and thus obtain the probability density of seed placements. The Darcyan space consists of a countable number of seeds (ξ_{1_i}, ξ_{2_j}), $1 \leq i \leq n$, $1 \leq j \leq m$, with coordinates ξ_{1_i} and ξ_{2_j} enumerating, respectively, radial and angular level sets. The normalized intensity function $\lambda(\xi)$ becomes the probability mass function defined at all seed points (ξ_{1_i}, ξ_{2_j}). An example of such probability mass function is shown in Figure 3.1.3. Here, we are given an organism Ω in the form of a unit disc ideally comprised of a continuum of seeds $x(\xi) \in \Omega$ that is numerically approximated by a large number of seeds located at the nodes of the Darcyan grid. The probability mass has been assigned to all Darcyan nodal points in the form of a radially decreasing function towards the organism's boundary. In the case of pure growth (only cell divisions) such a genetic setup predicts faster growth in the neighborhood of the Darcyan origin (due to higher intensity of cell divisions) that slows down towards the boundary.

Remark 3.1.1. *During embryonic development, various genes are activated expressing themselves through cells and subdividing an embryo's domain into regions that designate future internal organs (hands, limbs, etc.). The inhomogeneous Poisson point process presented above models the action of genes defined earlier as a function of seeds and time and reflects not only interregional differences but intraregional differences as well expressing heterogeneity as a rule on a lower scale. In this way, we hope to build a realistic model of biological growth.*

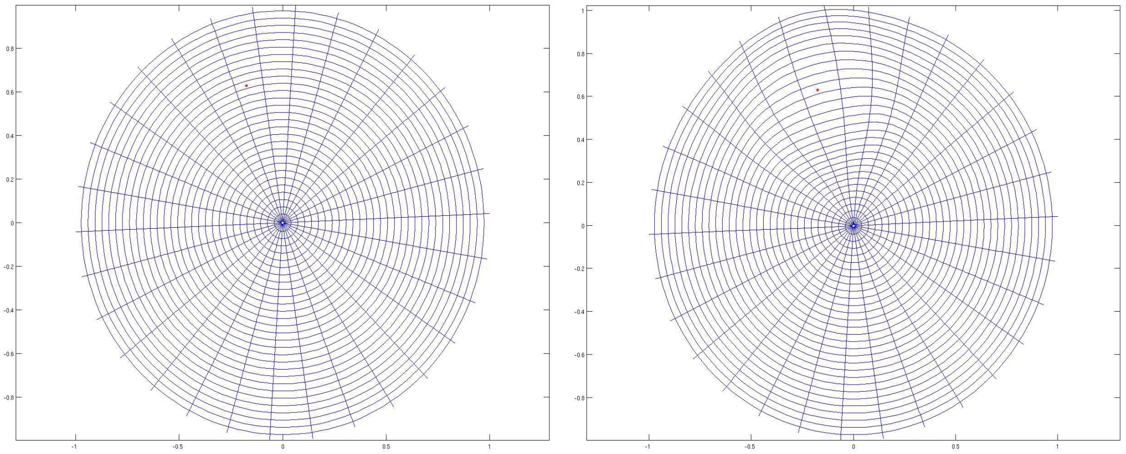

(a)

(b)

Figure 3.1.4: (a) The initial Darcyan coordinate system of a circular organism with a growth seed denoted by a red star, (b) The resulting deformed Darcyan coordinate system.

3.1.3 Local deformations

We now focus on the deformation effect resulting from a single cell decision taking place at $x(\xi_{seed}) \in \Delta X(\xi)$, where $\Delta X(\xi) \subseteq X(\xi)$ is a subset of the Darcyan coordinate system of an organism under study. An elementary biological event occurring at a time instant t according to the Poisson point process results in a local change of the structure and shape of the developing organism or a deformation of its Darcyan coordinate system. Therefore, a change in the X-field due to an activated seed can be expressed by a transformation

$$\phi^{\xi_{seed},t} : x(\xi) \Rightarrow \phi^{\xi_{seed},t}(x(\xi)). \tag{3.1.2}$$

We require that such a transformation be diffeomorphic. The diffeomorphic nature of the mappings is biologically meaningful: as the organism grows changing its internal structure and shape it can not overlap itself. We emphasize that the mapping is time dependent, it changes as the organism develops.

How do we define diffeomorphisms? Intuitively, we would expect an elementary event to cause deformation in the form of local expansion or contraction in the neighborhood of the seed and a lesser change outside the active area. The deformation then takes place relative to the position of the activated seed $x(\xi_{seed})$ in the X-field. Shown in Figure 3.1.4.a is a growth seed indicated with a red star. The points to be moved by the diffeomorphism $\phi^{\xi_{seed},t}$ comprise the continuum of the Darcyan coordinate system $X(\xi)$. The resulting deformed Darcyan coordinate system is shown in Figure 3.1.4.b.

Also, relying on the fact that in most cases the developing organism does not know the absolute space we would expect this deformation to be independent of the position of the organism $X(\xi)$ in the absolute space. Therefore, it is reasonable to consider the set of diffeomorphisms $\phi^{\xi_{seed},t}$ that are invariant with respect to the translation group in $\Re^2$. Then, there exists a diffeomorphism $\psi^{\xi_{seed},t}$ such that

$$\phi^{\xi_{seed},t}(x(\xi)) = x(\xi_{seed}) + \psi^{\xi_{seed},t}(x(\xi) - x(\xi_{seed})). \tag{3.1.3}$$

The mapping ψ depends on the nature of the seed, but not on its location. Instead, it depends on the relative distance between a point $x(\xi)$ and the seed $x(\xi_{seed})$. We will see later that the nature of the seed can be defined as a sink or a source of material, or a combination of both. The ψ transformation basically models a local deformation effect resulting from the activated seed that can represent a decay or growth in a preferential direction or mixed development. It determines the effect of growth on the relative location vector $v = x(\xi) - x(\xi_{seed})$ (see Fig.3.1.5) for a point $x(\xi)$ resulting in a decrease or increase of the magnitude of v, $\|v\|$, or, in other words, in a displacement undergone by $x(\xi, t)$ in a coordinate system centered at $x(\xi_{seed})$ in the radial direction only. Hence,

$$\tilde{v} = \phi^{\xi_{seed},t}(x(\xi)) - x(\xi_{seed}) = \psi^{\xi_{seed},t}(x(\xi) - x(\xi_{seed})) = \psi^{\xi_{seed},t}(v). \tag{3.1.4}$$

We can rewrite (3.1.4) as $\tilde{v} = v + \Delta v$, where Δv is a growth increment in unit time

(a) in the direction of the vector v if the cell decision at ξ_{seed} is a growth event,

(b) in the opposite direction of the vector v if the cell decision at ξ_{seed} is a decay, a local arrest of growth.

Illustrated in Figure 3.1.5 is the growth increment $\Delta v = \tilde{v} - v$ or the displacement of a seed $x(\xi)$ obtained with the mapping ψ that changes only the magnitude of a vector $v = x(\xi) - x(\xi_{seed})$. It is convenient to introduce local polar coordinates (r, τ) of the vector v and formulate constraints for the mapping ψ in terms of r and τ. We restrict ψ to be a radial, angle-preserving function: $(r, \tau) \to (\rho(r, \tau), \tau)$, where $\rho(r, \tau) = |\tilde{v}|$ is determined by the nature of the seed. In relative Cartesian v coordinates the transformation $\psi^{\xi_{seed},t}(v) = \tilde{v}$ with $|\tilde{v}| = \rho(r, \tau)$. We assume the following form of ψ-mapping expressed in local polar coordinates

$$\rho(r, \tau) = r + \mathcal{R}(r)k(\tau), \tag{3.1.5}$$

where $k(\tau) : S^1 \to \Re$ is called *the angular deformation function* and $\mathcal{R} : \Re \to \Re$ is called *the radial deformation function* [33]. We shall study two examples of the radial mapping ψ that describe isotropic and anisotropic growth patterns.

Radial deformation function

Observations of growth-related deformation fields suggest radial nature of displacements concentrated around the activated seed. Consider, for example, distribution of a growth hormone *auxin efflux carrier* in the cross-section of the shoot vegetative apex that specifies formative regions of leaf primordia (see Fig.3.1.6) [55]. Here, the

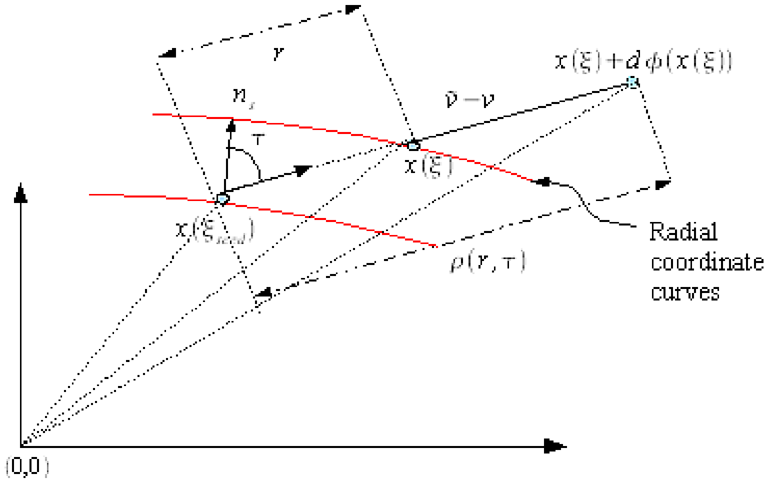

Figure 3.1.5: Illustration of displacement of a single seed $x(\xi)$ due to activation of a seed $x(\xi_{seed})$. A radial transformation $\psi^{\xi_{seed},t}$ takes local polar coordinates (r, τ) of $x(\xi)$ to $(\rho(r,\tau), \tau)$. The initial and radially transformed local coordinate systems are represented by points $v = (r, \tau)$ and $\tilde{v} = (\rho(r,\tau), \tau)$.

activated seed is the auxin signal located in their centers and is the focal point of local growth that acts as a source of a biological material. It outlines the deformed circular shape of each region with the radius of auxin influence varying from one region to another.

As a consequence of experimental observations we introduce a GRID parameter s that measures the range of influence of the activated seed $x(\xi_{seed})$ or the radius of growth or decay. Then an active gene area can be simply represented by a disc of radius $s(x(\xi_{seed}))$ centered at $x(\xi_{seed})$. For $|v| \gg s$, that is for those points $x(\xi)$ located away from the current seed, the displacements undergone by them will be of a lesser magnitude. To accommodate for a diminishing deformation effect away from the seed we employ a Gaussian function

$$\mathcal{R}(r) = r \exp\left(-\frac{r^2}{s^2}\right), \quad \text{for } r \geq 0,\ s > 0. \tag{3.1.6}$$

Hence, in the coordinate system with the origin at $x(\xi_{seed})$ we define the growth increment Δv as follows

$$\Delta v = k(\tau) v \exp\left(-\frac{|v|^2}{s^2}\right). \tag{3.1.7}$$

Then the point located at $v = x(\xi) - x(\xi_{seed})$ due to a change in magnitude moves to a new location $\tilde{v}$ according to

$$\tilde{v} = \psi^{\xi_{seed},t}(v) = v\left(1 + k(\tau)\exp\left(-\frac{|v|^2}{s^2}\right)\right) \tag{3.1.8}$$

or

$$\phi^{\xi_{seed},t}(x(\xi)) - x(\xi_{seed}) = (x(\xi) - x(\xi_{seed}))\left(1 + k(\tau)\exp\left(-\frac{|v|^2}{s^2}\right)\right). \tag{3.1.9}$$

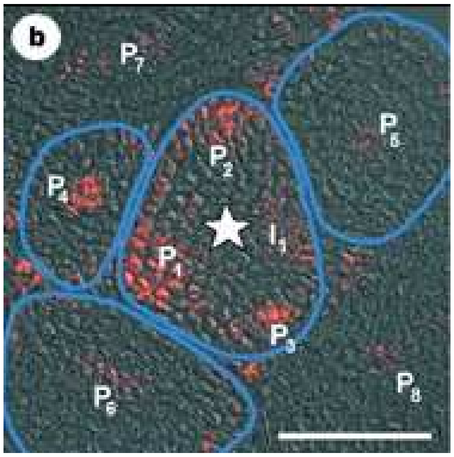

Figure 3.1.6: Polar transport of a growth hormone auxin in the cross-section of the shoot vegetative apex. $P_1,\ P_2,\ P_3$ are young leaf primordia, $P_4 - P_8$ are older leaf primordia.

{Courtesy of D. Reinhardt and E. R. Pesce, University of Bern, Switzerland [55]}

From equation (3.1.9) it follows that all points of the Darcyan coordinate system $x(\xi)$ will be moved to new locations $\phi^{\xi_{seed},t}(x(\xi))$ defined by

$$\phi^{\xi_{seed},t}(x(\xi)) = x(\xi) + (x(\xi) - x(\xi_{seed}))k(\tau)\exp\left(-\frac{\|x(\xi) - x(\xi_{seed}\|^2}{s^2}\right). \quad (3.1.10)$$

The Gaussian model of the radial deformation function (3.1.6) ensures that the significant part of the deformation $\phi^{\xi_{seed},t}$ at a time t takes place inside a neighborhood of $x(\xi_{seed})$ whose size depends on s. Given an elementary displacement field in the form (3.1.10) we can compute a relative area increase or decrease via the determinant of the Jacobian matrix J

$$J(x(\xi)) = \begin{pmatrix} \frac{\partial \phi_1^{\xi_{seed},t}}{\partial x_1} & \frac{\partial \phi_2^{\xi_{seed},t}}{\partial x_1} \\ \frac{\partial \phi_1^{\xi_{seed},t}}{\partial x_2} & \frac{\partial \phi_2^{\xi_{seed},t}}{\partial x_2} \end{pmatrix}. \quad (3.1.11)$$

Elements of J are given by

$$\frac{\partial \phi_i^{\xi_{seed},t}}{\partial x_j} = \begin{cases} 1 + k(\tau)e^{-\frac{\|x(\xi)-x(\xi_{seed})\|^2}{s^2}}\left(1 - 2\frac{(x_i(\xi)-x_i(\xi_{seed}))^2}{s^2}\right), & \text{if } i = j \\ -\frac{2}{s^2}k(\tau)(x_i(\xi) - x_i(\xi_{seed}))(x_j(\xi) - x_j(\xi_{seed}))e^{-\frac{\|x(\xi)-x(\xi_{seed})\|^2}{s^2}}, & \text{if } i \neq j \end{cases}. \quad (3.1.12)$$

Taking into account the local action of the ϕ-mapping within the disk of radius s, we find approximate values of its partial derivatives

$$\frac{\partial \phi_i^{\xi_{seed},t}}{\partial x_j} \approx \begin{cases} 0, & \text{if } i \neq j \\ 1 + k(\tau), & \text{if } i = j \text{ and } \|x(\xi) - x(\xi_{seed})\| < s \\ 1, & \text{if } i = j \text{ and } \|x(\xi) - x(\xi_{seed})\| \geq s \end{cases}. \quad (3.1.13)$$

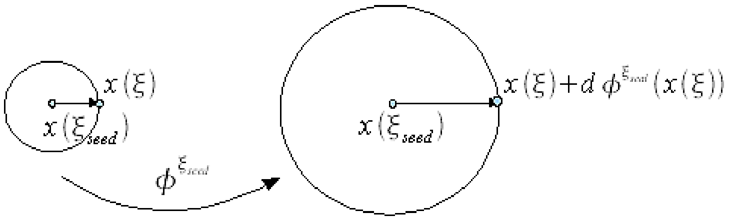

Figure 3.1.7: The action of the isotropic diffeomorphism $\phi^{\xi_{seed},t}$ on a disk centered at $x(\xi_{seed})$.

Therefore, the determinant of $J(x(\xi))$ can take approximate values of 1 or $(1+k(\tau))^2$, depending upon whether none (or one) or both coordinates of $x(\xi)$, $x_1(\xi)$ and $x_2(\xi)$, in the Darcyan coordinate system $X(\xi)$ are close to coordinates of $x(\xi_{seed})$. With respect to the local polar coordinate system centered at $x(\xi_{seed})$, the Jacobian of the transformation $\phi^{\xi_{seed},t}$ at a point $x(\xi)$ defines the ratio of the area elements $\rho \times d\rho \times d\tau$ and $r \times dr \times d\tau$ that can represent either an increase or a decrease, or no change in the area depending upon the sign of $k(\tau)$.

Remark 3.1.2. *To model the decay of deformations away from the gene activity zone we took a guess and constructed the diffeomorphic ψ-mapping using the Gaussian function. This is an attempt to mathematically model the decay in an elastic or viscoelastic medium. Other functions are also possible such as* $\mathcal{R}(r) = \left(\frac{r}{s}\right)^{p-1} \exp\left(-\frac{r}{s}\right)$, *with $p > 0$, for example. They are not explored further in this thesis. For future research, it would be desirable to find functions that are consistent with continuum mechanical models of elastic solids. But a detailed continuum mechanical treatment of growth-induced deformations is not expected to change the overall qualitative nature of the GRID model.*

Angular deformation function as a relative expansion/contraction rate

Having defined the radial deformation function $\mathcal{R}(r) \geq 0$ it remains to specify the angular deformation function $k(\tau)$, where τ is the angle between a normal vector n_s to the radial coordinate curve passing through $x(\xi_{seed})$ (see Fig.3.1.5). Given the change in magnitude of v along τ direction $|v| = \rho(r,\tau) = r + \mathcal{R}(r)k(\tau)$ the active gene area is expanded or contracted at the rate given by $k(\tau) : S^1 \to \Re$. Clearly, from the definition of $\rho(r,\tau)$ it follows that $k(\tau) < 0$ implies contraction or decay and $k(\tau) > 0$ implies expansion or growth in that direction.

If $k(\tau)$ is constant in all directions, or angle-independent, then the deformation $\phi^{\xi_{seed},t}$ (3.1.10) is called *isotropic*. Shown in Figure 3.1.7 is the local deformation effect of the isotropic mapping $\phi^{\xi_{seed},t}$ acting on a disk centered at $x(\xi_{seed})$. It is clear from the definition of ϕ-mapping that the activated seed $x(\xi_{seed})$ does not move. Note from (3.1.8) that the direction of a new displacement vector $\tilde{v} = \phi^{\xi_{seed},t}(x(\xi)) - x(\xi_{seed})$ coincides with the direction of vector $v = x(\xi) - x(\xi_{seed})$. So, directional independence of the k-function provides allomorphic growth behav-

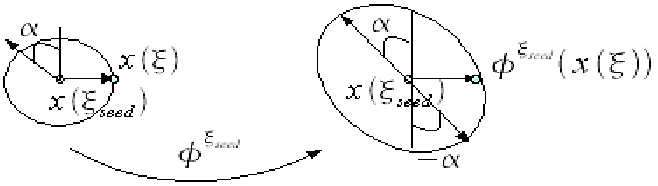

Figure 3.1.8: The action of the anisotropic diffeomorphism $\phi^{\xi_{seed},t}$ on a disk centered at $x(\xi_{seed})$.

ior within each neighborhood of an activated seed.

If $k(\tau)$ is angle-dependent, then the deformation $\phi^{\xi_{seed},t}$ (3.1.10) is called *anisotropic*. Intuitively, anisotropic diffeomorphism defines local deformation with one or more preferred directions of growth or decay. The action of the anisotropic mapping on a disk centered at $x(\xi_{seed})$ with preferred directions of growth α and $-\alpha$ is schematically illustrated in Figure 3.1.8. A rich family of deformations can be generated by simply changing the angular deformation function. In practice, it is convenient to define the angular deformation function as a function dependent on $\cos(\tau)$ since it is faster to compute $\cos(\tau)$ associated with each point $x(\xi)$ than the actual angle τ in the relative coordinate system centered at $x(\xi_{seed})$. Given that $0 \leq \tau \leq 2\pi$, or, equivalently $-1 \leq \cos(\tau) \leq 1$ we construct a tabulated function $k(\cos(\tau))$ by dividing the interval $[-1, 1]$ into 10 subintervals and assigning a value to the k-function defined at the right endpoint of each subinterval. In the left panel of Figures 3.1.9 and 3.1.11 we display some simple examples of $k(\cos(\tau))$ versus $\cos(\tau)$.

Notice that the resulting deformation type $\phi^{\xi_{seed}}$ applied to a uniform polar grid of a disk centered at $x(\xi_{seed})$ is determined by extrema of the angular deformation function (see the right panel of Figures 3.1.9 and 3.1.11). Here, we refer to the principal axes of the polar coordinate system as ξ_1 and ξ_2 with respective 0 and $\pi/2$ directions. A single maximum of a positive k-function attained at the boundary point $\cos(\tau) = 1$ suggests growth along the direction of the principal axis ξ_1 (see Fig.3.1.9.a). A single maximum of the positive k-function at the middle point $\cos(\tau) = 0$ suggests growth midwards along $-\pi/2$ and $\pi/2$ directions (see Fig.3.1.9.c). We call the angular deformation function the *unipolar growth* if it is mostly positive and it has a single maximum. Then the corresponding seed is called a *source*. If we slightly modify the profile of the “uni-source-forwards” k-function to the so called “uni-source-skew-forwards” function shown in Figure 3.1.10.a then the resulting ϕ-deformation of the polar grid will mimick growth forward in a straight line (see Fig.3.1.10.b).

A single negative minimum of k-function results in compression along τ_{min} direction, where $\cos(\tau_{min}) \in [-1, 1]$ is a point of minimum as seen from the right panel of Figure 3.1.11. If the angular function is mostly negative and it has a single minimum then it is called *unipolar decay*. In this case, the corresponding seed is called a *sink*.

We further construct more complex, *bipolar* angular deformation functions that exhibit mixed development in the neighborhood of $x(\xi_{seed})$. Figures 3.1.11.b and

3.1.11.d show examples of a bipolar behavior where the deformation results in growth in one direction and decay in the opposite direction. The corresponding k-functions possess two extrema, one minimum and one maximum, as seen from Figures 3.1.12.a and 3.1.12.c. A seed associated with the k-function that has two or more extrema in the interval $[-1, 1]$ is called *composite*. Another possibility is a multipolar behavior when growth occurs in both positive and negative directions of the principal ξ_1 axis and decay occurs in other directions, $\pi/2$ and $-\pi/2$, for example. Such a multipolar deformation is illustrated in Figure 3.1.12.f with the corresponding graph of k-function given in Figure 3.1.12.e. The seed here acts as a source in both positive and negative horizontal directions and as a sink in the positive and negative vertical directions.

This way we can construct a whole catalog of angular deformation functions that would generate elementary biological deformation patterns $\phi^{\xi_{seed},t}$ (3.1.10) around the seed. The principal directions of growth or decay ξ_1 (0 radians) and ξ_2 ($\pi/2$ radians) shown in Figures 3.1.9, 3.1.11, 3.1.12 can be modified by specifying a preferential direction α and defining k-function for $\alpha \leq \tau \leq 2\pi + \alpha$. Thus, the proposed model of the elementary deformation field $\phi^{\xi_{seed},t}(x(\xi))$ with the angle-dependent deformation function allows to capture a variety of biological growth modes.

The catalog of elementary local deformations can be used for classification of observed growth patterns and representation of anatomical growth under study. Given the statistics of deformations for specific growth conditions, one can create a probabilistic catalog that would associate them with angular deformation functions of high probability. Then such probabilistic catalogs can be used as prior models for Bayesian estimation of GRID growth parameters.

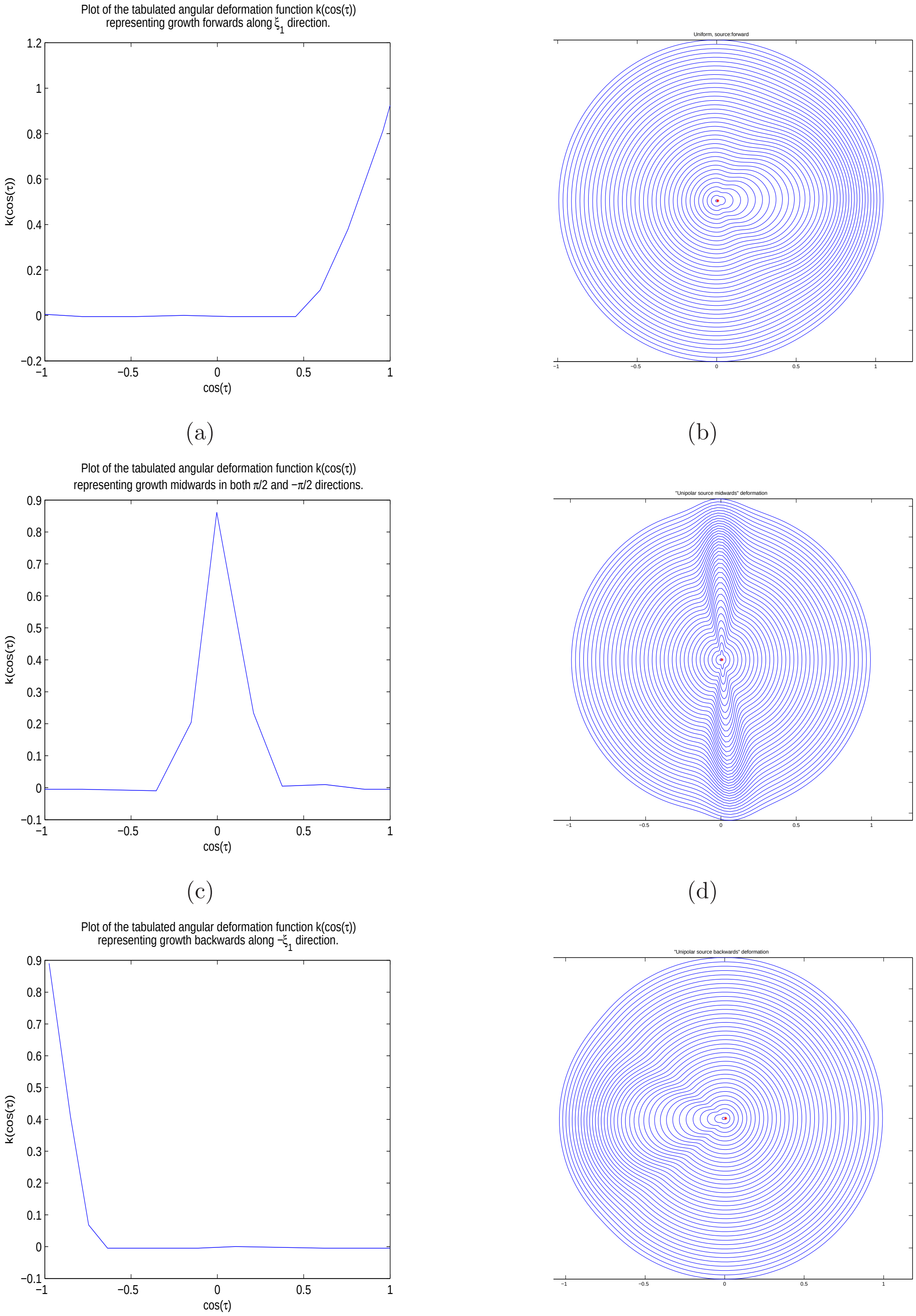

(a) (b)

(c) (d)

(e) (f)

Figure 3.1.9: Unipolar growth angular deformation functions: (b) “uni-source-forwards”, (d) “uni-source-midwards”, (f) “uni-source-backwards” and (a), (c), (e) the corresponding ϕ-mappings applied to a uniform polar grid. The “source” seed is placed in the origin of the polar coordinate system.

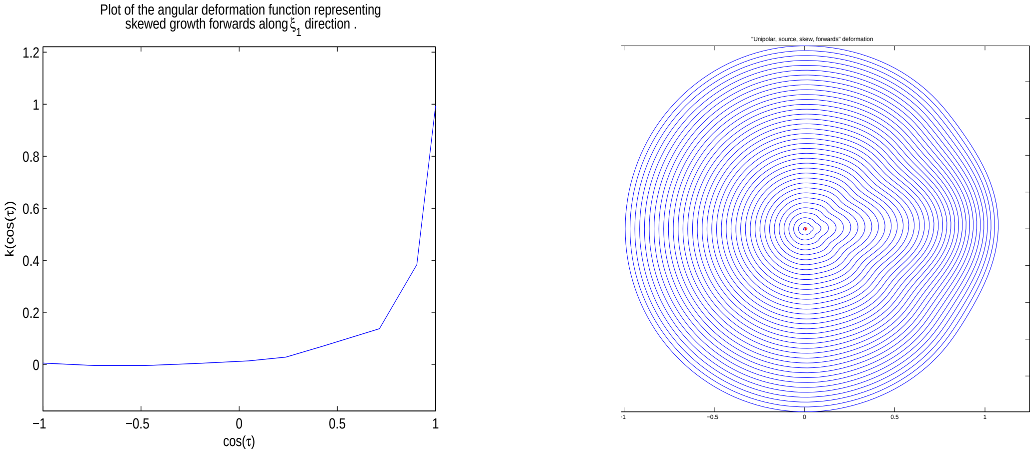

(a) (b)

Figure 3.1.10: (g) Unipolar growth angular deformation function "uni-source-skew-forwards" and (h) the corresponding ϕ-mapping applied to a uniform polar grid.

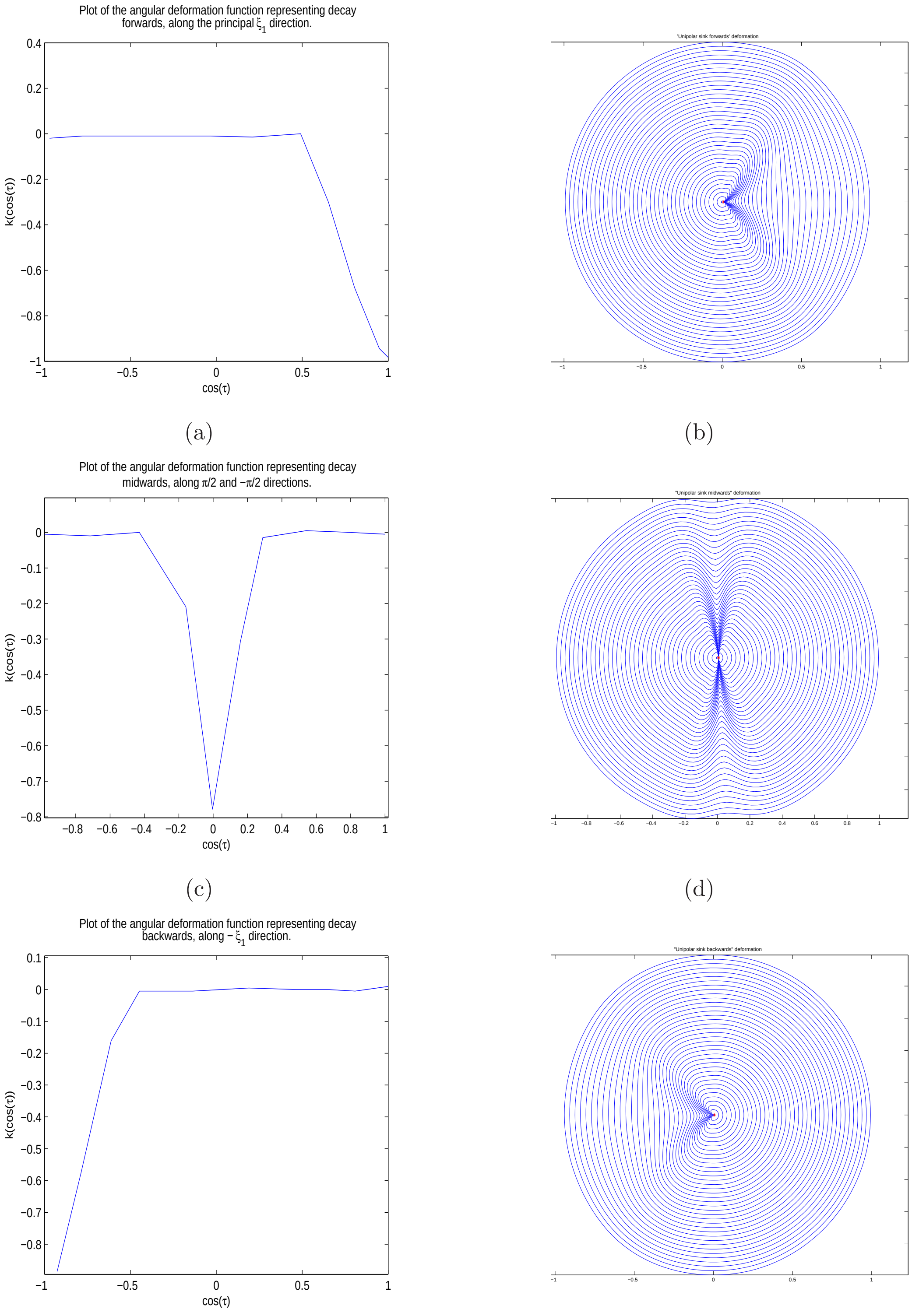

(a) (b)

(c) (d)

(e) (f)

Figure 3.1.11: Unipolar decay angular deformation functions: (a) “uni-sink-forwards”, (c) “uni-sink-midwards”, (e) “uni-sink-backwards” and (b), (d), (f) the corresponding ϕ-mappings applied to a uniform polar grid. The “sink” seed is placed in the origin of the polar coordinate system.

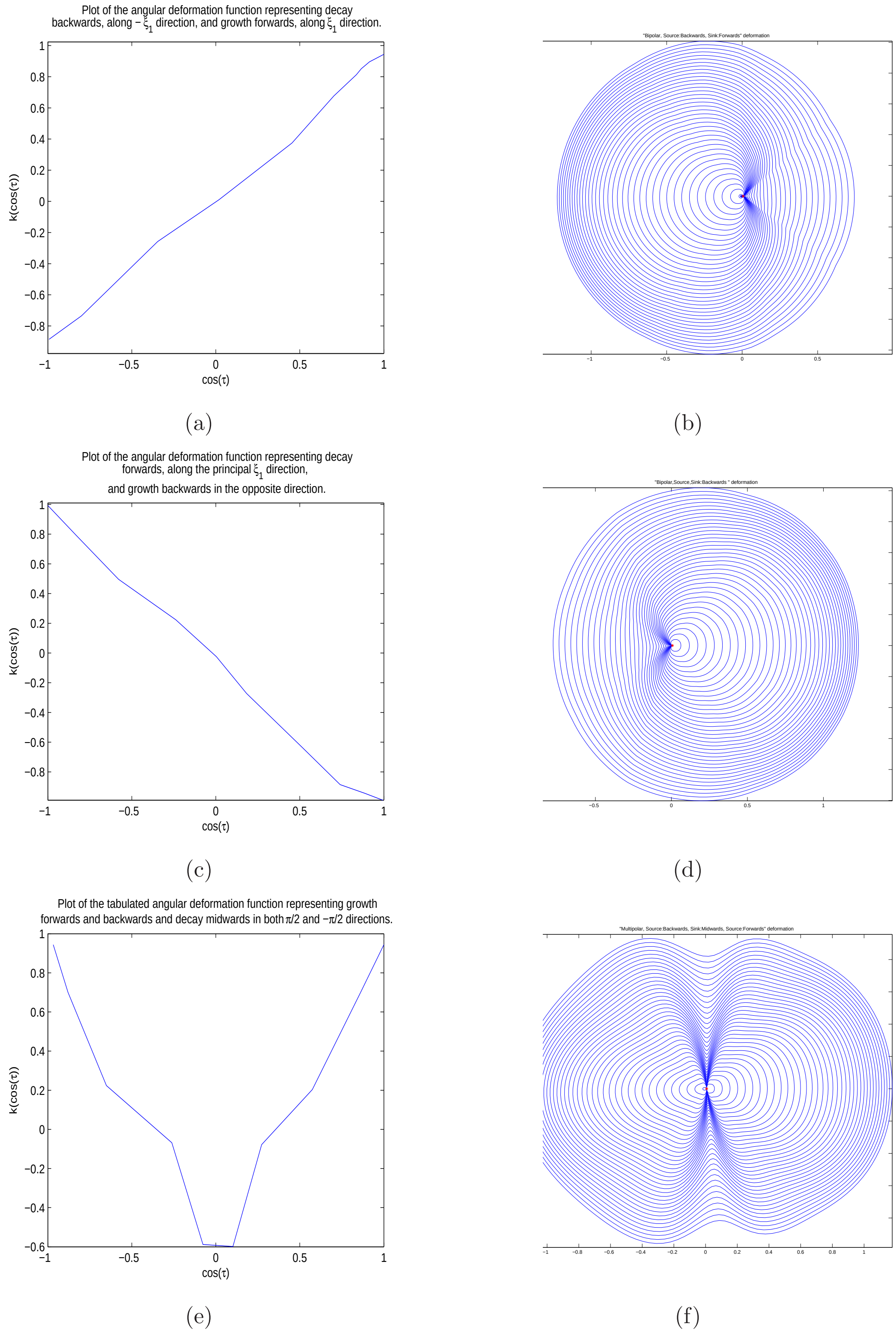

(a) (b)

(c) (d)

(e) (f)

Figure 3.1.12: Bipolar angular deformation functions: (a) “bi-source-forwards-sink-backwards”, (b) “bi-source-backwards-sink-forwards”, multipolar angular deformation function (c) “multi-source-backwards-sink-midwards-source-forwards” and (d), (e), (f) the corresponding ϕ-mappings applied to a uniform polar grid. The “composite” seed is placed in the origin of the polar coordinate system.

Diffeomorphic property of local deformations

We derive conditions under which the proposed transformation $\phi^{\xi_{seed},t}$ defined by (3.1.10) is diffeomorphic for all times t [33]. Consider the vector $v = x(\xi) - x(\xi_{seed})$ in the relative coordinate system with the origin $x(\xi_{seed})$ and the new location of this vector $\tilde{v} = \psi^{\xi_{seed},t}(v)$ with polar representation, respectively, $v = (r, \tau)$ and $\tilde{v} = (\rho(r,\tau), \tau)$. Clearly, the mapping $\phi^{\xi_{seed},t}(\cdot) = x(\xi_{seed}) + \psi^{\xi_{seed},t}(\cdot - x(\xi_{seed}))$ is diffeomorphic if the mapping $\psi^{\xi_{seed},t}$ is diffeomorphic. Expressed in local polar coordinates, $\psi^{\xi_{seed},t} : (r,\tau) \to (\rho(r,\tau),\tau)$ will be diffeomorphic as long as $\rho(\cdot,\tau) : \Re^+ \to \Re^+$ is a diffeomorphism for all τ.

Proposition 3.1.3. *The mappings* $\phi^{\xi_{seed},t}$ *and* $\rho(\cdot,\tau) = \cdot + \mathcal{R}(\cdot)k(\tau) : \Re^+ \to \Re^+$ *with the radial deformation function* $\mathcal{R}(r) = r\exp\left(-\frac{r^2}{s^2}\right)$ *are diffeomorphic if the range of the angular deformation function* $k(\tau)$ *satisfies*

$$-1 < k(\tau) < 2.2408 \text{ for all } \tau. \tag{3.1.14}$$

Proof. Fix an angle τ and $k(\tau) \equiv k$. $\rho(\cdot,\tau)$ is a diffeomorphic mapping as long as it has a piecewise-continuous derivative $\frac{\partial\rho}{\partial r} > 0$.

Given that $\rho(r,\tau) = r + kr\exp\left(-\frac{r^2}{s^2}\right)$ we obtain

$$\frac{\partial\rho}{\partial\tau} = 1 + k\exp\left(-\frac{r^2}{s^2}\right)\left(1 - 2\frac{r^2}{s^2}\right). \tag{3.1.15}$$

From $\frac{\partial\rho}{\partial r} > 0$ it follows that $1 + k\exp\left(-\frac{r^2}{s^2}\right)\left(1 - 2\frac{r^2}{s^2}\right) > 0$. We consider three cases:

1. For the value of $\frac{r^2}{s^2} = 0$ the partial derivative is positive.
2. For $1 - 2\frac{r^2}{s^2} > 0$ we have the following condition $k > \frac{-\exp\left(\frac{r^2}{s^2}\right)}{\left(1-2\frac{r^2}{s^2}\right)}$. Denote $w = \frac{r^2}{s^2}$. Since the maximum value of the function on the right-hand side is -1 at $w = 0$, we obtain the lower bound on the range of k, $k > -1$.
3. For $1 - 2\frac{r^2}{s^2} < 0$ we have the following condition $k < \frac{-\exp\left(\frac{r^2}{s^2}\right)}{\left(1-2\frac{r^2}{s^2}\right)}$. Since the minimum value of the function on the right-hand side is $\frac{\exp(1.5)}{2} \approx 2.2408$ at $r = 1.5$. Therefore, we obtain the upper bound on the range of k, $k < 2.2408$.

□

3.2 Fundamental equation of the GRID model

Using seed locations and a catalog of elementary deformations we can now build growth patterns in the form of cumulative growth deformations. A growth pattern is a sequence of random elementary events at ages $t_1,\ t_2,\ \ldots, t_n$ expressed in a change of shape. More precisely, the growth pattern is a cascade of random iterated diffeomorphisms applied to the initial organism $\Omega(t_0) \subset \Re^n,\ \ n = 1, 2, 3$ with the initial Darcyan coordinate system $X(\xi, t_0)$

$$X(\xi, t) = \phi^{\xi_{seed_{\sigma_n}}, t_n} \circ \phi^{\xi_{seed_{\sigma_{n-1}}}, t_{n-1}} \circ \ldots \circ \phi^{\xi_{seed_{\sigma_1}}, t_1} X(\xi, t_0), \tag{3.2.1}$$

where an elementary deformation at each time of seed activation t_i is defined by (3.1.10). Equation (3.2.1) is a general formulation of the **Growth as Random Iterated Diffeomorphisms Model**. Growth is basically composed of elementary deformations $\phi^{(\xi^i{}_{seed}, t_i)}$ occurring at times $t_0 \le t_1 \le \ldots \le t_n \le t$ or a map of composite nature $\phi(t_0, t)$

$$X(\xi, t) = \phi(t_0, t) X(\xi, t_0),\ \ t_0 \text{ is fixed}, \tag{3.2.2}$$

where $\phi(t_0, t) = \phi^{\xi_{seed_{\sigma_n}}, t_n} \circ \phi^{\xi_{seed_{\sigma_{n-1}}}, t_{n-1}} \circ \ldots \circ \phi^{\xi_{seed_{\sigma_1}}, t_1}$. It belongs to a composition semi-group Φ of diffeomorphisms

$$\phi(t_0, t) \in \Phi = \{\phi(s, t) : -\infty < s < t < \infty\}$$

with the following properties

$$\phi(s, t) \text{ is continuous w.r.t. } s,\ t \tag{3.2.3}$$

$$\phi(t_1, t_2) \circ \phi(t_2, t_3) = \phi(t_1, t_3) \in \Phi;\ \ t_1 < t_2 < t_3 \tag{3.2.4}$$

$$\phi(t, t) = id(\Phi). \tag{3.2.5}$$

Note that random placements of seeds induced by the Poisson point process lead to random diffeomorphisms and the Poisson probability distribution of seed activations induces a probability measure on the space of all possible diffeomorphisms Φ. Since equation (3.2.1) describes the evolution of the Darcyan coordinate system in the iterative form we can rewrite it as

$$X(\xi, t_n) = \phi^{\xi_{seed}, t_n}(X(\xi, t_{n-1})). \tag{3.2.6}$$

Hence, we have a growth recording in time interval $[t_1, t_n]$ of snapshots of a growing organism $X(\xi, t_1), X(\xi, t_2), \ldots, X(\xi, t_n)$ that looks like a solution to a flow equation. In fact, the random nature of diffeomorphisms hints to a growth law represented in the form of a stochastic differential equation. The derivation of the stochastic version of the GRID model is the subject of Chapter 4.

So far, we have developed a model representing growth of an organism as a discrete structure made up of seeds. We shall restrict further study of the GRID model to the case of diffeomorphisms invariant to the translation group in $\Re^2$ and consider two cases: isotropic growth defined by the angle-independent k-function and anisotropic growth defined by the k-function representing the amplitude of growth in any direction.

All in all, taking into account that there is order and logic to biological shape generation, the growth pattern is controlled by the following GRID variables of growth that are not necessarily numerical:

1. p, a symbolic variable that enumerates phases of growth that are time intervals during which certain internal organs develop,
2. $d(p)$, a time duration of the phase "p",
3. $\Delta\Xi^p \in \Xi$ is a subset of seeds representing patches of genetic activity during the phase "p",
4. k-function, the type of angular deformation resulting from a single cell decision,
5. s, the range of influence of each activated seed,
6. $\lambda(\xi)$, the Poisson intensity of seed activations per unit area,
7. λ_t, the Poisson intensity of seed activations per unit time.

In order to realize the fundamental GRID equation of growth (3.2.1) we need to specify the initial conditions. Clearly, the initial conditions should contain the genetic program of the organism's development expressed in terms of the GRID variables. The initial conditions (IC) are basically "generators" of growth that are naturally given in the form of an algebraic structure [28]. IC admits the following structure:

$$IC = \langle phase \mid duration \mid sets \mid type \mid range \mid Poisson\, intensities \rangle \,. \qquad (3.2.1)$$

A set *phase* contains symbolic names for phases of the development p considered. For example, the phase set can be {"limb", "forelimb", "wrist"} to generate wrist growth. Each phase has its duration denoted by $d(p)$. The different phase duration sets need not be disjoint. *Sets* are the seed subsets of the Darcyan system Ξ each corresponding to a certain phase of development and representing gene activity regions. *Type* is an elementary deformation in effect during each phase that may vary from seed to seed. It is represented by the k-function that would be position dependent in a differentiated tissue. *Range* is the range of influence of each activated seed that may also vary within the *sets* and from *phase* to *phase*. Finally, *Poisson intensities* are the probability mass functions defined within *sets* and *durations*.

In what follows we assume that at each phase the growth properties of the organism are homogeneous (the probability distribution of seed activations is uniform over the gene activity sets) and heterogeneity is represented by changes from one phase to another. That means that the initial value parameters are piecewise constant. This simplifying assumption has to be verified experimentally.

3.3 A pattern-theoretic definition of a growth pattern

Modeling a biological growth process as a homogeneous Poisson point process defined on the given subsets of seeds in the Darcyan space Ξ at each phase of development simplifies the gene control structure. In this case, how do we formalize the initial conditions with the minimal set of parameters? We introduce "atoms" of growth $g \in G_{prim}$ forming a primitive space

$$g = \langle \Delta T \mid \Delta\Xi \mid k(\tau) \rangle \,, \tag{3.3.1}$$

where

1. $\Delta T = [0,1]$ is a standardized time interval of growth during which the generator is applied;
2. $\Delta\Xi \subset \Xi$ is a subset of the Darcyan space of seeds;
3. $k(\tau)$ is the amplitude of growth in any direction τ.

The similarity transformation group acting on the space G_{prim} of growth generators is a product

$$S = S^T \times S^{\Xi} \times S^{ampl} \times S^{angle} \;\; with \tag{3.3.2}$$

1. $S^T = SA(1)$, affine 1D transformations $(a,b); t \rightarrow a + bt$ applied to the standard time interval ΔT;
2. $S^{\Xi} = DIFFEO(\Xi)$, diffeomorphic mappings applied to subsets of Ξ;
3. $S^{ampl} = R^1_+$, additive group of real numbers acting on the values of $k(\tau)$;
4. $S^{angle} = T^1$, translation group acting on directions τ of the k-function.

Using these generators and group elements s_1, s_2,$\ldots$, $s_n \in S$ we can create growth configurations $C = \sigma(s_1 g_1, s_2 g_2, \ldots, s_n g_n)$ that demonstrate various deformation behaviors. Here, σ denotes a linear chain graph connecting transformed generators [26]. The similarity group (3.3.2) describes the similarity relations between the generators within the growth pattern. Indeed, at the first GRID iteration the generator of growth becomes $g_2 = s_1 g_1$, at the second GRID iteration the generator g_2 is updated to $g_3 = s_2 g_2$ and so on.

For a global growth pattern behavior we introduce a Galilean space-time group

$$G = (-\infty < t < \infty) \times SE(3) \tag{3.3.3}$$

that is a group of spatial and time translations and rotations:

1. spatial translations: $t \rightarrow t$; $\vec{x} \rightarrow \vec{x} + \vec{a}$;

2. time translations: $t \to t + \tau$; $\vec{x} \to \vec{x}$;
3. boosts: $t \to t$; $\vec{x} \to \vec{x} + \vec{v}t$;
4. rotations: $\vec{x} \to T\vec{x}$, where T is an orthogonal matrix.

Definition 3.3.1. *(A pattern theoretic definition of a growth pattern.)* ***A growth pattern*** *of an organism* $\Omega(t_0) \subset \Re^n,\ n = 1, 2, 3$*, is the set of all growths* $\{(t, \phi(t_0, t)) : t \geq t_0\}$ *invariant with respect to Galilean transformations in space-time, where a diffeomorphic mapping* $\phi(t_0, t)$ *is an element of the composition semi-group* $\Phi = \{\phi(s, t) : -\infty < s < t < \infty\}$.

3.4 2D GRID illustrations

In this section we numerically solve the following problem: Assume that the Poisson intensities λ_t and $\lambda(\xi)$ are piecewise constant functions of time and space. That is, λ_t changes only from phase to phase and $\lambda(\xi)$ changes only from region $\Delta\Xi^p$ to region $\Delta\Xi^u$, where p and u are different phases of development. Given an initial organism $\Omega(t_0) \subset \Re^2$ in the form of a unit disk with polar coordinate representation $X(\xi, t_0),\ \xi = (r, \theta) :\ 0 \leq r \leq 1, 0 \leq \theta \leq 2\pi$ and its genetic control structure (initial conditions)

$$\begin{aligned} IC = [&phase,\ p \mid duration,\ d(p) \mid gene\ sets,\ \Delta\Xi \mid \\ &amplitude\ of\ growth,\ k(\tau) \mid range\ of\ growth,\ s] \end{aligned}$$

find the solution to the fundamental GRID equation of growth

$$X(\xi, t) = \phi^{\xi_{seed_{\sigma_n}}, t_n} \circ \phi^{\xi_{seed_{\sigma_{n-1}}}, t_{n-1}} \circ \ldots \circ \phi^{\xi_{seed_{\sigma_1}}, t_1} X(\xi, t_0). \tag{3.4.1}$$

3.4.1 Isotropic growth patterns

We consider a special case of the GRID model that generates isotropic growth as a diffeomorphism $\phi(t_0, t)$ composed of elementary radial mappings ϕ^{ξ_{seed}, t_i} meaning radial growth or decay from the seed $x(\xi_{seed})$ with a constant angular rate $k(\tau) = k$ (amplitude of growth). To emphasize the fact that the Darcyan coordinate system of $\Omega(t)$ deforms in time as the organism develops we refer to points in the Darcyan coordinates system as $x(\xi, t)$. Then at time of seed activation t_i the Darcyan grid points move to new locations according to

$$\begin{aligned} \phi^{\xi_{seed}, t_i}(x(\xi, t_{i-1})) = x(\xi, t_{i-1}) + (x(\xi, t_{i-1}) - x(\xi_{seed}, t_{i-1}))k(\xi_{seed}, t_{i-1}) \cdot \\ \exp\left(-\frac{\|x(\xi, t_{i-1}) - x(\xi_{seed}, t_{i-1})\|^2}{s^2}\right). \end{aligned} \tag{3.4.2}$$

Recall that in case of isotropic growth, small disks centered at the activated seeds will grow or decay into bigger or smaller disks with the constant amplitude of growth

k in all directions. Isotropic GRID produces irrotational[2] flow $\phi(t_0, t)$ generated by a sequence of locally radial displacements whose magnitudes are defined by the values of the amplitude of growth k. The k-function may vary from seed to seed within gene activity regions $\Delta\Xi \subseteq \Xi$ or from region $\Delta\Xi^p$ to region $\Delta\Xi^u$ (p and u are diferent phases of development). The amplitude of growth k may also vary in time. In what follows we perform growth experiments using radial diffeomorphisms defined by the k-function that is piecewise constant with respect to time and changes only from phase to phase.

Due to the assumption of piecewise constant Poisson intensities, we have a uniform distribution of seeds over the subset $\Delta\Xi^p \subseteq \Xi$ during each phase of development p. We set up the gene control structure,

$$\begin{aligned} IC = [&phase,\ p = 1 \mid duration,\ d(p) = [1, 60] \mid gene\ sets,\ \Delta\Xi = \cup_{1=1}^{4}\Delta\Xi_i \mid \\ &amplitude\ of\ growth,\ k = \{0.4,\ 0.3,\ 0.2,\ 0.1\} \mid range\ of\ growth,\ s = 0.2] \end{aligned} \tag{3.4.3}$$

where the subset $\Delta\Xi$ is in the form of four disjoint subregions of Ξ as shown in Figure 3.4.1.a. We subsequently apply 60 GRID iterations to the initial polar coordinate system of the organism $\Omega(t_0)$. At each iteration t_i, we obtain a realization of a random elementary ϕ-mapping as follows:

(i) Place a focal point of local growth $x(\xi_{seed}, t_{i-1})$ according to a spatially uniform probability distribution of seeds over $\Delta\Xi$ on a Darcyan coordinate system $X(\xi, t_{i-1})$,

(ii) Deform the neighborhood around the seed using an elementary deformation function

$$\begin{aligned} x(\xi, t_i) = \phi(x(\xi, t_{i-1})) = x(\xi, t_{i-1}) + (x(\xi, t_{i-1}) - x(\xi_{seed}, t_{i-1})) \cdot k(\xi_{seed}, t_{i-1}) \\ \cdot \exp\left(-\frac{(\|x(\xi, t_{i-1}) - x(\xi_{seed}, t_{i-1})\|)^2}{s^2}\right). \end{aligned}$$

Figures 3.4.1.b-3.4.1.d show snapshots of a growing organism recorded at ages $t = 10$, $t = 30$ and $t = 60$, respectively. Observe overall heterogeneous growth of an organism as four suborganisms within it develop with time locally expanding the Darcyan grid with different amplitudes of growth. As expected from the genetic setup (3.4.3), the magnitude of cumulative deformation $\phi(t_0, t_{60})$ is the largest in the region grown out of seeds in $\Delta\Xi_1$, where the amplitude of growth $k = 0.4$ and the smallest in the region grown out of seeds in $\Delta\Xi_4$ where $k = 0.1$.

Due to random nature of elementary diffeomorphisms the solution to the fundamental GRID equation of growth (3.2.1) is not unique. If the Darcyan space of seeds is continuous then there is an infinite number of possible GRID growth realizations for any time t. This way the GRID model captures biological variability of growth patterns. Figures 3.4.2.a-3.4.2.d show four solutions to the $GRID$ equation

---

[2] This analytic property of the isotropic GRID model has been shown in [33]

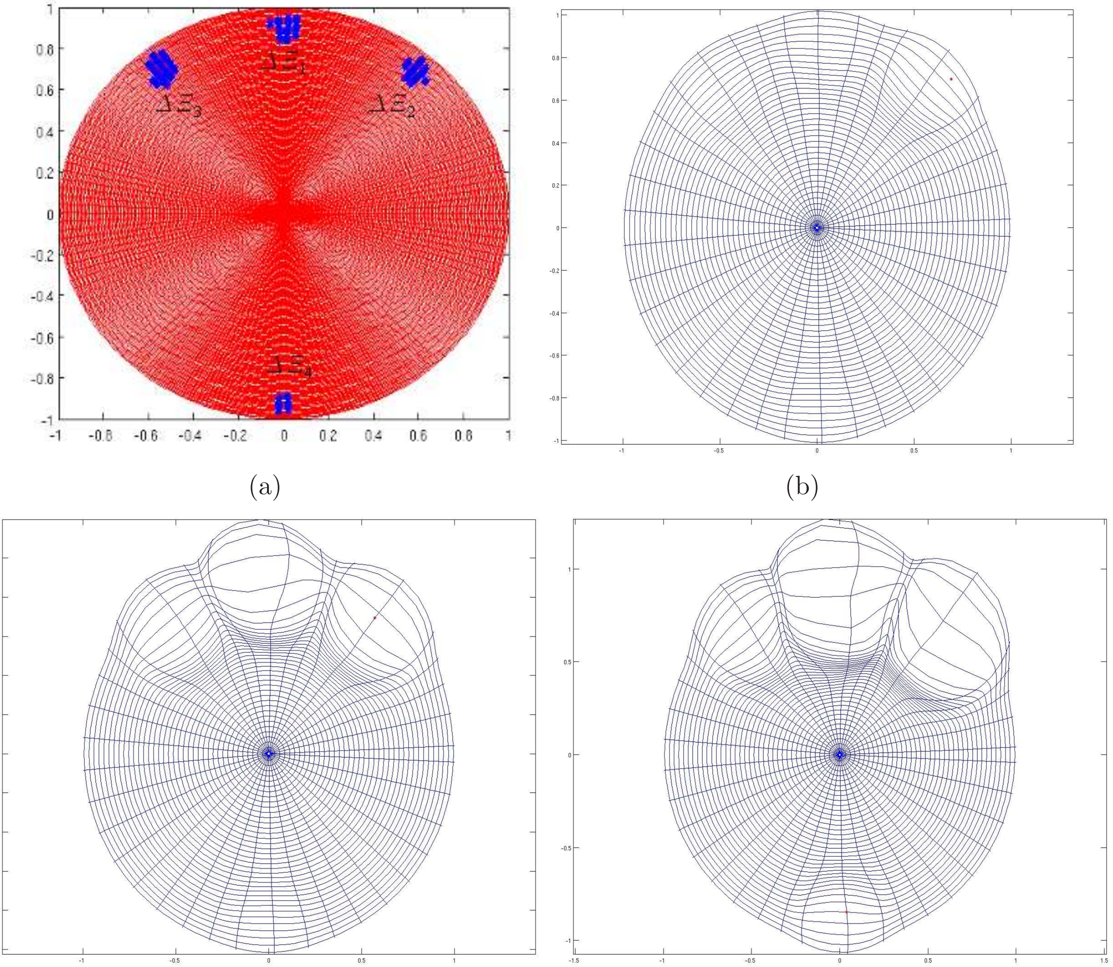

(a) (b)

(c) (d)

Figure 3.4.1: Illustration of GRID isotropic growth based on the genetic control structure (3.4.3). (a) Subset of seeds $\Delta\Xi = \cup_{i=1}^{4} \Delta\Xi_i$; Snapshots of the growing organism at ages (b) $t = 10$, (c) $t = 30$, (d) $t = 60$.

of growth each obtained in result of 40 GRID iterations applied to a uniform polar grid of the unit disk with the genetic program of development given by (3.4.3). Observe that the deformed polar grids of the grown disk at age $t = 40$ appear variable in internal structure and shape.

3.4.2 Anisotropic growth patterns

We are now ready to experiment with more complex, anisotropic growth configurations. For a synthesis of anisotropic growth patterns it is convenient to use auxiliary *Matlab functions* that then will be called by the main program of gene control execution. It takes a bit of an effort to write a general program since such growth scenarios as overlapping of different phases may occur and, therefore, have

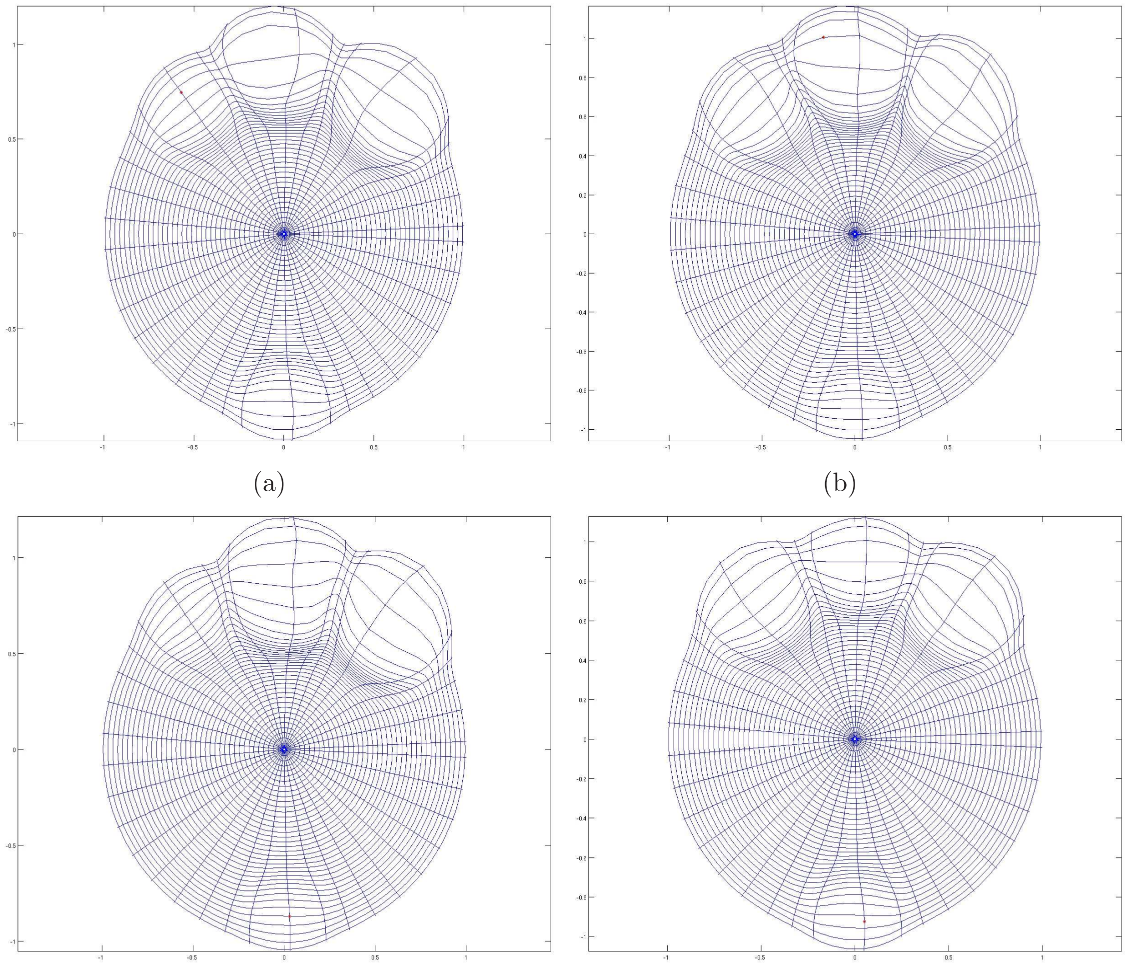

(a) (b)

(c) (d)

Figure 3.4.2: Various solutions to the GRID equation of isotropic growth based on the genetic control structure (3.4.3) and obtained at age $t = 40$. A sequence of 40 GRID transformations is applied to the initially uniform polar grid of a unit disk.

to be handled. First, we give a brief outline of an algorithm for anisotropic growth synthesis with an emphasis on its tricky parts and, second, we implement it for simulations of growth described by some typical angular deformation functions. All Matlab scripts described below are provided in Appendix D.

An algorithm for generation of 2D GRID anisotropic growth patterns

Gene control structure setup.
The main program “gene_contr.m” inputs values for the fields of the structure called “gene_control”, where each field is a Matlab cell object.

1. Given polar Darcyan grid of the unit disk computed by a Matlab script “disk.m” input a number of phases with their names and a number of disjoint gene sets in each phase of growth.

2. Input phase duration, contrast and magnifying factor for k-values using an auxiliary function “inp_data.m”.
3. Call a function “x_genesets.m” to select a geometric shape of each of the gene sets from the menu `c1,1=['point set']; c1,2=['line element']; c1,3=['area set']` and record gene sets in absolute space coordinates. All sets are specified by means of a Matlab command `ginput` that allows a user to pick seeds in the X-field interactively. If the gene set is an area then its selected boundary points are polygonal vertices and seeds comprising the polygon are then found using a Matlab command `inpolygon`.
4. Call a function “x2xi.m” to transform Cartesian coordinates of seeds in the X-field into Darcyan ξ-coordinates enumerating radial and angular coordinate curves. Computing Euclidean distances from each seed xp in the given gene sets to all Darcyan grid nodes $x(\xi)$ this code finds the Darcyan node at the minimal distance from xp and the corresponding integer ξ_1 and ξ_2 coordinates.
5. For each of the sets choose an angular deformation function from the menu `m=menu('Choose k-function', 'uni-source-for', 'uni-source-mid', 'uni-source-back', 'uni-sink-for', 'uni-sink-mid','uni-sink-back', 'bi-source-for-sink-back', 'bi-source-back-sink-for', 'multi-source-back-sink-mid-source-for', 'uni-source-skew-for')`. Set the principal direction of growth or decay `direction=input(['direction in radians =\n'])` and the range of influence of a seed in each gene set.

Simulation of 2D GRID growth pattern governed by the gene control structure. The main program “execute_gene_control.m” iteratively builds a growth pattern as a realization of the fundamental GRID equation governed by the specified structure “gene_control”.

1. Form a duration $n_{phase} \times 2$ matrix “ts”, where n_{phase} is the number of phases. First and second columns of the matrix contain, respectively, starting and ending times.
2. Compute the total time length of growth t_{iter} and run GRID iterations.

   While $t \leq t_{iter}$

   (a) Identify overlapping phases at a time t: Compute a vector of zeros and ones `w=(t>=ts(:,1))&(t<=ts(:,2))`. Indices of non-zero components of w correspond to overlapping phase numbers.

   (b) If the number of overlapping phases is $n_w \neq 0$ then a function “select.m” (see a remark below) is called in line `s=select(ones(1,n_w)./n_w)` for a random choice of the phase given that all phases are equally likely to occur.
   If the number of overlapping phases is $n_w = 0$ then there is no phase overlap at the time t. Proceed to the next step of the algorithm.

(c) Load field values of the structure “gene_control” for the chosen phase. Compute a total number n_{set} of uniformly distributed seeds in a current gene set and activate one seed at random using a function “select.m”. This operation is performed in program line
`j=select(ones(1,n_set)./n_set)` and `seed=set(j,:)`.
Here, “ones(1,n_set)./n_set” is a vector of probabilities with components equal to $\frac{1}{n_{set}}$ reflecting uniform probability distribution of seeds, and “seed” is a selected point with Darcyan coordinates (ξ_1, ξ_2) and with an index j.

(d) Call a function “get_new_x.m” to deform the Darcyan grid “x” into “x_new”.
Denote Darcyan coordinates of the activated seed by “seed(1), seed(2)”. Evaluate k-function at all nodes of the Darcyan grid $x(\xi_1, \xi_2)$: For each node compute a cosine of an angle between a unit vector “u”
`v=x(:,xi1,xi2)-x(:,seed(1),seed(2));u=v./(norm(v)+.0001)` and a unit vector “u1” collinear to a radius-vector “x(seed(1),seed(2))” and normal to a radial coordinate curve at the point “x(seed(1),seed(2))”
`vv1=x(:,seed(1)+1,seed(2))-x(:,seed(1),seed(2));`
`u1=vv1./(norm(vv1)+.0001)`.
Note that the positive xi_1 axis is oriented along “u1” direction. Thus, “u1” is a preferential direction of local growth/decay. Then interpolate to evaluate k-function at “kappa”, a scalar product of “u” and “u1”
`kappa=u'*u1; k(xi1,xi2)=interp1(xs,ys,kappa)`.
Here, arrays “xs” and “ys” represent tabulated k-function evaluated at 10 values of the argument $\cos(\tau) \in [-1, 1]$.
Apply elementary *phi*-mapping given by equation (3.1.10) to the current Darcyan grid “x”.

(e) Display the resulting Darcyan grid “x_new” using an auxiliary function “see_x_mod.m” along with the activated seed
`xi_seed=x(:,seed(1),seed(2))`.
Reinitialize the Darcyan grid `x=x_new`, reset `t=t+1` and repeat GRID iteration steps.

Remark 3.4.1. *A function “select.m” is an important utility that picks a phase or a seed at random given the probability mass function defined over the gene set of seeds. The function’s input is a probability vector “probs” with entries* $probs(1), probs(2), \ldots, probs(n)$ *equal to* $\frac{1}{n}$ *in case of the uniform probability distribution of a random seed placement over the gene set comprised of* n *seeds. This simple program simulates a stochastic variable that takes the value* i *with probability* $probs(i)$.

First, the Matlab random number generator `rand(1)` *yields a sample from the univariate uniform distribution of a random number over the interval* (0, 1). *Second, Matlab command* `cumsum` *computes a vector of the partial sums* $s_1 = probs(1)$, $s_2 = probs(1) + probs(2)$, $s_3 = probs(1) + probs(2) + probs(3)$, $\ldots$, $s_n = probs(1) + probs(2) + \ldots + probs(n) = 1$. *If the sample* $y > s_1,\ s_2,\ \ldots, s_i$ *but not* s_{i+1} *then the* *event* $s_i < y \leq s_{i+1}$ *has the probability* $s_{i+1} - s_i = p_{i+1}$. *Hence, the program returns a number* $i+1$ *that selects the* $(i+1)$*st seed in the given gene set (where all seeds are enumerated and expressed in Darcyan* ξ *coordinates).*

As an organism develops, the Jacobian determinant of the composite mapping $\phi(t_0, t)$ changes with respect to the initial polar Darcyan grid $X(\xi, t_0)$. At each time instant t_i of seed activation the Jacobian determinant $J(x(\xi, t_i))$ is a scalar field in the absolute space evaluated as

$$\begin{aligned} J(x(\xi,t_i)) &= J(\phi^{\xi_{\sigma_i},t_i} \circ \phi^{\xi_{\sigma_{i-1}},t_{i-1}} \circ \ldots \circ \phi^{\xi_{\sigma_1},t_1}(x(\xi,t_0))) \\ &= J\left(\phi^{\xi_{\sigma_i},t_i}(x(\xi,t_{i-1}))\right) \cdot J\left(\phi^{\xi_{\sigma_{i-1}},t_{i-1}}(x(\xi,t_{i-2}))\right) \cdot \ldots \cdot J\left(\phi^{\xi_{\sigma_1},t_1}(x(\xi,t_0))\right), \end{aligned} \tag{3.4.4}$$

with each factor on the right-hand side $J(\phi^{\cdot,\cdot}(x(\cdot,\cdot))) = \left|\frac{\partial(\phi_1,\phi_2)}{\partial(x_1,x_2)}\right|$.

It predicts an increase ($J > 1$) or decrease ($J < 1$) of the area around each Darcyan grid node $x(\xi, t_i)$ relative to the area around the corresponding initial polar grid node $x(\xi, t_0)$. How does the Jacobian determinant develop with time? We address this question experimentally, by visualizing evolution of the scalar field $J(x(\xi, t))$ along with the deformation of the polar Darcyan grid of the circular organism as it develops in time-space. This is accomplished by a Matlab program "growth_rates.m" (see Appendix D). The main body of this program is the same as that of "execute_gene_control.m" with an addition of the command line calling an auxiliary function "get_jacob.m" (see Appendix D). The program "get_jacob.m" computes the Jacobian determinant (3.4.4) at each time iteration $t = i$ and updates the Darcyan grid.

Note that evaluation method of the k-function at the Darcyan grid nodes is different from the one realized by "execute_gene_control.m". Here, the positive ξ_1 axis is not aligned with the radius-vector $x(\xi_{seed})$ in the absolute space. If the direction of growth specified by a user $\theta \neq 0$ then the set of points $\cos(\tau_i) : 0 \leq \tau_i \leq 2\pi$ at which the k-function is defined is modified to the set of points $xs = \cos(\tau_i + \theta)$.

With each Darcyan grid node $x(\xi)$ we associate a vector v defined in the function line `v=x(:,xi1,xi2)-x(:,seed(1),seed(2))` in the Cartesian coordinate system centered at $x(\xi_{seed})$ with its length given by `r=norm(v)`. Then in order to evaluate k-function at $x(\xi)$ we compute its argument $cos(\tau)$ called "kappa" `kappa=v(1)/(norm(v)+.0001)`. Here, "kappa" is a cosine of an angle τ between the vector v and the positive horizontal axis ξ_1 (that coincides with the positive direction of x_1-axis in the Cartesian coordinate system with the origin $x(\xi_{seed})$). Finally, we interpolate $k(xs) = ys$ at "kappa" in line `k(xi1,xi2)=interp1(xs,ys,kappa)`.

It is important to realize that the two proposed procedures for simulation of 2D GRID growth patterns differ in the way orientation of growth or decay is specified. The procedure "execute_gene_control.m" sets up local direction of growth/decay along the radius-vector $x(\xi_{seed})$ normal to the radial coordinate curve (enumerated by ξ_{seed_1}) at this point. The preferential direction θ is not needed. The procedure "growth_rates.m" sets up local direction of growth/decay θ given by a user. In this case, θ measures an angle between the positive horizontal x_1-axis in the Cartesian coordinate system centered at $x(\xi_{seed})$ and the vector $x(\xi) - x(\xi_{seed})$. Thus, the user has a choice which one of the two main programs to implement.

We start computer experiments with some simple single-phase anisotropic growth patterns. Let us assemble a growth pattern out of elementary deformations ϕ^{ξ_{seed},t_i} labeled by "uni-source-forward" and illustrated in Figure 3.1.9.b. Setting up the gene control Matlab structure as follows

gene_control(1).phase="first",

gene_control(1).sets=[$n_{seeds} \times 2$] (see Fig.3.4.3.a),

gene_control(1).durations=[110],

gene_control(1).contrasts=[1],

gene_control(1).k_values=[2×10],

gene_control(1).directions=[1],

gene_control(1).steps=[1],

where $[\cdot \times \cdot]$ or $[\cdot]$ specifies the size of an array containing field values and applying the Matlab program "growth_rates.m" we simulate the growth pattern classified as "uni-source-forward" with

1. "durations"= $[1, 10]$,
2. "sets"="area set" illustrated in Figure 3.4.3.a,
3. "k_values"= angular deformation function "uni-source-forward" (see Fig.3.1.9.a),
4. "steps"= range of growth equal to 0.2,
5. "directions"=local direction of growth $\theta = 0$ along the positive horizontal x_1 axis.

Figure 3.4.3 shows snapshots of a disk growing forward taken at times $t = 2$, $t = 4$, $t = 6$, $t = 8$ and $t = 10$. Observe from the color-coded plots of the Jacobian determinant how it becomes more spatially concentrated near the seed. This is due to the fact that Darcyan grid nodes $x(\xi)$ initially located inside the local disks of radius $s = 0.2$ centered at seeds $x(\xi)$ of the given gene set have moved out of it along the positive x_1-axis direction. Thus, only points of the Darcyan coordinate system closely located to the activated seed have a chance to move forward.

Another simple example of a single-phase growth pattern is "uni-sink-forward" representing a tissue decay. We now specify two gene sets as shown in Figure 3.4.4.a and let one of them be chosen at random at each iteration t. With "k_values" of a tabulated angular deformation function "uni-sink-forward" (see Fig.3.1.11.a) and other fields of the gene control structure identical in their values to the ones in the previous example we simulate a decay of a circular organism from two different gene activity regions. From the color-coded graphs of the Jacobian determinant seen in Figure 3.4.4 we observe a spread of decay in the neighborhood of an activated seed shown in blue color that becomes wider as the organism's boundary is pushed in. As time progresses, more Darcyan grid nodes become influenced by the activated seeds since they move closer to the specified gene sets resulting in widening of decay.

We now generate growth patterns of some natural shapes like a fish fin, for example, using elementary deformations. The fish fin can be seen approximately as a 2D shape and, therefore, the 2D GRID model is applicable. In this pattern synthesis, the initial circular shape is viewed as the germ out of which the fish fin develops. Therefore, we disregard the disk following the developing organ seen in images of its growth pattern. The shape of the grown fish fin evolves under a certain spatial order of seed activations. First, the organ develops into the form of a bulge and, second, fin ray segments develop out of the bulge. We then use a two-phase gene control structure with the following field values

phase="first":

1. "duration"$= [1, 30]$,
2. "gene sets"="area set" illustrated in Figure 3.4.5.a,
3. "amplitude of growth"= angular deformation function "uni-source-forward" (see Fig.3.1.9.a),
4. "range of growth"$= 0.8$,
5. "direction"=local direction along the normal vector to the radial coordinate curve at each activated seed $x(\xi_{seed})$,

phase="second":

1. "duration"$= [31, 450]$,
2. "gene sets"="point set" illustrated in Figure 3.4.5.b,
3. "amplitude of growth"= angular deformation function "uni-source-skew-forward" (see Fig.3.1.10.a),
4. "range of growth"$= 0.3$,
5. "direction"=local direction along the normal vector to the radial coordinate curve at each activated seed $x(\xi_{seed})$

and run the program "execute_gene_control.m". We chose the deformation function "uni-source-skew-forward" to capture a narrow and pointy growth of fin segments.

At the end of the first stage, namely, at $t = 30$ the developing fin takes the shape as shown in Figure 3.4.5.b. Then a new set of genes seen as uniformly distributed 12 seed points near the propagating boundary (see Fig.3.4.5.b) initiates the development of fin ray segments. The deformed Darcyan grid obtained as a realization of the first phase of growth can be thought of as the initial Darcyan grid at the second phase of growth. Figure 3.4.5.c shows a grown fish fin with 12 fin ray segments at time $t = 450$ and final locations of growth seeds in the X-field denoted by red stars.

These examples of growth patterns show that the GRID model reflects variability, logic and order of biological shape generation as controlled by the genes and constructs realistic structures of grown organisms.

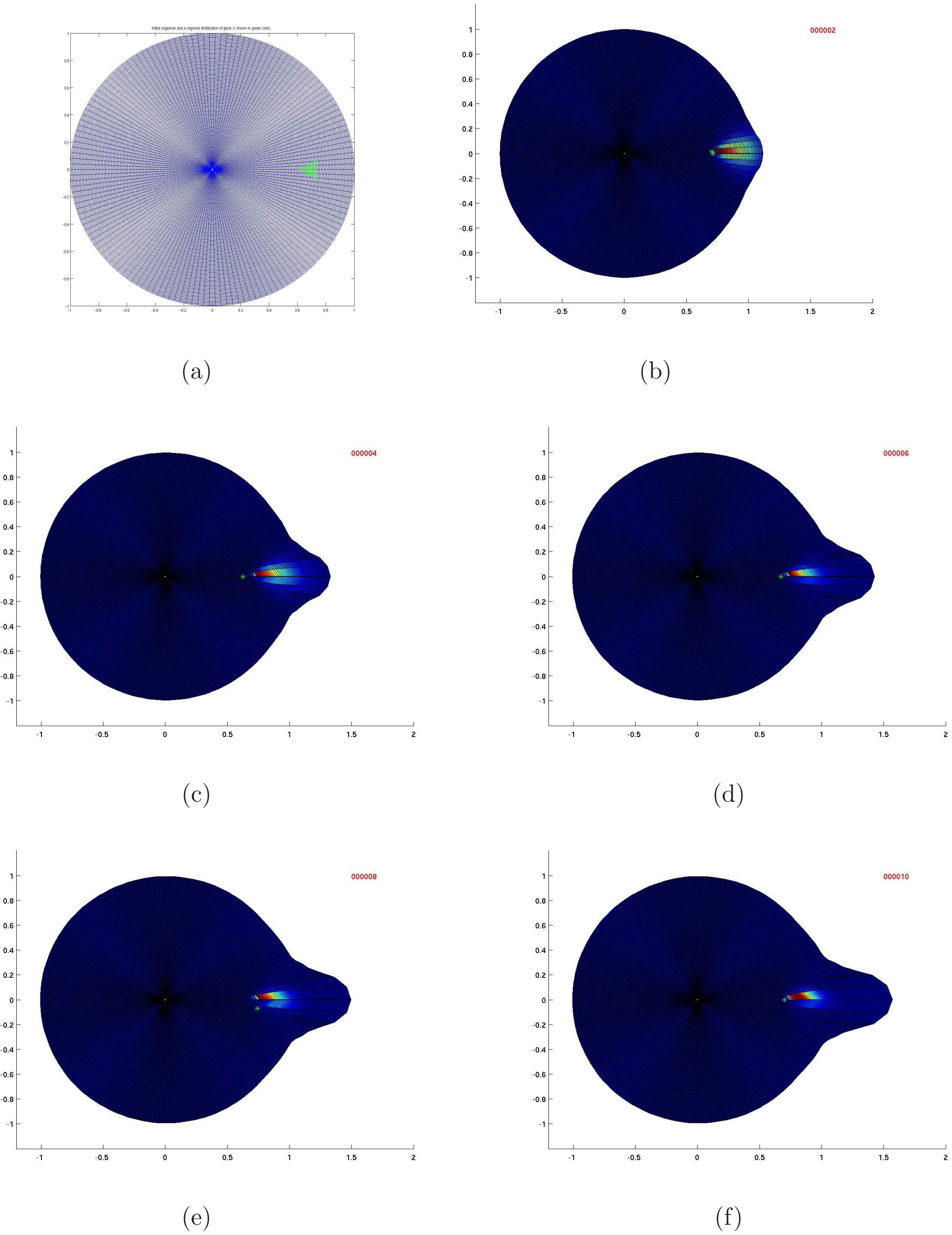

(a) (b) (c) (d) (e) (f)

Figure 3.4.3: Illustration of 2D GRID single-phased growth pattern "uni-source-forward" and the corresponding evolution of the Jacobian determinant. (a) Subset of seeds $\Delta\Xi$; Snapshots of a disk growing forward at ages (b) $t = 2$, (c) $t = 4$, (d) $t = 6$, (e) $t = 8$, (f) $t = 10$. Active gene sites are indicated by green stars.

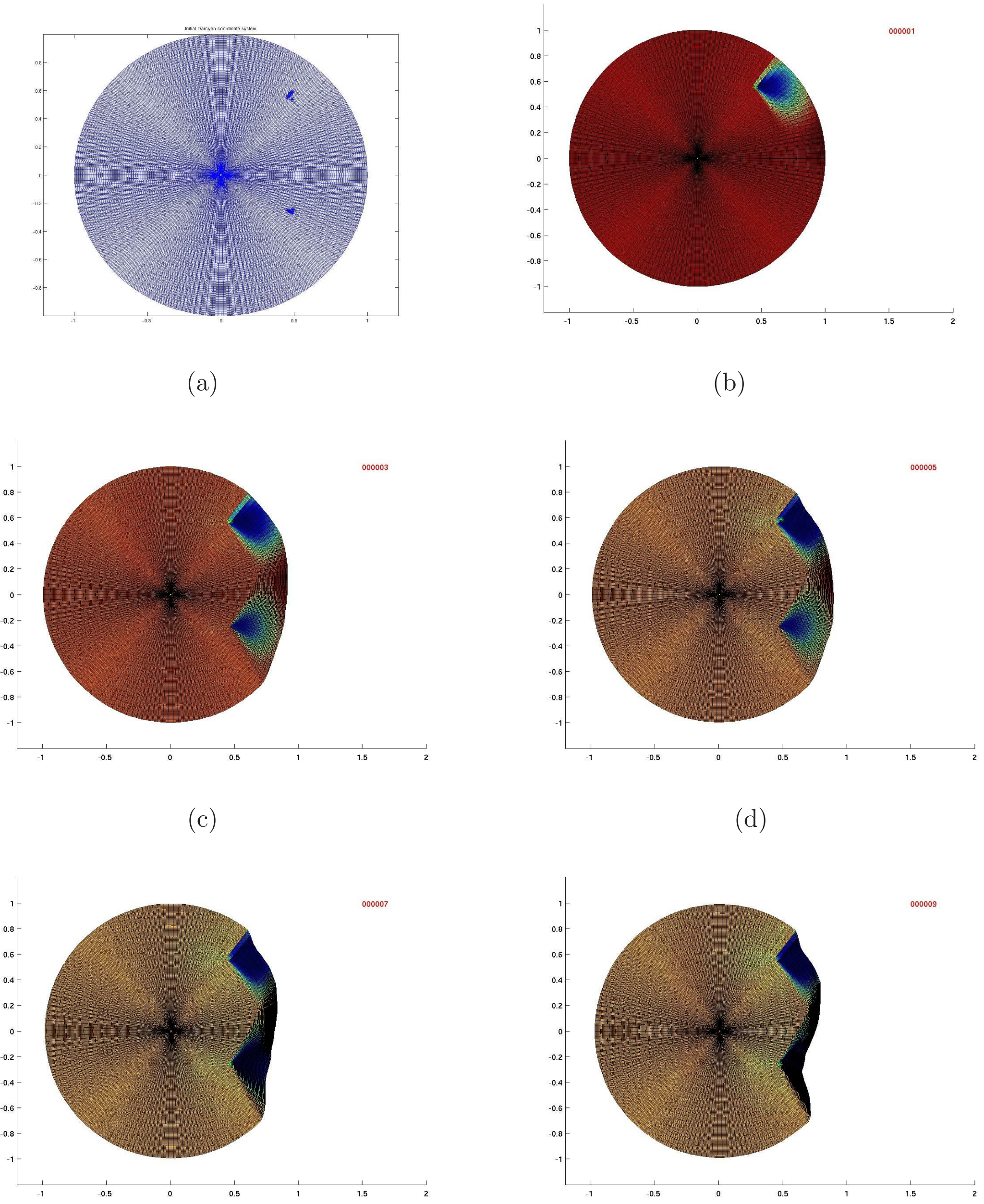

(a) (b)

(c) (d)

(e) (f)

Figure 3.4.4: Illustration of 2D GRID single-phased growth pattern "uni-sink-forward" and the corresponding evolution of the Jacobian determinant. (a) Subset of seeds $\Delta\Xi = \cup_{i=1}^{2} \Delta\Xi_i$; Snapshots of a disk growing forward at ages (b) $t = 1$, (c) $t = 3$, (d) $t = 5$, (e) $t = 7$, (f) $t = 9$. Active gene sites are indicated by green stars.

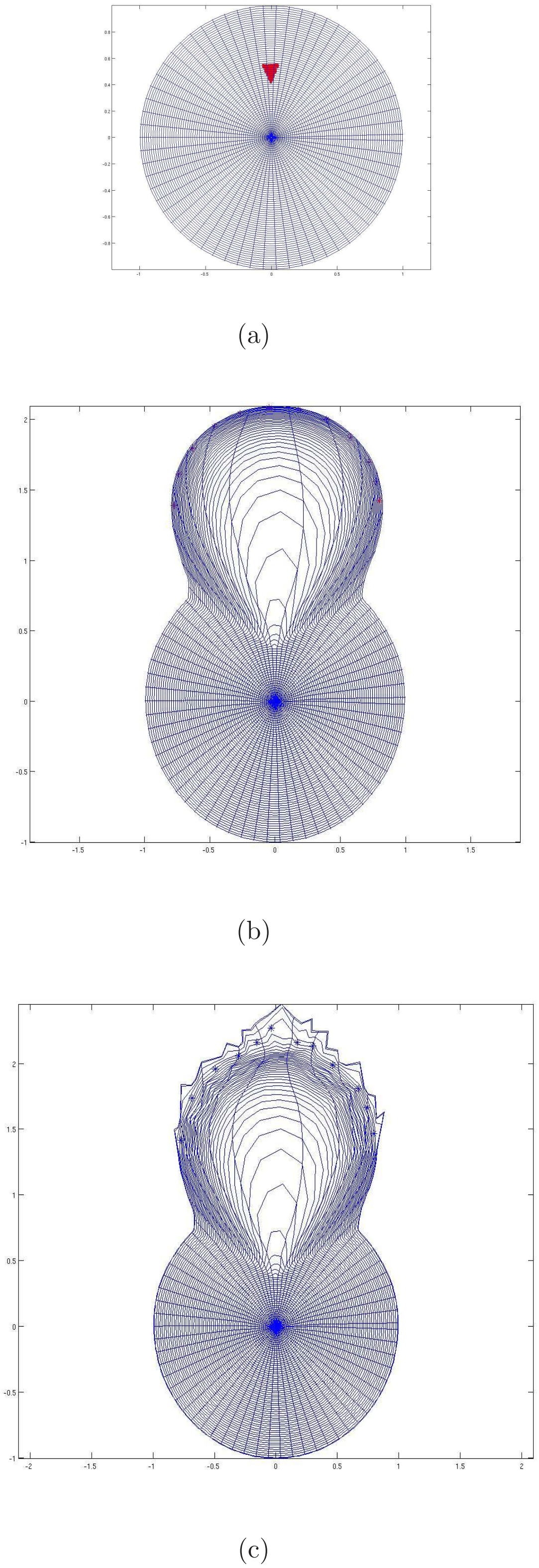

(a)

(b)

(c)

Figure 3.4.5: GRID two-phase growth pattern of a fish fin. (a) Subset of seeds $\Delta\Xi^1$ activated during the first phase $[1, 30]$, (b) Initial Darcyan coordinate system at the second phase with a point set of 12 seeds $\Delta\Xi^2$ shown by red stars, (c) Grown fish fin at time $t = 450$.

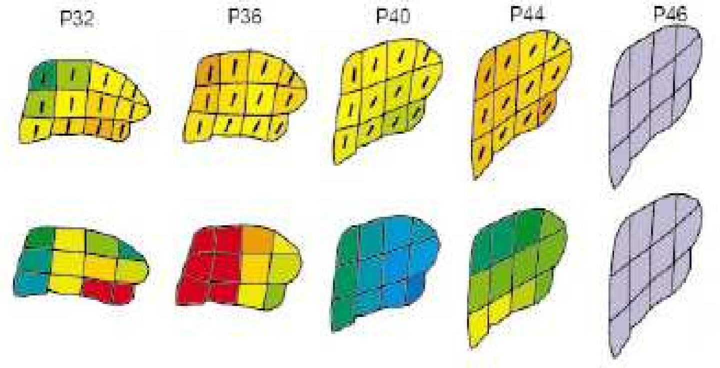

Figure 3.5.1: Anisotropic growth of a petal lobe in a snapdragon flower.
{Courtesy of A. G. Rolland-Lagan, J. A. Bangham, E. Coen, Norwich, UK [56]}

3.5 Biological scrutiny of the angular deformation function

Most growth phenomena in nature exhibit anisotropic behaviour. Such anisotropy may be characterized by regional differences in values of the following GRID growth parameters

(i) the growth rate in size and time expressed with the Poisson parameters,

(ii) the direction-dependent amplitude of growth,

(iii) the angle at which the principal growth direction is oriented relative to an underlying coordinate system.

How would a developmental biologist interpret the angular deformation function? To address this question we consider an example of anisotropic growth of a snapdragon petal lobe shown in Figure 3.5.1 where shapes are scaled to the same size [56]. Observe the partitioning of the petal lobe domain into regions with different growth properties. The main growth direction (averaged over each region) is shown at the centre of each region. The color coding in the upper row refers to growth rate in time ranging from cell doubling time of 15 hours(h) (orange) to 45h (blue) and the color coding in the bottom row refers to anisotropy, the ratio of the increase along the main growth direction to the increase along the direction perpendicular to this, ranging from 1.04 (blue) to 1.5 (red). In biology, the effect of anisotropic growth is geometrically represented as a transformation of a circular disk into an ellipse with a major axis oriented along the preferential direction of growth θ (see Figure 3.5.2). Here, a and b denote semi-minor and semi-major axes of an ellipse and the ratio $\frac{b}{a}$ is an estimate of the average anisotropy over a local region of gene activity ΔX that is determined experimentally as the ratio of the increase of cell divisions along the principal (x_2 axis in our conjecture) direction of growth to the

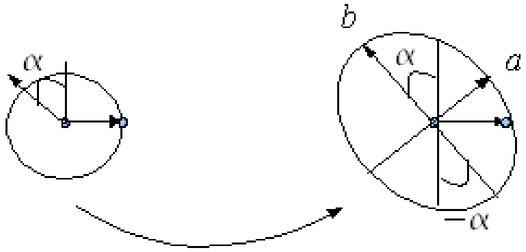

Figure 3.5.2: Deformation effect due to anisotropic growth.

increase of cell divisions along the minor one.

In the anisotropic GRID model, the angular deformation function sets up the degree of growth in any direction that depends on the nature of an activated seed (unipolar, bipolar, etc.). Then the k-function averaged over all directions for each fixed seed $x(\xi_{seed})$ becomes primarily a function of seed locations $\bar{k}(x(\xi_{seed}))$. $\bar{k}(x(\xi_{seed}))$ can be interpreted as the probability density defined over the Darcyan coordinate system of an organism that measures intensity of cell divisions (in case of pure growth) concentrated along the averaged regional principal directions of growth. Such a definition allows incorporation of experimental anisotropy measurements directly into the GRID model. Then anisotropic growth studied by a biologist can be represented by the isotropic GRID transformations defined by the angular deformation function independent of direction but dependent on seed locations.

We now derive a scalar function $\bar{k}(x(\xi_{seed}))$ such that the corresponding transformation $\phi^{\xi_{seed},t}$ iteratively deforms a disk of a given radius r comparable with the average radius of the region ΔX into an ellipse (and its interior) with a given ratio $\frac{b}{a}$ in an angle-preserving way during some time interval $0 \leq t \leq T$. Clearly, $\frac{b}{a}$ is a piece-wise constant function that varies from region to region implying that $\bar{k}(x(\xi_{seed}))$ will also have a regional variation within the X-field of the organism. In order to obtain the probability density we shall normalize the derived result over the X-field of an organism. We assume that seeds occupy all nodes of the Darcyan grid.

For simplicity, we consider a circular region of gene activity with radius r and set one preferential direction of growth along the positive vertical x_2 axis (see Fig.3.5.3). Other directions of growth can be easily handled by simply defining the same function $\bar{k}(x(\xi_{seed}))$ over the translated interval of directions $[\alpha + \frac{\pi}{2}, \alpha + 5\frac{\pi}{2}]$.

We emphasize the fact that we seek an angular deformation function dependent on the seed location only. With each activated seed position we associate an angle τ between the principal axis of growth x_2 and the normal direction to the radial curve at the seed point $x(\xi_{seed})$ (or radius-vector $x(\xi_{seed})$). Such a transformation is locally isotropic, transforming a small disk centered at the activated seed into a larger disk, and in a long time run it deforms a circular region of radius r (not a GRID parameter s!) into an elliptic one with the major axis aligned with the principal direction of growth x_2. We expect the $\bar{k}$-function to achieve its maximum in both $\frac{\pi}{2}$ and $-\frac{\pi}{2}$ directions meaning that seeds activated along thew cause maximal radial displacements of the neighboring seeds.

First, let us think of an angle-preserving mapping of a circle into an ellipse when all points of the circle move simultaneously to points of the ellipse. Basically, this is the transformation $K(\tau)$ acting on the radius-vector of the circle $v = x(\xi)$ with polar coordinates $\xi = (r, \tau)$ that changes its length depending upon the direction τ such that

$$\tilde{v} = K(\tau)v \text{ and } K(\tau) : (r, \tau) \rightarrow (K(\tau)r, \tau). \tag{3.5.1}$$

Graphically, the action of the mapping $K(\tau)$ is illustrated in Figure 3.5.3 as a transformation of a circle into an ellipse with the ratio of major semiaxis to minor semiaxis equal to $\frac{b}{a}$.

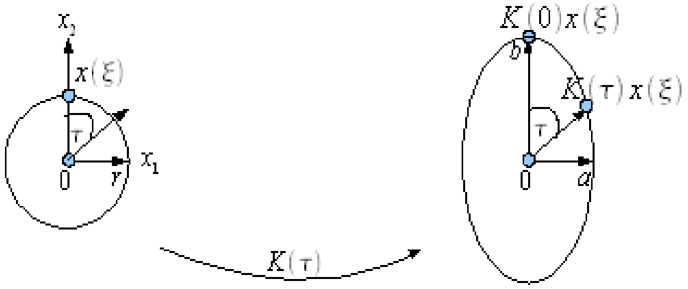

Figure 3.5.3: Geometric illustration of the angle-preserving transformation of a disk into an ellipse with its interior.

Given an angle τ between the radius-vector $v = x(\xi)$ and the x_2-axis a new radius-vector $\tilde{v}$ of the ellipse is defined as

$$\tilde{v} = \begin{bmatrix} \tilde{x}_1(\xi) \\ \tilde{x}_2(\xi) \end{bmatrix} = \begin{bmatrix} K(\tau)x_1(\xi) \\ K(\tau)x_2(\xi) \end{bmatrix}. \tag{3.5.2}$$

We denote $\tilde{x}_1(\xi) = K(\tau)v \sin\tau$ and $\tilde{x}_2(\xi) = K(\tau)v\cos\tau$ by $\tilde{v}_1$ and $\tilde{v}_2$, respectively, based on the fact that a new radius-vector traces points on the ellipse. The equation of the ellipse is

$$\frac{\tilde{v}_1^2}{a^2} + \frac{\tilde{v}_2^2}{b^2} = 1. \tag{3.5.3}$$

From (3.5.3) it follows that

$$K(\tau)^2 \sin^2\tau + K(\tau)^2 \frac{a^2}{b^2}\cos^2\tau = \frac{a^2}{v^2} \text{ and} \tag{3.5.4}$$

in polar (r, τ) coordinates we have

$$K(\tau) = \frac{a}{r\sqrt{\sin^2\tau + \frac{a^2}{b^2}\cos^2\tau}}. \tag{3.5.5}$$

Remark 3.5.1. *In view of the GRID model, the disk radius r is the range of influence of the activated seed s comparable to the size of a cell. For small disks of radius $\|v\| \leq s$ centered at the activated seeds $x(\xi_{seed})$ we can obtain an analytic formula for the angular deformation function $k(\tau)$ and the growth increment Δv from* (3.5.5)

$$\Delta v = \tilde{v} - v = v \cdot (K(\tau) - 1) = v \cdot k(\tau) \text{ for } \|v\| \leq s. \tag{3.5.6}$$

Therefore, the expression for the amplitude of growth in anisotropic case is

$$k(\tau) = \frac{ab}{r\sqrt{b^2 \sin^2 \tau + a^2 \cos^2 \tau}} - 1. \tag{3.5.7}$$

Then the elementary $\phi^{\xi_{seed}}$ mapping (3.1.10) *defined with such k-function locally deforms disks into ellipses similar to the effect of "unipolar-source-midwards" transformation described earlier.*

Here, we are interested in evolving an ellipse from a large disk comprised of a considerable number of seeds by means of smooth local iterated transformations. The mapping $K(\tau)$ given by (3.5.5) depends on the angle τ between the radius-vector $x(\xi)$ and the principal direction of growth x_2. Directions τ basically identify angular coordinates of seeds placed at all nodes of the polar grid of the disk. It follows from the definition of $K(\tau)$ (3.5.5) that the largest displacements are undergone by the seeds located along $\frac{\pi}{2}$ and $-\frac{\pi}{2}$ directions as desired. This result leads to modeling the angular deformation function $\bar{k}(x(\xi_{seed}))$ as the normalized function $K(\tau)$,

$$\bar{k}(x(\xi_{seed})) = \bar{k}(\tau) = \frac{ab}{rZ\sqrt{b^2 \sin^2 \tau + a^2 \cos^2 \tau}}, \tag{3.5.8}$$

where τ is the angular coordinate of a seed point $x(\xi_{seed})$ and Z is a normalizing constant providing that $\int_{\Xi} k(\tau) d\xi_{seed} = 1$. Without normalizing, the $\bar{k}$-function is simply a weight function defined over the X-field of the circular organism as shown in Figure 3.5.4.a. Diffeomorphisms (3.1.10) with the k-function given by (3.5.8) are locally isotropic since $\bar{k}\tau$ depends on the angular coordinate or the position of the activated seed. Thus, small discs or radius s with centers located along the principal x_2-axis grow into the largest disks, and those with centers located along the x_1-axis remain almost unchanged.

We implement such diffeomorphisms for simulation of growth of an organism initially occupying the unit disk $S^1 \subset \Re^2$ with seeds located at all nodes of its Darcyan polar grid (gene set $\Delta\Xi = \Xi$), range of influence $s = 0.05$ and anisotropy $\frac{b}{a}$ equal to 1.36 ($a = 1.1$ and $b = 1.5$). Seeds are activated one at a time and at random according to the uniform probability distribution in space-time. Here, the value of $\frac{b}{a}$ set to 1.36 means that 36% more cell divisions is expected along the x_2 axis in the absolute space. Figure 3.5.4.b displays the deformed Darcyan coordinate system of the grown organism as a result of a sequence of 3000 random cell divisions. Observe that the concentric level sets have been smoothly transformed into the elliptical level sets with the occasional presence of oscillations on the outer boundary.

All in all, we have attempted to modify the GRID angular deformation function in order to reflect the reality of a growth process and to incorporate experimental measurements of anisotropic growth into the model. In case of pure growth, the derived formula for the angular deformation function (3.5.8) can be used by a biologist as a model of a spatially varying measure of anisotropy within each region of gene activity.

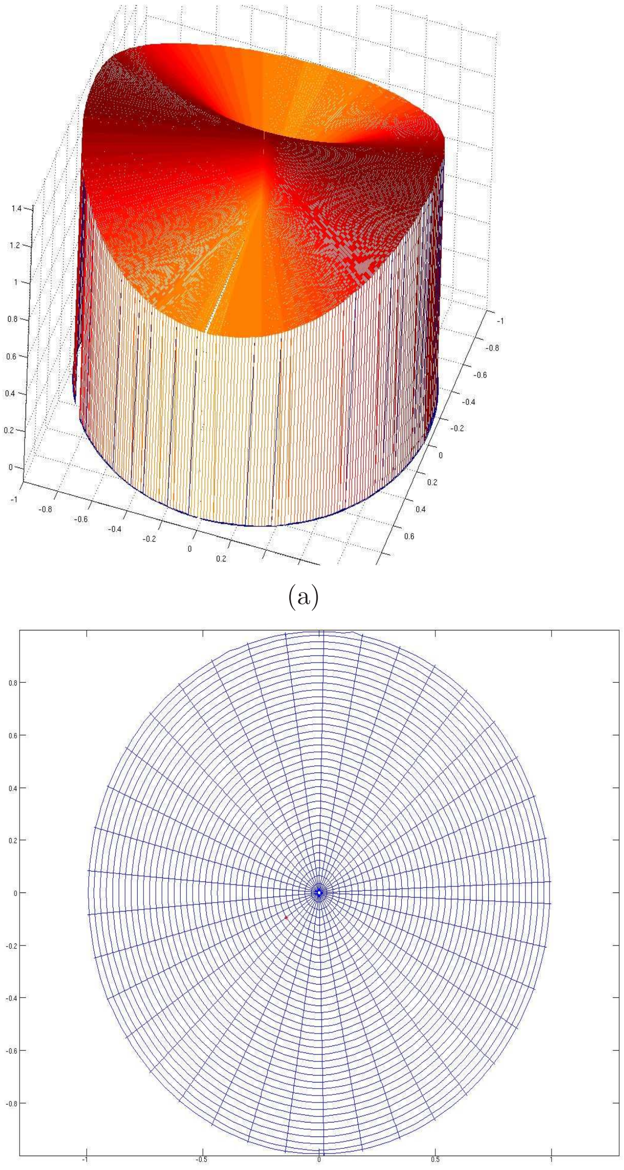

(a)

(b)

Figure 3.5.4: (a) The graph of the angular deformation function $\bar{k}(x(\xi_{seed}))$ as a measure of the degree of growth in any direction; (b) The deformed Darcyan grid of the initially circular organism obtained with the use of the weight $\bar{k}$-function.

Chapter 4

Stochastic aspects of 1D isotropic GRID model

4.1 A continuous-time stochastic GRID model

We have introduced and explored the discrete-time GRID model whose fundamental equation of growth describes the dynamics of development by means of random iterated diffeomorphisms. In this section we give a formal definition of the GRID model using theory of stochastic processes. We then study 1D position process generated by the stochastic version of the GRID model.

According to the discrete-time GRID model the growth of an organism $\Omega \subset \Re^m, m \in \{1,2,3\}$ is produced by a diffeomorphism of composite and random nature.

$$\phi_n(X(\xi)) = \phi^{\xi_{\sigma_n}} \circ \phi^{\xi_{\sigma_{n-1}}} \circ \phi^{\xi_{\sigma_{n-2}}} \circ \ldots \circ \phi^{\xi_{\sigma_1}} (X(\xi)),$$

where $X(\xi)$ is the Darcyan coordinate system of the organism's domain Ω. Thus, a growing organism undergoes a series of Darcyan coordinate transformations each resulting at a random seed position ξ_{σ_i} with some probability mass function $P(\xi)$ over the set of its possible values $\{\xi_{\sigma_i},\ \sigma_i \in \{1,2,\ldots,N\}\}$, where N is the total(large) number of seeds.

$$x_n(\xi) = \phi^{\xi_{\sigma_n}} \circ \phi^{\xi_{\sigma_{n-1}}} \circ \phi^{\xi_{\sigma_{n-2}}} \circ \ldots \circ \phi^{\xi_{\sigma_1}} (x_0(\xi)) \text{ or } x_n(\xi) = \phi^{\xi_{\sigma_n}}(x_{n-1}(\xi)) \quad (4.1.1)$$

We can also associate the GRID growth pattern (4.1.1) with a sequence of snapshots of the growing organism $\{\Omega(t_i)\}_{i=1}^n$, where $t_1 < t_2 < t_3 < \ldots < t_n$ is a sequence of occurrence times of seed activation. What is a continuous-time formulation of the GRID model?

We distinguish between the compact space of absolute Cartesian coordinates representing the organism's domain Ω and the underlying space of Darcyan coordinates Ξ. The absolute and Darcyan coordinate spaces are the subsets of the Euclidean space $E^n : n \in \{1,2,3\}$. In 2D, for example, the curvilinear Darcyan coordinate system $\{X(\xi) = (x_1(\xi_1,\xi_2), x_2(\xi_1,\xi_2)) \in \Omega\}$ is obtained by a smooth mapping of the Darcyan coordinate space $\{(\xi_1, \xi_2) \in \Xi : 0 \leq \xi_1 \leq 1, 0 \leq \xi_2 \leq 2\pi\}$. Such a map X generates a natural coordinate system in the organism's domain Ω in the form of a boundary-conforming continuum grid with radial ξ_1 and angular ξ_2 coordinate curves. It is required to be a diffeomorphism to ensure that each point in the Darcyan space is mapped to a unique point in the absolute space and vice versa. Then the relationship between Darcyan and Riemannian metrics is given by the *First Fundamental Form* in differential geometry

$$(dx_1)^2 + (dx_2)^2 = \sum_{i,j=1}^{2} g_{ij} d\xi_i d\xi_j, \quad \text{where } g_{ij} = \sum_{l=1}^{2} \frac{\partial x_l}{\partial \xi_i} \frac{\partial x_l}{\partial \xi_j}.$$

For an arbitrary biological shape in $\Re^2$ an explicit expression for the mapping X is not known. Therefore, a discrete grid is usually constructed by choosing the numbers of radial and angular coordinate curves M and N and a uniform discrete Darcyan grid with $N \times M$ grid nodes. Given a discrete boundary diffeomorphism ∂X defined at a finite number of Darcyan seeds with coordinates $(\xi_{1_1} = 1, \xi_{1i} = i\frac{2\pi}{N}), i = 1, 2, \ldots, N$, we extend it to a diffeomorphism X of Ξ to the interior of Ω using the Level Set Method.

The discrete Darcyan space Ξ is a countable set comprised of many isolated points or *seeds*. Such discrete space reflects the discrete structure of an organism comprised of a large number of cells. Strictly speaking, specifying a metric given by the Euclidean distance $d(\xi_a, \xi_b) = |\xi_b - \xi_a|$ and the discrete topology by letting every subset of Ξ be an open set we define Ξ as a *discrete metric space*. In 2D, such Ξ-space and the corresponding absolute space $X(\xi)$ of the organism Ω are illustrated as rectangular and curvilinear grids (see Figure 4.1). Observe from the Figure above that points in the absolute space are given by $x_{ij} = (x_{1_{ij}}, x_{2_{ij}})$, where

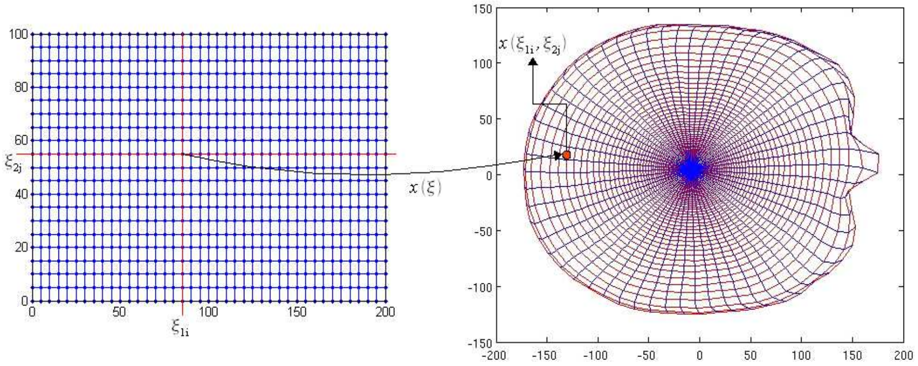

Figure 4.1.1: Discrete Darcyan space $\Xi = \{(\xi_{1_i}, \xi_{2_j}) : i = 1, 2, \ldots, M; j = 1, 2, \ldots, N\}$ and the corresponding absolute coordinate space of a 2D brain slice $X(\xi) = \{x_1(\xi_{1_i}, \xi_{2_j}), x_2(\xi_{1_i}, \xi_{2_j}) : i = 1, 2, \ldots, M; j = 1, 2, \ldots, N\}$.

$$x_{1_{ij}} = x_1(i, j),\ 0 \leq i \leq M,$$
$$x_{2_{ij}} = x_2(i, j),\ 0 \leq j \leq N$$

and j refers to an angle $j\frac{2\pi}{N}$. The ξ coordinates simply enumerate radial and angular coordinate curves in Ω. The ξ_1 and ξ_2 curves are given by drawing line segments $[(x_{1_{ij}}, x_{2_{ij}}), (x_{1_{i+1_j}}, x_{2_{ij}})], 0 \leq i \leq M-1$ and $[(x_{1_{ij}}, x_{2_{ij}}), (x_{1_{ij}}, x_{2_{i_{j+1}}})], 0 \leq j \leq N-1$ respectively.

Since activated seeds represent highly localized random events (cell death/division) in a continuum they can be viewed as points in time-space $[t_0, \infty] \times \Xi$ distributed with the intensity $\Lambda(t, \xi)$ per unit volume. We assume the simplest form of the intensity function that allows heterogeneity of growth in both space and time

$$\Lambda(t, \xi) = \lambda_t \times \lambda_x.$$

Here, λ_t is the instantaneous average rate of seed activation at a time t. For instance, a constant rate $\lambda_t = \frac{1}{4}$ means average occurrence of one biological event every four units of time (e.g. seconds, minutes, days, etc.). λ_x is the average rate of event occurrences at x per unit volume dx and not $d\xi$ since the cell density is measured in absolute coordinates x.

Given the time scale $t_c = \frac{1}{\lambda_t}$ we record variations in the position of an organism $\Omega(t)$ in time periods comparable to t_c or on the fine time scale. With each occurrence time t_k we associate a seed ξ_{σ_k}. We are led to a spatial-temporal counting Poisson process (see Appendix A),

$$\{\mu(T, B) : T \subset [t_0, \infty], B \subset \Omega\}, \tag{4.1.2}$$

such that the expected value is given by

$$E(\mu(T, B)) = \int_T \int_B \Lambda(t, x) dt dx = \int_T \lambda_t dt \cdot \int_B \lambda_x dx. \tag{4.1.3}$$

Here, $\mu(T, B)$ is a counting measure, a random number of seeds activated in a time interval T and region B in organism's domain.

It is preferable to define the Poisson process (4.1.2) underlying shape and interior changes of the organism Ω in the Darcyan continuum Ξ. We introduce the Poisson intensity of seed placements $\lambda(\xi)$ that can be normalized to represent the spatial probability density of seeds in Ξ-space,

$$p(\xi) = \frac{\lambda(\xi)}{\int_\Xi \lambda(\xi) d\xi}. \tag{4.1.4}$$

$\lambda(\xi)$ represents the average genetically-controlled rate of seed activation per unit volume $d\xi$, an intrinsic growth property of the organism. We construct the spatial-temporal Poisson process characterized by this intensity parameter using the bijective property of the mapping $x = x(\xi)$.

To express the expected value of a random variable $\mu(T, B)$ given by (4.1.3) in Darcyan coordinates we apply the change of variable $x = x(\xi)$. Then any subset $\{x : x \in B \subset \Omega\}$ is converted into $\{\xi : \xi \in A = x^{-1}(B) \subset \Xi\}$. We obtain

$$E(\mu(T, B)) = \int_T \lambda_t dt \cdot \int_{x^{-1}(B)} \lambda_x(\xi) \cdot \left| \frac{\partial(x_1, \ldots, x_m)}{\partial(\xi_1, \ldots, \xi_m)} \right| d\xi \tag{4.1.5}$$

The intrinsic intensity parameter $\lambda(\xi)$, determined as

$$\lambda(\xi) = \lambda_x(\xi) \cdot \left| \frac{\partial(x_1, \dots, x_m)}{\partial(\xi_1, \dots, \xi_m)} \right| \tag{4.1.6}$$

on the RHS of (4.1.5), leads to the equivalent definition of the Poisson counting process (4.1.2) with respect to the Darcyan space. That is,

$$\{\mu(T, A) : T \subset [t_0, \infty], A \subset \Xi\} \tag{4.1.7}$$

such that the expected value is given by

$$E(\mu(T, A)) = \int_T \lambda_t dt \cdot \int_A \lambda(\xi) d\xi \text{ and } A = x^{-1}(B). \tag{4.1.8}$$

From (4.1.6) follows the important definition of $\lambda_x(\xi)$.

Definition 4.1.1. *Let $\lambda(\xi)$ be the Poisson intensity of seed placements in the Darcyan space Ξ and the compact domain of an organism Ω be represented by the Darcyan coordinate system $x(\xi)$ with $\xi \in \Xi$ and $x \in \Omega \subset \Re^m$, $m \in \{1, 2, 3\}$. Then the intensity of biological events in Ω is*

$$\lambda_x(\xi) = \frac{\lambda(\xi)}{\left| \frac{\partial(x_1, \dots, x_m)}{\partial(\xi_1, \dots, \xi_m)} \right|}. \tag{4.1.9}$$

Example 4.1.2. *Let the Darcyan space be a lattice with $n \times m$ equidistant nodes and let seeds be uniformly distributed over the set of nodes. Assume that the Poisson intensity $\lambda(\xi)$ is a unit mass function. Consider an organism $\Omega \subset \Re^2$ in the form of a unit disc whose Darcyan coordinate system is the polar grid with n radial and m angular coordinate lines. The seeds $\xi_{ij} = (\xi_{1_i}, \xi_{2_j}) = (r_i, \theta_j)$ with $(i, j) \in \{1, 2, \dots n\} \times \{1, 2, \dots m\}$ appear non-uniformly distributed in Ω with high density near the origin of the polar grid due to the non-linear transformation of Darcyan coordinates into absolute coordinates of the organism*

$$(x_1, x_2) = (r \cos\theta, r \sin\theta).$$

Since the Jacobian determinant of polar coordinate transformation is equal to r the intensity of biological events in Ω according to (4.1.9) becomes

$$\lambda_x(\xi) = \frac{1}{r}.$$

The Poisson process (4.1.2) has a complex structure in the continuum absolute space of an organism. Let dx_k be an element of volume in $\Omega \subset \Re^m$. Having broken up Ω into non overlapping unit volumes $dx_k = [x_k, x_k + dx_k]$, $k = 1, 2, \dots$, the Poisson processes $\{\mu_t(dx_j) : t \geq t_0\}$,$j = 1, 2, \dots$, count the number of seeds for $t \geq$

t_0 activated in the elemental volumes dx_j of Ω. Then at a time t, $\mu_t(A) = \int_A \mu_t(dx)$ is a counting measure of a spatial Poisson process in Ω where $\mu_t(dx) = \int_{t_0}^{t} \mu(dt, dx)$. In a similar fashion we can define temporal Poisson processes $\{\mu_x(dt_j) : x \in B\}$ counting the number of activated seeds for a fixed volume $B \subset \Omega$ in non overlapping time intervals $dt_k = [t_k, t_k + dt_k]$, $k = 1, 2, \ldots$, such that over a longer time period T $\mu_x(T) = \int_T \mu_x(dt)$. Thus, the counting measure in time-space $[t_0, \infty] \times \Omega$ is

$$\mu(T, B) = \int_T \mu_x(dt) = \int_B \mu_t(dx).$$

We now formulate the time-space counting Poisson process (4.1.7) with a normalized intensity function $p(\xi)$ given by (4.1.4). If ξ is a continuous random variable then the probability density for it exists and the intensity for this Poisson process is $\lambda_t \cdot p(\xi)$. Otherwise, the probability density is simply the probability mass function $Pr(\xi = \xi_{seed})$. Generally speaking, the number of seeds in the region $T \times A$ is Poisson distributed with the expected value

$$E[\mu(T, A)] = \int_T \int_{\xi_{seed} \in A} \lambda_t dt \; dPr(\xi_{seed}). \tag{4.1.10}$$

Theorem 4.1.3. ***(Representation of a time-space Poisson process of seed placements.)*** *Let T be a time interval in $[t_0, \infty]$ and A be a region in Ξ . Let $\mu(T, A)$ be the number of activated seeds with time-space coordinates in $T \times B$. Seeds are then placed in time-space $[t_0, \infty] \times \Xi$ as Poisson points with intensity λ_t and spatial probability distribution $Pr(\xi)$.*

Then $\{\mu(T, A) : T \subset [t_0, \infty], A \subset \Xi\}$ is a time-space Poisson process such that

$$E(\mu(T, A)) = \int_T \int_A \lambda_t dt \; dPr(\xi).$$

If the seeds are continuous random variables with probability density $p(\xi)$, the intensity function for μ is $\lambda_t p(\xi)$.

Such a Poisson process is characterized by the joint probability density for the n seeds activated at times $t_1 < t_2 < \ldots < t_n$ and locations $\xi_1 = \xi_{\sigma_1}$, $\xi_2 = \xi_{\sigma_2}$,..., $\xi_n = \xi_{\sigma_n}$. For the Poisson process with a countable high-dimensional Darcyan space the probability density will be $p(\vec{t}, \vec{\xi_\sigma}, n)$, where $\vec{t} = (t_1, t_2, \ldots, t_n)$, $\vec{\xi_\sigma} = (\xi_{\sigma_1}, \xi_{\sigma_2}, \ldots, \xi_{\sigma_n})$. It is given by

$$\begin{aligned} p(\vec{t}, \vec{\xi}, n) &= p(\vec{\tau} = \vec{t}, \vec{\xi} = \vec{\xi_\sigma}, \mu(T, \Xi) = n) \\ &= Pr(\mu(T, \Xi) = n | \vec{\tau} = \vec{t}, \vec{\xi} = \vec{\xi_\sigma}) \\ &\quad \times Pr(\vec{\xi} = \vec{\xi_\sigma} | \vec{\tau} = \vec{t}) \cdot p_t(\vec{t}), \end{aligned} \tag{4.1.11}$$

where $\vec{\tau}$ is a random n-dimensional vector of times of seed occurrences, $\vec{t} = (t_1, t_2, ..., t_n)$ is a particular realization of the Poisson process on the time interval $[t_0, t]$ with the corresponding seed coordinates $\xi_{\sigma_1}, \xi_{\sigma_2}, \dots, \xi_{\sigma_n}$ in Ξ-space. By the theorem in Appendix A, the probability density (4.1.11) is given by

$$p(\vec{t}, \vec{\xi} = \vec{\xi_\sigma}, \mu(T, \Xi) = n) = \left[\prod_{i=1}^{n} \lambda_{t_i} Pr(\xi_{\sigma_i}) \right] \exp\left(- \int_{t_0}^{t} \lambda_s ds \right) \qquad (4.1.12)$$

So far, we have established a rigorous definition of seeds as Poisson points occurring in time-space. According to the GRID model they cause a cascade of local deformation effects or motion of a growing structure. What is the interpretation of the fundamental GRID equation of motion due to growth in theory of stochastic processes?

As a result of a realization of the time-space Poisson process in $[t_0, t] \times \Xi$ the position of the organism Ω in the absolute space is defined by the diffeomorphism ϕ_t composed of n elementary deformations $\phi^{\xi_{\sigma_i}}$, $i = 1, 2, \dots, n$,

$$x_t = \phi_t(x_{t_0}) = \phi^{\xi_{\sigma_n}} \circ \phi^{\xi_{\sigma_{n-1}}} \circ \phi^{\xi_{\sigma_{n-2}}} \circ \dots \circ \phi^{\xi_{\sigma_1}} (x_{t_0}) . \qquad (4.1.13)$$

If a single seed ξ_{σ_k} is activated in a small time interval $[t, t + \Delta t]$ then the counting measure $\mu(\Delta t, \Delta\xi) = 1$, and the organism moves to a new position $x_{t+\Delta t}$ given by

$$x_{t+\Delta t}(\xi) = \phi^{\xi_{\sigma_k}}(x_t(\xi)) = x_t(\xi) + (x_t(\xi) - x_t(\xi_{\sigma_k})) \cdot k(\xi, \xi_{\sigma_k}) \exp\left(- \frac{\|x_t(\xi) - x_t(\xi_{\sigma_k})\|^2}{s^2} \right) . \qquad (4.1.14)$$

Here, $k(\xi, \xi_{\sigma_k})$ is the angular deformation function that depends on an angle τ between a vector $[x(\xi) - x(\xi_{\sigma_k})]$ and a positive x_1-axis in $\Re^2$. From (4.1.14) the displacement field in x or instantaneous growth increment is given by

$$\begin{aligned} \Delta x_t &= x_{t+\Delta t}(\xi) - x_t(\xi) \\ &= (x_t(\xi) - x_t(\xi_{\sigma_k})) \cdot k(\xi, \xi_{\sigma_k}) \exp\left(- \frac{\|x_t(\xi) - x_t(\xi_{\sigma_k})\|^2}{s^2} \right) . \end{aligned} \qquad (4.1.15)$$

Denoting the RHS of (4.1.15) by $y^{\xi_{\sigma_k}}(x_t)$, the displacement Δx undergone by each point of the X-field $x_t(\xi)$ is a deterministic function y that depends on the distance from a random seed location $x(\xi_{\sigma_k})$ to $x_t(\xi)$

$$\Delta x_t = y^{\xi_{\sigma_k}}(x_t).$$

The Poisson point process of seed activations in time and Ξ-space induces a probability measure on the displacement field Δx_t. Indeed, the probability of the event $\{\Delta x_t = y^{\xi_{\sigma_k}}(x_t)\}$ is

$$Pr\{\Delta x_t = y^{\xi_{\sigma_k}}(x_t)\} = Pr\{\mu(\Delta t, \xi_{\sigma_k}) = 1 \mid \mathcal{H}_{t,\xi}\}, \qquad (4.1.16)$$

where $\mathcal{H}_{t,\xi}$ is the history of the process at time t, i.e. specification of all points in $[t_0, t] \times \Xi$. By the property of the Poisson process (see Appendix A) the probability that the increment $\mu(\Delta t, \xi_{\sigma_k}) = 1$ conditioned on $\mathcal{H}_{t,\xi}$ is

$$\begin{aligned} Pr\{\mu(\Delta t, \xi_{\sigma_k}) = 1 | \mathcal{H}_{t,\xi}\} = & \left(\int_t^{t+\Delta t} \lambda_s ds \right) (Pr\{\xi = \xi_{\sigma_k}\}) \\ & \cdot \exp\left(- \int_t^{t+\Delta t} \lambda_s ds \cdot Pr\{\xi = \xi_{\sigma_k}\} \right) . \end{aligned} \qquad (4.1.17)$$

Letting $\Delta t \to 0^+$ in (4.1.17) we compute the probability of the instantaneous growth increment $\Delta x(\xi)$ as follows

$$Pr\{\Delta x_t = y^{\xi_{\sigma_k}}(x_t)\} = \lambda_t \Delta t \cdot Pr\{\xi = \xi_{\sigma_k}\} + o(\Delta t). \tag{4.1.18}$$

If during the time interval $[t, t + \Delta t]$ no seeds are activated, then $\mu(\Delta t, \xi) = 0$ and the increment in x $\Delta x_t = 0$. Clearly,

$$Pr\{\Delta x_t = 0\} = 1 - \lambda_t \Delta t \cdot Pr\{\xi = \xi_{\sigma_k}\} + o(\Delta t).$$

Thus, we arrive at a position stochastic process $\{x_t : t \geq t_0\}$ whose structure is illustrated in Figure 4.1.2. We conclude that $\{x_t : t \geq t_0\}$ is a jump stochastic process with the size of the jump occurring at a time t of seed activation defined by the formula (4.1.15). In the stochastic processes literature [61] this is known as a *Poisson driven Markov process*. We summarize the development of the continuous-time stochastic GRID model in the following theorem.

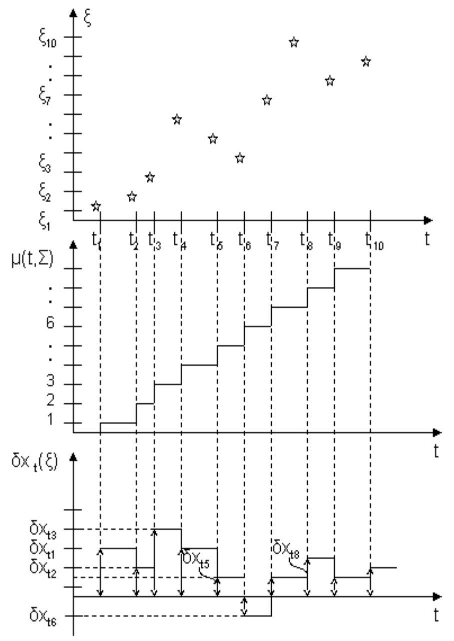

Figure 4.1.2: Top panel: Seeds (ξ_i, t_i) activated randomly in time-space. Middle panel: The corresponding Poisson process $\mu(t, \Xi)$ counting the number of activated seeds at occurrence times $\{t_i\}_{i=1}^n$. Bottom panel: Displacements $\{\delta x_{t_i}\}_{i=1}^n$ undergone by a point in the organism's domain with initial coordinates $x_{t_0}(\xi)$ as a result of a realization of the Poisson point process shown in the above panels.

Theorem 4.1.4. *The continuous-time stochastic GRID model for a biological growth is a Poisson driven Markov process $\{x_t, t \geq t_0\}$ that satisfies an integral equation of the form*

$$x_t = x_0 + \int_{t_0}^{t} \int_{\Xi} y^{\xi_{seed}}(x_s) \mu(ds, d\xi_{seed}), \tag{4.1.19}$$

where $\{\mu(T, A), T \subset [t_0, \infty],\ A \subset \Xi\}$ *is the spatial-temporal Poisson process introduced in Theorem 4.1.3. The integral term in* (4.1.19) *is evaluated as follows*

$$\int_{t_0}^{t} \int_{\Xi} y^{\xi_{seed}}(x_s)\mu(ds, d\xi_{seed}) = \begin{cases} 0, & \mu(t, \Xi) = 0 \\ \sum_{i=1}^{n} y^{\xi_{seed_i}}(x_{t_i}), & \mu(t, \Xi) \geq 1, \end{cases} \tag{4.1.20}$$

where $\mu(t, \Xi)$ *is the number of activated seeds during* $[t_0, t)$ *regardless of their positions in* Ξ *and* $y^{\xi_{seed}}(x_\sigma)$ *is the displacement field given by* (4.1.15).

The differential form of the equation for $\{x_t, t \geq t_0\}$ *is*

$$dx_t = \int_{\Xi} y^{\xi_{seed}}(x_t)\mu(dt, d\xi_{seed}), \tag{4.1.21}$$

with the initial condition $x_{t_0} = x_0$*. The* X*-field of the growing organism* Ω *at time* t *is represented by* x_t*, the state of the Poisson driven Markov process. The state space of the process is a high-dimensional (ideally infinite-dimensional) Euclidean space* $\mathcal{X}$*.*

Remark 4.1.5. *The stochastic differential equation* (4.1.21) *can be viewed as a non-linear transformation of the Poisson process* μ *into the jump process* x_t *in the absolute space. The differential* $dx_t = x_{t+dt} - x_t$ *is an infinitesimal growth increment that occurs during* $[t, t+dt)$*. The increment in* x *is either zero or* $y^{\xi_{seed}}(x_t)$ *depending on the occurrence of a single biological event during* $[t, t+dt)$ *in* Ξ*-space. Clearly,* x_t *has discontinuities at occurrence times of seed activation with the size of the discontinuity defined by* $y^{\xi_{seed}}(x_t)$*.*

4.2 Experimental study of 1D GRID stochastic equation of growth

In this section we consider a continuous-time one-dimensional (1D) isotropic GRID model represented by the stochastic differential equation (4.1.21) of growth. We assume that growth of a 1D "organism" is isotropic and is comprised of cell divisions that divide uniformly and at the constant rate in time. Then cell division locations are seeds uniformly distributed in Ξ-space with a constant intensity of seed activations per unit time. This translates into the following GRID formalism.

1. The angular deformation function is constant, $k(\xi, \xi_k) = K$,
2. $\xi \in \Xi$ with a countable Darcyan space Ξ is an activated seed, a random variable with the uniform discrete probability measure over the set of all of its possible values $\{\xi_{\sigma_i}, \sigma_i \in \{1, 2, \ldots, N\}\}$,
3. At any time n, the probability $Pr(\xi = \xi_{\sigma_i}) = \frac{1}{N}$,
4. The intensity of cell divisions per unit time dt $\lambda_t = 1$.

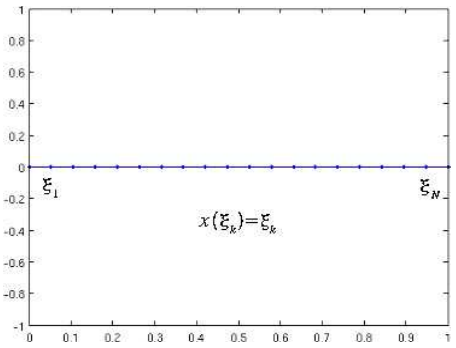

Figure 4.2.1: Initial 1D organism $\Omega = x_0(\xi)$ comprised of N uniformly distributed seeds ξ_i.

4.2.1 Empirical and analytical average growth estimates

In this subsection we simulate short and long time growth of a 1D organism and estimate the mean growth rate empirically and analytically.

Without loss of generality, we represent the initial 1D organism by an interval of unit length, that is, $\Omega(0) = [0, 1]$. At time $t = 0$ the Darcyan grid of Ω is a set of N seeds uniformly distributed over the length of the organism, that is $x(\xi_k) = \xi_k$ as shown in Figure 4.2.1. At some observation time $t > 0$ the grown organism $\Omega(t)$ will be represented by the state x_t of the Poisson driven stochastic process

$$x_t(\xi) = \xi + \int_0^t \int_\Xi y^{\xi_{seed}}(x_s)\mu(ds, d\xi_{seed}), \tag{4.2.1}$$

The practical version of (4.2.1) is given by

$$x_t(\xi) = \xi + \sum_{t_k<t} (x_{t_k}(\xi) - x_t(\xi_{\sigma_k})) \cdot K \cdot \exp\left(-\frac{\|x_{t_k}(\xi) - x_t(\xi_{\sigma_k})\|^2}{s^2}\right), \tag{4.2.2}$$

where ξ_{σ_k} is the seed activated at time t_k and in the countable Darcyan space $\Xi = \{\xi_1, \xi_2, \ldots, \xi_N\} \subset [0, 1]$, as shown in Figure 4.2.1. In order to simulate 1D isotropic growth we use the Matlab script called "grid1d.m"(see Appendix E) that executes the following algorithm:

1. Given the positions of seeds $x_n(\xi_i)$, $i = 1, 2, \ldots, N$ in absolute coordinates at the nth time iteration, pick randomly an index j distributed uniformly over the set of indices $\{1, 2, \ldots, N\}$.

2. Apply the transformation y^{ξ_j} to all seeds x_n to update the current organism's position to

$$x_{n+1}(\xi_i) = x_n(\xi_i) + (x_n(\xi_i) - x_n(\xi_j)) \cdot K \cdot \exp\left(-\frac{\|x_n(\xi_i) - x_n(\xi_j)\|^2}{s^2}\right) \quad \text{for all } i \in \{1, 2, \ldots, N\}.$$

We now perform the "worm growth" experiment based on the assumption that the organism grows due to cell divisions whose locations are roughly represented by 30 seeds uniformly distributed over its length (see Fig.4.2.1). Then the elemental length (or the length scale) $\Delta\xi$ is equal to $\frac{1}{30}$. It can be interpreted as a distance between neighboring active gene sites that does not necessarily represent the dimension of a cell.

Choosing the GRID parameter values for the amplitude of growth $K = 1.0$ and the range of influence of each seed $s = 2\Delta\xi$ we run 30 iterations of the GRID algorithm. The resulting evolution of the seed configuration of the growing worm in time-space is illustrated in Figure 4.2.2. As seen from Figure 4.2.2, at the first occurrence time $n = 1$ the initially uniform distribution of seeds in the space of Cartesian coordinates x_1 of the organism becomes perturbed in the neighborhood of the activated seed. (Note that in Ξ space the uniform distribution is preserved in the course of time). This is expected due to the non-linear model of elementary growth deformation $y^{\xi_{seed}}(x_t)$. Basically, each time iteration n introduces a new perturbation as a cell divides at a random seed location $x_n(\xi_i)$ (shown by a red star) pushing its neighbors and causing local expansions. Observe that motions of individual seeds $x_n(\xi_i)$ are not independent as their positions in $\mathcal{X}$ are influenced by their neighbors $x_n(\xi_{i-2})$, $x_n(\xi_{i-1})$ and $x_n(\xi_{i+1})$, $x_n(\xi_{i+2})$. When one of these neighboring seeds is activated it pushes $x_n(\xi_i)$ forward or backward. Otherwise, a change in the position of $x_n(\xi_i)$ is hardly visible due to the range of influence

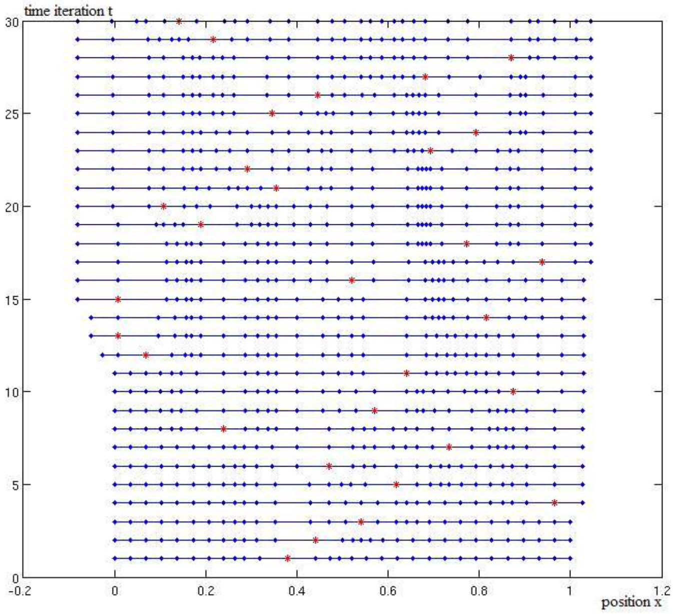

Figure 4.2.2: Evolution of the seed configuration of a 'worm' in time-space $[0,t] \times \mathcal{X}$ with uniform distribution of seeds in Ξ space, amplitude of growth $K = 1$ and the range of influence $s = 2\Delta\xi$. The distance between cells $\Delta\xi = \frac{1}{30}$ and the total number of seeds as well as time occurrences is 30. Activated seeds are denoted by red stars.

restricted to only 2 neighboring cells.

In another long-time 'worm growth' experiment shown in Figure 4.2.3 we have performed $10,000$ realizations of the GRID stochastic differential equation of growth with the GRID parameter values $K = 1.0$ and $s = 0.1$. Here, the organism is comprised of $10,000$ seeds and, therefore, the distance between the neighboring active gene sites $\Delta\xi$ is 0.1^4 and the range of influence is 1000 seeds. In other words, the Darcyan space $\Xi = \{\xi_1, \xi_2, \ldots, \xi_{10,000}\} \subset [0, 1]$. Due to a large number of seeds it is hard to observe evolution of the seed configuration of the organism as it grows in the long course of time. The graph of the growing worm clearly suggests that the rate of length change decreases in time. A question arises immediately: How does the rate of length increase decrease in the course of time? Does it depend on the range of influence parameter s? Since the length L_n is random as a deterministic function of a random seed placement ξ_j

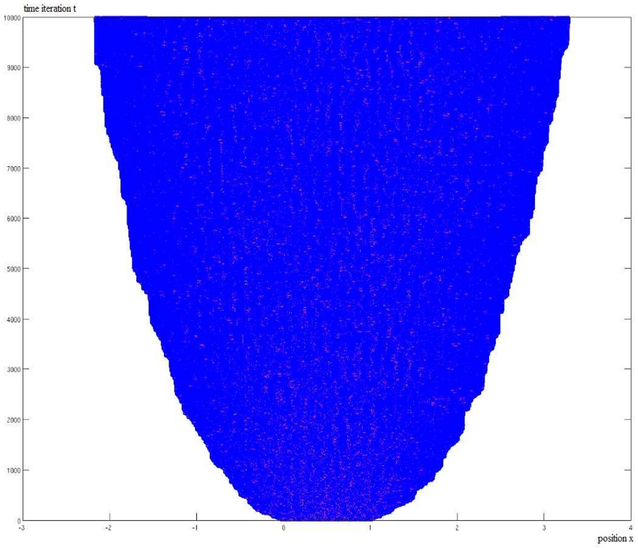

Figure 4.2.3: Long-time 'worm growth' in $[0, \infty] \times \mathcal{X}$ with uniform distribution of seeds in Ξ space, amplitude of growth $K = 1$ and the range of influence $s = 1000\Delta\xi$. The distance between cells $\Delta\xi = 0.1^4$ and the total number of seeds as well as time occurrences is $10,000$. Activated seeds are denoted by red stars.

$$L_n = x_n^{N+1} - x_n^0, n = 1, 2, \ldots, \tag{4.2.3}$$

where x_n^0, x_n^{N+1} are the left and right endpoints of the organism at time n defined by (4.2.3) we can only evaluate the rate of its average increase.

To address this question we first find empirical estimates of the mean length $\overline{L_n}$ from a large collection of possible lengths L_n at each time n for different s sizes. We perform 1000 numerical experiments, each time starting with an organism comprised of $N = 1000$ uniformly distributed seeds over $[0, 1]$ and applying $niter = 300$ iterations of the GRID algorithm. Note that $niter << N$ to ensure that each seed is picked only once with high probability at each time iteration.

In each experiment i we compute the lengths L_n^i of the grown organism for all times n, $n = 1, 2, \ldots, niter$ using formula (4.2.3). Then the empirical mean of the statistical sample of 1000 possible lengths is $\overline{L_n} = \frac{1}{1000}\sum_{i=1}^{1000} L_n^i$. In what follows, we plot all length values as realizations of a stochastic process $\{L_n = x_n^{N+1} - x_n^0,\, t > 0\}$ and the mean length curve as a function of time $\overline{L_n}$ for various orders of magnitude of the s parameter. In Figure 4.2.4 we illustrate the effects of the s value of the order of magnitude $O(\Delta\xi)$. When the s parameter is comparable to the length

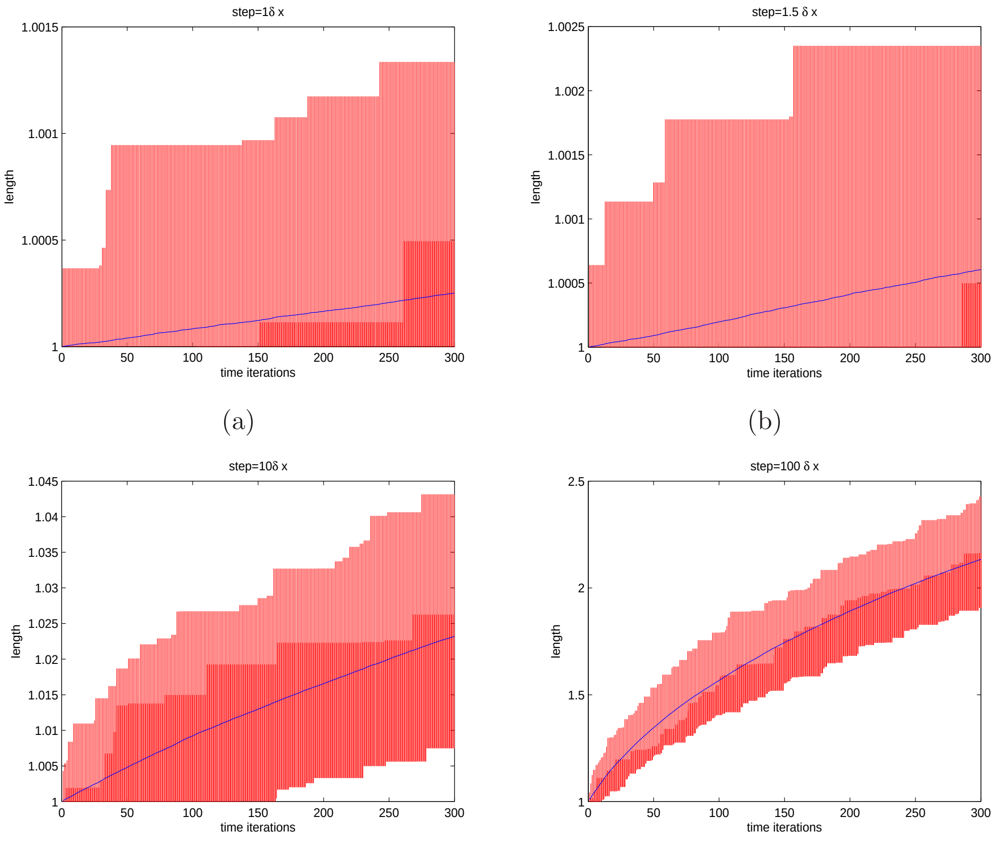

(a) (b)

(c) (d)

Figure 4.2.4: Lengths L_n for ensembles of 1000 organisms along with the mean length $\overline{L_n}$ plotted with a solid blue line for the value of the GRID parameter (a) $s = \Delta\xi$, (b) $s = 1.5\Delta\xi$, (c) $s = 10\Delta\xi$ and (d) $s = 100\Delta\xi$. The amplitude of growth is fixed $K = 1$.

scale $\Delta\xi = \frac{1}{1001}$ an activated seed has a small range of influence. Thus, only the seeds lying next to it slightly move and the rest of the seed configuration remains unchanged. As a consequence of such s parameter choice the growth increment $\Delta L_n = L_n - L_{n-1}$ will contribute to a slight increase in the length L_{n-1} at each iteration n, so that L_n stays close to the initial length $L_0 = 1$. Therefore, we obtain the mean length $\overline{L_n}$ curve with a slow rate of change of $\overline{L_n}$ per unit time $\Delta n = 1$ as shown in Figures 4.2.4.a, 4.2.4.b.

With the increased range of influence up to 10 seeds, that is, $s = 10\Delta\xi$, the mean length behavior becomes non-linear with a faster rate of increase in the beginning of growth period that slows down in the end (see Fig.4.2.4.c). Having significantly increased the value of the s parameter to $s = 100\Delta\xi$ we obtain the mean length estimate in the form of a more profound non-linear function of time as seen in Figure 4.2.4.d. These results are expected since in the beginning at each time n an activated seed causes a significant increase in the organism's length by pushing 10 or 100 seeds on both sides of it and the seeds outside of the range of influence with a lesser deformation effect. Clearly, the larger range of influence results in the larger growth increment ΔL_n. As time progresses the seeds move farther away from one another (due to repeated applications of the GRID transformations y^{ξ_i}), so that the fixed range of influence does not comprise as many seeds. Such seed configuration evolution leads to a slower rate of length increase in later times.

We now analytically compute the average length $\overline{L_n}$ and then compare it to its empirical estimates obtained above for the GRID parameter values $s = O(\Delta\xi)$, $s = 10\Delta\xi$ and $s = 100\Delta\xi$. At the nth iteration, the organism is defined by the seed configuration $x_n(\xi_i)$, $i = 1, 2, \ldots, N$ in the absolute space. We denote the left and right endpoints by $A_n = x_n^0$ and $B_n = x_n^{N+1}$. After n iterations, we choose a seed $x_n(\xi_{\sigma_i})$ randomly, where the index σ_i is chosen from the set $\{1, 2, \ldots, N\}$ with equal probability. Applying $y^{\xi_{\sigma_i}}$ transformation to the nth generation of seeds the length L_{n+1} becomes

$$\begin{aligned}
L_{n+1} &= |B_{n+1} - A_{n+1}| = \left|y^{\xi_{\sigma_i}}(B_n) - y^{\xi_{\sigma_i}}(B_n)\right| \\
&= \left|(B_n - A_n) + K \cdot (B_n - x_n(\xi_{\sigma_i}))e^{-\frac{\|B_n - x_n(\xi_{\sigma_i})\|^2}{s^2}} - K \cdot (A_n - x_n(\xi_{\sigma_i}))e^{-\frac{\|A_n - x_n(\xi_{\sigma_i})\|^2}{s^2}}\right| \\
&= L_n + K\left|(B_n - x_n(\xi_{\sigma_i}))e^{-\frac{\|B_n - x_n(\xi_{\sigma_i})\|^2}{s^2}} - (A_n - x_n(\xi_{\sigma_i}))e^{-\frac{\|A_n - x_n(\xi_{\sigma_i})\|^2}{s^2}}\right|.
\end{aligned}$$

Thus the length increment per unit time is given by

$$\Delta L_{n+1} = L_{n+1} - L_n = K\left|(B_n - x_n(\xi_{\sigma_i}))e^{-\frac{|B_n - x_n(\xi_{\sigma_i})|^2}{s^2}} - (A_n - x_n(\xi_{\sigma_i}))e^{-\frac{|A_n - x_n(\xi_{\sigma_i})|^2}{s^2}}\right|. \tag{4.2.4}$$

Given that A_n and B_n denote the positions of, respectively the left and right endpoints of the seed chain (4.2.4) may be simplified to

$$\Delta L_{n+1} = K \cdot \left[(B_n - x_n(\xi_{\sigma_i}))e^{-\frac{|B_n - x_n(\xi_{\sigma_i})|^2}{s^2}} + (A_n - x_n(\xi_{\sigma_i}))e^{-\frac{|A_n - x_n(\xi_{\sigma_i})|^2}{s^2}}\right]. \tag{4.2.5}$$

The first term represents the length of the displacement of the right endpoint $B_n = x_n^{N+1}$ and the second term represents the length of the displacement of the left endpoint $A_n = x_n^0$. Denoting the first term by ΔL_{n+1}^r and the second term by ΔL_{n+1}^l we have the total average displacement

$$\Delta L_{n+1} = \Delta L_{n+1}^r + \Delta L_{n+1}^l. \tag{4.2.6}$$

Clearly, the increase in length ΔL_{n+1} is a random variable since its value depends on a random seed placement ξ_{σ_i}. For a fixed position of the right endpoint x^{N+1} or the left endpoint x^0 we can determine the maximum magnitude of the displacement that makes a major contribution to the length increment.

Proposition 4.2.1. *Let* $\Omega(n)$ *be a continuous compact space of Cartesian coordinates of 1D organism at time* n *and its rightmost and leftmost endpoints be fixed at positions* $A_n = x^0$ *and* $B_n = x^{N+1}$*. Then the maximum magnitude of the displacement produced by the GRID transformation* $y^{\xi_i}(x_n)$ *for either of the endpoints at time* $n+1$ *is*

$$\max_{x(\xi_i)\in\Omega(n)} \left|y^{\xi_i}(x^{N+1\,or\,0})\right| = \frac{s}{\sqrt(2)} K e^{-\frac{1}{2}}. \tag{4.2.7}$$

Proof. It is sufficient to show that the expression (4.2.7) holds for the maximum magnitude of the displacement for B_n since for A_n the proof is identical. Given that $B_n = x^{N+1}$ we find a point of maximum of the displacement function $y^{\xi_i}(x^{N+1})$. Equating the derivative of the displacement function $y^{\xi_i}(x^{N+1})'$ to zero

$$K(-1 + 2\frac{(x^{N+1} - x(\xi_i))^2}{s^2}) \cdot e^{-\frac{(x^{N+1}-x(\xi_i))^2}{s^2}} = 0$$

we obtain two critical points $x(\xi_i) = x^{N+1} \pm \frac{s}{\sqrt{2}}$. Then the maximum magnitude of the displacement $\left|y^{\xi_i}(x)\right|$ is achieved at the critical point $x(\xi_i) = x^{N+1} - \frac{s}{\sqrt{2}}$, the interior point of the organism located at a distance $\frac{s}{\sqrt{2}}$ from the rightmost endpoint. Substituting this critical point value into $\left|y^{\xi_i}(x^{N+1})\right|$ as a function of $x(\xi_i)$

$$\left|y^{\xi_i}(x^{N+1})\right| = \left|K(x^{N+1} - x(\xi_i)) \cdot e^{-\frac{(x^{N+1}-x(\xi_i))^2}{s^2}}\right|$$

we obtain the maximum magnitude given by (4.2.7). □

This proposition defines an upper bound in terms of s parameter on all possible magnitudes of displacements of the endpoints valid for all times.

Now we estimate the mean length increment of a large ensemble of 1D organisms (or chains of N interior seeds) by averaging over all possible seed selections. Keeping in mind that each seed is chosen randomly with equal probability $Pr\{\xi = \xi_{\sigma_i}\} = \frac{1}{N}$ we compute the average displacement of the right endpoint B_n per unit time $\Delta n = 1$

$$\overline{\Delta L^r_{n+1}} = \frac{1}{N}\sum_{i=1}^{N} K(x^{N+1} - x_n(\xi_i))e^{-\frac{(x^{N+1}-x_n(\xi_i))^2}{s^2}}. \tag{4.2.8}$$

Remark 4.2.2. *Operation of averaging over all possible seed placements* $x_n(\xi_i)$ *does not cancel out the randomness of* $\overline{\Delta L^r_n}$*. Since* B_n *is a random variable the mean increase in length* $\overline{\Delta L^r_n}$ *given by* (4.2.8) *is a function of a random variable. In what follows, we evaluate the mean length increment at time* $n+1$ *conditioned on the* *previous average position of the right endpoint* $B_n \approx \overline{B_n}$ *using* (4.2.8). *We refer to* $\overline{\Delta L^r_n}$ *as the conditional mean length increment,*

$$\overline{\Delta L^r_{n+1}} = \left\langle \Delta L^r | B_n \approx \overline{B_n} \right\rangle, \text{ where } B_n \approx B_0 + \sum_{k=1}^{n} \overline{\Delta L^r_{t_k}}.$$

For the range of influence comparable to the seed spacing size $\Delta\xi$, $s = O(\Delta\xi)$, at each time iteration a change in length due to a single seed activation is very small. Since only the seeds lying next to the activated seed slightly change their positions at each nth generation and there is a large number of seeds the overall seed distribution stays close to uniform for a short time period. That is, $x_n(\xi_i) \approx x_(t_{n-1})(\xi_i) \approx \ldots \approx x_0(\xi_i)$ for all $i \in \{1, 2, \ldots, N\}$. Therefore, it is reasonable to assume that the average increase per unit time changes very slowly in time, that is

$$\overline{\Delta L_n} = \overline{L_{n+1}} - \overline{L_n} \approx const \text{ for } n \ll \infty. \tag{4.2.9}$$

This is also suggested by experimental evidence of a slow growth of the mean length $\overline{L_n}$ shown in Figures 4.2.4.a and 4.2.4.b.

For a larger range of influence comprising 10 seeds or more the increase in average length appears to be significant in the beginning of growth period and decreasing as time progresses. In this case, it is also reasonable to approximate the average length increment per unit time by a constant for short times $n \ll \infty$. Indeed, at each time instant, an activated seed causes displacements of 10 or more seeds on both sides of it thus resulting in a larger length increment. Since there is a large number of seeds N single seed placements occurring at times $1, 2, \ldots, n$, $i \ll N$ have approximately equal contributions to the increase in length. Therefore, at the nth generation we have the average length $\overline{L_n}$

$$\overline{L_n} \approx L_0 + n\overline{\Delta L_n}. \tag{4.2.10}$$

In order to estimate $\overline{\Delta L_n}$ we use the following proposition.

Proposition 4.2.3. *Let* $\{x_n(\xi_i), i = 1, 2, \ldots, N\}$ *be a chain of seeds representing a grown 1D organism* $\Omega(t)$ *at time* n *initially occupying* $[0\ L_0]$ *in the absolute space. Assuming that (i)the average length of* $\Omega(t)$ *satisfies*

$$\overline{L_n} \approx L_0 + n \cdot \overline{\Delta L_n}, \tag{4.2.11}$$

where $\overline{\Delta L_n}$ *is the length increment in unit time* $\Delta n = 1$ *and (ii) the left and right endpoints* A_n *and* B_n *of the organism stay close to their averages* $\overline{x^0_n}$ *and* $\overline{x^{N+1}_n}$

$$\overline{x^0_n} \approx -n \cdot \overline{\Delta L^l_n} \text{ and } \overline{x^{N+1}_n} \approx L_0 + n \cdot \overline{\Delta L^r_n} \tag{4.2.12}$$

for a short time period $[0, T], T \ll \infty$ *with a small number of seed occurrences* $n \ll N$ *the average displacements for the right and left endpoints are equal*

$$\overline{\Delta L^r_n} = -\overline{\Delta L^l_n}. \tag{4.2.13}$$

Moreover, the total average length increment at time n is approximately

$$\overline{\Delta L_n} \approx \frac{K \cdot s^2}{(L_0 + n\overline{\Delta L_n})}. \tag{4.2.14}$$

Proof. We first find the average displacement of the right endpoint B_n at time $n+1$. Given the average length $\overline{L_n}$

$$\overline{L_n} = L_0 + n(\overline{\Delta L_n^r} + \overline{\Delta L_n^l}) = L_0 + n \cdot \overline{\Delta L_n}$$

that gives the average spacing between two consecutive seeds close to the initial spacing $\Delta\xi = \frac{L_0}{N+1}$ $\Delta x_n = \frac{\overline{L_n}}{N+1} = \frac{L_0}{N+1} + n \cdot \frac{\overline{\Delta L_n}}{N+1}$. the position of B_n

$$B_n \approx \overline{x_n^{N+1}} = L_0 + n \cdot \overline{\Delta L_n^r}$$

can equivalently be determined as

$$B_n \approx (N+1) \cdot \Delta x_n = L_0 + n \cdot \overline{\Delta L_n}.$$

Taking into account approximately uniform distribution of the interior seeds $x_n(\xi_i) \approx i \cdot \Delta x_n$ or $x(\xi_i) \approx \frac{i}{N+1}(L_0 + n\overline{\Delta L})$ we calculate the average right endpoint displacement $\overline{\Delta L_n^r}$ (4.2.8) as follows

$$\overline{\Delta L_n^r} = \frac{K}{N} \sum_{i=1}^{N} \left(\frac{N+1-i}{N+1} \right) (L_0 + n\overline{\Delta L_n}) e^{-\left(\frac{(N+1-i)^2}{(N+1)^2}\right) \cdot \frac{(L_0 + n\overline{\Delta L_n})^2}{s^2}} \tag{4.2.15}$$

At time n the endpoints of the organism occupy $B_n \approx \overline{x_n^{N+1}} = L_0 + n \cdot \overline{\Delta L_n^r}$ and $A_n \approx \overline{x_n^0} = -n \cdot \overline{\Delta L_n^l}$ yielding the length $\overline{L_n} \approx B_n - A_n$ consistent with the assumption (i) of this proposition. Since the GRID elementary transformation $y^{\xi_i}(x_n)$ modeling the deformation effect of a single seed is translation-invariant the average displacement of the left endpoint of the organism $[A_n, B_n]$ is equal to the average displacement of the left endpoint of the organism translated in space by the value of $n\overline{\Delta L_n^l}$ to the right. Thus, we calculate $\overline{\Delta L_n^l}$ undergone by the left endpoint of the organism $[0, B_n + A_n]$ as follows

$$\overline{\Delta L_n^l} = \frac{K}{N} \sum_{i=1}^{N} \left(\frac{0-i}{N+1} \right) (L_0 + n\overline{\Delta L_n}) e^{-\left(\frac{(0-i)^2}{(N+1)^2}\right) \frac{(L_0 + n\overline{\Delta L_n})^2}{s^2}}. \tag{4.2.16}$$

Denote $\Delta y = y_{i+1} - y_i = \frac{1}{N+1}$ in both equations (4.2.15) and (4.2.16), $y_i = \frac{N+1-i}{N+1}$ in (4.2.15) and $y_i = \frac{i}{N+1}$ in (4.2.16) where $i = 1, 2, \ldots, N$. Then $0 \leq y_i \leq 1$ and on the right hand side of (4.2.15) we have the Riemann sum approximation to the integral

$$\begin{aligned} K \cdot (L_0 + n\overline{\Delta L_n}) \int_0^1 y e^{-y^2 \frac{(L_0 + n\overline{\Delta L_n})^2}{s^2}} dy = \\ \frac{K \cdot s^2}{2(L_0 + n\overline{\Delta L_n})} \cdot (1 - e^{-\frac{(L_0 + n\overline{\Delta L_n})^2}{s^2}}). \end{aligned} \tag{4.2.17}$$

Similarly, the average displacement of the left endpoint 0 given by (4.2.16)can be interpreted as the Riemann sum approximation to the integral

$$\begin{aligned} -K\cdot(L_0+n\overline{\Delta L_n})\int_0^1 ye^{-y^2\frac{(L_0+n\overline{\Delta L_n})^2}{s^2}}dy = \\ -\frac{K\cdot s^2}{2(L_0+n\overline{\Delta L_n})}\cdot(1-e^{-\frac{(L_0+n\overline{\Delta L_n})^2}{s^2}}). \end{aligned} \tag{4.2.18}$$

Comparing both results (4.2.17) and (4.2.18) we arrive at

$$\overline{\Delta L_n^r} = -\overline{\Delta L_n^l}. \tag{4.2.19}$$

Since $s \ll \overline{L_n}$ the exponential term on the right hand side of (4.2.17) and (4.2.18) may be ignored. The sum of the magnitudes of the endpoint average displacements yields

$$\overline{\Delta L_n} \approx \frac{K\cdot s^2}{(L_0+n\overline{\Delta L_n})}. \tag{4.2.20}$$

□

From (4.2.14) we obtain a quadratic equation with the unknown average displacement $\overline{\Delta L_n}$

$$n\overline{\Delta L_n}^2 + L_0\overline{\Delta L_n} - K\cdot s^2 = 0 \tag{4.2.21}$$

and find its roots

$$\overline{\Delta L_{n}}_{1,2} = \frac{-L_0 \pm \sqrt{L_0^2+4K\cdot n\cdot s^2}}{2n}. \tag{4.2.22}$$

Clearly, the average growth rate cannot be negative since the organism increases in length as it grows. Dropping the negative root we arrive at

$$\overline{\Delta L_n} = \frac{-L_0 + \sqrt{L_0^2+4K\cdot n\cdot s^2}}{2n}. \tag{4.2.23}$$

Equation(4.2.23) describes the average growth increment per unit time $\Delta n = 1$ as a slowly decreasing non-linear function of time. Frow equation (4.2.23) arises another important result for the average displacement of the organism from its initial position as a square root function of time

$$\overline{\Delta L_n} = \overline{L_n} - L_0 = n\cdot\overline{\Delta L_n} = \frac{1}{2}\left(-L_0+\sqrt{L_0^2+4K\cdot n\cdot s^2}\right). \tag{4.2.24}$$

Thus, the equation for the average length $\overline{L_n}$ becomes

$$\overline{L_n} = \frac{L_0}{2} + \frac{1}{2}\cdot\sqrt{L_0^2+4K\cdot n\cdot s^2}. \tag{4.2.25}$$

Plots of the analytical estimates of the mean length given by (4.2.25) versus its empirical estimates for the values of the GRID parameter $s = \frac{1}{1001}$, $s = \frac{1.5}{1001}$,

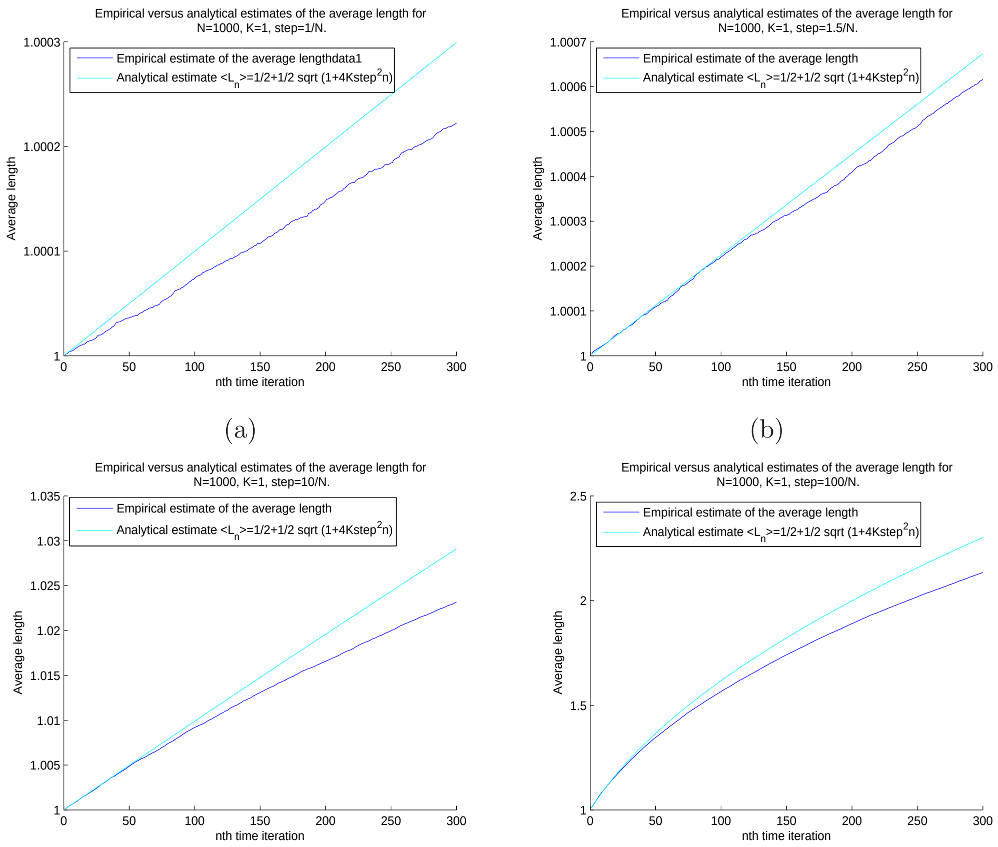

(a) (b) (c) (d)

Figure 4.2.5: Empirical versus analytical estimates of the average length of 1D organism comprised of $N = 1000$ seeds for various values of the s parameter (a) $s = \frac{1}{N}$, (b) $s = \frac{1.5}{N}$, (c) $s = \frac{10}{N}$, (d) $s = \frac{100}{N}$.

$s = \frac{10}{1001}$ and $s = \frac{100}{1001}$ obtained earlier are shown in Figures 4.2.5.a and 4.2.5.b. The growth is overestimated for longer times since in the derivation of $\overline{L_n}$ we did not account for the decrease in the density of seeds $x_n(\xi)$ in the course of time. Observe that the experimental results agree well with the predicted average length $\overline{L_n}$ (4.2.25) for about 50 first time iterations. This is expected since the analytical result (4.2.25) has been obtained based on the assumption that $\overline{L_n} \approx L_0 + n \cdot \overline{\Delta L_n}$ is valid for a slowly changing average growth rate $\overline{\Delta L_n} \approx const$.

Observe that the validity of this assumption can be maintained for longer times if we let the number of seeds $N \to \infty$ thus making the s parameter infinitesimally small. In this case, the contribution from a single seed to the growth increment at each nth time iteration becomes infinitesimally small so that the uniform distribution of seeds is preserved. Thus, taking the limit of the mean length increment (4.2.23) as $n \to \infty$ and $N \to \infty$ we arrive at

$$\lim_{\substack{n\to\infty \\ N\to\infty}} \overline{\Delta L_n} = \lim_{\substack{n\to\infty \\ N\to\infty}} \frac{-L_0 + \sqrt{L_0^2 + 4K \cdot n \cdot O(\frac{w}{N^2})}}{2n} = 0, \tag{4.2.26}$$

where w is the squared fixed number of seeds contained in the range of influence of each activated seed. From the calculus point of view letting the number of seeds $N \to \infty$ leads to the exact evaluation of the average value of the length increment (4.2.17). It also leads to the GRID model with the continuum Darcyan space $\Xi = [0, 1]$, where the seeds ξ are distributed uniformly in Ξ. Thus, in a long run the average length increment $\overline{\Delta L_n}$ decreases to 0, reflecting the fact that the biological organism has a finite time period of growth.

Given that $t_n = n \cdot \Delta t$ it is plausible to formulate the expression for the average length $\overline{L}_n$ in terms of time t_n

$$\overline{L}_{t_n} \approx L_0 + \frac{t_n}{\Delta t} \cdot \overline{\Delta L_n}. \tag{4.2.27}$$

Then the change in average length $\frac{\overline{\Delta L_n}}{\Delta t}$ given by (4.2.23) can be interpreted as the increase in average length per time s Δt. Substituting $\overline{\Delta L_n}$ by $\frac{\overline{\Delta L_n}}{\Delta t}$ into the equation (4.2.21) with time iteration n replaced by t_n we find that the solution of (4.2.21) $\overline{\Delta L_n}$ as a function of time t_n is a finite-difference approximation of the ordinary differential equation

$$\frac{d\overline{L_t}}{dt} = \frac{-L_0 + \sqrt{L_0 + 4K \cdot s^2 \cdot t}}{2t}, \text{where} \tag{4.2.28}$$

$\overline{L_t} \approx L_0 + t\frac{d\overline{L_t}}{dt}$ for short times $t \ll \infty$. Clearly, $\overline{\Delta L_{t_i}}$ and $\overline{L_{t_i}}$ with $i = 1, 2, \ldots, n$ are numerical approximations to the instantaneous average growth rate $\frac{d\overline{\Delta L_t}}{dt}$ and the average length $\overline{L_t}$ correspondingly on a finite time interval $(0, T]$. We summarize our derivation results in a theorem below.

Theorem 4.2.4. *Consider the continuous-time stochastic GRID model for isotropic growth of a 1D organism $\Omega(t)$ with a high-dimensional countable Darcyan space $\Xi = \{\xi_1, \xi_2, \ldots, \xi_N\} \subset [0, L_0]$ and time-independent uniform probability distribution of seeds over Ξ. For the first $n \ll N$ occurrence times $t_1 < t_2 <, \ldots, < t_n, : t_n \ll \infty$ the estimate of the mean growth rate conditioned on the average positions of the left and right endpoints x_t^0 and x_t^{N+1} is given by*

$$\frac{d\overline{L_t}}{dt}|_{t=t_i} \approx \frac{-L_0 + \sqrt{L_0 + 4Ks^2 \cdot t_i}}{2t_i} \tag{4.2.29}$$

based on the following relation with the corresponding mean length of $\Omega(t)$

$$\overline{L_t}|_{t=t_i} \approx L_0 + t_i \frac{d\overline{L_t}}{dt}|_{t=t_i}, \text{ where } i = 1, 2, \ldots, n. \tag{4.2.30}$$

Thus evolution of the average displacement $\overline{L_t}$ of $\Omega(t)$ from its initial position $\Omega(0)$ in the beginning of growth period approximately satisfies

$$\overline{\Delta L_t}|_{t=t_i} = \overline{L_t} - L_0|_{t=t_i} = \frac{1}{2}\left(-L_0 + \sqrt{L_0 + 4Ks^2 \cdot t_i}\right). \tag{4.2.31}$$

4.2.2 Empirical study of individual seed trajectories

In this subsection we study individual seed trajectories depending on the starting position of seeds and the range of seed influence defined by the s parameter for short and long times.

We first investigate the influence of the s parameter $s = w \cdot \Delta\xi$ on variability of the seed trajectories for short growth period. Recall that $\Delta\xi$ is the fixed distance between active gene sites and w is the magnifying factor (usually the number of seeds) defining the range of each seed influence. As in the subsection above we run realizations of the Poisson driven Markov process simplified to have sure time occurrences of seed activations with intensity of 1 seed per unit time equal to the average of the interarrival times $\Delta t = \frac{1}{\lambda_t}$. Due to the constant intensity of biological events characterization of seed trajectories generated by n iterations of the simplified version of the stochastic GRID model is equivalent to characterization of seed trajectories produced by the Poisson driven Markov process in time interval $[0, T]$ with n random occurrence times.

Let an organism be comprised of $N = 100$ interior seeds with $K = 1$ and $w = 10$ implying that the s parameter $s = wd\xi = \frac{10}{101}$. Selecting particular seeds at initial positions near the endpoints $x_0(1) = 0.0099$, $x_0(2) = 0.9901$, $x_0(26) = 0.2574$ and $x_0(50) = 0.5$ we generate their paths in time-space applying 100 iterations of the GRID algorithm coded in Matlab script “grid1d.m” (see Appendix E). The Figures below show the results of two experiments yielding different seed trajectories computed with the range of influence $s = 10\Delta\xi$. This is expected since, generally speaking, each individual ith seed path corresponds to a particular realization of the N-dimensional spatial Poisson driven Markov process $\{x_t(\xi) : \xi \in \Xi\}$ at time instants $t_1 < t_1 + \Delta t < \ldots < t_1 + (n-1)\Delta t \leq T$. It represents evolution of the ith seed position in the “chain” configuration of N seeds moving in time-space. The solution space $\mathcal{X}$ of this stochastic process consists of all sample configurations of N seeds that are initially $\{x_0(\xi_1) < x_0(\xi_2) < \ldots < x_0(\xi_N)\}$ and have n occurrences of seed activations.

Motions of seeds shown in Figure 4.2.6 are not independent from motions of their neighbors that at instants of their activation push the displayed seeds back or forth. In both experiments the seed trajectories appear irregular and variable as a consequence of a relatively large range of influence.

In the second set of experiments shown in Figure 4.2.7 we have restricted the range of influence of the active seed to $s = \frac{1.5}{101}$. The resulting motion appears more regular and less variable due to the absence of interaction between neighboring seeds (in the form of pushes). Seed trajectories are relatively independent.

Observations of the statistical characteristics of random seed trajectories such as the mean and variance can be obtained from an ensemble of sample paths emanating from a certain initial position $x_0(\xi_i)$. We perform 500 realizations of 1D GRID algorithm for short times (choosing the number of iterations $niter = 100$) and record 500 different paths only for the seeds initially located near the boundary $x_0(1)$, $x_0(100)$, in the middle $x_0(50)$ and at $x_0(26)$. We run two such experiments

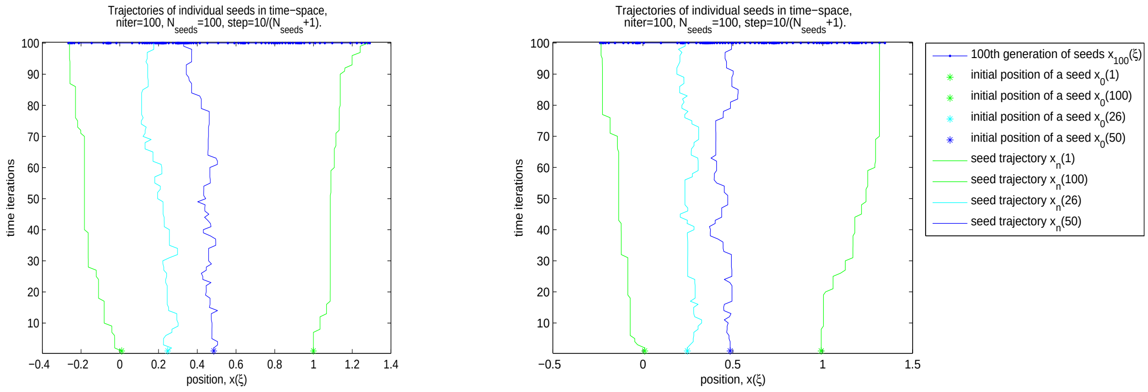

(a) (b)

Figure 4.2.6: Two different sets of seed trajectories emanating from initial seed positions at $x_0(1)$, $x_0(26)$, $x_0(50)$ and $x_0(100)$ generated by the 1D GRID stochastic equation of motion. The value of the s parameter is chosen to be $\frac{10}{N_{seeds}+1}$ for both experiments (a) and (b).

for different values of s parameter $s = 10\Delta\xi$ and $s = 1.5\Delta\xi$ and display their results in Figure 4.2.8. Obviously, the seeds near the endpoints always "travel" outwards since all of the interior seeds have positive "growth power" expressed by $K > 0$ that ensures deformation effects in the form of local expansions. Also, the choice of a larger range of influence s results in a larger variance of the seed position in time-space independently of the initial location. For the small range of influence the mean seed position seems to stay nearly constant in time as seen from Figure 4.2.8.b. For the seeds near endpoints we expect their mean positions to increase in time as a square root function of time. Indeed, we have $\overline{x_n(\xi_{N_{seeds}})} \approx \overline{x_n^{N+1}}$ and $\overline{x_n(\xi_1)} \approx \overline{x_n^0}$ evaluated according to the Proposition 4.2.3 and equation (4.2.23)) as follows

$$\overline{x_n^{N+1}} = L_0 + n \cdot \overline{\Delta L_n^r} \text{ and } \overline{x_n^0} = -n \cdot \overline{\Delta L_n^l},$$
$$\overline{\Delta L_n^r} = -\overline{\Delta L_n^l} = \frac{1}{2}\overline{\Delta L_n} = \frac{1}{2}\left(\frac{-L_0 + \sqrt{L_0^2 + 4K \cdot n \cdot s^2}}{2n}\right).$$

Both experiments suggest that the variance of the seed position $\langle\langle x_t(\xi)\rangle\rangle$ is a slowly increasing function of time independent of the initial seed position. These observations lead to the following questions:

1. What are the mean or the most likely positions of the interior seeds $x_t(\xi_i), 1 < i < N_{seeds}$ in time-space?
2. Where do the seed trajectories end up in a long run as time $t \to \infty$?

We now perform a series of experiments with a long-time evolution of individual seed positions depending on their initial locations and the range of influence. In

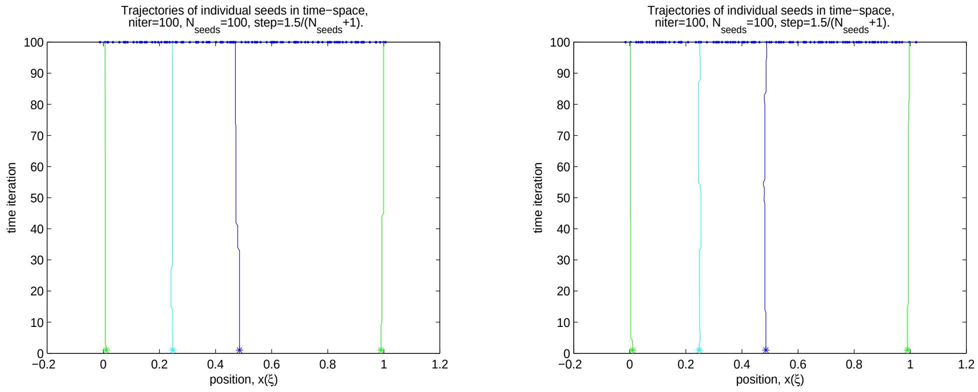

(a) (b)

Figure 4.2.7: Two different sets of seed trajectories emanating from initial seed positions at $x_0(1)$, $x_0(26)$, $x_0(50)$ and $x_0(100)$ generated by the 1D GRID stochastic equation of motion. The value of the s parameter is chosen to be $\frac{1.5}{N_{seeds}+1}$ for both experiments (a) and (b).

order to make sure that each seed is picked only once at each time iteration we set the Darcyan space to be a compact continuum $\Xi = (0, 1)$ with the Lebesgue measure or the uniform probability density of seeds $p\{x_n(\xi) \in (a_n, b_n) : (a_n, b_n) \subset (A_n, B_n)\} = b_n - a_n$ at all times n. Note that modeling growth in a long run with the continuum Darcyan space of seeds is more natural since biological events occur anywhere within the growing organism's domain not only at a set of N_{seed} possible locations $x_n(\xi_i), i = 1, 2, \ldots N_{seed}$ prescribed by the GRID transformation $y^{\xi_j}(x_{n-1})$.

As in previous computations we represent a growing organism $\Omega(t)$ by its Darcyan grid, a chain of $N = 1000$ initially equally spaced seeds or rather material points. At each time instant n a seed $x_n(\xi_i)$ is activated as a sample from the uniform probability distribution over $\Omega_n = (A_n, B_n)$ causing outward motions of the neighboring material points $x_n(\xi)$. Choosing the range of influence $s = \frac{10}{N+1}$ and applying $20,000$ iterations of 1D GRID algorithm in each experiment we obtain various seed trajectories for the seeds starting in the middle, at the position of the first one third of the unit interval and near the endpoints as displayed in Figures 4.2.9.a-4.2.9.c correspondingly.

The experimental results suggest clear differences in the long-time evolution of seed positions initially located near the endpoints and in the interior of the organism for the value of the s parameter $s = \frac{10}{N+1}$. The middle seed trajectory appears to be jagged and highly variable with the largest range of ending locations between 0.2 and 0.62. One of its trajectories seemingly leads to left endpoint. The paths emanating from the initial seed location at $x_0 = 0.33$ also demonstrate high variability with the range of ending locations between 0.2 and 0.45. The trajectories of seeds near the endpoints exhibit quite regular behavior similar to the mean curve proportional to the square root of time.

For the small range of influence $s = \frac{1}{N+1}$ variability of seed trajectories appears

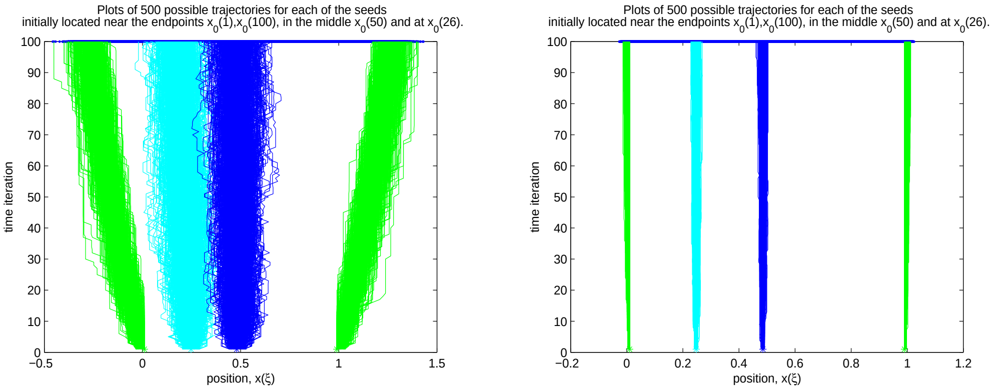

(a) (b)

Figure 4.2.8: Four sets of 500 seed trajectories emanating from initial seed positions at $x_0(1)$, $x_0(26)$, $x_0(50)$ and $x_0(100)$ generated by the 1D GRID stochastic equation of motion. The value of the s parameter is (a) $\frac{10}{N_{seeds}+1}$, (b) $\frac{1.5}{N_{seeds}+1}$.

to be significantly reduced (see Fig.4.2.9.d) as expected. The seed trajectories emanating from different initial positions slowly change in time and all look similar to lines. Plots of the seed paths displayed in Figure 4.2.9.d suggest that for the small range of influence the average displacement of a seed from its initial position is a slowly increasing function of time. All in all, seeds generated by 1D stochastic differential equation (4.1.21) perform a random walk or a kind of restricted Brownian motion on a fine time scale in the sense that at each time instant of gene activation the seeds will undergo a prescribed random displacement

$$x_{t+\Delta t} - x_t = y^{\xi_{sigma_k}}(x_t) = (x_t(\xi) - x_t(\xi_{\sigma_k})) \cdot k(\xi, \xi_{\sigma_k}) \exp\left(-\frac{\|x_t(\xi) - x_t(\xi_{\sigma_k})\|^2}{s^2}\right). \tag{4.2.32}$$

To address the questions posed above we need to find the singlet probability density function $f(x,t)$ that would describe the probability distribution of any individual seed in the $x-t$ plane conditioned on its initial position and the stationary probability density $f_s(x) = \lim_{t\to\infty} f(x,t)$. In what follows we derive the evolution differential equation of $f(x,t)$ for the special case of 1D isotropic GRID model with uniform distribution of seeds and constant intensity of seed activation λ_t.

Remark 4.2.5. ***Comparison with the 1D Brownian motion model.*** *The continuous-time stochastic 1D GRID model* (4.1.21) *is reminiscent of the 1D Brownian motion model on the fine time scale (in the absence of external forces) given by the Langevin equation in the form*

$$dV_t = -\gamma V_t dt + dU_t, \text{ where } dU_t = \int_{\mathcal{U}} \frac{u}{m}\mu(dt, du). \tag{4.2.33}$$

Here, γ *is a friction coefficient,* $\{U_t : t \geq t_0\}$ *is a mark accumulator Poisson process with a mark space* $\mathcal{U}$ *(see Appendix A). It is represented as* $U_t = \int_{t_0}^{t}\int_{\mathcal{U}} \frac{u}{m}\mu(dt, du)$

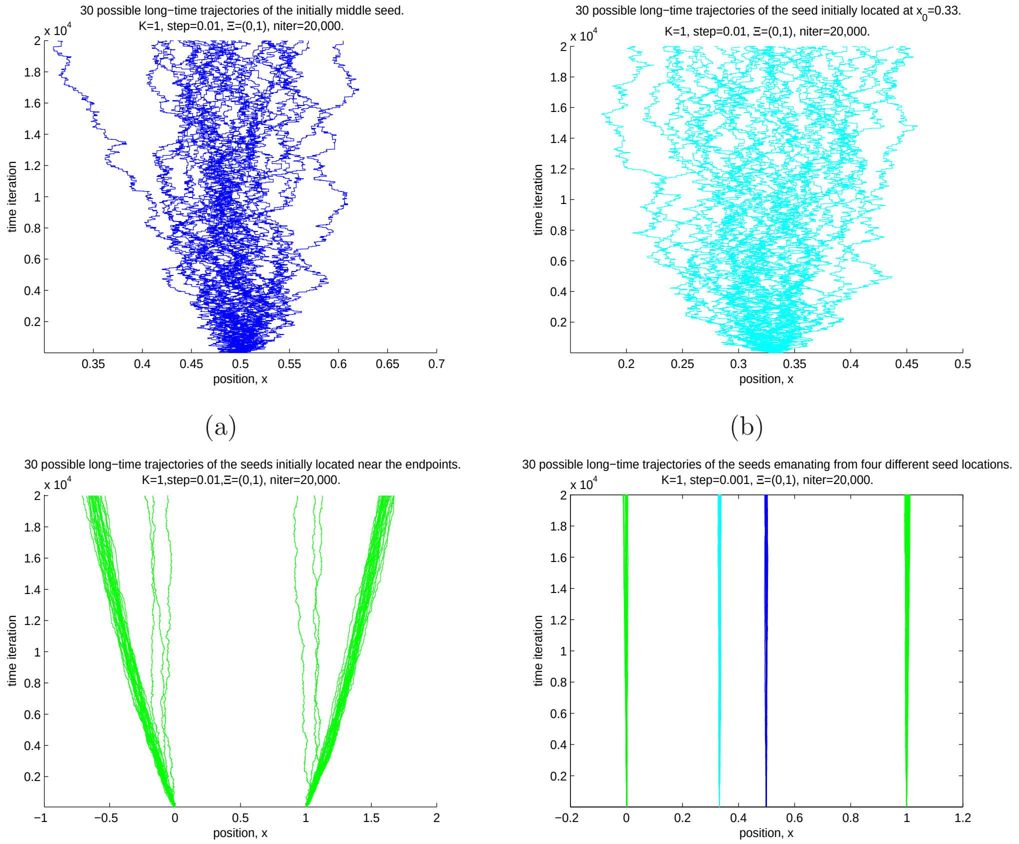

(a) (b) (c) (d)

Figure 4.2.9: 30 long-time seed trajectories emanating from initial seed positions at (a) $x_0 = 0.5$, (b) $x_0 = 0.33$, and (c) $x_0 = 0.01$ and $x_0 = 0.99$. The value of the s parameter is (a-c) $\frac{10}{N+1}$, (d) $\frac{1}{N+1}$.

where $\{\mu(T, B) : T \subset [t_0, \infty), B \subset \mathcal{U}\}$ *is a time-space Poisson process. The occurrence times* $t_1 < t_2 < \ldots < t_{N_t}$ *and marks of this point process* $\{u_1, u_2, \ldots, u_{N_t}\}$ *correspond to the instants collisions of a Brownian particle with water molecules take place and the force magnitude induced on the particle, respectively. The velocity process* $\{V_t, t \geq t_0\}$ *describing the motion of a Brownian particle of mass* m *suspended in a fluid is a Poisson driven Markov process. In this formulation, the velocity and position of the particle at time* t *is defined by the action of friction* $(F = -\gamma V_t)$ *and fluctuating impulsive forces modeled by the Poisson perturbation term evaluated as* $U_t = \sum_{i=1}^{N_t} \frac{u_i}{m}$ *in case if* N_t *impacts occur during* $[t_0, t)$.

Similarly, in the stochastic GRID model the seed position is defined by the Poisson perturbation term evaluated as $\sum_{i=1}^{N_t} y^{\xi_i}(x_{t_i})$ *or, in other words, the cumulative effect of impulsive pushes from the seeds activated in time period* $[t_0, t)$. *Both processes* V_t *and* x_t *are continuous-time jump processes.*

4.3 Derivation of the Fokker-Planck equation

We are interested in the evolution equation of the probability density function $f(x,t)$ that would describe the probability distribution of any individual seed in the $x-t$ plane. In this section we derive the Fokker-Planck equation of the evolution of $f(x,t)$ for the special case of the stochastic 1D GRID model with the uniform distribution of seeds and constant intensity of seed activation λ_t. As we have already seen from experimental data this problem is reminiscent of the problem of diffusion from a single point, an initial seed position. Indeed, long-time realizations of the Poisson driven Markov process for interior seeds hint on the diffusive nature of the seed trajectories produced by the stochastic GRID model. The Fokker-Planck equation derived here provides a continuous time-space approximation of the 1D GRID model in the form of a diffusion process.

It is important to realize that the uniform distribution of seeds in the absolute compact space of a growing organism at all times is a simplifying assumption. We have already observed that the uniformity of seed distribution is not preserved over the course of time.

Jump processes are most appropriately described by means of an integro-differential Master Equation which requires knowledge of the transition probability per unit time $w(\acute{x}_t|x_t)$. The general Master Equation for a continuous state space $\mathcal{X}$ is formulated as follows,

$$\frac{\partial f(x,t)}{\partial t} = \int_{\Omega} [w(x_t|\acute{x}_t) f(\acute{x}_t,t) - w(\acute{x}_t|x_t) f(x_t,t)] d\acute{x}_t, \tag{4.3.1}$$

The first integral term on the right hand side of (4.3.1) exhibits transitions to state x_t from all other states (gain term), and the second integral term exhibits transitions from state x_t into all other states (loss term).

Since the transition rates are unknown, we use an approximation to the Master Equation in the form of the Fokker-Planck (FPE) equation according to which the states x_t are continuous. We derive the FPE equation using method of δ-functions based on knowledge of the Langevin equation of motion [34]. The Langevin equation representing seed motion in time-space produced by the stochastic 1D GRID model is given in the differential form (since x_t is not a differentiable function),

$$dx_t = \int_{\xi_{seed} \in \Xi} y^{\xi_{seed}}(x_t) \mu(dt, d\xi_{seed}). \tag{4.3.2}$$

Solving (4.3.2) over a short time interval $[t, t+\Delta t]$, we obtain the growth increment,

$$\Delta x_t(\xi) = x_{t+\Delta t}(\xi) - x_t(\xi) \approx \sum_{i=1}^{N_{\Delta t}} y^{\xi_i}(x_t(\xi)),$$

where ξ_i's are the random seeds activated during a short time interval with their total number $N_{\Delta t}$ and distributed as a Poisson process with intensity $\lambda_t \times \lambda(\xi)$.

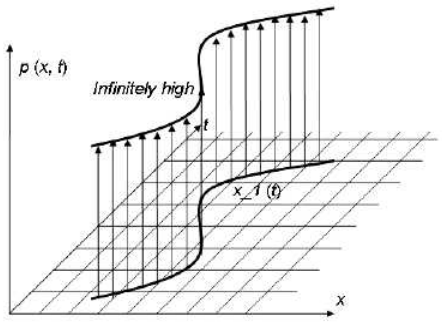

Figure 4.3.1: Infinitely peaked "probability" density function.

Assuming that the time interval Δt is small enough that the state $x_t(\xi)$ does not change much during Δt we investigate the change of the probability density $f(x,t)$ in the time interval Δt. First of all, how do we formally define $f(x,t)$ for the Poisson driven Markov process (4.3.2)?

In the course of time a seed proceeds along a path in $x - t$ plane. Let

$$P_n(x_n, t_n; x_{n-1}, t_{n-1}; \ldots; x_1, t_1)$$

be the probability of finding the seed positions $x_1, x_2, \ldots, x_n$ at times $t_1, t_2, \ldots, t_n$ respectively. In general, P_n is the probability distribution of the paths in $[t_0, t) \times \mathcal{X}$ given by

$$x_n(\xi) = x_0(\xi) + \sum_{i=1}^{n} y^{\xi_{\sigma_i}}(x_i(\xi)) = \phi^{\xi_{\sigma_n}} \circ \phi^{\xi_{\sigma_{n-1}}} \circ \ldots \circ \phi^{\xi_{\sigma_1}}(x_0(\xi)) = \phi(t_1, t_n)(x_0(\xi)), \tag{4.3.3}$$

where $\phi^{\xi_{\sigma_i}}(x_i(\xi)) = x_i(\xi) = (x_i(\xi) - x_i(\xi_{\sigma_i}))\exp\left(-\frac{\|x_i(\xi)-x_i(\xi_{\sigma_i}\|^2}{s^2}\right)$ and $t_0 < t_1 < t_2 \ldots < t_n < t$. The equation of growth (4.3.2) generates a variable trajectory that can be described by the composition semi-group of diffeomorphisms $\{\phi(s,t) : -\infty < s < t < \infty\}$ with the property that

$$\phi(t_1, t_2) \circ \phi(t_2, t_3) = \phi(t_1, t_3) \text{ for } t_1 < t_2 < t_3.$$

If we fix a path $x_t^{(1)} = \phi(t_1, t)(x_0(\xi))$, $t_1 < t$ then the probability density for this path, p_1, is equal to the Dirac δ-function $p_1 = \delta(x - x_t^{(1)})$ shown in Figure 4.3.1. One can think of this path as a solution to the deterministic equation of growth. It is evident that such a density function yields the probability equal to 1 if $x = x_t^{(1)}$ and zero otherwise. For another path, say, $x = x_t^{(2)}$, the probability density is $p_2 = \delta(x - x_t^{(2)})$. If the probability of the occurrence of a path $x_t^{(i)}$ is $P_n(x_n^{(i)}, t; x_{n-1}^{(i)}, t_{n-1}; \ldots; x_1^{(i)}, t_1) = P_t^{(i)}$ then the average over all these paths can be written in the form

$$f(x,t) = \langle p(x,t) \rangle = \sum_i P_t^{(i)} \delta(x - x_t^{(i)}) = \left\langle \delta(x - x_t^{(i)}) \right\rangle. \tag{4.3.4}$$

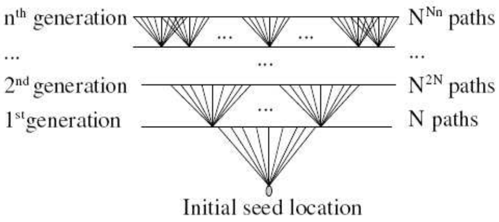

Figure 4.3.2: A path tree for an individual seed.

$f(x_t^{(i)}, t)$ is the probability measure of a seed trajectory captured by the specific transformation $\phi(t_1, t)(x_0(\xi))$. $x_t^{(i)}$ can also be viewed as the unique ending position of the seed path at time t. We can now calculate the probability of finding the seed $x_t(\xi)$ at the position x in the time interval dx at time t

$$f(x,t)dt = Pr(x \leq x_t \leq x + dx, t) \tag{4.3.5}$$

For the 1D GRID stochastic model with a countable Darcyan space and a finite number of seeds N we have a finite number of all possible paths for an individual seed at time instants $t = t_i,\ i = 1, 2, \ldots, n$. The number of all possible paths for the time sequence $t_1 < t_2 < \ldots < t_n$ is N^{Nn} as seen from Figure 4.3.2. Basically, an individual seed of a 1D organism at each time instant undergoes one of N^{Nn} possible displacements. It is interesting to investigate the symmetric property of the probability distribution of the displacements. Is the equality $f(\Delta x, t) = f(-\Delta x, t)$ preserved in time?

We compute the point probability $Pr\{X = x_t\}$ where X designates a random ending position of a seed at time t using the definition of the cumulative density function $F(x)$ in terms of a Dirac δ-function:

$$\begin{aligned}
F(x_t) &= Pr(X \leq x_t) \\
&= \sum_{i:x_t^{(i)} \leq x_t} P_t^{(i)} \int_R \mathbf{1}_{(-\infty, x_t)}(x) \delta(x - x_t^{(i)}) dx \\
&= \sum_{i:x_t^{(i)} \leq x_t} P_t^{(i)} \mathbf{1}_{(-\infty, x_t)}(x_t^{(i)}) = \sum_{i:x_t^{(i)} \leq x_t} P_t^{(i)} h(x_t - x_t^{(i)}),
\end{aligned} \tag{4.3.6}$$

where $h(x_t - x_t^{(i)})$ is the Heaviside function

$$h(x_t - x_t^{(i)}) = \begin{cases} 1 & \text{if} \quad x_t - x_t^{(i)} > 0, \\ 0 & \text{if} \quad x_t - x_t^{(i)} \leq 0. \end{cases} \tag{4.3.7}$$

Finally, we have

$$\begin{aligned}
Pr\{X = x_t\} &= F(x_t) - \lim_{x \to x_t^-} F(x) \\
&= \sum_{i:x_t^{(i)} \le x_t} P_t^{(i)} h(x_t - x_t^{(i)}) - \lim_{x \to x_t^-} \sum_{i:x_t^{(i)} \le x} P_t^{(i)} h(x - x_t^{(i)}) \\
&= \sum_{i:x_t^{(i)} \le x_t} P_t^{(i)} (h(x_t - x_t^{(i)}) - \lim_{x \to x_t^-} h(x - x_t^{(i)})) = \sum_{i:x_t^{(i)} \le x_t} P_t^{(i)} H(x_t - x_t^{(i)}),
\end{aligned}$$

where

$$H(x_t - x_t^{(i)}) = \begin{cases} 1 & \text{if} \quad x_t = x_t^{(i)}, \\ 0 & \text{otherwise.} \end{cases} \tag{4.3.8}$$

The calculation above yields the probability of finding a seed at the final coordinate x_t and at time t irrespective of the special path chosen. With the use of Dirac δ-function representation (4.3.4) of the probability density function $f(x,t)$ we can derive a differential equation for it directly avoiding computation of path probabilities $P_t^{(i)}$. We should consider the conditional probability density function $f(x,t|x_0,t_0)$ because the displacements undergone by the seeds depend on the initial coordinates $x_0(\xi)$.

Choosing a small time interval Δt the change of $f(x,t)$ during Δt is

$$\Delta f(x,t) = f(x, t + \Delta t) - f(x,t). \tag{4.3.9}$$

Substituting (4.3.4) for $f(x,t)$ into (4.3.9) we obtain

$$\Delta f(x,t) = \langle \delta(x - x_{t+\Delta t}) \rangle - \langle \delta(x - x_t) \rangle , \tag{4.3.10}$$

where $x_{t+\Delta t} = x_t + \Delta x_t$. Indeed, from 1D GRID continuous time stochastic differential equation (4.3.2) it follows that

$$x_{t+\Delta t} = x_t + \int_t^{t+\Delta t} \int_{\xi_i \in \Xi} y^{\xi_i}(x_t) \mu(dt, d\xi) = x_t + \sum_{i=1}^{N_{\Delta t}} y^{\xi_i}(x_{t_i}), \tag{4.3.11}$$

where t_i's are biological decision occurrence times. For example, suppose that two biological events have occurred in time interval $[t, t + \Delta t]$. Then denoting the occurrence times by $t_1, t_2 : t < t_1 < t_2 < t + \Delta t$, we have

$$\begin{aligned}
x_{t+\Delta t} = x_{t_1} + (x_{t_1} - x_{t_1}(\xi_2)) K e^{-\frac{\|x_{t_1} - x_{t_1}(\xi_2)\|^2}{s^2}} &= x_t + (x_t - x_t(\xi_1)) K e^{-\frac{\|x_t - x_t(\xi_1)\|^2}{s^2}} \\
+ x_{t_1} + (x_{t_1} - x_{t_1}(\xi_2)) K e^{-\frac{\|x_{t_1} - x_{t_1}(\xi_2)\|^2}{s^2}} &= x_t + \sum_{i=1}^{2} y^{\xi_i}(x_{t_{i-1}}).
\end{aligned} \tag{4.3.12}$$

Hence, in this case we have $x_{t+\Delta t} = x_t + \Delta x_t = x_t + \sum_{i=1}^{2} y^{\xi_i}(x_{t_{i-1}})$. We expand the δ-function with respect to powers of Δx retaining terms up to derivatives of second order. This expansion yields

$$\left\langle \delta(x-x_t) - \left(\frac{d}{dx}\delta(x-x_t)\right)\cdot\Delta x + \left(\frac{d^2}{dx^2}\delta(x-x_t)\right)\cdot\frac{\Delta x^2}{2} + \dots \right\rangle - \langle\delta(x-x_t)\rangle \tag{4.3.13}$$

$$\approx \left\langle -\frac{d}{dx}\delta(x-x_t)\cdot\Delta x_t \right\rangle + \frac{1}{2}\left\langle \frac{d^2}{dx^2}\delta(x-x_t)\cdot\Delta x^2 \right\rangle \approx \Delta f(x,t).$$

We evaluate the first term on the right-hand side of (4.3.13) $\left\langle -\frac{d}{dx}\delta(x-x_t)\cdot\Delta x_t\right\rangle$. Note that differentiation with respect to x must also involve Δx_t. That is,

$$\left\langle -\frac{d}{dx}\delta(x-x_t)\cdot\Delta x_t \right\rangle = -\frac{d}{dx}\{\langle\delta(x-x_t)\cdot\Delta x_t\rangle\}. \tag{4.3.14}$$

The following lemma proves the equality (4.3.14).

Lemma 4.3.1. *Let x_t be the coordinate of a seed in $x-t$ plane and $g(x_t)$ be a continuous function representing the force acting on the seed or the seed displacement at time t. Then the product of the derivative of Dirac δ-function $\frac{d}{dx}\delta(x-x_t)$ in a distributional sense and $g(x_t)$ is equal to the derivative of the product of $\delta(x-x_t)$ and $g(x_t)$*

$$\frac{d}{dx}\delta(x-x_t)\cdot g(x_t) = \frac{d}{dx}\left[\delta(x-x_t)\cdot g(x)\right]. \tag{4.3.15}$$

Proof. We choose an arbitrary function $h(x)$ from the Schwartz space or space of smooth, rapidly decreasing functions and form the following expression by multiplication with $h(t)$ and integration over the real space $\Re$

$$\int_{\Re} h(x)\frac{d}{dx}\delta(x-x_t)\cdot g(x_t)dx.$$

Integration by parts leads to

$$-\int_{\Re} h'(x)\delta(x-x_t)\cdot g(x_t)dx = -h'(x_t)g(x_t). \tag{4.3.16}$$

On the other hand, if we start from

$$\int_{\Re} h(x)\frac{d}{dx}\left[\delta(x-x_t)\cdot g(x)\right]dx$$

replacing the coordinate x_t in $g(x_t)$ by x then evaluation of this integral leads to the same result on the right-hand side of (4.3.16)

$$-\int_{\Re} h'(x)\delta(x-x_t)\cdot g(x)dx = -h'(x_t)g(x_t).$$

□

The change of x_t in time interval $[t, t+\Delta t]$ contains all displacements undergone by the seed after the time t due to random activation of $N_{\Delta t}$ seeds (one at a time) that push their neighbors to the right and to the left. The position x_t is determined by all pushes prior to this time. Due to independence of random variables x_t and Δx_t we may split the total average $-\frac{d}{dx}\langle\delta(x-x_t)\cdot\Delta x_t\rangle$ into the product of the averages

$$-\frac{d}{dx}\langle\delta(x-x_t)\cdot\Delta x_t\rangle = -\frac{d}{dx}\langle\delta(x-x_t)\rangle\langle\Delta x_t\rangle \tag{4.3.17}$$

We now find the average value of the growth increment in time Δt. From the definition of time-space Poisson counting process $\{\mu(T,A)\}$ it follows that for a fixed seed position x_t at time t

$$\Delta x_t = x_{t+\Delta t} - x_t = \begin{cases} y^{\xi_{\sigma_i}}(x_t) & \text{with probability } \lambda_t\Delta t\cdot\frac{1}{N} + o(\Delta t), \\ \sum_{i=1}^{N_{\Delta t}} y^{\xi_{\sigma_i}}(x_{t_{i-1}}) & \text{with probability } o(\Delta t), \\ 0 & \text{with probability } 1-\lambda_t\cdot\Delta t\cdot\frac{1}{N} + o(\Delta t). \end{cases} \tag{4.3.18}$$

Retaining terms linear in Δt we find that

$$\langle\Delta x_t|x_t\rangle = \sum_{i=1}^{N}\lambda_t\cdot\Delta t\cdot\frac{1}{N}(x_t - x_t(\xi_i))Ke^{-\frac{\|x_t-x_t(\xi_i)\|^2}{s^2}}. \tag{4.3.19}$$

Now we evaluate the second term on the right-hand side of (4.3.13). Using the same independence argument and evaluating the second moment of the displacement Δx_t

$$\left\langle\Delta x_t^2|x_t\right\rangle = \sum_{i=1}^{N}\lambda_t\cdot\Delta t\cdot\frac{1}{N}(x_t - x_t(\xi_i))^2K^2e^{-2\frac{\|x_t-x_t(\xi_i)\|^2}{s^2}} \tag{4.3.20}$$

and keeping only linear contributions in Δt we finally find the change of $f(x,t)$ conditioned on $\{x_0, t_0\}$

$$\begin{aligned}\Delta f(x,t) = &-\frac{d}{dx}\left[\langle\delta(x-x_t)\rangle\cdot\sum_{i=1}^{N}\frac{1}{N}y^{\xi_{\sigma_i}}(x_t)\right]\cdot\lambda_t\Delta t \\ &+\frac{1}{2}\frac{d^2}{dx^2}\left[\langle\delta(x-x_t)\rangle\cdot\sum_{i=1}^{N}\frac{1}{N}{y^{\xi_{\sigma_i}}}^2(x_t)\right]\cdot\lambda_t\Delta t + O(\Delta t, \langle\Delta x^3\rangle).\end{aligned} \tag{4.3.21}$$

Higher moments of Δx_t will contain terms linear in Δt. Indeed, for any integer n

$$\langle\Delta x_t^n|x_t\rangle = \sum_{i=1}^{N}\lambda_t\cdot\Delta t\cdot\frac{1}{N}(x_t - x_t(\xi_i))^nK^ne^{-n\frac{\|x_t-x_t(\xi_i)\|^2}{s^2}}. \tag{4.3.22}$$

We now divide the equation (4.3.21) by Δt and take limit $\Delta t \to 0$ to arrive at the approximate Fokker-Planck equation

$$\frac{\partial f(x,t)}{\partial t} = -\lambda_t\frac{\partial}{\partial x}\left(f(x,t)\cdot\sum_{i=1}^{N}\frac{1}{N}y^{\xi_{\sigma_i}}(x)\right) + \frac{\lambda_t}{2}\frac{\partial^2}{\partial x^2}\left(f(x,t)\cdot\sum_{i=1}^{N}\frac{1}{N}y^{\xi_{\sigma_i}}(x)^2\right) \tag{4.3.23}$$

subject to the initial condition $f(x, t_0|x_0, t_0) = \delta(x - x_0)$. The Fokker-Planck equation (4.3.23) is a reasonable approximation of the probability density evolution in $x - t$ plane since higher moments of Δx_t are negligible compared to the magnitudes of the first two moments and are increasingly small as n increases

$$\lim_{n\to\infty} \langle \Delta x_t^n | x_t \rangle = 0.$$

Observe that as a result of the limiting process in time $\Delta t \to 0$ the average displacement defined by (4.3.19) becomes infinitesimally small $\langle \Delta x_t | x_t \rangle \to 0$ thus leading to a continuous time-space approximation of the 1D GRID model. The seeds are activated one after another instantaneously in time and with certainty on any finite time interval $T = [t_0, t)$. To ensure that each seed is activated only once at each time instant we let the total number of seeds $N \to \infty$ in (4.3.23). Denoting $x(\xi_{\sigma_i})$ by ξ, a random placement of a seed in the continuous compact space of the initial organism $\Omega = (0, 1)$, and recalling the definition of $y^{\xi_{\sigma_i}}(x)$ (4.1.15) we obtain the coefficients of the Fokker-Planck equation in the following integral form

$$a(x,t) = \lim_{N\to\infty} \lambda_t \sum_{i=1}^{N} \frac{1}{N} y^{\xi_{\sigma_i}}(x) = \lambda_t \int_0^1 (x - \xi) \cdot K \exp\left(-\frac{\|x - \xi\|^2}{s^2} \right) d\xi \quad (4.3.24)$$

$$b(x,t) = \lim_{N\to\infty} \lambda_t \sum_{i=1}^{N} \frac{1}{N} y^{\xi_{\sigma_i}}(x)^2 = \lambda_t \int_0^1 (x - \xi)^2 \cdot K^2 \exp\left(-2\frac{\|x - \xi\|^2}{s^2} \right) d\xi. \quad (4.3.25)$$

Note that $a(x,t)$ and $b(x,t)$ satisfy the definition of the first and second jump moments

$$a(x,t) = \lim_{\Delta t \to 0} \frac{1}{\Delta t} \langle [x_{t+\Delta t} - x_t] | x_t \rangle \quad (4.3.26)$$

$$b(x,t) = \lim_{\Delta t \to 0} \frac{1}{\Delta t} \left\langle [x_{t+\Delta t} - x_t]^2 | x_t \right\rangle. \quad (4.3.27)$$

The Fokker-Planck equation (4.3.23) can be rewritten as

$$\frac{\partial f(x,t)}{\partial t} = -\frac{\partial}{\partial x} \left(f(x,t) \cdot a(x,t) \right) + \frac{1}{2} \frac{\partial^2}{\partial x^2} \left(f(x,t) \cdot b(x,t) \right) \quad (4.3.28)$$

and subject to the initial condition $f(x, t_0|x_0, t_0) = \delta(x - x_0)$.

Remark 4.3.2. *The FPE coefficients $a(x,t)$ and $b(x,t)$ are called the local characteristics of the Markov process $x_t, t \geq t_0$ [66]. $a(x,t)$ characterizes the mean value of the local velocity of the process and $b(x,t)$ characterizes the local rate of change of the dispersion of the growth increment.*

Let us take into account the correspondence of the FPE to the stochastic differential equation of motion (see Appendix A) and formulate the Langevin equation of motion. The continuous time-space approximation of the 1D GRID model (4.1.21) becomes a diffusion process $\{x(t), t \geq t_0\}$ with the drift coefficient $\alpha_1(x,t)$ (4.3.30) and diffusion coefficient $\alpha_2(x,t)$ (4.3.31)

$$dx = \alpha_1(x,t)dt + \alpha_2(x,t)dW(t) \tag{4.3.29}$$

with the initial condition $x(t_0) = \xi_{t_0}$,

where $dW(t)$ is a Wiener process increment (see Appendix A). Using relation of the Fokker-Planck equation with the Langevin equation (see Appendix A) in Stratonovich interpretation we find the drift and diffusion coefficients

$$\alpha_1(x,t) = a(x,t) - \frac{1}{4}\frac{\partial}{\partial x}b(x,t) \tag{4.3.30}$$

$$\alpha_2(x,t) = \sqrt{b(x,t)}. \tag{4.3.31}$$

Since we have assumed the uniform time-independent distribution of seeds and constant intensity of seed placements per unit time the first and second jump moments $a(x,t)$ and $b(x,t)$ depend only on the space variable.

All in all, a passage to the limit $\Delta t \to 0$ leads to a diffusion process, an approximation of the Poisson driven Markov jump process. By this limiting operation the seed trajectory x_t becomes a fractal curve that is a continuous and nowhere differentiable function. That is why the continuous time-space GRID stochastic model admits differential form (4.3.29). The diffusion process is a reasonable continuous time-space approximation of the stochastic GRID model since the displacements $y^{\xi_i}(x_t)$ are small and random and spaced so close in time that the resultant change in the position of an organism appears as a continuous motion.

4.4 A better approximation of the jump coefficients

In the previous section we have derived the Fokker-Planck equation (FPE) for the GRID model with a simplifying assumption of the uniform distribution of all possible seed placements conditioned on the previous seed location over the compact absolute space $(0,1)$ for all times. But we cannot rely on this assumption in order to correctly describe the statistical behavior of seed trajectories in a long run. In this section we find a more realistic model of the conditional probability density of seed positions in time-space.

We have obtained formulae (4.3.24) and (4.3.25) for the jump coefficients of the FPE (A.3.1) based on the assumption of the uniform time-independent density of seed activations conditioned on the previous seed coordinate x_t

$$p(\xi, t|x_t) = p(\xi) = \begin{cases} 1 & \text{if } \xi \in (0,1) \\ 0 & \text{otherwise} \end{cases} \tag{4.4.1}$$

subject to

$$p(\xi, t_0) = \delta(\xi - \xi_0).$$

In the case of the continuous uniform distribution of seeds at all times (that is a valid assumption for short times) the coefficients of the FPE

$$a(x) = \int_0^1 (x-\xi) K e^{-\frac{(x-\xi)^2}{s^2}} d\xi = K \frac{s^2}{2} \left[e^{-\frac{(x-1)^2}{s^2}} - e^{-\frac{x^2}{s^2}} \right], \tag{4.4.2}$$

$$b(x) = \int_0^1 (x-\xi)^2 K^2 e^{-2\frac{(x-\xi)^2}{s^2}} d\xi \tag{4.4.3}$$

give us insights into the statistical properties of the seed position process produced by the diffusion version of the 1D GRID model. Plots of the coefficients $a(x)$ and $b(x)$ for the range of influence values $s = 0.05$ and $s = 0.01$ given in Figure 4.4 show that "fast" growth regions are located near the endpoints of the interval. The average velocity $a(x)$ of motion of a seed initially located near either of the endpoints appears to be significantly larger in magnitude than of the ones in the middle part of the interval. The rate of dispersion $b(x)$ is lowest for seed trajectories emanating from points near the boundaries. This means that the closer the seed is to the endpoint the less diffusive its trajectory is. The middle seeds diffuse at a small constant rate $b(x) = b$. With the average velocity $a(x) = 0$ they tend to stay near their initial position. Observe that decreasing the s parameter results in shrinking of the regions of fast change of $a(x)$ and $b(x)$ and decreasing of the diffusion rate $b(x)$ for all seeds. This result is expected since smaller random pushes of the seed result in smaller deviations from its initial position.

We now give a more general definition of $a(x,t)$ and $b(x,t)$ dropping the simplifying assumption (4.4.1) and time index in x_t

$$\begin{aligned}
a(x,t) &= \lim_{\Delta t \to 0} \frac{1}{\Delta t} \langle \Delta x | x \rangle = \lambda_t \int_0^1 y^{\xi}(x) p(\xi|x) d\xi \\
&= \lambda_t \int_0^1 (x-\xi) \cdot K \exp\left(-\frac{\|x-\xi\|^2}{s^2} \right) p(\xi|x) d\xi, \\
b(x,t) &= \lim_{\Delta t \to 0} \frac{1}{\Delta t} \langle \Delta x^2 | x \rangle = \lambda_t \int_0^1 {y^{\xi}}^2(x) p(\xi|x) d\xi \\
&= \lambda_t \int_0^1 (x-\xi)^2 \cdot K^2 \exp\left(-2\frac{\|x-\xi\|^2}{s^2} \right) p(\xi|x) d\xi.
\end{aligned}$$

How one should model the probability density of seed activations in the absolute compact space of a growing organism $\Omega(t)$ given the time-space coordinate (x,t) of a seed starting its trajectory at ξ_0? To get an idea how the concentration of seeds $p(\xi, t|x)$ changes in time-space we perform a few iterations of 1D GRID algorithm applied to an organism initially occupying an interval $[0,1]$ with N seeds distributed uniformly over $(0,1)$ at time $t = t_0$. At each iteration we compute the FPE coefficients and plot them as functions of space.

Suppose the organism consists of $N = 19$ seeds with the range of influence

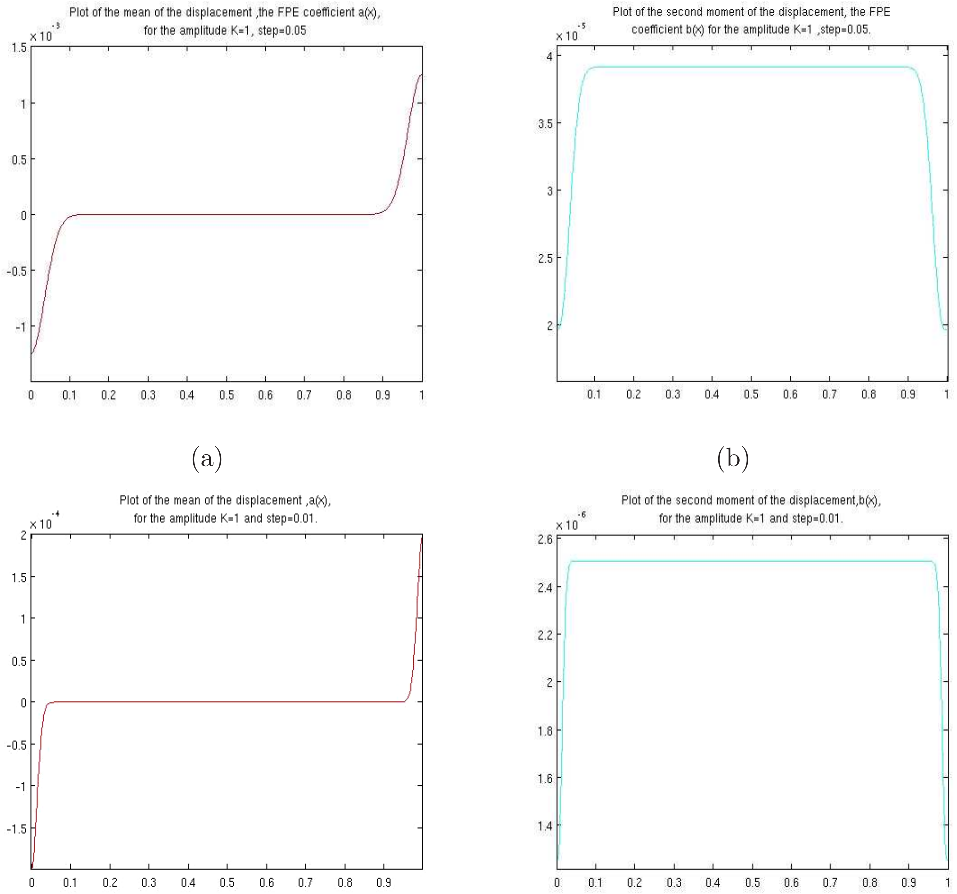

(a) (b)

(c) (d)

Figure 4.4.1: Plots of the FPE coefficients (a),(c) $a(x)$ and (b),(d) $b(x)$ computed with the assumption of the uniform probability density of the seeds for the amplitude $K = 1$ and (a),(b) $s = 0.05$, (c),(d) $s = 0.01$.

equal to the seed spacing $s = 0.05$ and constant rate of expansion $K = 1$. Let the initial position of a seed be at $x_0 = \xi_0 = 0.3$. After application of the first 1D GRID iteration seeds become accumulated near the initial point $x_0 = \xi_0 = 0.3$. Recorded below are all new possible positions $x(\xi_i)$ of the seed ξ_0 computed using the elementary GRID transformations $\phi^{\xi_j}(\xi_0)$

$$x_1(\xi_j) = \phi^{\xi_j}(\xi_0) = \xi_0 + (\xi_0 - \xi_j)\exp\left(-\frac{\|\xi_0 - \xi_j\|^2}{s^2}\right), \text{where } j = 1, 2, \ldots, 19.$$

We now find the FPE coefficients in accordance with the motion produced by 1D GRID. Using the definition of the FPE coefficients (4.3.26) and (4.3.27) we

ξ_i	$x_1(\xi_i)$
0.05	0.3000
0.1	0.3000
0.15	0.3000
0.20	0.3018
0.25	0.3184
0.3	0.3000
0.35	0.2816
0.40	0.2982
0.45	0.3000
0.5	0.3000
0.55	0.3000
0.6	0.3000
0.65	0.3000
0.7	0.3000
0.75	0.3000
0.8	0.3000
0.85	0.3000
0.9	0.3000
0.95	0.3000

Table 4.1: A list of all possible positions of a seed initially located at $x_0 = 0.3$ in an organism $\Omega = (0, 1)$ with $N = 19$ seeds obtained after the first 1D GRID algorithm application.

compute their approximations at times $t = i\Delta t, i = 1, 2, ..., n$

$$a(x, \Delta t) \approx \frac{\langle (x_{\Delta t} - x)|x\rangle}{\Delta t} = \lambda_t \frac{1}{N}\sum_{i=1}^{N}(x - \xi_i)Ke^{-\frac{(x-\xi_i)^2}{s^2}}, \text{ where } x = x_0$$

$$a(x, 2\Delta t) \approx \frac{\langle (x_{2\Delta t} - x)|x\rangle}{\Delta t} = \lambda_t \frac{1}{N}\sum_{i=1}^{N}(x - x(\xi_i))Ke^{-\frac{(x-x(\xi_i))^2}{s^2}}, \text{ where } x = x_{\Delta t} \text{ and}$$

$$x(\xi_i) = \xi_0 + (\xi_0 - \xi_i)Ke^{-\frac{(\xi_0 - xi_i)^2}{s^2}},$$

$$a(x, 3\Delta t) \approx \lambda_t \frac{1}{N^2}\sum_{i=1}^{N}\sum_{j=1}^{N}(x - x(x_i(\xi_j)))Ke^{-\frac{(x-x(x_i(\xi_j)))^2}{s^2}}, \text{ where } x = x_{2\Delta t}$$

$$\vdots$$

$$a(x, n\Delta t) \approx \lambda_t \frac{1}{N^{n-1}}\sum_{m=1}^{N}...\sum_{i=1}^{N}(x - x(x_m(...x_j(\xi_i))))Ke^{-\frac{(x-x(x_m(...x_j(\xi_i))))^2}{s^2}},$$

$$\text{where } x = x_{(n-1)\Delta t}.$$

Plots of $a(x, t)$ for each of $n = 7$ time iterations in Figure 4.4.2.a show a slow attenuation of the maximal and minimal average velocity of the seed in time and spatial dependency of $a(x, t)$ in the neighborhood of the starting position of the seed.

In a similar fashion we define the FPE coefficient $b(x, t)$:

$$b(x, \Delta t) \approx \frac{\langle (x_{\Delta t} - x)^2|x\rangle}{\Delta t} = \lambda_t \frac{1}{N}\sum_{i=1}^{N}(x - \xi_i)^2K^2e^{-2\frac{(x-\xi_i)^2}{s^2}}, \text{ where } x = x_0$$

$$b(x, 2\Delta t) \approx \frac{\langle (x_{2\Delta t} - x)^2|x\rangle}{\Delta t} = \lambda_t \frac{1}{N}\sum_{i=1}^{N}(x - x(\xi_i))^2K^2e^{-2\frac{(x-x(\xi_i))^2}{s^2}}, \text{ where } x = x_{\Delta t} \text{ and}$$

$$x(\xi_i) = \xi_0 + (\xi_0 - \xi_i)Ke^{-\frac{(\xi_0-\xi_i)^2}{s^2}},$$

$$\vdots$$

$$b(x, n\Delta t) \approx \lambda_t \frac{1}{N^{n-1}}\sum_{m=1}^{N}...\sum_{i=1}^{N}(x - x(x_m(...x_j(\xi_i))))^2K^2e^{-2\frac{(x-x(x_m(...x_j(\xi_i))))^2}{s^2}},$$

$$\text{where } x = x_{(n-1)\Delta t}.$$

A sequence of graphs of $b(x, t)$ obtained in $n = 7$ iterations given in Figure 4.4.2.b show a gradual decrease of the two peaks of the rate of dispersion along with its minimum in a symmetric manner about the line $x_0 = 0.3$. Analogous to the behaviour of $a(x, t)$, $b(x, t)$ is localized to the neighbourhood of the seed initial position at $x_0 = 0.3$.

We analyze a change in the rate of dispersion with respect to space x. The

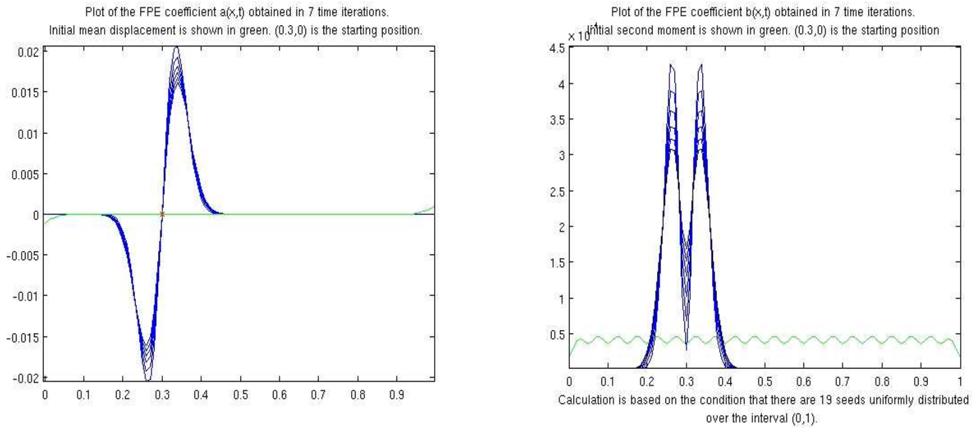

(a) (b)

Figure 4.4.2: Plots of the FPE jump coefficients obtained in 7 consecutive time iterations (a) the first jump moment $a(x,t)$, (b) the second jump moment $b(x,t)$.

derivative $b_x(x,t)$ at time $t = \Delta t$ is

$$b_x(x, \Delta t) = \frac{2K^2}{N} \sum_{i=1}^{N} (x - \xi_i) e^{-2\frac{(x-\xi_i)^2}{s^2}} \left(1 - 2\frac{(x-\xi_i)^2}{s^2} \right). \tag{4.4.4}$$

Choose x near one of the seeds ξ_i. Then the terms on the right hand side of (4.4.4) containing $\xi_j, j \neq i$ are negligible compared to the term with a factor $(x-\xi_i)$. Then the equation (4.4.4) can be rewritten as follows

$$b_x(x, \Delta t) \approx \frac{2K^2}{N} (x - \xi_i) e^{-2\frac{(x-\xi_i)^2}{s^2}} \left(1 - 2\frac{(x-\xi_i)^2}{s^2} \right). \tag{4.4.5}$$

The derivative b_x is positive if $(x - \xi_i) \left[1 - 2\frac{(x-\xi_i)^2}{s^2} \right] > 0$ which implies that

$$\{x < \xi_i \text{ and } |x - \xi_i| > \frac{s}{\sqrt{2}}\} \text{ or } \{x > \xi_i \text{ and } |x - \xi_i| < \frac{s}{\sqrt{2}}\}. \tag{4.4.6}$$

Hence, $b(x, \Delta t)$ increases for $\xi_i < x < \xi_i + \frac{s}{\sqrt{2}}$ and decreases for $\xi_i - \frac{s}{\sqrt{2}} < x < \xi_i$. Clearly, ξ_i is a point of local minimum. At the second iteration the points of

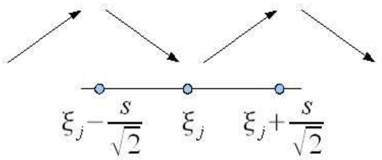

Figure 4.4.3: Local behaviour of $b(x, \Delta t)$ in the first iteration of 1D GRID algorithm.

maximum of $b(x, \Delta t)$ will have coordinates $x(\xi_0) - \frac{s}{\sqrt{2}}$ and $x(\xi_0) + \frac{s}{\sqrt{2}}$ as seen from the graph of $b(x,t)$ in Figure 4.4.2.b. Clearly, there are only two peaks of $b(x,t)$ present at times $i\Delta t > \Delta t$ due to accumulation of seeds near the initial seed position as suggested by the table 4.4.

These simple experiments give an idea how to model the conditional probability density of seed positions $p(\xi|x)$. In order to reflect concentration of seeds in the neighborhood of the starting position $x_0 = \xi_0$ we modify $p(\xi|x)$ to

$$p(\xi|x) = \frac{N}{\epsilon + (\xi - \xi_0)^2}, \tag{4.4.7}$$

where N is a normalizing constant. Integrating $p(\xi|x)$ over the set of seeds $(0,1)$ we evaluate the constant N

$$\int_0^1 \frac{N}{\epsilon + (\xi - \xi_0)^2} d\xi = 1 \Rightarrow N = \frac{\sqrt{\epsilon}}{\arctan \frac{1-\xi_0}{\sqrt{\epsilon}} - \arctan \frac{-\xi_0}{\sqrt{\epsilon}}}. \tag{4.4.8}$$

Therefore, we have the first jump moment

$$\begin{aligned} a(x,t) &= \lim_{\delta t \to 0} \frac{\langle x_{t+\delta t} - x | x \rangle}{\delta t} = \lambda_t \int_0^1 y^{\xi}(x) p(\xi|x) d\xi \\ &= K\lambda_t \int_0^1 (x-\xi) e^{-\frac{(x-\xi)^2}{s^2}} \cdot \frac{N}{\epsilon + (\xi - \xi_0)^2} d\xi. \end{aligned} \tag{4.4.9}$$

In a similar fashion we define the second jump moment $b(x,t)$

$$b(x,t) = K^2 \lambda_t \int_0^1 (x-\xi)^2 e^{-2\frac{(x-\xi)^2}{s^2}} \cdot \frac{N}{\epsilon + (\xi - \xi_0)^2} d\xi, \text{ where } x = x_t. \tag{4.4.10}$$

Employing the probability density function (4.4.7) with $\epsilon = 0.001$ we compute the FPE coefficients (4.4.9) and (4.4.10) using numerical integration. For evaluation of $a(x)$ and $b(x)$ we discretize the interval $(0,1)$ into 1000 subintervals of length $\Delta_\xi = 0.001$ and choose the range of influence of each seed $\xi_i \in ((i-1)\Delta_\xi, i\Delta_\xi)$ $s = 0.05$. As a result, the FPE coefficients plotted in Figure 4.4.4 rapidly change in the neighbourhood of the initial seed coordinate and decay towards the boundary points in a similar way shown in Figure 4.4.2. The proposed model for $p(\xi|x)$ yields a better approximation of $a(x,t)$ and $b(x,t)$ with respect to space. However, it does not capture the decay of the average velocity and the rate of dispersion in time as shown in Figure 4.4.4.

It is important to note that the Riemann sum approximation of $a(x)$ and $b(x)$ does not necessarily capture the correct local behavior in the neighborhood of the initial seed coordinate ξ_0. If we choose the s parameter of the order of magnitude of the seed spacing $\Delta\xi$ then the two peaks of $b(x)$ will not be present. Indeed, suppose that $s = \Delta\xi$. Then the locations of these two peaks can be found solving $\frac{db}{dx} = 0$ for $x \in (0,1)$.

$$\begin{aligned} \frac{db(x)}{dx} &= \int_0^1 \frac{\partial}{\partial x} (x-\xi)^2 K^2 e^{-2\frac{(x-\xi)^2}{\Delta\xi^2}} \frac{N}{0.001 + (\xi - \xi_0)^2} d\xi = \\ & 2NK^2 \int_0^1 (x-\xi)(1 - 2\frac{(x-\xi)^2}{\Delta\xi^2}) e^{-2\frac{(x-\xi)^2}{\Delta\xi^2}} \frac{1}{0.001 + (\xi - \xi_0)^2} d\xi = 0. \end{aligned} \tag{4.4.11}$$

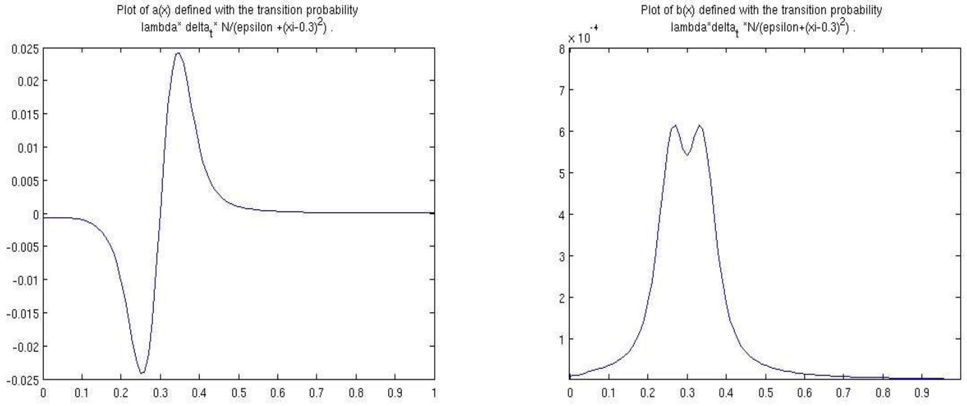

(a) (b)

Figure 4.4.4: Plots of the FPE jump coefficients defined with the conditional probability density $p(\xi|x) = \frac{N}{0.001+(\xi-\xi_0)^2}$ with $\xi_0 = 0.3$ (a) the first jump moment $a(x,t)$, (b) the second jump moment $b(x,t)$.

Since the integrand is a continuous function of ξ we can apply the Mean Value Theorem to evaluate the integral. We have

$$(x-\bar{\xi})(1-2\frac{(x-\bar{\xi})^2}{\Delta\xi^2})e^{-2\frac{(x-\bar{\xi})^2}{\Delta\xi^2}}\frac{1}{0.001+(\bar{\xi}-\xi_0)^2} = 0, \tag{4.4.12}$$

where $\bar{\xi} \in (0,1)$. Solving (4.4.12) for x we find critical points

$$x_1 = \bar{\xi},\ x_2 = \bar{\xi} + \frac{\Delta\xi}{\sqrt{2}},\ x_3 = \bar{\xi} - \frac{\Delta\xi}{\sqrt{2}}. \tag{4.4.13}$$

It is straightforward to show that x_2 and x_3 are local maxima of $b(x)$. They are at a distance $\frac{\Delta\xi}{\sqrt{2}}$ apart from the point of local minimum $\bar{\xi}$ that is less than the seed spacing $\Delta\xi$. Clearly, such close positioning of x_2 and x_3 will not be captured by numerical integration with seed spacing equal to the value of s parameter as seen from Figure 4.4.5.a. If the number of seeds is chosen very large such as $N_{seeds} = 10000$ then the s parameter of a higher order of magnitude than the seed spacing can still be very small to capture the differences in values of $b(x)$ at the three critical points x_1, x_2, x_3. This effect is demonstrated in a Figure 4.4.5.b for the value of $s = 0.001$ that is of order $O(10\Delta\xi)$. Therefore, the range of influence s should be chosen sufficiently large to reflect the two-peak behavior of $b(x)$ produced by the GRID model.

Remark 4.4.1. *The conditional probability density $p(\xi|x)$ can be thought of as the transition probability density $p(x'|x)$ from a state x to a new state x'. Indeed,*

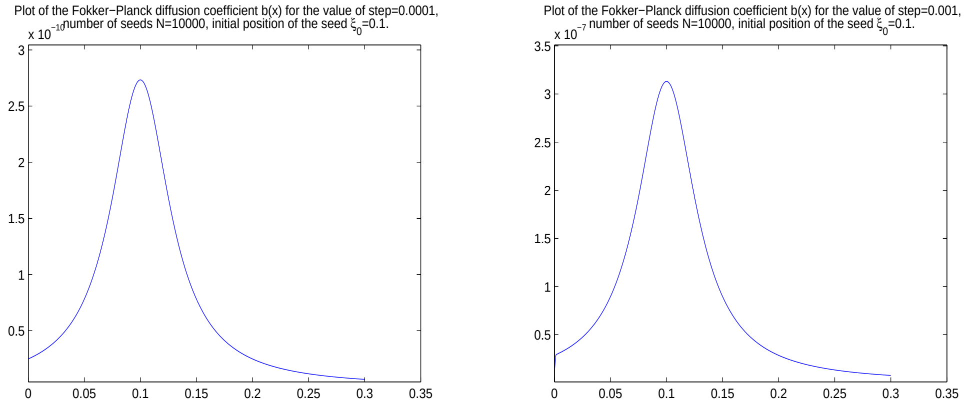

(a) (b)

Figure 4.4.5: Plot of the Fokker-Planck diffusion coefficient $b(x)$ for the number of seeds $N_{seeds} = 10000$, the initial position of a seed $\xi_0 = 0.1$ and the s parameter (a) $s = 0.0001$, (b) $s = 0.001$.

according to the definition of the Fokker-Planck coefficients

$$\begin{aligned} a(x,t) &= \lim_{\Delta t \to 0} \frac{1}{\Delta t} \left\langle (x_{t+\Delta t} - x) | x \right\rangle \qquad (4.4.14) \\ &= \lim_{\Delta t \to 0} \frac{1}{\Delta t} \int_{x_{t+\Delta t} \in \mathcal{X}} (x_{t+\Delta t} - x) p(x_{t+\Delta t} | x) dx_{t+\Delta t}, \\ b(x,t) &= \lim_{\Delta t \to 0} \frac{1}{\Delta t} \left\langle (x_{t+\Delta t} - x)^2 | x \right\rangle \qquad (4.4.15) \\ &= \lim_{\Delta t \to 0} \frac{1}{\Delta t} \int_{x_{t+\Delta t} \in \mathcal{X}} (x_{t+\Delta t} - x)^2 p(x_{t+\Delta t} | x) dx_{t+\Delta t}. \end{aligned}$$

(4.4.16)

Since the displacement is a deterministic function of a random variable or a Poisson point ξ (an activated seed at time t in the absolute compact space of a growing organism $\Omega(t)$) then in a small time interval Δt for a fixed seed position at time t $x_t = x$

$$x_{t+\Delta t} - x = y^{\xi}(x) = (x - \xi) \cdot K \exp\{-\frac{\|x - \xi\|^2}{s^2}\} \qquad (4.4.17)$$

with probability $\lambda_t \Delta t \cdot p(\xi|x) + o(\Delta t)$.
Also, it is possible that the displacement takes the value

$$x_{t+\Delta t} - x = \sum_{i=1}^{N_{\Delta t}} y^{\xi_{\sigma_i}}(x) \ \textit{with probability } o(\Delta t) \qquad (4.4.18)$$

and

$$x_{t+\Delta t} - x = 0 \textit{ with probability } 1 - \lambda_t \Delta t \cdot p(\xi|x) + o(\Delta t). \qquad (4.4.19)$$

Incorporating (4.4.17),(4.4.18) *and* (4.4.19) *into the average value of the displacement conditioned on the seed position* x *at time* t *and taking the limit* $\Delta t \to 0$ *we have*

$$a(x,t) = \lim_{\Delta t \to 0} \frac{\langle x_{t+\Delta t} - x | x \rangle}{\Delta t} = \lambda_t \int_0^1 y^{\xi}(x) p(\xi | x) d\xi \tag{4.4.20}$$

$$b(x,t) = \lim_{\Delta t \to 0} \frac{\langle (x_{t+\Delta t} - x)^2 | x \rangle}{\Delta t} = \lambda_t \int_0^1 {y^{\xi}}^2(x) p(\xi | x) d\xi. \tag{4.4.21}$$

Since activation of a particular seed ξ *determines a new position* $x' = x + y^{\xi}(x)$ *of a seed previously located at the coordinate* (x,t) *then the conditional probability density of seeds* $p(\xi|x)$ *is equal to the probability density of transition from* x *to* $x' = x + y^{\xi}(x)$ $p(x'|x)$*.*

4.5 Numerical solution of the Fokker-Planck equation

In this section we present a computational algorithm that numerically solves the Fokker-Planck equation. The choice of the boundary conditions remains hypothetical and needs experimental justification.

All in all, we have derived the Fokker-Planck equation (A.3.1) that represents a linear parabolic partial differential equation of the second order with space-dependent coefficients $a(x,t) = a(x)$, $b(x,t) = b(x)$

$$\frac{\partial f(x,t)}{\partial t} = -\frac{\partial}{\partial x}\left(f(x,t) \cdot a(x)\right) + \frac{1}{2}\frac{\partial^2}{\partial x^2}\left(f(x,t) \cdot b(x)\right) \tag{4.5.1}$$

subject to the initial and boundary conditions

$$f(x,0) = \delta(x - \xi_0),\ \xi_0 \in (0,1) \tag{4.5.2}$$

$$f(0,t) = f(1,t) = 0. \tag{4.5.3}$$

In the conjecture above, the absorbing boundary conditions are hypothetical. We will see later when studying the equilibrium solution that other boundary conditions appear consistent with our observations of seed trajectories in a long run.

Remark 4.5.1. ***Natural and attractive boundary conditions.*** *Since an organism* $\Omega(t)$ *grows to a finite limiting size* (c,d) *as suggested by GRID experiments of its long-time growth it is natural to restrict the domain of existence of stochastic variables* x_t *by the limiting left and right endpoints* c *and* d*. Such boundary points cannot be reached by the seed trajectories in the course of time. They are usually called natural or attractive boundaries. Since we don't know the limiting values* c *and* d *of the left and right endpoints of* $\Omega(t)$ *we can choose the boundary points* A *and* B *that satisfy the definition of natural or attractive boundaries [23] given in* *terms of local characteristics of the diffusion process* $a(x)$ *and* $b(x)$.

If, for any $\beta \in (A, B)$,

$$L_1 = \int_A^\beta \exp\left(-\int_\beta^x \frac{2a(z)}{b(z)} dz\right) dx = +\infty$$

then A *is a natural boundary.*

If, for any $\beta \in (A, B)$, $L_1 < +\infty$ *and*

$$L_2 = \int_A^\beta \frac{1}{b(y)} \left(\int_c^y \exp\left(-\int_\beta^x \frac{2a(z)}{b(z)} dz\right) dx\right) \exp\left(\int_\beta^y \frac{2a(z)}{b(z)} dz\right) dy = +\infty.$$

then A *is an attractive boundary.*

In this case it makes no difference which boundary conditions we impose.

Before we state a finite difference equation approximating the solution to (4.5.1) with some accuracy we put (4.5.1) into the following equivalent form

$$\frac{\partial f(x,t)}{\partial t} = \frac{1}{2} b(x) \frac{\partial^2 f(x,t)}{\partial^2 x} + \left(\frac{db(x)}{dx} - a(x)\right) \frac{\partial f(x,t)}{\partial x} + \left(\frac{1}{2}\frac{d^2 b(x)}{d^2 x} - \frac{da(x)}{dx}\right) f(x,t). \tag{4.5.4}$$

Consider a rectangular mesh of nodes $(x, t) = (ih, jl)$ with $i = 1, 2, \ldots, M$, $M = \frac{1}{h}$ and $j = 1, 2, \ldots$. Boundary nodes are given by $(0, 0)$ and $(1, 0)$. We approximate first and second partial derivatives with respect to space by central differences

$$\frac{\partial f}{\partial x} \approx \frac{f_{i+1,j} - f_{i-1,j}}{2h}, \ \frac{\partial^2 f}{\partial^2 x} \approx \frac{f_{i+1,j} - 2f_{i,j} + f_{i-1,j}}{h^2}, \text{ where } f_{i,j} = f(ih, jl). \tag{4.5.5}$$

The time derivative of the density function is replaced by

$$\frac{\partial f}{\partial t} \approx \frac{f_{i,j+1} - f_{i,j}}{l}, \ j \geq 0 \tag{4.5.6}$$

We substitute (4.5.5) and (4.5.6) into (4.5.4) to obtain the finite difference equation

$$f_{i,j+1} = \alpha_i f_{i+1,j} + \beta_i f_{i,j} + \gamma_i f_{i-1,j}, \text{ where} \tag{4.5.7}$$

$$\alpha_i = \alpha(ih) = \left[\frac{l}{2h^2} b(x) + \frac{l}{2h}\left[\frac{db(x)}{dx} - a(x)\right]\right]_{x=ih} \tag{4.5.8}$$

$$\beta_i = \beta(ih) = \left[1 - \frac{l}{2h^2} b(x) + l\left[\frac{1}{2}\frac{d^2 b(x)}{d^2 x} - \frac{da(x)}{dx}\right]\right]_{x=ih}, \tag{4.5.9}$$

$$\gamma_i = \gamma(ih) = \left[\frac{l}{2h^2} b(x) - \frac{l}{2h}\left[\frac{db(x)}{dx} - a(x)\right]\right]_{x=ih}. \tag{4.5.10}$$

From the initial and boundary conditions it follows that

$$f_{i,0} = \begin{cases} 1 & \text{if } i = m \\ 0 & \text{otherwise,} \end{cases} \tag{4.5.11}$$

where m is an index of the initial point $\xi_0 = mh$ and $f_{0,j} = f_{N,j} = 0$.

The discretized FPE (4.5.7) contains values of $f(x,t)$ at four nodes of the computational time-space grid (ih, jl),$((i-1)h, jl)$,$((i+1)h, jl)$ and $(ih, (j+1)l)$. It approximates the FPE with the order of accuracy $O(l + h^2)$. The finite difference equation (4.5.7) along with the initial and boundary conditions (4.5.11) represent an explicit Euler forward scheme. Indeed, from the initial conditions (4.5.11) we have the values of $f(x,t)$ at the nodes of the initial "layer" $j = 0$ and plugging them into (4.5.7) we find $f(x,t)$ at the interior nodes of the first layer $j = 1$ and so on. Therefore, (4.5.7) and (4.5.11) yield an explicit solution $f(x,t)$ at the $(j+1)$st layer expressed through already found values of $f(x,t)$ at the jth layer.

Practical application of explicit difference schemes leads to the necessity of satisfying a special stability condition. From numerical methods of partial differential equations it is known that the difference scheme (4.5.7) is stable if the following inequalities hold in the computational domain

$$b(x,t) > 0, \quad \frac{l}{h^2} < \frac{1}{b(x,t)}. \tag{4.5.12}$$

From the second inequality it follows that the explicit difference scheme needs a very small time s l. Therefore, in order to find a stable numerical solution to the Fokker-Planck equation in a finite time interval T a number of layers j must be large.

A Matlab script "FPE_sol.m" (see Appendix E) fulfills the following computational algorithm.

1. *Initialization.* Seeds ξ_i, $i = 1, 2, \ldots, n = 1000$ are uniformly distributed over the interval $(0, 1)$. The mesh spacing $h = 0.01$ and time step $l = 0.00005$. Growth period $T = [0, 10]$. The range of influence of an active seed $s = 0.05$. The amplitude of growth $K = 1.0$. The initial position of a seed is fixed $x_0 = \xi_0$, $\xi_0 \in \{\xi_1, \xi_2, \ldots, \xi_{1000}\}$.

2. *Calculation of the Fokker-Planck equation coefficients and its derivatives.*

```
for i=1 to 100
    $a(ih) = K \cdot h \sum_{j=1}^{1000} (ih - \xi_j) \exp\left(-1 \frac{(ih - \xi_j)^2}{s^2}\right) \frac{N}{(0.001 + (\xi_j - \xi_0)^2)};$
    $b(ih) = K^2 \cdot h \sum_{j=1}^{1000} (ih - \xi_j)^2 \exp\left(-2 \frac{(ih - \xi_j)^2}{s^2}\right) \frac{N}{0.001 + (\xi_j - \xi_0)^2};$
    $\frac{db}{dx}(ih) = 2K^2 \cdot h \sum_{j=1}^{1000} (ih - \xi_j) \exp\left(-2 \frac{(ih - \xi_j)^2}{s^2}\right) \frac{N}{(0.001 + (ih - \xi_j)^2)} \cdot \left(1 - 2\frac{(ih - \xi_j)^2}{s^2}\right);$
    $\frac{d^2b}{d^2x}(ih) = 2K^2 \cdot h \sum_{j=1}^{1000} \exp\left(-2 \frac{(ih - \xi_j)^2}{s^2}\right) \frac{N}{0.001 + (\xi_j - \xi_0)^2} \cdot \left(1 - \frac{10}{s^2}(ih - \xi_j)^2 + \frac{8}{s^4}(ih - \xi_j)^4\right);$
    $\frac{da}{dx}(ih) = K \cdot h \sum_{j=1}^{1000} \exp\left(-\frac{(ih - \xi_j)^2}{s^2}\right) \frac{N}{0.001 + (\xi_j - \xi_0)^2} \left(1 - 2\frac{(ih - \xi_j)^2}{s^2}\right);$
end
```

3. *Calculation of the finite difference equation coefficients.* Compute space-dependent finite difference equation coefficients $\alpha_i = \alpha(ih)$, $\beta_i = \beta(ih)$ and $\gamma_i = \gamma(ih)$ using formulae (4.5.8), (4.5.9), (4.5.10) respectively.

4. *Update of $f(x,t)$ at each jth time iteration.*

```
for j=1 to $\frac{10}{l}$
for i=1:100
    $f(ih, jl) = \alpha(i) f((i+1)h, (l-1)j) + \beta(i) f(ih, (l-1)j) + \gamma(i) f((i-1)h, (l-1)j)$
end
Compute a normalizing constant C and reinitialize
    $2C = h \sum_{i=1}^{100} f(i,j), \quad f(:,j) = \frac{f(:,j)}{C}.$
end
```

Note that if we assume a continuous uniform distribution of seeds at all times

$$p(\xi|x) = \begin{cases} 1 & \text{if } 0 < \xi < 1 \\ 0 & \text{otherwise} \end{cases}$$

then the derivatives of the FPE coefficients can be found explicitly

$$\begin{aligned}
\frac{da(x)}{dx} &= K\left[xe^{-\frac{x^2}{s^2}} - (x-1)e^{-\frac{(x-1)^2}{s^2}}\right] \\
\frac{db(x)}{dx} &= \int_0^1 \frac{\partial}{\partial x}(x-\xi)^2 K^2 e^{-2\frac{(x-\xi)^2}{s^2}} d\xi = \\
&\quad K^2 s^2 \left[e^{-2\frac{(x-1)^2}{s^2}} - e^{-2\frac{x^2}{s^2}}\right] - K^2\left[x^2 e^{-2\frac{x^2}{s^2}} - (x-1)^2 e^{-2\frac{(x-1)^2}{s^2}}\right] \\
\frac{d^2b(x)}{d^2x} &= 2K^2\left[xe^{-2\frac{x^2}{s^2}} - (x-1)e^{-2\frac{(x-1)^2}{s^2}}\right] + \frac{4K^2}{s^2}\left[(x-1)^3 e^{-2\frac{(x-1)^2}{s^2}} - x^3 e^{-2\frac{x^2}{s^2}}\right].
\end{aligned}$$

Using these explicit expressions for the derivatives we compute the coefficients α, β and γ of the finite difference equation (4.5.7) and thus find numerically the probability density function in time-space conditioned on a particular initial seed position ξ_0. Choosing GRID parameters $s = 0.05$, the amplitude $K = 1$ and initial seed coordinates $\xi_0 = 0.5$ and $\xi = 0.1$ we obtain respective probability distributions of seed trajectories diffusing according to the diffusion equation (4.5.4) where the FPE jump coefficients are defined with the constant transition probability density $p(\xi|x)$. The diffusive evolution of the probability density of seed locations during time interval $[0, 6]$ is shown in Figure 4.5.1.

We now apply the computational algorithm described above to solve the FPE

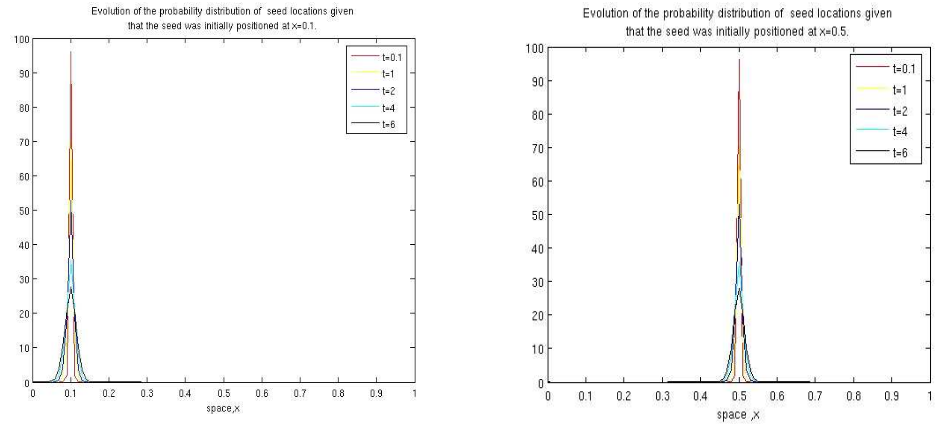

(a) (b)

Figure 4.5.1: Time-space evolution of the probability density of seed trajectories emanating from the initial position (a) $\xi_0 = 0.1$, (b) $\xi_0 = 0.5$ computed with constant transition probability $p(\xi|x) = 1$.

(4.5.4) with the transition probability density $p(\xi|x)$ given by (4.4.7) and various initial seed positions ξ_0. We are interested in the statistical behavior of seed trajectories when the range of influence of each activated seed is sufficiently large. It is clear that if the order of magnitude of the s parameter is $O(\Delta\xi)$, where $\Delta\xi$ is a spacing between two neighboring seeds (chosen for computational purposes) then the corresponding distribution of seed trajectories will be diffusing in time-space very slowly. Therefore, choosing the total number of seeds $N_{seeds} = 1000$ for numerical evaluation of $a(x)$ and $b(x)$ on an interval $(0, 1)$, the range of influence $s = 0.05 > \Delta\xi = 0.001$ and the amplitude $K = 1$ we find the numerical approximation to $f(x, t)$ for $t \in [0, 6]$ and display the solutions satisfying initial conditions $f(x, 0) = \delta(x - 0.1)$ and $f(x, 0) = \delta(x - 0.3)$ in Figure 4.5.2.

Plots of the probability density $f(x, t)$ as a function of time t and space x presented in Figure 4.5.2 show a qualitative change from an unimodal to a bimodal probability distribution of seed positions during the course of time. Apparently, the velocity of the process $a(x)$ that is an odd function of an argument $\xi - \xi_0$ (see Fig.4.4.4.a) gives rise to such symmetric separation of concentrations of seed trajectories. Indeed, seeds located in the neighborhood of ξ_0 to the left of ξ_0 and to the right of ξ_0 will be moving respectively in the negative and positive directions. The velocities of seeds located at ξ_0 and away from ξ_0 rapidly decay to zero thus leading to formation of the two peaks of the probability density of seed trajectories. In the beginning the most probable position is $x = \xi_0$ but also other positions are possible due to the random pushes from the neighboring seeds. The variance of the seed position increases slowly in time since a large number of pushes is necessary to deviate the seed path far from $x = \xi_0$. The probability density becomes more spread out and eventually forms two peaks growing with time. This means that the seed will follow one of the two most probable paths with approximately equal probability. The question that arises immediately is will the symmetry of $f(x, t)$ be preserved in a very long time? What is the time-independent or stationary solution to the FPE?

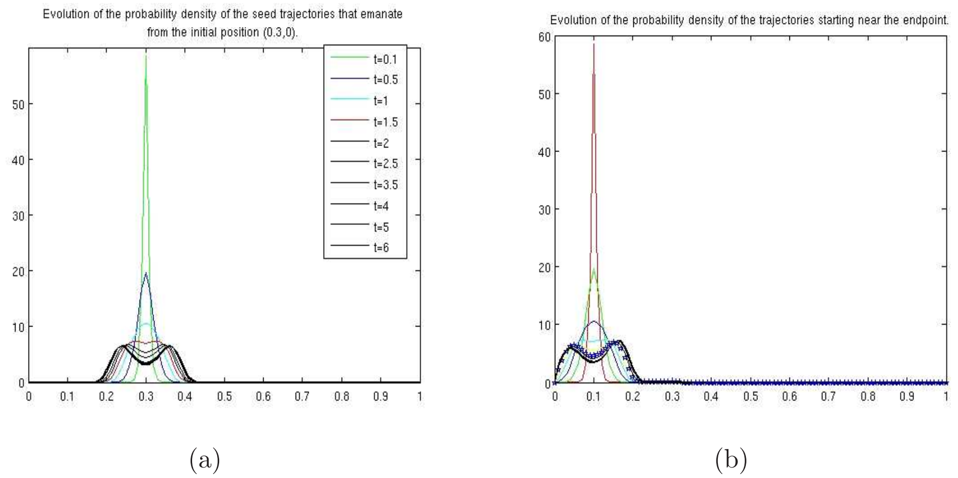

(a) (b)

Figure 4.5.2: Time-space evolution of the probability density of seed trajectories emanating from the initial position (a) $\xi_0 = 0.1$, (b) $\xi_0 = 0.3$ computed with transition probability $p(\xi|x) = \frac{N}{\epsilon + (\xi - \xi_0)^2}$.

4.6 Stationary solution of the Fokker-Planck equation

We have obtained time-dependent solution to the Fokker-Planck equation for the continuous time-space approximation of 1D GRID model. It describes the statistical behavior of a seed while it has not reached either of the endpoints 0 or 1. In this section we explore various boundary conditions and find the corresponding equilibrium probability densities.

4.6.1 Absorbing boundary conditions

When absorbing boundary conditions $f(0,t) = f(1,t) = 0$ are imposed all possible seed trajectories will eventually end up at one of the "screens" $x = 0$ and $x = 1$ independently of the initial position of the seed. In the limit $t \to \infty$ within the interval $(0,1)$ and at the endpoints all seeds will be absorbed by one of the screens, that is $\lim_{t\to\infty} f(x,t) = 0$. Does this result agree with the long-time motion of the seed produced by the 1D GRID model?

We generate sets of 100 various trajectories of the seed starting at $\xi_0 = 0.25$, $\xi_0 = 0.5$ and near the endpoints ξ_0 running 30,000 1D GRID iterations for each individual trajectory. At each time iteration one seed is activated according to the continuous uniform distribution of seeds over the interval $(0,1)$ (using Matlab command "rand"). The s parameter is set to be relatively large $s = 0.05$ to ensure high variability of seed trajectories. The resulting trajectory picture is shown in Figure 4.6.1.

Observe that various trajectories converge to the boundary points with the stationary probability dependent on the initial coordinate of the seed. For seed paths starting from the middle point we expect two equally high peaks of the equilibrium density function located at the endpoints of a grown organism.

The seeds initially located near the boundaries always move outwards, and as such the corresponding equilibrium probability distribution will have a high concentration of seeds at the boundary point of the grown organism. The trajectories emanating from an initial position at a considerable distance from one endpoint and a smaller distance from another endpoint are more likely to end up at the boundary point located closer to the initial seed coordinate. Therefore, we expect the probability density to have a peak at this boundary point higher than at another one.

All in all, the hypothetical form of the stationary probability density $f_s(x)$ can be written as a sum of two weighted δ-functions

$$f_s(x) = A_1\delta(x) + A_2\delta(x-1). \tag{4.6.1}$$

Simulations of a long-time seed motion using 1D GRID algorithm suggest that an equilibrium density satisfying the absorbing boundary conditions does not capture probability mass concentrations at the endpoints. But in the interior part of the

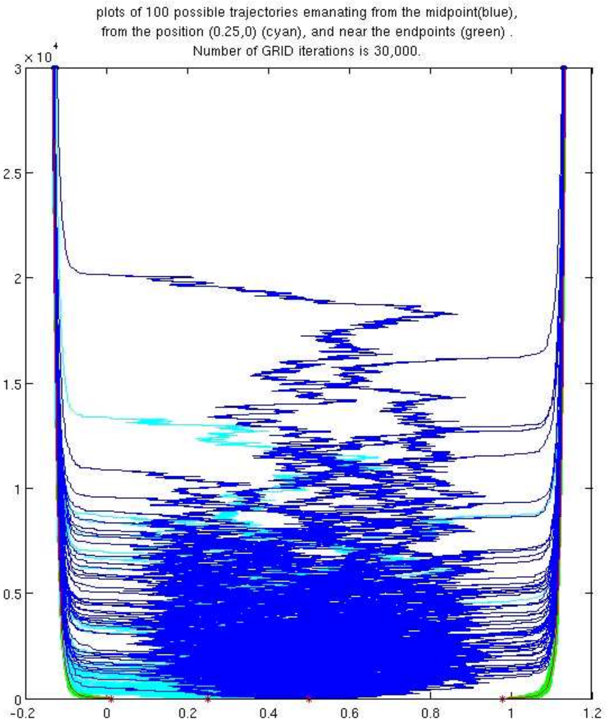

Figure 4.6.1: Plots of 100 possible seed trajectories emanating from the midpoint $\xi_0 = 0.5$ (blue), from the coordinate $\xi_0 = 0.25$ (cyan) and near the endpoints (green). Number of GRID iterations is $30,000$.

grown organism $(0,1)$ it correctly predicts the zeroth value. Indeed, there are no possible seed positions there since the seed gets moved far away from its initial position by an infinite number of random pushes from its neighbors. The probability density in an interval $(0,1)$ approaches zero as time $t \to \infty$.

In what follows we explore other boundary conditions and their effects on the stationary solution of the Fokker-Planck equation.

4.6.2 Reflecting boundary conditions

Since the stochastic variable x_t has a bounded domain of definition (due to a simple fact that organisms cannot grow unboundedly) we solve the stationary Fokker-Planck equation only in this domain. Without loss of generality, we restrict the domain to an interval $(0,1)$. We have seen in illustrations of long-time trajectories that seeds eventually "escape" the initial organism's interior $(0,1)$ as a new material is being created locally within the organism's domain pushing seeds outwards and resulting in the length increase. An operation of rescaling of the grown organism occupying an interval (c,d) to a unit interval $(0,1)$ does not alter the behavior of the probability density qualitatively. Therefore, in a conjecture below we treat the endpoints $x = 0$ and $x = 1$ as the boundary points of the grown organism in the limit $t \to \infty$.

We impose the boundary conditions with zero probability flux and solve the stationary Fokker-Planck equation. The FPE (4.5.4) represents the continuity equation

$$\frac{\partial}{\partial t} f(x,t) + \frac{\partial}{\partial x} G(x,t) = 0, \text{ where} \tag{4.6.2}$$

$$G(x,t) = a(x) f(x,t) - \frac{1}{2}\frac{\partial}{\partial x}[b(x) f(x,t)] \tag{4.6.3}$$

is the probability flux. In this set up the probability density $f(x,t)$ can be interpreted as the concentration of seed positions at the coordinate x and time instant t. The flux of seeds G along the x-axis is the sum of an average flux $a(x)f(x,t)$, where $a(x)$ is the local velocity of the average seed motion and a random or diffusion flux $-\frac{1}{2}\frac{\partial}{\partial x} b(x) f(x,t)$. Since there is no seed flux across the boundaries $x = 0$ and $x = 1$ we set the following boundary conditions

$$G(0,t) = G(1,t) = 0.$$

The boundary points $x = 0$ and $x = 1$ play a role of the reflecting "screens", that is, if a seed reaches these screens then it gets reflected from them in a mirror-like fashion.

We find the stationary probability density $f_s(x) = \lim_{t\to\infty} f(x,t)$ analytically. In the equilibrium state $\frac{\partial f}{\partial t} = 0$ and the FPE becomes

$$\frac{\partial}{\partial x}(b(x) f_s(x)) - 2a(x) f_s(x) = -2G. \tag{4.6.4}$$

With the zero probability flux the stationary FPE (4.6.4) simplifies to

$$\frac{\partial}{\partial x}(b(x) f_s(x)) - 2a(x) f_s(x) = 0. \tag{4.6.5}$$

Let $g(x) = b(x) f_s(x)$ and since $b(x) > 0$ on $(0,1)$ we can rewrite the equation above as

$$\frac{\partial}{\partial x} g(x) - 2\frac{a(x)}{b(x)} g(x) = 0. \tag{4.6.6}$$

It is a linear differential equation that is easily solved multiplying the left-hand side and the right-hand side by $e^{-2\int_0^x \frac{a(y)}{b(y)}dy}$. We have

$$\frac{\partial}{\partial x}\left(g(x)\cdot e^{-2\int_0^x \frac{a(y)}{b(y)}dy}\right) = 0. \tag{4.6.7}$$

Therefore, we obtain the following stationary solution $f_s(x)$

$$g(x) = b(x) f_s(x) = C \cdot e^{2\int_0^x \frac{a(y)}{b(y)}dy} \Rightarrow f_s(x) = \frac{C}{b(x)} \cdot e^{2\int_0^x \frac{a(y)}{b(y)}dy}, \tag{4.6.8}$$

where C is the normalizing constant determined by $\int_0^1 f_s(x) = 1$. Denote $U(x) = -\int_0^x \frac{a(y)}{b(y)} dy$. $U(x)$ has the meaning of a potential. Since the FPE coefficients $a(x)$ and $b(x)$ depend on the initial position of a seed ξ_0 so does the equilibrium solution $f_s(x)$.

The graphs of $U(x)$ and $f_s(x)$ for the initial position $x_0 = \xi_0 = 0.5$ are given in a Figure below. Observe from the graph of $f_s(x)$ that the probability mass is concentrated at the endpoints. The seed may be found with equal probability at either of the boundary points. This result is consistent with the experimental observations of the long-time motion of the middle seed illustrated in Figure 4.6.1.

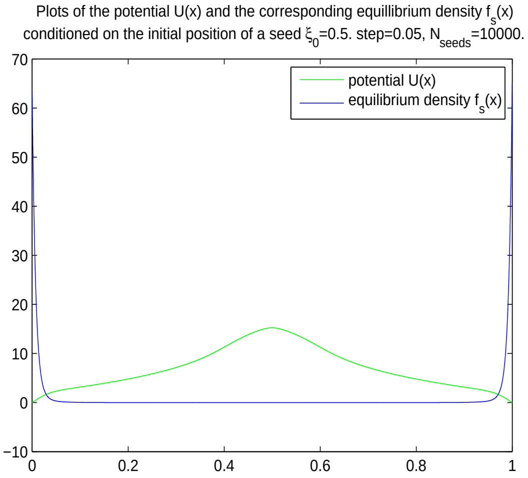

Figure 4.6.2: Plot of the potential $U(x)$ and the corresponding stationary probability density $f_s(x)$ conditioned on the initial position of a seed $\xi_0 = 0.5$. The range of influence $s = 0.05$ and the number of seeds used for numerical integration of $a(x)$ and $b(x)$ $N_{seeds} = 10000$.

For the seed starting at $\xi_0 = 0.3$ the diffusion Markov process becomes singular near the endpoint $x = 1$ due to the vanishing diffusion coefficient $b(x)$. As a result, the probability density $f_s(x)$ becomes infinitely high at the right endpoint that is not the most probable ending location of seed trajectories emanating from $\xi_0 = 0.3$ near the left endpoint. Shown below are graphs of the potential $U(x)$ and the corresponding probability density $f_s(x)$ on the subinterval $(0, 0.7)$. The reflecting boundary conditions do not yield the desired equilibrium probability density with a higher peak at the boundary point located closer to the initial seed coordinate.

4.6.3 Boundary conditions with the non-zeroth probability flux.

When the probability flux (4.6.3) $G(0) = G(1) = const \neq 0$ then the general solution to the stationary Fokker-Planck equation

$$\frac{\partial}{\partial x}(b(x)f_s(x)) - 2a(x)f_s(x) = -2G.$$

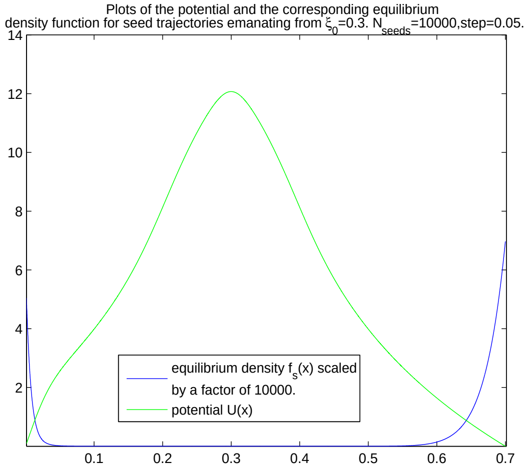

Figure 4.6.3: Plot of the potential $U(x)$ and the corresponding stationary probability density $f_s(x)$ conditioned on the initial position of a seed $\xi_0 = 0.3$. The range of influence $s = 0.05$ and the number of seeds used for numerical integration of $a(x)$ and $b(x)$, $N_{seeds} = 10,000$.

is given by

$$f_s(x) = \frac{C}{b(x)} e^{2\int_0^x \frac{a(y)}{b(y)}dy} - \frac{2G}{b(x)} \int_0^x e^{2\int_y^x \frac{a(t)}{b(t)}dt} dy, \text{ where } 0 < y < x \tag{4.6.9}$$

and C is the normalizing constant. When the probability flux is positive then the seeds tend to approach and pass through the right endpoint. And vice versa, when the probability flux is negative the seeds tend to move in the left direction. For example, for seed trajectories emanating from $\xi_0 = 0.7$ close to the right endpoint we set up positive stationary probability flux $G = 1$ since they are attracted to the right boundary point. We compute $f_s(x)$ using formula (4.6.9) and compare it with the stationary probability density obtained with the reflecting boundary conditions according to formula (4.6.8). From their plots given in Figure 4.6.3 we observe that the non-zeroth positive probability flux yields an equilibrium probability density with a significantly higher concentration of seeds at the right boundary as desired.

We conclude that for a seed starting its "journey" near one of the boundary points the boundary conditions with the non-zeroth positive probability flux should be chosen. Namely, for an organism Ω initially occupying an interval $(0, 1)$

$$G = \begin{cases} C_1 > 0 & \text{if } \xi_0 > 0.5 \\ C_2 < 0 & \text{if } \xi_0 < 0.5, \end{cases} \tag{4.6.10}$$

where C_1 and C_2 are constants.

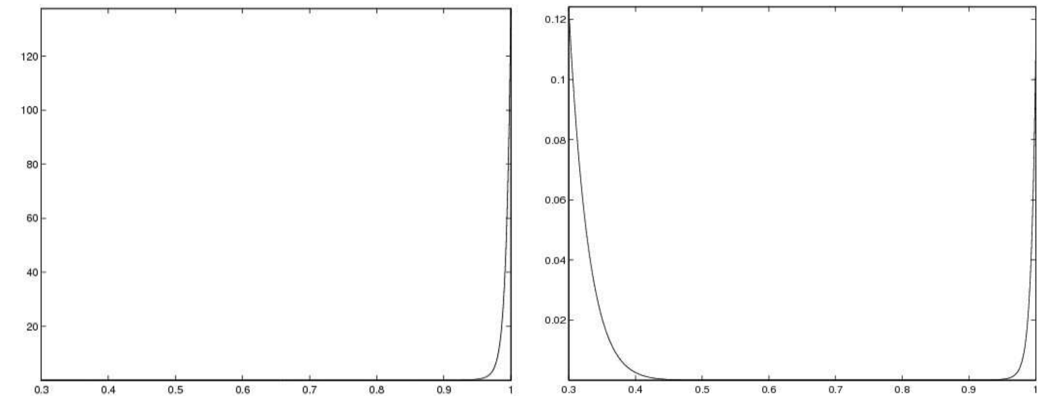

(a) (b)

Figure 4.6.4: Plots of the equilibrium probability density corresponding to (a) the boundary conditions with the non-zeroth positive probability flux, (b) the reflecting boundary conditions. The initial seed position $\xi_0 = 0.7$, the range of influence $s = 0.05$ and the number of seeds used for numerical integration of $a(x)$ and $b(x)$, $N_{seeds} = 10,000$.

4.7 Theorems for the diffusion approximation of the GRID model.

In this section we summarize the development of the Fokker-Planck equation and its time-dependent and independent solutions along with the local characteristics of the diffusion Markov process derived from the "microstructure" of the continuous-time stochastic GRID model.

Theorem 4.7.1. *Consider a special case of the stochastic 1D GRID model that is a Poisson driven Markov process with the constant intensity of seed activations per unit time* $\lambda_t = const$*, continuous and compact Darcyan space of seeds* $\Xi = (0, 1)$*. Then a continuous space approximation of the Poisson driven Markov process is a diffusion process with the probability density of seed trajectories* $f(x, t|\xi_0, t_0)$ *in time-space satisfying the Fokker-Planck equation*

$$\frac{\partial f(x,t)}{\partial t} = -\frac{\partial}{\partial x}\left(f(x,t)\cdot a(x)\right) + \frac{1}{2}\frac{\partial^2}{\partial x^2}\left(f(x,t)\cdot b(x)\right) \tag{4.7.1}$$

with initial conditions $f(x, t_0) = \sigma(x - \xi_0)$ *and space-dependent jump coefficients*

$$a(x) = \lim_{\Delta t \to 0} \frac{\langle x_{t+\Delta t} - x|x\rangle}{\Delta t} = K\lambda_t \int_0^1 (x-\xi)e^{-\frac{(x-\xi)^2}{s^2}} \cdot \frac{N}{\epsilon + (\xi - \xi_0)^2} d\xi \tag{4.7.2}$$

$$b(x) = \lim_{\Delta t \to 0} \frac{\langle (x_{t+\Delta t} - x)^2|x\rangle}{\Delta t} = K^2\lambda_t \int_0^1 (x-\xi)^2 e^{-2\frac{(x-\xi)^2}{s^2}} \cdot \frac{N}{\epsilon + (\xi - \xi_0)^2} d\xi, \tag{4.7.3}$$

where

1. $\xi_0 \in (0, 1)$ *is the initial position of a seed,*

2. $p(\xi|x) = \frac{N}{\epsilon+(\xi-\xi_0)^2}$ *is the probability density of transition from* x *to a new state* $x' = x + dx$,

3. $N = \frac{\sqrt{\epsilon}}{\arctan\frac{1-\xi_0}{\sqrt{\epsilon}} - \arctan\frac{-\xi_0}{\sqrt{\epsilon}}}$ *is a normalizing constant.*

The Fokker-Planck equation describes the evolution of the probability density $f(x,t|\xi_0,t_0)$ of finding a seed at the coordinate x at a time instant t. For simplicity of computations and for approximation of the statistical behavior of the seed in time-space while it has not reached the boundaries of a grown organism absorbing boundary conditions can be used.

Corollary 4.7.2. *The Fokker-Planck equation for the diffusion approximation of 1D GRID model given in Theorem 4.7.1 is statistically equivalent to the following nonlinear Langevin stochastic differential equation of seed motion* $\{x(t) : t \geq t_0\}$ *in Stratonovich sense*

$$dx(t) = \alpha_1(x)dt + \alpha_2(x)dW(t), \tag{4.7.4}$$

where $dW(t)$ *is a Wiener process increment and* $\alpha_1(x)$ *and* $\alpha_2(x)$ *are the drift and diffusion coefficients expressed in terms of the FPE jump coefficients* $a(x)$ *and* $b(x)$

$$\alpha_1(x,t) = a(x,t) - \frac{1}{4}\frac{\partial}{\partial x}b(x,t), \;\; \alpha_2(x,t) = \sqrt{b(x,t)}. \tag{4.7.5}$$

Corollary 4.7.3. *Consider a finite difference approximation of the diffusion 1D GRID model given by theorem 4.7.1. For a sufficiently large range of influence* s *the probability distribution of seed trajectories concentrated near the initial seed coordinate* ξ_0 *evolves into the bimodal probability distribution symmetric with respect to* ξ_0 *as time progresses. For a small range of influence comparable to the size of seed spacing* $\Delta\xi$, $s = O(\Delta\xi)$, *the probability density of seed trajectories slowly diffuses from the initial seed position* ξ_0 *in time-space with space-dependent dispersion rate*

$$b(x) = K^2\lambda_t \int_0^1 (x-\xi)^2 e^{-2\frac{(x-\xi)^2}{s^2}} \cdot \frac{N}{\epsilon+(\xi-\xi_0)^2} d\xi$$

peaked at the initial seed coordinate ξ_0.

Theorem 4.7.4. *Consider the diffusion 1D GRID model with the uniform probability of seed placements in the absolute space of 1D organism* $(0,1)$ *independent of time. Then the seeds are activated with equal probability in an interval* $(0,1)$ *at all times and the transition probability density is constant*

$$p(\xi,t|x) = p(\xi) = \begin{cases} 1 & \textit{if } \xi \in (0,1) \\ 0 & \textit{otherwise.} \end{cases} \tag{4.7.6}$$

This implies the following formulae of the first and second jump moments

$$a(x) = \int_0^1 (x-\xi)Ke^{-\frac{(x-\xi)^2}{s^2}} d\xi = K\frac{s^2}{2}\left[e^{-\frac{(x-1)^2}{s^2}} - e^{-\frac{x^2}{s^2}}\right] \tag{4.7.7}$$

$$b(x) = \int_0^1 (x-\xi)^2 K^2 e^{-2\frac{(x-\xi)^2}{s^2}} d\xi. \tag{4.7.8}$$

Then the solution to the corresponding Fokker-Planck equation approximates short-time statistical behavior of seed trajectories.

For consistency of time-dependent solutions with stationary solutions of the FPE the reflecting boundary conditions can be imposed for seed trajectories emanating from the middle point of the initial organism. Such trajectories end at either of the boundary points with equal equilibrium probability. For seed paths starting close to the boundary a constant probability flux allows construction of stationary probability distribution consistent with observations of long-time seed trajectories. The equilibrium probability represents a higher concentration of trajectory "ends" at the left boundary if the probability flux is negative and at the right boundary if it is positive.

Theorem 4.7.5. *Without loss of generality, let the grown organism Ω in the limit $t \to \infty$ occupy $(0, 1)$ and the s parameter be sufficiently large. The general solution to the stationary Fokker-Planck equation for the diffusion 1D GRID model described in Theorem 4.7.1*

$$\frac{\partial}{\partial x}(b(x) f_s(x)) - 2a(x) f_s(x) = -2G$$

is given by

$$f_s(x) = \frac{C}{b(x)} e^{2\int_0^x \frac{a(y)}{b(y)} dy} - \frac{2G}{b(x)} \int_0^x e^{2\int_y^x \frac{a(t)}{b(t)} dt} dy, \text{ where } 0 < y < x \tag{4.7.9}$$

and $G = const$ is the probability flux.

The stationary solution $f_s(x)$ depends on the initial position of a seed ξ_0. For the middle seed the reflecting boundary conditions $G = 0$ allow equal probability mass at the boundary points. For seed trajectories emanating from points close to the boundaries a constant probability flux allows a higher distribution concentration at the left boundary if the flux is negative or at the right boundary if the flux is positive. That is,

$$G = \begin{cases} C_1 > 0 & \text{if } \xi_0 > 0.5 \\ C_2 < 0 & \text{if } \xi_0 < 0.5, \end{cases} \tag{4.7.10}$$

where C_1 and C_2 are constants.

It is straightforward to define the FPE for the two-dimensional diffusion GRID model. Given a 2D GRID model of growth of an organism occupying a compact space $\Omega(t) \in \Re^2$ at a time t the position of a seed is described by a two-dimensional random vector $\vec{x}(t) = (x_1(t), x_2(t))$ in a two-dimensional domain $\Omega(t)$. In this case the probability density $p(\vec{\xi}|\vec{x})$ characterizes the probability of transition from the fixed position $\vec{x}$ to $\vec{x} + \Delta\vec{x}$ in time interval Δt. According to the properties of the Poisson process of seed placements in 2D domain the displacement vector $\Delta\vec{x} = \vec{x}(t + \Delta t) - \vec{x}(t)$ conditioned on $\vec{x}(t)$ takes the following random values

$$\Delta\vec{x} = \begin{cases} y^{\vec{\xi}}(\vec{x}) & \text{with probability } \lambda_t \Delta t \frac{N}{\epsilon + \|\vec{\xi} - \vec{\xi}_0\|^2} + o(\Delta t) \\ \sum_{i=1}^{N_{\Delta t}} y^{\vec{\xi}_{\sigma_i}}(\vec{x}_{t_{i-1}}) & \text{with probability } o(\Delta t) \\ 0 & \text{with probability } 1 - \lambda_t \Delta t \frac{N}{\epsilon + \|\vec{\xi} - \vec{\xi}_0\|^2} + o(\Delta t), \end{cases} \tag{4.7.11}$$

where the GRID elementary displacement due to a single seed activation is given by

$$y^{\vec{\xi}}(\vec{x}) = \begin{pmatrix} (x_1 - \xi_1)K \exp\{-\frac{\|\vec{x}-\vec{\xi}\|^2}{s^2}\} \\ (x_2 - \xi_2)K \exp\{-\frac{\|\vec{x}-\vec{\xi}\|^2}{s^2}\}. \end{pmatrix} \tag{4.7.12}$$

Repeating the same procedure for the FPE derivation as in one-dimensional case we arrive at the following result.

Theorem 4.7.6 (Two-dimensional Fokker-Planck equation.). *Consider the diffusion two-dimensional isotropic GRID model of growth of an organism* $\Omega(t) \subset \Re^2$ *with the intensity of seed activations per unit time* λ_t *(not necessarily constant) and the Darcyan coordinate system* $\{x(\xi, t) : x \in \Omega(t), \xi \in \Xi\}$, *where* Ξ *is a continuous Darcyan space of seeds.*
The corresponding Fokker-Planck equation describing evolution of the probability density $f(\vec{x}, t|\vec{\xi_0}, t_0)$ *of seed trajectories in* $\Omega(t) \times [t_0, T]$ *takes the form*

$$\frac{\partial}{\partial} f(\vec{x}, t) = -\sum_{i=1}^{2} \frac{\partial}{\partial x_i}[\vec{a}(\vec{x}, t) f(\vec{x}, t)] + \frac{1}{2} \sum_{i,j=1}^{2} \frac{\partial^2}{\partial x_i \partial x_j}[b_{ij}(\vec{x}, t) f(\vec{x}, t)] \tag{4.7.13}$$

and satisfies initial conditions

$$f(\vec{x}, t_0|\vec{\xi_0}, t_0) = \delta(x_1 - \xi_{01})\delta(x_2 - \xi_{02}). \tag{4.7.14}$$

The coefficients of the Fokker-Planck equation $\vec{a}(\vec{x}, t) = (a_1(\vec{x}, t), a_2(\vec{x}, t))$ *and* $\vec{b}(\vec{x}, t) = (b_{11}(\vec{x}, t), b_{12}(\vec{x}, t), b_{22}(\vec{x}, t))$ *are defined by*

$$a_i(\vec{x}, t) = \lim_{\Delta t \to 0} \frac{1}{\Delta t} \langle \Delta \vec{x} | \vec{x} \rangle = \tag{4.7.15}$$

$$\lambda_t \int_0^1 (x_i - \xi_i) K \exp\left(-\frac{\|\vec{x} - \vec{\xi}\|^2}{s^2}\right) \frac{N}{\epsilon + \|\vec{\xi} - \vec{\xi_0}\|^2} d\vec{\xi},$$

$$b_{ij}(\vec{x}, t) = \lim_{\Delta t \to 0} \frac{1}{\Delta t} \langle \Delta x_i \Delta x_j | \vec{x} \rangle = \tag{4.7.16}$$

$$\lambda_t \int_0^1 (x_i - \xi_i)(x_j - \xi_j) K^2 \exp\left(-2\frac{\|\vec{x} - \vec{\xi}\|^2}{s^2}\right) \frac{N}{\epsilon + \|\vec{\xi} - \vec{\xi_0}\|^2} d\vec{\xi}.$$

Note that the probability density $f(\vec{x}, t)$ satisfying the FPE (4.7.13) exists for the process $\{\vec{x}(t) : t \geq t_0\}$ if the quadratic form $\sum_{i,j=1}^{2} b_{ij}(\vec{x}, t) x_i x_j$ is nonnegative-definite. Questions of existence and finding two-dimensional time-dependent and independent solutions to the FPE (4.7.13) are not addressed in this manuscript. Having gained insights into the nature of the probability density evolution produced by the 1D diffusion GRID model and the effects of boundary conditions on the equilibrium distribution we expect qualitatively the same statistical behavior of seed trajectories in 3D space $\{\Omega(t) \subset \Re^2\} \times [t_0, \infty)$.

We now outline some important applications of the Fokker-Planck equation that are left for the future development of GRID analysis of growth. The macroscopic equation approximating growth of a 1D or 2D organism as motion of a discretized compact continuum $\langle x(\xi,t)\rangle$ in the average sense can be deduced from the FPE by multiplying equation (4.5.1) or (4.7.13) by x and integrating over x. For example, in 1D case the evolution equation for the mean position of an individual seed in absolute coordinates x is given by

$$\frac{d}{dt}\langle x(t)\rangle = -\int_0^1 x\frac{\partial}{\partial x}\left(f(x,t)\cdot a(x)\right)dx + \int_0^1 x\frac{1}{2}\frac{\partial^2}{\partial^2 x}\left(f(x,t)\cdot b(x)\right)dx \tag{4.7.17}$$

with initial condition $\langle x(t_0)\rangle = \xi_0$. If we assume that $f(x,t)$ satisfies absorbing and reflecting boundary conditions then equation (4.7.17) takes its simplest form

$$\frac{d}{dt}\langle x(t)\rangle = \langle a(x(t))\rangle . \tag{4.7.18}$$

Multiplying the Fokker-Planck equation by x^2 we can also deduce the evolution equation for the variance $\langle\langle x^2(t)\rangle\rangle = \langle x^2(t)\rangle - \langle x(t)\rangle^2$. Using

$$\frac{\partial}{\partial t}\left\langle x^2\right\rangle = \frac{\partial}{\partial t}\left(\int_0^1 xf(x,t)dx\right)^2 = 2\left\langle x(t)\right\rangle\int_0^1 x\frac{\partial}{\partial t}f(x,t)dx \tag{4.7.19}$$

and assuming that $f(1,t_0) = f(0,t_0) = \frac{\partial}{\partial x}f(1,t_0) = \frac{\partial}{\partial x}f(0,t_0) = 0$ we obtain the following equation for the variance of seed trajectories

$$\frac{d}{dt}\langle\langle x(t)\rangle\rangle = \langle b(x,t)\rangle + 2\left\langle [x(t) - \langle x(t)\rangle]a(x(t))\right\rangle \tag{4.7.20}$$

subject to the initial condition $\langle\langle x(t_0)\rangle\rangle = 0$.

The right-hand side of (4.7.17) represents the average growth rate that varies within the domain of an organism Ω. This is due to dependency of the FPE coefficients on the initial seed coordinate. The discretized integro-differential equation (4.7.17) applied to each of the mesh points $\{x(\xi_i,t), 1\le i\le n\}$ leads to a system of autonomous differential equations describing average growth trajectories of seeds $x(\xi_i,t)$ that constitute the average motion of a growing organism. We can only claim that such system describes the average growth pattern (at least approximately) if seeds move independently from one another. To ensure independent seed motion we have to choose the range of influence s parameter comparable to the mesh size Δx, $s = O(\Delta x)$, so that the neighbouring seeds do not interact with one another to a greater extent.

If independency of seed motions is not maintained then the macroscopic growth equation (4.7.18) for the whole organism Ω cannot be deduced from the Fokker-Planck equation stated in Theorem 4.7.1. Taking into account seed configuration $\{x_1(t), x_2(t),\dots,x_n(t)\}$ of Ω that is a n-dimensional stochastic process $\{\vec{x}(t), t\ge t_0\}$, the average position of a particular seed at fixed time t is evaluated as follows

$$\langle x_i(t)\rangle = \int_{\Omega^n} x_i(t)f(x_1(t),x_2(t),\dots,x_{i-1}(t),x_i(t),x_{i+1}(t),\dots,x_n(t))d^n\vec{x}.$$

If only neighboring seeds $x_{i-1}(t)$,$x_i(t)$ and $x_{i+1}(t)$ interact then the average position of $x_i(t)$ simplifies to $\langle x_i(t)\rangle = \int_{\Omega^3} x_i(t) f(x_{i-1}(t), x_i(t), x_{i+1}(t)) dx_i dx_{i+1} dx_{i-1}$. But the joint probability density $f(x_{i-1}(t), x_i(t), x_{i+1}(t))$ is not known since the Fokker-Planck equation gives the evolution of the singlet probability density $f(x_i, t)$ conditioned by the initial distribution.

Therefore, only under the condition that seed positions $x_i(t), i \in \{1, 2, \ldots, n\}$ are independent from one another for all times can we claim that the equations for the mean and variance of seed trajectories become meaningful macroscopic equations of growth. In 2D they have a power to predict the average structure and shape of the organism in a finite time interval $[t_0, T]$ given the initial Darcyan coordinate system $\vec{x}(\vec{\xi}, t_0)$ and a certain spatial distribution of seeds $\vec{\xi} \in \Xi$.

Part II

2D GRID Macroscopic Growth Law and Its Application to Image Inference

Chapter 5

2D GRID macroscopic growth law

5.1 Derivation of "Thermodynamic limit" equation

Motivation for the GRID macroscopic growth law comes from developmental biology of multicellular organisms. The phenomenon of biological growth manifests itself in a time-varying deformation of shape and internal structure of a developing organism. A multitude of elementary biological events such as cell divisions and/or enlargements, cell deaths and cell movements results in visible shape and interior changes of the growing multicellular organism and its suborganisms seen in images collected over time.

It seems natural to represent an underlying biological transformation on a large time scale by a diffeomorphic flow that evolves in time as a collective effect of a large number of cell decisions. The diffeomorphic property of the transformation preserves integrity of the deforming Darcyan curvilinear grid representing the growing multicellular structure as it does not allow local overlaps. To generate such flows U. Grenander proposed the "thermodynamic limit" equation [29], a deterministic integro-differential equation emphasizing dependency of the solution on such GRID variables as the Poisson intensity of cell decisions and the relative rate of expansion/contraction $k(\xi_{seed})$. In this section we derive the "thermodynamic limit" equation referred to as the GRID macroscopic growth law.

The purpose of the thermodynamic limit equation is to approximate the average growth-induced deformation pattern of an organism $\Omega(t)$ represented by the Darcyan coordinate system $x(\xi, t)$ given a random displacement field $\Delta x(\xi, t)$ at a time t. A particular realization of a random GRID transformation due to a particular seed activation at the location ξ_{seed} results in the displacement field value $\Delta x^{\xi_{seed}}(\xi, t)$. By the Law of Large Numbers, under the certain conditions on the random field $\Delta x(\xi, t)$, as the number of samples of $\Delta x(\xi, t)$ increases, the sample mean approaches the expected value at a fixed time t. Thus, we can evaluate the average growth increment at each time instant t as the mean value of the displacement field taken over an infinite number of seed contributions. We first derive the macroscopic growth equation using the Law of Large Numbers.

According to the isotropic GRID model the displacement field due to a single seed contribution, ξ_{seed}, is modeled as an exponential decay of the radial distance from the seed.

$$\begin{aligned}\Delta^{\xi_{seed}}x(\xi,t) =& k(\xi_{seed},t)\cdot(x(\xi,t)-x(\xi_{seed},t))\cdot\\ & \exp\left(-\frac{\|x(\xi,t)-x(\xi_{seed},t)\|^2}{s(x(\xi_{seed},t))^2}\right).\end{aligned} \tag{5.1.1}$$

Here,

1. $\{x(\xi,t)=(x_1(\xi,t),x_2(\xi,t))\in\Omega(t)\}$ with $\xi=(\xi_1,\xi_2)\in\Xi$ is a curvilinear Darcyan coordinate system of the organism's domain $\Omega(t)$ or the X-field $x(\xi,t)\in\Re^2$.

2. Ξ is the Darcyan space of biological coordinates of cell decisions. Given the Darcyan grid with n radial and m angular coordinate curves the Ξ-space is a product of two finite sets of integers $\{1,2,3,...,n\}$ and $\{1,2,3,...,m\}$.

3. $k(\xi_{seed},t)$ is the relative rate of expansion/contraction independent of angle or direction of growth/decay. $0<k(\xi,t)<1$ implies expansion of the small area around $x(\xi,t)$ and $-1<k(\xi,t)<0$ implies local contraction. So, small areas centered at seeds grow or decay isotropically.

4. $s(x(\xi_{seed},t))$ is the radius of influence of the seed. In Grenander's paper [29], this quantity is denoted as “step”. Since $x(\xi,t)$ provides a computational grid with non-uniformly distributed nodes, the s parameter should be proportional to the Jacobian of the transformation $x(t)=x(\xi,t)$.
   Here, we set $s(x(\xi,t))=\left|\frac{\partial(x_1,x_2)}{\partial(\xi_1,\xi_2)}\right|$ (see Fig.5.1.1).
   In this way we compensate for the non-uniformity of grid quadrilaterals and establish independency of displacements in the sense that they don't overlap when they occur simultaneously in the neighborhoods of seeds located at the nodes of the Darcyan grid.

For a fixed seed $x(\xi_{seed},t)$ we define the following translation-invariant diffeomorphism $\theta(x(\xi,t)-x(\xi_{seed},t)):\Re^2\to\Re^2$.

$$\theta(x(\xi,t)-x(\xi_{seed},t))=(x(\xi,t)-x(\xi_{seed},t))\exp\left(-\frac{\|x(\xi,t)-x(\xi_{seed},t)\|^2}{s(x(\xi_{seed},t))^2}\right) \tag{5.1.2}$$

At a time t the points $x(\xi,t)$ of the X-field move relative to the location of that seed. The displacement field given in (5.1.1) can be rewritten in terms of θ-function as follows

$$\Delta^{\xi_{seed}}x(\xi,t)=k(\xi_{seed},t)\cdot\theta(x(\xi,t)-x(\xi_{seed},t))$$

According to the stochastic version of the GRID model for growth on a fine

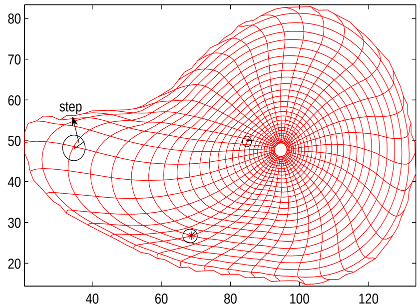

Figure 5.1.1: Illustration of the s parameter as a function defined on the computational Darcyan grid of the Drosophila wing disc.

time-scale, seeds are activated within the growing organism as an inhomogeneous space-time Poisson point process (see Appendix A, [16]) with the intensity parameter $\Lambda(\xi, t) = \lambda_t \cdot \lambda_x(\xi)$. For a fixed time t we have an ensemble of all possible displacement fields $\Delta^{\xi_{seed}}(x(\xi, t))$ with the spatial probability density of seeds ξ_{seed} in the X-field $p_x(\xi) = \frac{\lambda_x(\xi_{seed})}{\int_X \lambda_x(\xi_{seed})dx}$. Suppose that we take samples from this probability distribution and record each ith observation of the displacement field $\Delta_i^{\xi_{seed_i}}(x(\xi, t))$ corresponding to the seed sample ξ_{seed_i}. By the Law of Large Numbers, as the number of observations increases, the sample average,

$$\frac{\sum_{i=1}^{n} \Delta_i^{\xi_{seed_i}}(x(\xi, t))}{n}, \tag{5.1.3}$$

approaches the expected value or the mean of the displacement field $\Delta^{\xi_{seed}}(x(\xi, t))$. Thus, letting a number of cell decisions (seeds) n that occur randomly and independently in the growing organism's domain become arbitrarily large at each time instant we arrive at the mean of the growth increment given by

$$\lim_{n \to \infty} \frac{\sum_{i=1}^{n} \Delta_i^{\xi_{seed_i}}(x(\xi, t))}{n} = \langle \Delta x(\xi, t) \rangle \, . \tag{5.1.4}$$

Note that on the right-hand side the averaging operation $\langle \cdot \rangle$ is taken over all seed contributions $\xi_{seed_i}, i = 1, 2, \dots, \infty$. It cancels out the randomness of seed placements in Ξ-space.

Since the spatial-temporal probability density of seeds induces the probability measure on the displacement field $\Delta^{\xi_{seed}}(x(\xi, t))$, a deterministic function of a random variable ξ_{seed}, we have the following evaluation of the mean growth increment

$$\begin{aligned} \langle \Delta x(\xi, t) \rangle &= \int_{\xi_{seed} \in \Xi} \Delta^{\xi_{seed}} x(\xi, t) F(d\xi_{seed}) \\ &= \int_{\xi_{seed} \in \Xi} k(\xi_{seed}, t) \cdot \theta(x(\xi, t) - x(\xi_{seed}, t)) \cdot p_x(\xi_{seed}) d\xi_{seed}, \end{aligned} \tag{5.1.5}$$

where $p_x(\xi_{seed}, t)$ is the normalized Poisson intensity of cell decisions expressed in absolute space coordinates x that depend on Darcyan coordinates ξ of local gene activity cites.

Remark 5.1.1. *The evaluation of the mean growth displacement field* (5.1.5) *is valid only if the displacements of the seeds $\Delta x(\xi_{1_i}, \xi_{2_j}, t)$ of the organism $\Omega \subset \Re^2$ (the nodes of the Darcyan computational grid) are uncorrelated. Evolution of an organism $\Omega(t)$ represented by the Darcyan coordinate grid of size $n \times m$ is a high-dimensional Poisson-driven stochastic process in space-time characterized by an $n \times m$-dimensional probability density $p(x(\xi_{1_1}, \xi_{2_1}, t), x(\xi_{1_1}, \xi_{2_2}, t), \ldots, x(\xi_{1_n}, \xi_{2_m}, t))$. If the seed trajectories interact, or in other words, if their displacements intersect, then the joint probability density of interacting seed displacements should be used for computing the average value of each displacement field component $\Delta x(\xi_{1_i}, \xi_{2_j}, t)$.*

Since the dependency on the space variable ξ_{seed} has been integrated out, our spatial-temporal Poisson process of seed placements simplifies to a temporal Poisson process driving Markov position process $\{x(\xi, t) : t \geq t_0\}$,

$$x(\xi, t) = x(\xi, t_0) + \int_{t_0}^{t} \overline{\Delta x}(\xi, t)\mu(dt), \tag{5.1.6}$$

where $\mu(dt)$ is an inhomogeneous temporal counting Poisson process (see Appendix A) and $\overline{\Delta x}(\xi, t)$ denotes the mean growth increment given by (5.1.5). The Poisson process $\mu(dt)$ induces the following probabilities on the displacement field $\Delta x_t(\xi) = x(\xi, t + \Delta t) - x(\xi, t)$ in a small time interval Δt,

$$Pr\{\Delta x(\xi, t) = \overline{\Delta x}(\xi, t)\} = \int_{t}^{t+\Delta t} \lambda_{t'} dt' + o(\Delta t), \tag{5.1.7}$$

$$Pr\{\Delta x(\xi, t) = 0\} = 1 - \int_{t}^{t+\Delta t} \lambda_{t'} dt' + o(\Delta t), \tag{5.1.8}$$

$$Pr\{\Delta x(\xi, t) = \sum_{i=1}^{\mu(\Delta t)} \overline{\Delta x}(\xi, t_i)\} = o(\Delta t). \tag{5.1.9}$$

Then the expected value of $\Delta x(\xi, t)$ in time interval Δt becomes

$$\begin{aligned} \langle \Delta x(\xi, t)\rangle = \overline{\Delta x}(\xi, t) \cdot \left(\int_{t}^{t+\Delta t} \lambda_{t'} dt' + o(\Delta t)\right) \\ + \left(\sum_{i=1}^{\mu(\Delta t)} \overline{\Delta x}(\xi, t_i)\right) \cdot o(\Delta t). \end{aligned} \tag{5.1.10}$$

Dividing both sides of the equation (5.1.10) by Δt and letting $\Delta t \to 0$ we obtain the mean velocity field

$$\overline{V}(x(\xi, t), t) = \lim_{\Delta t \to 0} \frac{\langle \Delta x(\xi, t)\rangle}{\Delta t} = \lambda_t \overline{\Delta x}(\xi, t). \tag{5.1.11}$$

Now, in order to compute the average growth pattern of an organism $\Omega(t)$ given initially by the Darcyan coordinate system $x_0(\xi)$ we simply employ the ordinary differential continuum mechanics equation of motion,

$$\frac{\partial}{\partial t} x(\xi, t) = \overline{V}(x(\xi, t), t), \tag{5.1.12}$$

subject to the initial condition $x(\xi, t_0) = x_0(\xi)$. Substituting expression (5.1.5) for the mean growth increment to the right hand side of the equation (5.1.11) we obtain the macroscopic growth integro-differential equation

$$\begin{aligned}\frac{\partial x(\xi, t)}{\partial t} &= \lambda_t \int_{\xi_{seed} \in \Xi} \Delta^{\xi_{seed}} x(\xi, t) F(d\xi_{seed}) \\ &= \lambda_t \int_{\xi_{seed} \in \Xi} k(\xi_{seed}, t) \cdot \theta(x(\xi, t) - x(\xi_{seed}, t)) \cdot p_x(\xi_{seed}) d\xi_{seed}\end{aligned} \tag{5.1.13}$$

with initial conditions $x(\xi, t_0) = x_0(\xi)$ and the probability density of cell decisions in the X-field $p_x(\xi_{seed})$ evaluated at seed locations. The preceding discussion now leads to the following rigorous statement of the GRID macroscopic growth law

Theorem 5.1.2. *Consider an organism* $\Omega(t) \subset \Re^m$, $m = 1, 2$, *whose domain is represented by the Darcyan coordinate grid* $x(\xi, t) = \{x(\xi_i, t) : i = 1, 2, \ldots, N\}$. *For a continuous-time stochastic GRID model in the form of an* N*-dimensional Poisson driven process with*

(i) countable Darcyan space of seeds Ξ,

(ii) the Poisson intensity of seed placements $\Lambda(\xi_{seed}, t) = \lambda_t \cdot p_x(\xi_{seed})$ *in time-space* $[t_0, \infty) \times \Re^m$,

(iii) seeds $x(\xi_{seed}, t)$ *activated randomly and independently from one another with the range of influence* $s(x(\xi_{seed}, t)) = \left|\frac{\partial x}{\partial \xi}\right|$ *defined by the Jacobian of the transformation* $x(t) = x(\xi, t)$,

the average diffeomorphic flow $x(\xi, t)$ *at any time instant* t *satisfies the GRID macroscopic growth integro-differential equation*

$$\frac{\partial x(\xi, t)}{\partial t} = \lambda_t \int_{\xi_{seed} \in \Xi} k(\xi_{seed}, t) \cdot (x(\xi, t) - x(\xi_{seed}, t)) e^{-\frac{\|x(\xi, t) - x(\xi_{seed}, t)\|^2}{s(x(\xi_{seed}, t))^2}} dPr\{\xi = \xi_{seed}\}, \tag{5.1.14}$$

subject to the initial condition $x(\xi, t_0) = x_0(\xi)$.

The range of influence comparable to the variable grid size $\Delta x(t) = \left|\frac{\partial x}{\partial \xi}\right| \Delta\xi$, *where* $\Delta\xi$ *is a unit volume in continuous Darcyan space* $\Xi \subset \Re^m$, $m = 1, 2$, *approximately maintains independency of the neighboring seed displacements.*

All in all, the macroscopic growth equation approximates observed growth in instantaneous time as a result of an infinite number of cell decisions that occur at random in the growing organism's domain. When the GRID variables such as the Poisson intensity $\Lambda(\xi, t)$ and the amplitude of growth $k(\xi, t)$ are known this equation predicts a typical growth pattern in the average sense.

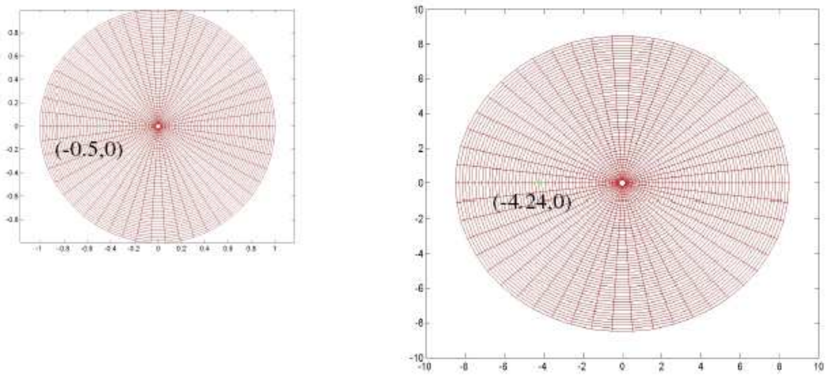

Figure 5.2.1: Example of macroscopic growth with constant Poisson intensity and constant amplitude of growth $k = 0.003$. Result: the unit disc grows homogeneously into a larger disc.

5.2 Illustrations of 2D GRID macroscopic growth patterns

For an intuitive understanding of this equation we give a couple of synthetic examples of a macroscopic growth of the organism $\Omega(t) \subset \Re^2$ in the initial form of a unit disc. We start with a simple example of an isotropic growth with the Poisson intensity $\Lambda(\xi, t) = const$ in space and time and constant amplitude of growth $k = 0.003$. In this setup the macroscopic growth law leads to an autonomous system of ordinary differential equations

$$\frac{\partial}{\partial t} x(\xi = \xi_{seed_j}, t) = \sum_{i=1}^{N} k \cdot \theta(x(\xi = \xi_{seed_j}, t) - x(\xi_{seed_i}, t)) \cdot F_i, j = 1, 2, \ldots, N, \quad (5.2.1)$$

where F_i is a bounded measure putting a unit mass on N seeds located at the polar grid nodes $x(\xi_i, t)$ at a time t. Using the Matlab script “macroscopic.m” (see Appendix F) we compute the solution to the system of differential equations (5.2.1) in the form of the macroscopic growth transformation $x(\xi, t)$. At each time instant $t = j$, $(j = 1, \ldots, 10)$, a realization of (5.2.1) calculates the average displacement of seeds in $\Omega(t)$ as a collective deformation effect of all growth seeds. Shown in the left panel of Figure 5.2.1 is an initial organism represented by the Darcyan grid in the form of the polar coordinate system $x_0(\xi_1, \xi_2) = x_0(r, \phi)$. A grown organism generated by a sequence of 10 transformations $x(\xi, t_i)$, $i = 1, 2, \ldots, 10$ applied to its initial Darcyan grid is shown in the right panel of Figure 5.2.1. For instance, it predicts that the location of the point with initial coordinates $(-0.5, 0)$ will be $(-4.24, 0)$.

In another example we consider growth of an organism with space-dependent distribution of seeds $p_x(\xi)$ and constant intensity $\lambda_t = const$ of seed placements in time. Initially, the Darcyan grid is the polar grid that deforms as the disc grows. The Poisson intensity $\lambda_x(\xi)$ (normalized) is the probability mass function assigned

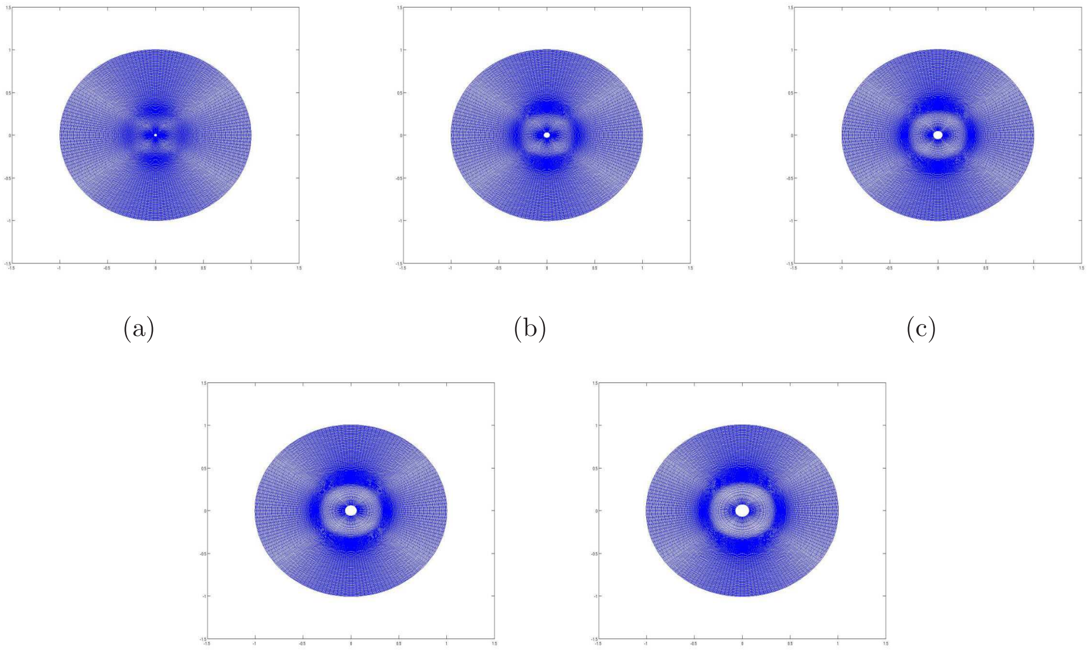

(a) (b) (c)

(d) (e)

Figure 5.2.2: (a-e) Example of macroscopic growth with space-dependent Poisson intensity. The Poisson intensity is the probability mass function which decreases with respect to radial distance. Result: the central part grows faster.

to all the nodes of the Darcyan coordinate grid. The center of mass is located at the origin of the coordinate system and the probability mass decays radially from it (see Fig.3.1.3). With the preassigned Poisson intensity of cell divisions and constant amplitude of growth $k = 2$ we have run a few realizations of the system of macroscopic growth equations on the Darcyan grid of the disc implementing Matlab script “macroscopic.m”. As a result of a higher intensity of cell divisions near the origin of the coordinate system, organism’s central part grows faster than the rest of it (see Fig.5.2.2). These simple experiments demonstrate an overall effect of the space-dependent intensity of seed placements on the interior structure of the growing organism.

5.3 Macroscopic growth law in the operator form

We now develop a practical version of the macroscopic growth equation suitable for analysis and applications that will follow below. To simplify the statement of the macroscopic growth law

$$\frac{\partial x(\xi,t)}{\partial t} = \lambda_t \int_{\xi_{seed}\in\Xi} k(\xi_{seed},t)\cdot(x(\xi,t)-x(\xi_{seed},t))e^{-\frac{\|x(\xi,t)-x(\xi_{seed},t)\|^2}{s(x(\xi_{seed},t))^2}} p_x(\xi_{seed})d\xi_{seed}, \tag{5.3.1}$$

U. Grenander introduced a bounded function, $a(\xi_{seed}, t)$, called the *growth magnitude* [29],

$$a(\xi_{seed}, t) = k(\xi_{seed}, t)\lambda_t p_x(\xi_{seed}) = k(\xi_{seed}, t)\lambda_t \frac{p(\xi_{seed})}{J(x(\xi_{seed}, t))}, \tag{5.3.2}$$

where $J(x(\xi_{seed}, t))$ is the Jacobian of the transformation $x(t) = x(\xi_{seed}, t)$ at a time t. Recall that

$$\begin{aligned} p_x(\xi_{seed}) &= \frac{\lambda_x(\xi_{seed})}{\int_X \lambda_x(\xi_{seed})dx} = \frac{\lambda_x(\xi_{seed})}{\int_\Xi \frac{\lambda(\xi_{seed})}{J(x(\xi_{seed}))} J(x(\xi_{seed}))d\xi_{seed}} \\ &= \frac{\lambda(\xi_{seed})}{J(x(\xi_{seed}))} \frac{1}{\int_\Xi \lambda(\xi_{seed})d\xi_{seed}} = \frac{p(\xi_{seed})}{J(x(\xi_{seed}, t))}. \end{aligned} \tag{5.3.3}$$

Indeed, with only one GRID parameter characterizing macroscopic growth, equation (5.3.1) becomes

$$\frac{\partial x(\xi, t)}{\partial t} = \int_{\xi_{seed}\in\Xi} (x(\xi, t) - x(\xi_{seed}, t))e^{-\frac{\|x(\xi,t)-x(\xi_{seed},t)\|^2}{s(x(\xi_{seed},t))^2}} a(\xi_{seed}, t)d\xi_{seed}. \tag{5.3.4}$$

However, such a simplified macroscopic growth law formulation hides the important growth parameter $\lambda_t \cdot p(\xi_{seed})$ within itself. It represents the intrinsic intensity of biological events in Darcyan space Ξ and time $[t_0, \infty)$ determined by the genetic program of an organism's development. Setting

$$\lambda_t \cdot p(\xi_{seed}) = \lambda(\xi_{seed}, t), \tag{5.3.5}$$

we would like to establish the dependency of the flow $x(\xi, t)$ on the intensity of cell decisions $\lambda(\xi_{seed}, t)$.

We distinguish between two types of growth, namely, growth with uniform distribution of elementary events and growth with non-uniform distribution of elementary events in space-time. If the intensity of biological events $\lambda(\xi, t) = const$ then the macroscopic growth equation is formulated in terms of k-function as follows from (5.3.1) and (5.3.3)

$$\frac{\partial x(\xi, t)}{\partial t} = \int_{\xi_{seed}\in\Xi} k(\xi_{seed}, t)\cdot(x(\xi, t) - x(\xi_{seed}, t))e^{-\frac{\|x(\xi,t)-x(\xi_{seed},t)\|^2}{s(x(\xi_{seed},t))^2}} \frac{1}{J(x(\xi_{seed}, t))} d\xi_{seed}. \tag{5.3.6}$$

In the latter case, since there are seemingly many biological events contributing to growth, it is reasonable to approximate seed deformation effects by the local rate of expansion/contraction $k(\xi_{seed}, t)$ that is constant in magnitude and varying in sign throughout the X-field. That is,

$$k(\xi_{seed}, t) = sgn(k) \cdot const.$$

For convenience, we let $k(\xi_{seed}, t) \in \{-1, 1\}$, letting λ absorb this constant for simplicity. Then the sign of $\lambda(\xi_{seed}, t)$ will define the nature of the seed ξ_{seed} (growth or decay). The Poisson intensity of events in the Darcyan space is $|\lambda(\xi_{seed}, t)|$ and the growth magnitude becomes

$$a(\xi_{seed}, t) = \frac{\lambda(\xi_{seed}, t)}{J(x(\xi_{seed}, t))}. \tag{5.3.7}$$

We reformulate the macroscopic growth equation with respect to the λ-field

$$\frac{\partial x(\xi, t)}{\partial t} = \int_{\xi_{seed} \in \Xi} \theta(x(\xi, t) - x(\xi_{seed}, t)) \cdot \frac{\lambda(\xi_{seed}, t)}{J(x(\xi_{seed}, t))} d\xi_{seed}. \tag{5.3.8}$$

Equation 5.3.8 is suitable for characterization of growth patterns with non-uniform intensity of elementary cell decisions.

The macroscopic growth equation (5.3.8) can be rewritten in the operator form as follows

$$\begin{aligned}\frac{\partial x(\xi, t)}{\partial t} &= (\Theta\lambda)(x(\xi, t)) \\ &= \int_{\xi_{seed} \in \Xi} \frac{\theta(x(\xi, t) - x((\xi_{seed}, t))}{J(x(\xi_{seed}, t))} \cdot \lambda(\xi_{seed}, t) d\xi_{seed},\end{aligned} \tag{5.3.9}$$

where

$$(\Theta\lambda)(x(\xi, t)) = \begin{pmatrix} (\Theta_{x_1}\lambda) \\ (\Theta_{x_2}\lambda) \end{pmatrix}. \tag{5.3.10}$$

Θ is an integral operator acting on a scalar λ-field, $\lambda : (\xi_1, \xi_2) \in \Xi \rightarrow \Re$ that assigns a vector to each point of the λ-field, that is $(\Theta\lambda) : \Re \rightarrow \Re^2$. Thus, the Θ operator returns the average velocity field at a time t.

5.4 Discrete macroscopic growth operator

In practical applications we implement a discrete version of the macroscopic growth operator Θ. Let the Darcyan coordinate system of an organism be a curvilinear grid with n radial and m angular coordinate curves. Then the organism's domain is represented by a configuration of the Darcyan grid nodes

$$\{x(\xi_1, \xi_2, t) : \xi_1 \in \{1, 2, ..., n\},\ \xi_2 \in \{1, 2, ..., m\}\}$$

For simplicity of notation the Darcyan coordinate system is referred to as $\{x(\xi_i, t), 1 \leq \xi_i \leq N,\ N = m \cdot n\}$.

We consider space-time discretization of the macroscopic growth equation. At a time $t = j$ a finite-dimensional approximation $\Delta x(\xi, l)$ of the infinite-dimensional displacement field is

$$\Delta x(\xi, j) \approx (\Theta_N \lambda) = \sum_{\xi_{seed} \in \Xi} \frac{\theta(x(\xi, (j-1)) - x(\xi_{seed}, (j-1)))}{J(x(\xi_{seed}, (j-1)))} \cdot \lambda(\xi_{seed}, j), \tag{5.4.1}$$

where $\xi,\ \xi_{seed} \in \Xi = \{1, 2, ..., N\}$ and

$$(\Theta_N \lambda)(x(\xi, j)) = \begin{pmatrix} \Theta_{N_{x_1}} \lambda \\ \Theta_{N_{x_2}} \lambda \end{pmatrix}. \tag{5.4.2}$$

As $N \to \infty$, $\Theta_N \to \Theta$. Θ_N is a discrete macroscopic growth operator

$$\begin{aligned}\Theta_N \lambda(x(\xi_i, j)) = \sum_{l=1}^{N} &(x(\xi_i, j-1) - x(\xi_l, j-1)) \\ &\cdot \exp\left(-\frac{\|(x(\xi_i, j-1) - x(\xi_l, j-1))\|^2}{s(x(\xi_l, j-1))^2}\right) \cdot \frac{\lambda(\xi_l, j)}{J(x(\xi_l, j-1))}.\end{aligned} \tag{5.4.3}$$

For each grid node i $\Theta_N \lambda(x(\xi_i, l)) = \Delta x(\xi_i, l)$, where $\Delta x(\xi_i, l) = x(\xi_i, l) - x(\xi_i, l-1)$ is a 2D displacement vector. According to (5.4.2)-(5.4.3) the displacement field is computed by multiplying each component $\Theta_{N_{x_k}}$ of a 2D array Θ_N by an N-dimensional vector λ. Clearly, $\Theta_{N_{x_k}}$ is an $N \times N$ matrix whose i^{th} row entries represent displacements of a seed ξ_i resulting from activation of seeds ξ_l, $1 \leq \xi_l \leq N$.

Definition 5.4.1. *The discrete macroscopic growth operator Θ_N at a time $t = l$ associated with the $n \times m$ Darcyan grid of an organism is a two-dimensional array of $N \times N$ matrices $\begin{pmatrix} \Theta_{N_{x_1}} \\ \Theta_{N_{x_2}} \end{pmatrix}$ with $N = n \cdot m$ and entries*

$$\begin{aligned}\Theta^{ij}_{N_{x_k}} = &\frac{1}{J(x_k(\xi_j, l-1))} \\ &\cdot (x_k(\xi_i, l-1) - x_k(\xi_j, l-1)) \exp\left(-\frac{\|x_k(\xi_i, l-1) - x_k(\xi_j, l-1)\|^2}{s(x_k(\xi_j, l-1))^2}\right).\end{aligned} \tag{5.4.4}$$

5.5 Invariance of the inference of the intensity parameter under $E(2)$

In the biological growth patterns examined in this thesis, we assume that there are no preferred directions. This would not be the case, for example, in gravity-induced growth. In such cases, measurements of the GRID growth parameters of a developing organism should not depend upon the spatial coordinate system used by an observer. Therefore, it is important that the λ-field inferred from images using the macroscopic growth equation is independent of the rigid motion of an organism (rigid transformation of its coordinate system in space). In this section we show that the translation-invariant model of the deformation field due to a single seed given in (5.1.1) leads to the invariance of the inference of $\lambda(\xi, t)$ with respect to spatial translations, rotations and reflections.

Proposition 5.5.1. *The inference of $\lambda(\xi, t)$ is invariant under the Euclidean group of transformations $E(2)$.*

Proof. We prove that the inferred λ-field is invariant under the spatial translations, rotations and reflections of the Darcyan coordinate system of an organism.
Case 1*: Translation.* We apply a spatial transformation to the Darcyan coordinate system of an organism $x(\xi,t) \to x(\xi,t)+b$. For a fixed ξ, $x(\xi)$ is a 2D vector with x_1 and x_2 absolute coordinates. Let $\tilde{x}(\xi,t) = x(\xi,t)+b$. Clearly, the Jacobian of the transformation $\tilde{x}(\xi,t)$ with respect to ξ does not change, $J(\tilde{x}(\xi,t)) = J(x(\xi_{seed},t))$, as well as the s parameter since it is equal to the Jacobian.
Also, the displacement field for a fixed seed $\xi_{seed} \in \Xi$ remains the same due to its translation-invariance property

$$\begin{aligned}\theta(\tilde{x}(\xi,t)-\tilde{x}(\xi_{seed},t)) = (\tilde{x}(\xi,t)-\tilde{x}(\xi_{seed},t))\cdot \\ \exp\left(\frac{-\|(\tilde{x}(\xi,t)-\tilde{x}(\xi_{seed},t))\|^2}{s(\tilde{x}(\xi_{seed},t))^2}\right) \\ = \theta(x(\xi,t)-x(\xi_{seed},t))\end{aligned}$$

Therefore, at a time $t=j$ we obtain the average displacement field

$$\begin{aligned}\Delta\tilde{x}(\xi,j) = (\Theta_N\lambda)(\tilde{x}(\xi,j)) = \\ \sum_{\xi_{seed}\in\Xi} \theta(\tilde{x}(\xi,j-1)-\tilde{x}(\xi_{seed},j-1))\cdot\frac{\lambda(\xi_{seed},j)}{J(\tilde{x}(\xi_{seed},j-1))} = \\ \sum_{\xi_{seed}\in\Xi} \theta(x(\xi,j-1)-x(\xi_{seed},j-1))\cdot\frac{\lambda(\xi_{seed},j-1)}{J(x(\xi_{seed},j-1))} = \Delta x(\xi,j).\end{aligned}$$

Then $\lambda(\xi,j) = {\Theta_N}^{-1}\Delta\tilde{x}(\xi,j) = {\Theta_N}^{-1}\Delta x(\xi,j)$.
Case 2*: Rotation.* For the rotation transformation $x(\xi,t) \to Rx(\xi,t)$, where $R = \begin{pmatrix}\cos\theta & \sin\theta \\ -\sin\theta & \cos\theta\end{pmatrix}$. We let $\tilde{x}(\xi,t) = Rx(\xi,t)$. Then on the LHS of (5.4.1) at a time $t=j$ we have

$$\Delta\tilde{x}(\xi,j) = \Delta Rx(\xi,j) = R\Delta x(\xi,j). \tag{5.5.1}$$

Since rotation of the coordinate system preserves Euclidean distances

$$\|(\tilde{x}(\xi,j-1)-\tilde{x}(\xi_{seed},j-1))\| = \|(x(\xi,j-1)-x(\xi_{seed},j-1))\|$$

between seeds and areas around them

$$J(\tilde{x}(\xi_{seed},j-1)) = J(x(\xi_{seed},j-1)) = s(x(\xi_{seed},j-1))$$

then on the RHS of the discrete macroscopic growth equation we obtain

$$\begin{aligned}
&(\Theta_N\lambda)(Rx(\xi,j)) = \\
&\sum_{\xi_{seed}\in\Xi}(\tilde{x}(\xi,j-1)-\tilde{x}(\xi_{seed},j-1))\cdot\exp\left(\frac{-\|(x(\xi,j-1)-x(\xi_{seed},j-1))\|^2}{s(x(\xi_{seed},j-1))^2}\right)\cdot \\
&\frac{\lambda(\xi_{seed},j)}{J(x(\xi_{seed},j-1))} \\
&=R\left(\sum_{\xi_{seed}\in\Xi}(x(\xi,j-1)-x(\xi_{seed},j-1))\cdot\exp\left(\frac{-\|(x(\xi,j-1)-x(\xi_{seed},j-1))\|^2}{s(x(\xi_{seed},j-1))^2}\right)\right)\cdot \\
&\frac{\lambda(\xi_{seed},j)}{J(x(\xi_{seed},j-1))} \\
&=R\left((\Theta_N\lambda)(x(\xi,j))\right).
\end{aligned}$$

Equating the LHS (5.5.1) and the RHS leads to

$$\Delta\tilde{x}(\xi,j)=(\Theta_N\lambda)(\tilde{x}(\xi,j))=R\ \left((\Theta_N\lambda)(x(\xi,j))\right)=R\Delta x(\xi,j). \tag{5.5.2}$$

Equation (5.5.2) implies that the solution to the inverse problem

$$\lambda(\xi,j)=\Theta_N^{-1}\Delta\tilde{x}(\xi,j)={\Theta_N}^{-1}R^{-1}R\Delta x(\xi,j)=\Theta_N^{-1}x(\xi,j).$$

Case 3: *Reflection.* By the same argument as in the case 2 λ-field remains unchanged under the reflection transformation
$x(\xi,t)\to Rx(\xi,t)$, where $R=\begin{pmatrix}\cos\theta & \sin\theta\\ \sin\theta & -\cos\theta\end{pmatrix}$. □

The proposition reflects the fact that in this model a developing organism does not know the absolute space.

5.6 Regularity properties of the macroscopic growth operator

We now study the regularity properties of Θ_N to address the question of the numerical stability of the solution to the inverse problem $\lambda(\xi,t)=\Theta_{N_{x_k}}(\Delta x(\xi,t))^{-1}$, where $k=1$ or 2. Using (5.4.4) we compute the macroscopic growth matrix $\Theta_{10{,}000}$ associated with a 100 × 100 Darcyan grid of the Drosophila wing disc $x(\xi)$ (see Fig.5.6.1.a-5.6.1.b). Figure 5.6.1.c below provides an insight into the structure of the macroscopic growth matrix $\Theta_{10{,}000}$.

In Figure 5.6.1.c negative and positive displacements are shown in blue and red color, respectively, and zero displacements are shown in green. The structure of the macroscopic growth matrix is reminiscent of a skew-symmetric matrix whose elements satisfy $\Theta^{ij}_{N_{x_k}}=-\Theta^{ji}_{N_{x_k}}$. Although $\Theta_{N_{x_k}}$ is not skew-symmetric, as dictated

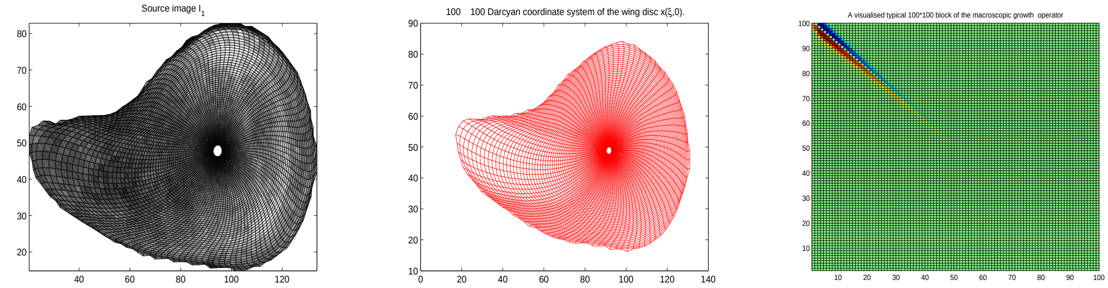

(a) (b) (c)

Figure 5.6.1: (a) Wingless gene expression pattern in the Drosophila wing disc interpolated onto (b) a 100 × 100 Darcyan coordinate system $x(\xi, 0)$, (c) Typical 100 × 100 'tile' of the macroscopic growth matrix $\Theta_{10{,}000_{x_1}}$.

by its definition (5.4.4) we can argue that for the seeds (nodes of the Darcyan grid) ξ_i and ξ_j located close to one another

$$\begin{aligned} J(x_k(\xi_i, l-1)) &\approx J(x_k(\xi_j, l-1)), \\ s(x_k(\xi_i, l-1)) &\approx s(x_k(\xi_j, l-1)), \\ \Theta^{ij}_{N_{x_k}} &\approx (x_k(\xi_i, l-1) - x_k(\xi_j, l-1)) \cdot const. \end{aligned}$$

Since the displacement decays exponentially to zero as the distance between ξ_i and ξ_j increases we have

$$\Theta^{ij}_{N_{x_k}} \approx 0.$$

Therefore, to a certain order of accuracy, the macroscopic growth matrix is approximately skew-symmetric. Then an eigenvalue decomposition can be applied to such approximation since it is a normal matrix. That is,

$$\Theta_{N_{x_k}} \approx \tilde{\Theta}_{N_{x_k}} \text{ and } \tilde{\Theta}_{N_{x_k}} = U \Lambda U^T,$$

where Λ is a block-diagonal matrix of the eigenvalues of $\tilde{\Theta}_{N_{x_k}}$ and U is an orthogonal matrix whose columns are the eigenvectors of $\tilde{\Theta}_{N_{x_k}}$.

In order that the numerical solution to the inverse problem be stable $\Theta_{N_{x_k}}$ should be well-conditioned. A well-conditioned matrix ensures that $\lambda(\xi, t)$ does not grow without bounds in response to small changes in $\Delta x(\xi, t)$. We show below that $\Theta_{10{,}000_{x_k}}$ associated with the Darcyan grid of the Drosophila wing disc (see Fig.5.6.1) is ill-conditioned.

Eigenvalues of the $\Theta_{10{,}000_{x_1}}$ matrix come in conjugate pairs of complex numbers (see Fig.5.6.2) similar to conjugate pairs of purely imaginary eigenvalues of the skew-symmetric matrix. The scatter plots in Figure 5.6.2 show that the eigenvalues μ_i, $1 \leq i \leq 10{,}000$, accumulate near zero with only a few of them having a large magnitude. Since $\Theta_{10{,}000_{x_1}}$ is approximately the skew-symmetric matrix $\tilde{\Theta}_{10{,}000_{x_1}}$ we can evaluate the condition number of $\Theta_{10{,}000_{x_1}}$ using a formula for the condition

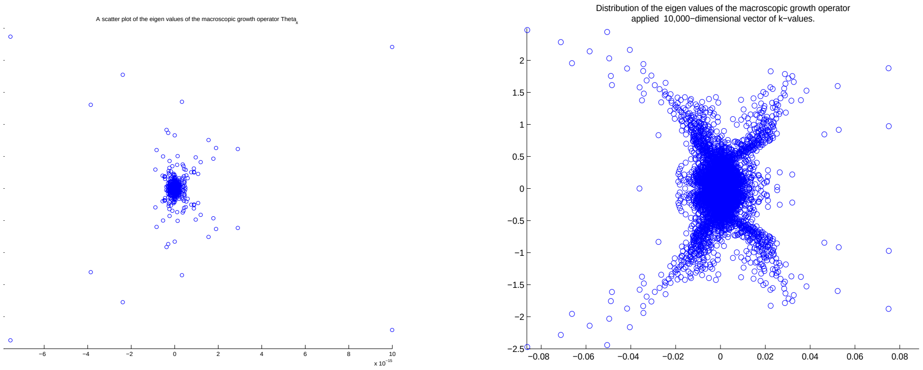

(a)

(b)

Figure 5.6.2: (a) Scatter plot of the eigenvalues of the macroscopic growth operator $\Theta_{10,000_{x_1}}$ and (b) a close-up view of the eigenvalue distribution in the complex plane.

number of a normal matrix

$$\kappa(\tilde{\Theta}) = \left| \frac{\mu_{max}(\tilde{\Theta})}{\mu_{min}(\tilde{\Theta})} \right|.$$

(The condition number measures the rate of change in $\lambda(\xi, t)$ with respect to a change in $\Delta x(\xi, t)$.) Since the smallest eigenvalue $\mu_{min} = 0$ and $\mu_{max} > 0$, $\kappa(\Theta_{10,000_{x_1}}) = \infty$ and we conclude that the solution to the linear system of equations

$$\Delta x(\xi, t) = \Theta_{10,000_{x_1}} \lambda(x(\xi, t)),\ \xi \in \Xi = \{1, 2, ..., 10,000\}$$

is numerically unstable.

In order to obtain a stable solution we must impose additional assumptions on the unknown λ-field. Statistically, we might assume, *a priori*, that $\lambda(\xi, t) \in \Re^N \times [0, T]$ is a random variable with a multivariate normal probability distribution at any time t (a random field). It is reasonable to take the mean $\langle \lambda(t) \rangle = \frac{1}{N}$ reflecting the fact that all cells have an equal chance to divide. For simplicity, we assume that each component $\lambda(\xi_i)$is independent with standard deviation σ_λ.

Since the image data are subject to errors, we can assume that the difference between the inferred image of a grown organism (target) and the target image, $I_1(x^{-1}(\xi, t)) - I_2(x(\xi, 0))$, is an error that is an N-dimensional normally distributed random vector with components $e_i \sim \mathcal{N}(0, \sigma_I^2)$. Using Bayes theorem we can find the most likely solution given the image data and the *a priori* distribution of $\lambda(\xi, t)$ that is equivalent to Tikhonov-regularized solution. This is the subject of Chapter 7.

Using Bayesian view of the unknown $\lambda(\xi, t)$ we might think of its absolute value as a random field controlling occurrences of cell decisions in a developing organism. In order to connect to the true biological process of growth we should not prescribe a probability distribution thus weakening the constraints on the λ-field. In Chapter 7 we propose representing an *a priori* knowledge about the Poisson intensity parameter $|\lambda(\xi,t)|$ as a sample-density function for a spatial Poisson point process. Since such an *a priori* model does not lead to a smooth solution we can regularize it by introducing a penalty function in the form of a squared L^2-norm of the operator $\Phi = \sum_i a_i \nabla^{2\cdot q_i}$ known as *Good's roughness* [30],

$$\phi(\lambda) = \parallel \Phi\lambda \parallel_2^2 .$$

Taking only $q_1 = 1/2$ we obtain the total variation integral

$$\phi(\lambda) = \parallel \nabla\lambda \parallel_2^2 = \int_{\xi\in\Xi} |\nabla\lambda(\xi,t)|^2 d\xi.$$

Since ξ spans a finite range of integers we use the total variation integral discretized in Ξ-space to constrain a *maximum a posteriori* estimate of $\lambda(\xi,t)$ to be a smooth function in the organism's domain.

Chapter 6

Inference of growth properties of a 2D organism from images

In this chapter we develop a systematic GRID-based approach for direct estimation of the GRID growth parameters such as the Poisson intensity and the relative rate of expansion/contraction from image data. We implement 2D GRID macroscopic growth equation that allows automatic generation of a biological transformation underlying observed shape changes via estimated GRID parameters.

6.1 Biological background

In this section we take a glimpse into the inner workings of the Drosophila wing disc development at larval stage, visualizing it in terms of wing-building genes in action. We identify “Master” genes in action via their spatial-temporal expression patterns and extract necessary biological information about larval growth of the wing disc to be taken into the GRID model.

6.1.1 Micrographs of gene expression patterns

Having acquired images of a growing organism, the question arises how they can be used to infer the properties of growth. We address this challenging image understanding problem by using the 2D macroscopic GRID model. Inspired by the book “Endless Forms Most Beautiful” by Sean B. Carroll [6], which provides a new look at biological development in terms of gene expression patterns, we perform a GRID-based analysis of a sequence of micrographs showing the dynamics of gene expression patterns in a growing Drosophila wing disc.

In developmental biology, spatial and temporal changes in certain gene expression patterns are closely tied to the growth process that consists of cell divisions/deaths, cell enlargements, etc. The open question is: How are these gene expression patterns linked to the generation of shape? Different strategies of modelling gene-controlled growth have been discussed [15],[25], however, they have not been cast into a precise mathematical form. It may be argued that the GRID approach is particularly well-suited for the modeling of biological growth in terms of gene expression patterns.

In the GRID model, growth patterns are composed of smaller, local deformations, each resulting from elementary biological events (e.g., cell divisions). A large number of such biological events, each occurring randomly and independently from one another, results in a visible growth pattern or biological shape change. A biological transformation underlying the observed shape changes is a solution to a GRID visible growth differential equation called the *GRID macroscopic growth law*. According to this law the source of the deformation driving shape changes seen in micrographs is defined by the Poisson intensity of elementary biological events. This important parameter controls occurrence of cell decisions in space-time as prescribed by the genetic program of an organism's development and relates gene expression patterns with the transformation induced by growth. Such a transformation cannot be directly observed from the sequence of images and, therefore, has to be estimated.

Estimation of a hidden growth-related transformation from a sequence of micrographs showing the dynamics of gene expression patterns would be biologically meaningful since the micrographs provide direct biological data in the form of levels of expression of a particular gene in the cells. In other words, we are given observations of a growth phenomenon as arrays of brightness intensities of the image pixels that correspond to concentrations of the particular gene product.

Such biological data is obtained by an optical imaging technique called *confocal microscopy*, an imaging technique that has been widely used by experimental biologists for its capability to visualize genes in action in embryos. Confocal microscopy depends on fluorescence: a sample is usually treated with fluorescent dyes to make objects of interest visible. To "light up" gene expression patterns the *green fluorescent protein* (gfp) is frequently used as a reporter of expression. Fused with the gene product (or protein) of interest, it determines whether the gene of interest has been taken up by or expressed in each individual cell of the cell population.

The biological samples tend to absorb and scatter a small amount of light. In tissue sections in which thickness is greater than $5\mu m$ the fluorescence intensity is gradually attenuated as a function of depth. As such, micrographs of these samples appear to be degraded images characterized by the presence of salt-and-pepper noise and poor signal-to-noise ratio. Therefore, a reduction of noise has to be performed in order to minimize the error in the GRID parameter estimates.

6.1.2 Example of larval growth of the Drosophila wing disc

Confocal microscopy plays a crucial role in understanding the logic of Drosophila wing formation. Gene expression patterns seen in micrographs of the growing Drosophila wing disc reveal the position and shape of adult wing and body struc-

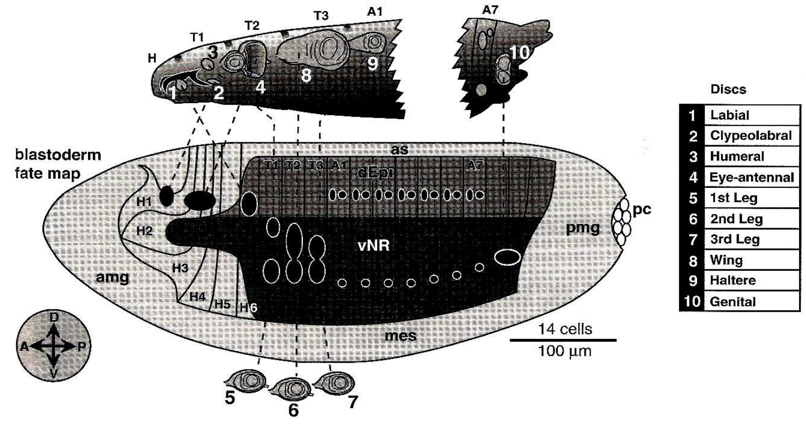

Figure 6.1.1: Origin of discs as "islands" within the embryonic ectoderm. Left side of an embryo below at the cellular blastoderm stage (D, dorsal; V, ventral; A, anterior; P, posterior). Spots indicate where discs later form. In this fate map segments are numbered in each region (H, head; T, thorax; A, abdomen). Areas shaded medium or dark form larval skin.
{Courtesy of Lewis I. Held, Jr., Texas Tech University, USA [40]}

tures long before they are formed. The *wing imaginal disc* is a group of epithelial cells that develops in the larva [40]. In the Drosophila fate map shown in Figure 6.1.1 the wing disc numbered by 8 develops in the segment of the thorax region $T2$ above the imaginal disc for the 2nd leg. The larval stage of the wing disc development starts at 24 hours after egg laying (AEL) and ends at 120 hours AEL as shown by a time line in Figure 6.1.2. Patterning of the wing disc is tightly linked to a program of growth according to which the size of the disc increases exponentially during larval life. By the end of the larval stage of development the wing disc becomes a hollow sack of $\approx 50,000$ cells.

One of the main reasons why biologists are interested in the study of the spatial-temporal gene expression patterns in the Drosophila wing disc is an understanding of the mechanisms by which the presumptive wing region of the wing imaginal disc is formed. This wing disc forms both distal (wing) and proximal (body wall) structures. The wing is a relatively recent evolutionary innovation (ancestral insects lacked wings) and may represent a primary division within this patterning cellular field [69].

The "Wingless protein" appears to be crucial in the patterning of the wing during larval growth. Its gene, "Wingless", was first identified as a mutation that removes the wing of Drosophila. Shown in Figure 6.1.2 is the dynamics of Wingless pattern that begins in a few cells (≈ 100 cells) at the distal tip of the early disc and remains largely restricted to the ventral region of the disc.

There are also other genes that are globally and specifically required for the wing development. Simultaneously, there are patterns of Apterous (Ap) and Vestigial (Vg) genes evolving, respectively, in the dorsal region of the disc with a relatively stable dorsal/ventral (D/V) boundary and at the dorsal edge of the wing

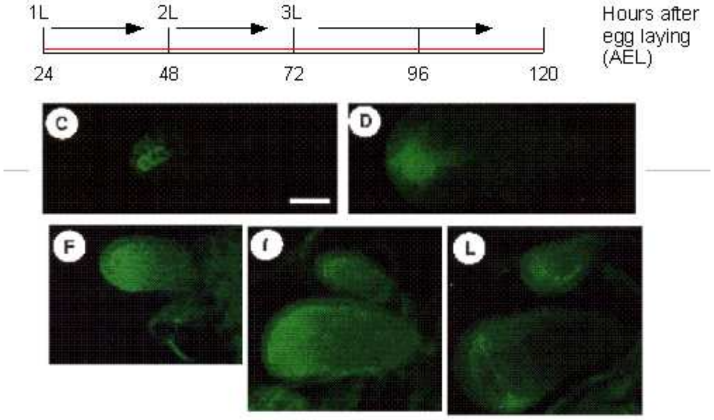

Figure 6.1.2: Confocal micrographs showing the dynamics of Wingless expression pattern during larval growth. (C) Middle second instar, (D) Late second instar, scale bar=25μm, (F,I) Early third instar, (L) Middle third instar, scale bar=50μm. {Courtesy of J. A. Williams, S. W. Paddock and S. B. Carroll [69]}

(see Fig.6.1.3). At the early third instar (72 hours AEL) the Vestigial protein pattern becomes more concentrated at the D/V boundary [69]. Ap is required for the formation of the entire wing, and Vg is required for identifying the wing subfield. The Wingless protein acts as the earliest member or a "Master" gene of the regulatory gene group, and in relation to Ap and Vg genes it regulates the boundary of the Apterous gene expression and promotes expression of the Vestigial gene.

By the end of larval stage of development the expression patterns of wing regulatory genes demarcate distinct regions of the wing fate map. Cells know their fates according to their positions. Figures 6.1.4(A-D) demonstrate the late third instar (120 hours AEL) expression patterns of Vestigial, Apterous and Wingless regulatory genes subdividing the wing disc into discrete subregions. The wing fate map in Fig.6.1.4.E shows the dorsal/ventral boundary as a future wing margin, the ventral and dorsal wing surfaces and notal(body wall) region.

Positional information that arises during larval development distinguishes not only the different subregions but also anterior and posterior compartments. The anterior/posterior boundary established early in embryogenesis (see the left panel of Figure 6.1.5) evolves into a more complex shape in the course of larval development, and by the end of larval stage it takes the form shown in the right panel of Figure 6.1.5.

We would like to use these observations to estimate the GRID growth parameters and the underlying growth-induced transformation. In what follows, we only take into account brightness intensities of the image pixels corresponding to the levels of expression (or densities) of Wingless gene in the cells shown in Figure 6.1.6. We ignore the effects of "secondary" regulatory genes, Apterous and Vestigial, as well as restrictions on the evolution of the anterior/posterior boundary in the wing disc, to avoid additional complexity of the inference problem.

Larval development of the wing disc is also characterized by the following

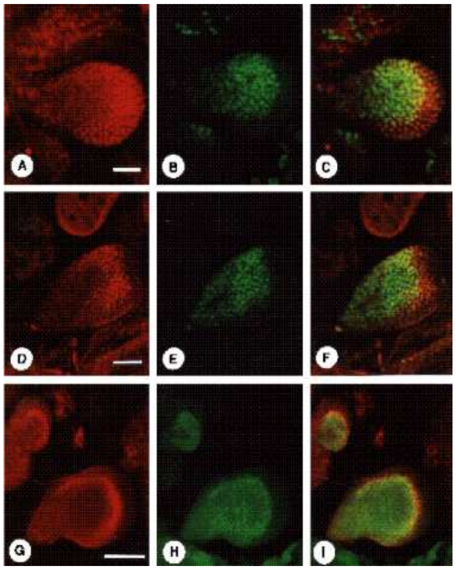

Figure 6.1.3: Development of the Vg and Ap expression patterns during the wing disc growth. (A,B,C) Middle second instar, scale bar=25μm, (D,E,F) Late second instar, (G,H,I) Early third instar discs expressing Vg, Ap and both proteins correspondingly.

{Courtesy of J. A. Williams, S. W. Paddock and S. B. Carroll [69]}

biological facts:

(a) The observed dynamics of Wingless gene expression is tightly linked to the biological process of cell divisions.

(b) Cells divide randomly and uniformly throughout the wing disc at larval stage of development.

(c) Cell number doubles on average every 9 hours during the second and early third instar.

(d) Most cell movements are due to passive displacements (newborn cells pushing extant ones).

(e) The disc epithelium is one cell thick, as in the ectoderm.

Therefore, a choice of a two-dimensional isotropic GRID model with constant Poisson intensities λ_t and $\lambda(\xi)$, respectively, per unit time and per unit space appears to be natural for the larval wing disc growth. Here, $\lambda(\xi) = const$ represents uniform distribution of cell divisions in Ξ-space of seeds. In this setup, the k-function that measures relative expansion/contraction rate varies with respect to space and time. It is an unknown GRID variable to be estimated. Having acquired micrographs of Wingless gene expression patterns associated with the larval development of the Drosophila wing disc, we would like to infer its growth properties in terms of the GRID variable of growth directly from images.

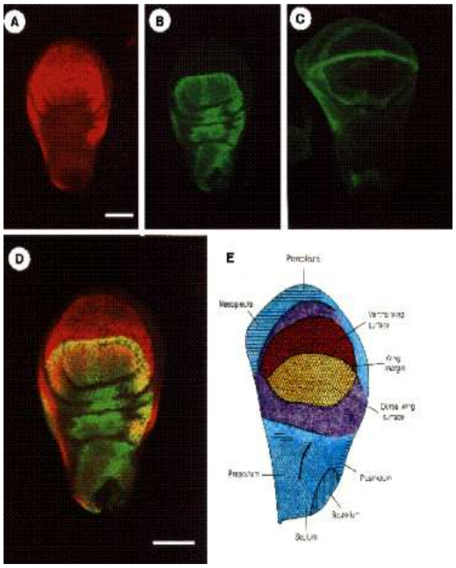

Figure 6.1.4: The mature wing disc as a geographic map of the adult wing and body elements.
(A) The expression patterns of Vg protein, (B) Ap protein and (C) Wg protein, (D) Overlapping of the Vg (red) and Ap (green) expression patterns, (E) Wing fate map, scale bar in (A-D) is 100 μm.
{Courtesy of J. A. Williams, S. W. Paddock and S. B. Carroll [69]}

6.2 Image inference problem formulation using macroscopic growth law

In this section we give a rigorous statement of the image inference problem in the form of an optimal control problem using the 2D GRID macroscopic growth equation.

6.2.1 Cost function model

We introduce an image function $I(x,t)$ to describe the spatial-temporal Wingless gene expression pattern given in Figure 6.1.6. $I(x_{ij},t)$ is the brightness intensity of the image pixel x_{ij} at time t corresponding to the concentration level of the Wingless protein in the cell located at x_{ij}. Given a pair of consecutive images $I_1(x(\xi),0)$ and $I_2(x(\xi),T)$ (see Fig.6.2.1) observed at time $t_0=0$ and time $t=T\geq t_0$ and interpolated on the Darcyan grid $x(\xi)$ of the wing disc given in I_1 we wish to estimate the rate of expansion/contraction $k(\xi,t)$ and the underlying biological transformation $x(\xi,t)$, $(0\leq\ t\ \leq T)$.

We follow a general approach of constructing the growth-induced transformation as a diffeomorphic flow with the least energy property adopted in computational anatomy [30]. Generated by the macroscopic growth equation of the form

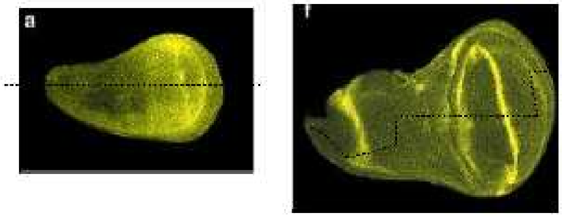

Figure 6.1.5: Evolution of the anterior/posterior boundary of the wing disc during larval growth. The left and right panels show the anterior/posterior boundary, respectively, in the early second instar and in the late third instar of the larval development. Adapted from [40].

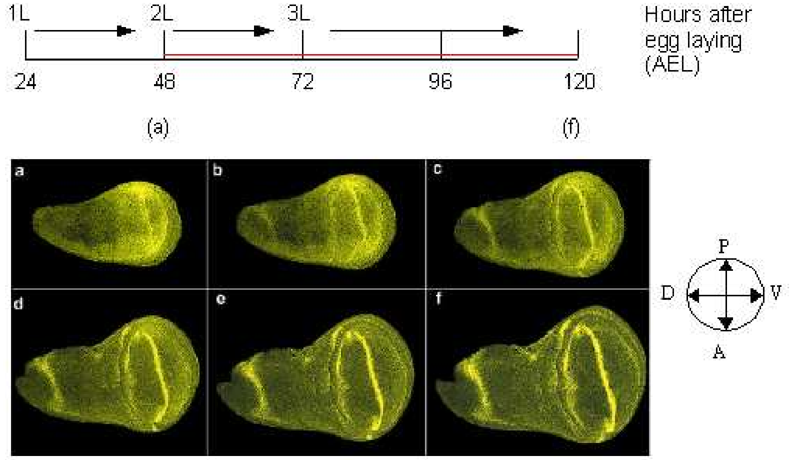

Figure 6.1.6: The dynamics of Wingless expression pattern from the early second instar through the third larval instar of larval stage of Drosophila wing disc development [50].

(5.3.6), such a transformation depends on the optimal value of $k(\xi, t)$. For a heterogeneous growth of an organism, the transformation also depends on the GRID intensity parameter $\lambda(\xi, t)$. In this case, for simplicity we assume that the relative rate of expansion/contraction $k(\xi, t)$ is constant in magnitude and varying in sign. Using the definition of $\lambda(\xi, t)$ developed in Chapter 5.3 on page 138 the corresponding transformation is the solution to the macroscopic growth equation of the form (5.3.8).

Thus, a single GRID variable of growth is either $k(\xi, t)$ or $\lambda(\xi, t)$ depending on type of growth under study. For the general inference problem formulation we denote the unknown GRID variable of growth by $w(\xi, t)$,

$$w(\xi, t) = \begin{cases} \lambda(\xi, t) & \text{if probability density of seeds is nonuniform,} \\ k(\xi, t) & \text{if probability density of seeds is uniform.} \end{cases} \tag{6.2.1}$$

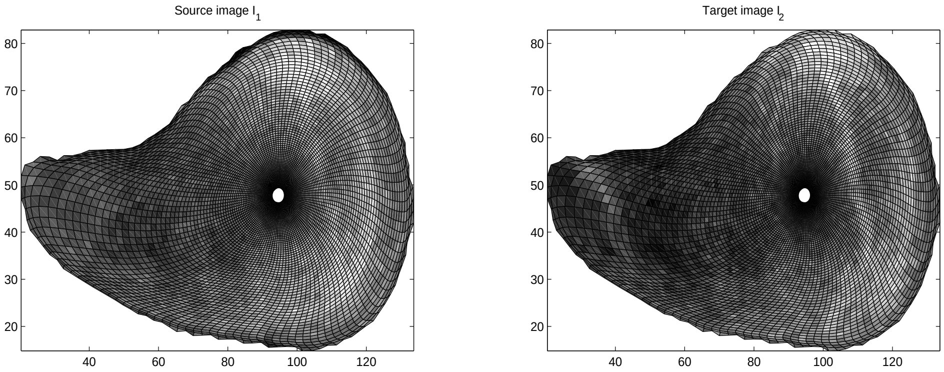

(a) (b)

Figure 6.2.1: (a) Source image $I_1(x(\xi), 0)$ and (b) target image $I_2(x(\xi), T)$ interpolated on the Darcyan grid of the wing disc in I_1.

Using Bayes theorem the optimal *maximum a posteriori* (MAP) estimate of $w(\xi, t)$ is the minimum of the following posterior energy (Gibbs potential),

$$\begin{aligned}
&E_{post}(w(\xi,t)) = E_{likelihood}(w(\xi,t)) + E_{prior}(w(\xi,t)),\\
&\text{where } E_{likelihood}(w(\xi,t)) = -\ln(p(I_2(x(\xi),T))|w(\xi,t))\\
&\text{and } E_{prior} = -\ln(p(w(\xi,t))).
\end{aligned} \tag{6.2.2}$$

Here, $p(I_2(x(\xi), T)|w(\xi, t))$ is the likelihood function that relates the observed pixel values to the growth parameter $w(\xi, t)$ and $p(w(\xi, t))$ is the prior probability density function (Gibbs measure).

We view the target image I_2 as a result of the evolution of the source image I_1 over time period of growth $[0, T]$, that is,

$$I_2 = I_2(x(\xi), T) = I_1(x(\xi, T)) + \epsilon, \tag{6.2.3}$$

where $x(\xi, T)$ is the solution to the macroscopic growth equation (6.2.2) at time T and

$$I_1(x(\xi, T)) = I_1(x(\xi), T) \tag{6.2.4}$$

is a source image interpolated onto the deformed Darcyan grid $x(\xi, T)$. Note that the initial Darcyan grid $x(\xi)$ in (6.2.4) is fixed, and pixel intensities of $I_1(x(\xi))$ are updated continuously in time under the background transformation $x(\xi, t)$ as time t progresses to T. Thus, equation (6.2.4) represents the result of evolution of pixel intensities of $I_1(x(\xi), t)$ at time $t = T$ as controlled by the underlying macroscopic growth law.

Here, $\epsilon \sim \mathcal{N}(0, \sigma_I^2)$ is independent, additive, homogeneous Gaussian noise that models the observation I_2 as a degraded version of the estimated image. The deviations $\sigma_{I_j} = \sigma_I$ are the same for all pixels $j = 1, 2, \ldots, N$. According to (6.2.3) the target image I_2 becomes a sample from the Gaussian process with the mean being the source image I_1 under the time-dependent deformation. Taking into account the dependency of $x(\xi, T)$ on the GRID parameter $w(\xi, T)$ we can compute the probability distribution of $I_2(x(\xi, T)) = \{I_{21}, I_{22}, ..., I_{2N}\}$ conditional on $w(\xi, T)$ or the *likelihood* of $w(\xi, T)$ expressed in Darcyan coordinates as follows

$$p(I_2(x(\xi,T))|w(\xi,T)) = \frac{1}{(\sqrt{2\pi\sigma_I^2})^N} \cdot \exp\left[-\frac{1}{2\sigma_I^2} \cdot \sum_{\xi\in\Xi}(I_2(x(\xi),T) - I_1(x(\xi,T)))^2 J(x(\xi))\right]. \tag{6.2.5}$$

Note that equation (6.2.5) represents a Gaussian observation model that relates the image data with the unknown GRID parameter $w(\xi, T)$. Using the left-hand side equation (6.2.2) we obtain the likelihood term in the form of the squared L^2 distance between the target image and the source image under the transformation.

Remark 6.2.1. *The likelihood function* (6.2.5) *is a special form of Gibbs distribution* $p(I_2|w) = \frac{1}{Z}e^{-U(I_2|w)}$ *whose energy* $U(I_2|w) = \sum_{i=1}^{N} V_i(x_i)$ *is due to single-site cliques in the zeroth order neighborhood system with the radius* $r = 0$ *and clique potentials* $V_i(x_i) = \frac{[I_{2i} - I_{1i}(w)]^2}{2\sigma_I^2}$ *[22].*

Given a model of the cost function as the Gibbs potential that is the sum of the likelihood and prior energies the challenge is to find an appropriate prior knowledge representation of the GRID growth parameter $w(\xi, t)$. Some prior models for the GRID intensity parameter $w(\xi, t) = \lambda(\xi, t)$ are discussed in Chapter 7.

6.2.2 Optimal control problem formulation

Thus, we are led to the discrete optimal control problem of the form,

$$\hat{w}(\xi,T) = \arg\min_{w\in\Re^N\times[0,T]} \left[\sum_{\xi\in\Xi} \frac{1}{2\sigma_I^2}[I_2(x(\xi),T) - I_1(x(\xi,T))]^2 \cdot J(x(\xi)) + E_{prior}(w(\xi,T))\right] \tag{6.2.1}$$

subject to the discretized macroscopic growth equation

$$x(\xi,T) - x(\xi,0) = \sum_{j=1}^{T} \sum_{\xi_{seed}\in\Xi} \frac{\theta(x(\xi,(j-1)) - x(\xi_{seed},(j-1)))}{J(x(\xi_{seed},(j-1)))} \cdot w(\xi_{seed}, j) \tag{6.2.2}$$

with the initial conditions

$$x(\xi,0) = x(\xi),\ \ w(\xi) = \begin{cases} \frac{1}{N} & \text{the probability density of seeds is non-uniform,} \\ 0 & \text{the probability density is uniform.} \end{cases} \tag{6.2.3}$$

Here, N is the total fixed number of seeds $x(\xi_{seed})$ occupying the Darcyan grid nodes of the wing disc. $J(x(\xi))$ is the Jacobian of the transformation $x(0) = x(\xi, 0) = x(\xi)$. If an increase in smoothness of the solution $w(\xi, t)$ is required, we may employ a regularization term such as the total squared variation

$$\sum_{\xi \in \Xi} |\nabla w(\xi, t)|^2 \tag{6.2.4}$$

in the cost function.

As time $t \to T$ the posterior energy E_{post} will decrease toward a local minimum whose value is not necessarily zero. Here, $\{w(\xi, t)\}_{t=1}^{T}$ is a sequence of optimal controls. We seek an estimate of $w(\xi) = \hat{w}(\xi, T) = \lim_{t \to T} w(\xi, t)$, such that $I_1((x(\xi), T)^{-1}) \sim I_2(x(\xi), T)$.

If there is no constraint on $w(\xi, t)$ in the form of a sample from a particular multivariate distribution p_{prior} (other than uniform) then the prior energy term E_{prior} is constant, and equations (6.2.1)-(6.2.2) represent an unconstrained optimal control problem. If there is a particular probabilistic model imposed on $w(\xi, t)$ then the prior energy term is a function of all N components of $w(\xi, t)$ that plays a role of the regularization term. In this case, (6.2.1)-(6.2.2) is a constrained optimal control problem.

With the smoothness constraint of (6.2.4) [32] the optimization problem (6.2.1) is formulated as follows

$$\begin{aligned} \hat{w}(\xi, T) = \arg\min_{w \in \Re^N \times [0,T]} & \sum_{\xi \in \Xi} \frac{1}{2\sigma_I^2} (I_2(x(\xi), T) - I_1(x(\xi, T)))^2 \cdot J(x(\xi)) \\ & + E_{prior}(w(\xi, T)) + \sum_{\xi \in \Xi} |\nabla w(\xi, T)|^2. \end{aligned} \tag{6.2.5}$$

For the penalty function we have to compute the gradient of the scalar w-field at each node of the Darcyan grid $\xi = (\xi_1, \xi_2)$, $1 \leq \xi_1 \leq n$, $1 \leq \xi_2 \leq m$, $N = n \times m$

$$\nabla w(\xi, T) = \frac{\partial w(\xi, t)}{\partial \xi_1} + \frac{\partial w(\xi, t)}{\partial \xi_2}. \tag{6.2.6}$$

6.3 An algorithm for direct estimation of the GRID variables

6.3.1 Image preprocessing

In order to solve the discrete optimal control problem for $\hat{w}(\xi, T)$ we first have to prepare the images for GRID analysis. We perform the following image representation and preprocessing steps

1. **Construction of the Darcyan coordinate representation of the wing disc given in source I_1 and target I_2 images using the Level Set**

Method as described in [52].
Comparing source and target images I_1 and I_2 given in Figure 6.2.1 we observe that grey level mismatch is mostly present near the edge of the anterior part and throughout the dorsal part of the wing disc. The density of the Darcyan grid quadrilaterals was increased by adding more angular grid curves and decreasing the average distance between evolving level sets (radial closed grid curves) closer to the boundary of the wing disc. Since there is no difference in the grey level content of both images in the neighborhood of the origin propagation of level sets into this area was halted. The resulting Darcyan grid contains 80 radial and 120 angular coordinate lines.
Since the image function $I(x,t)$ is defined on a rectangular uniform lattice we apply bilinear interpolation to estimate image values at the nodes of the curvilinear Darcyan coordinate system $I(x(\xi_i))$, where $1 \leq i \leq N$ and $N = 80 \times 120$.

2. **Image alignment about the origin of Darcyan coordinate system applying Principal Component Analysis (PCA).**
We remove rigid transformation from observed images using Darcyan coordinate representations of the initial and grown wing discs. Given the Darcyan grid nodes $x_i = x(\xi_{1_i}, \xi_{2_i})$, , $1 \leq i \leq N$, we define the covariance 2×2 matrix $K_j = \frac{1}{N}\sum_{i=1}^{N}\{(x_i - x_{c_{I_j}})(x_i - x_{c_{I_j}})^T\}$ and its eigen vectors for images I_j, $j = 1, 2$.
$x_{c_{I_j}}$ is the origin of the Darcyan coordinate system of the grown wing disc seen in I_j (denoted by red X in Figure 6.3.1). It is computed numerically as the middle point of a line segment whose length is the maximum of the distance $\sqrt{(x_i^2 - x_j^2)}$ between the Darcyan nodes x_i and x_j,$1 \leq i, j \leq N$ located along the last radial coordinate curve contouring the neighborhood of the origin. The relation between $x_{c_{I_1}}$ and $x_{c_{I_2}}$ is given by

$$x_{c_{I_2}} = R\, x_{c_{I_1}} + t, \tag{6.3.1}$$

where R is the rotation matrix and t is the translation vector.
The eigenvectors of K_j, $j = 1, 2$ give the principal axes of both Darcyans or the directions of maximal or minimal elongation of an organism. They are computed by singular value decomposition of the covariance matrix

$$K_j = H_j D_j H_j^T, \;\; j = 1, 2, \tag{6.3.2}$$

where H_j is an orthonormal matrix whose columns are the eigenvectors of K_j and D_j is a diagonal matrix whose elements are the eigenvalues of K_j. Since eigenvector matrices H_1 and H_2 are related by $H_2 = RH_1$, the rotation matrix in (6.3.1) is defined by

$$R = H_2 H_1^{-1}.$$

The translation vector t is directly obtained from (6.3.1) as follows

$$t = x_{c_{I_2}} - R\, x_{c_{I_1}}.$$

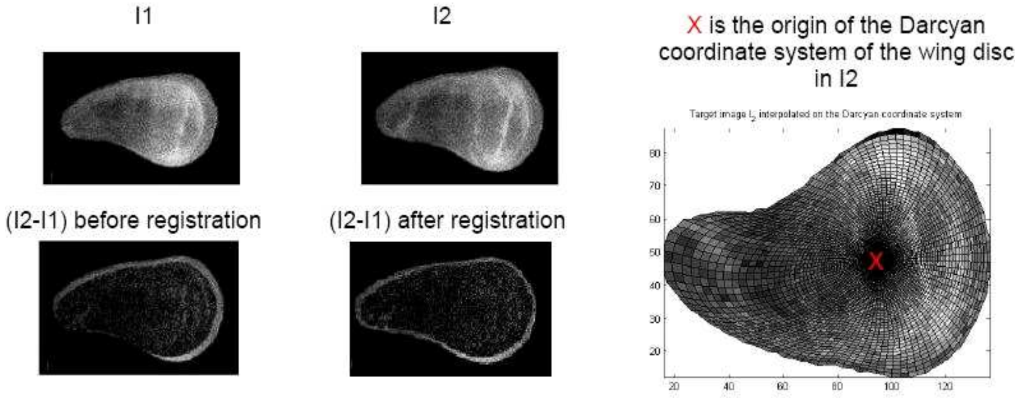

Figure 6.3.1: Given source and target images $I_1(x, 0)$ and $I_2(x, T)$ and their difference $I_2 - I_1$ before and after image alignment about the origin of the Darcyan coordinate system of the wing disc in I_2 denoted by red X.

Thus, we register I_1 with I_2 by aligning the principal axes of their Darcyans about the point of reference $x_{c_{I_2}}$. That is, $x_{i_{I_1(reg)}} = R\, x_{iI_1} + t$, $1 \leq i \leq N$. We demonstrate the effect of the Darcyan grid-based image alignment in Figure 6.3.1.

3. **Salt and pepper noise removal.** Salt and pepper noise is inherent to confocal microscopy imaging technique. A median filter using a 3×3 window can be applied as it has a property of removing this kind of noise while preserving edges.

Image preprocessing step described above is performed by a Matlab code "im_preproc.m" (see Appendix G).

6.3.2 Polak-Ribière conjugate gradient method

We would like to estimate the GRID growth parameter $w(\xi, t)$ directly from a given pair of preprocessed images (see Fig.6.2.1). As such, we wish to solve the following optimal control problem:

$$w(\xi) = \hat{w}(\xi, T) = \arg\min_{w \in \Re^N \times [0,T]} \sum_{\xi \in \Xi} \frac{1}{2\sigma_I^2} [I_2(x(\xi), T) - I_1(x(\xi) + \Delta(x(\xi, T)))]^2$$
$$\cdot J(x(\xi)) + E_{prior}(w(\xi, T)) + \sum_{\xi \in \Xi} |\nabla w(\xi, T)|^2, \qquad (6.3.3)$$

subject to

$$\begin{aligned} x(\xi, T) &= x(\xi, 0) + \Delta(x(\xi, T)) \\ &= x(\xi, 0) + \sum_{j=1}^{T} \sum_{\xi_{seed} \in \Xi} \frac{\theta(x(\xi,(j-1)) - x(\xi_{seed},(j-1)))}{J(x(\xi_{seed},(j-1)))} \cdot w(\xi_{seed}, j) \end{aligned} \tag{6.3.4}$$

and initial conditions (6.2.3). Clearly, $\Delta x(\xi, T)$ represents cumulative displacement over a time period $[0, T]$. Here, T is a free time such that as $t \to T$ the posterior energy $E_{post}(w(\xi, t))$ approaches its local minimum. For each time t the discretized macroscopic equation can be rewritten in the form

$$\begin{aligned} x(\xi, t+1) = x(\xi, t) + \sum_{\xi_{seed}=1}^{N} & (x(\xi, t) - x(\xi_{seed}, t)) \\ & \cdot \exp\left[-\frac{\|x(\xi, t) - x(\xi_{seed}, t)\|^2}{s^2(x(\xi_{seed}, t))}\right] w(\xi_{seed}, t+1) \end{aligned} \tag{6.3.5}$$

that we implement in numerical computations.

We consider the likelihood term $E_{likelihood}$ as a function of $w(\xi, t)$. In fact, this is a function of N unknown components of $w(\xi, t)$ evaluated at each time t at N Darcyan points $\xi_1, \xi_2, \ldots, \xi_N$ underlying the X-field $x(\xi, t)$,

$$E_{likelihood}(w(\xi, t)) = \sum_{\xi \in \Xi} \frac{1}{2\sigma_I^2} [I_2(x(\xi), T) - I_1(x(\xi) + \Delta(x(\xi, T)))]^2 \cdot J(x(\xi)). \tag{6.3.6}$$

Since (6.3.6) does not provide an explicit expression for the likelihood energy and $E_{likelihood}$ is a function of a large number of variables, it is difficult to establish its convexity. Recall that a function of several variables is convex if and only if its Hessian is a positive semi-definite matrix. To verify numerically if the Hessian matrix $\left[\frac{\partial^2}{\partial w_i \partial w_j} E_{likelihood}\right]$ is indeed positive semi-definite we would have to perform a task of high computational cost. Namely, using Sylvester's criterion, we have to compute the determinants of all of the leading principal minors (the upper left $i \times i$ corners of the Hessian matrix, $i = 1, 2, \ldots, N$) and show that they are all positive. This is a rather unnecessary endeavor since we are looking for a local minimum in the neighborhood of our initial guess defined by (6.2.3).

Since $E_{likelihood}$ is not necessarily convex, we are faced with a high-dimensional non-convex optimization problem for which, unfortunately, no "perfect" optimization algorithm exists. First, we have tried the steepest (gradient) descent method, which is not very reliable and efficient in N dimensions. Recall, that according to this method, we start at a point $w(\xi, 0) \in \Re^N$ and take many small time steps to move from point $w(\xi, j)$ to the point $w(\xi, j+1)$ by minimizing along the line from $w(\xi, j)$ in the direction of the local downhill gradient $-\Delta E_{post}(w(\xi, j))$. Then we compute the new gradient at the minimum point of the line minimization $w(\xi, j+1)$ that is perpendicular to the direction just traversed. Thus, at each time step j we must take a right angle turn that does not take us to the minimum. The steepest descent algorithm is also very slow, and this is another reason to look for an alternative minimization method.

We shall try to proceed in a direction *conjugate* (see Appendix B) to the previous gradient, and, if possible, to all old directions traversed towards a point of local minimum. Such a conjugate gradient search for the minimum is accomplished by typical *conjugate gradient methods* such as the well-known *Fletcher-Reeves algorithm* and its variation, the *Polak-Ribière algorithm* (see Appendix B). In $\Re^N$ for convex functions, the conjugate gradient method has a nice property: It constructs either a finite sequence $w(\xi, j)$, whose last element $w(\xi, T)$ minimizes the energy functional or an infinite sequence $\{w(\xi, j)\}_{j=1}^{\infty}$ such that $\lim_{j\to\infty} w(\xi, j) = \hat{w}(\xi)$ minimizes the energy functional. Its Polak-Ribière version can be used for finding the minimum of a non-convex function in $\Re^N$: The repeated cycles of N iterations will eventually converge to the minimum.

Since such algorithms rely on derivative information we need to compute the gradient of the posterior energy that is the sum of gradients of $E_{likelihood}$, E_{prior} and the penalty function. In what follows we find gradients of the likelihood energy and the penalty function and the description of the Polak-Ribière procedure. We refer a reader to Chapter 7 for the information on prior models for $w(\xi, t)$ and the corresponding gradients.

Fixing time t and keeping in mind the relation of $x(\xi, t)$ with $w(\xi, t)$ in the form

$$\begin{aligned} x(\xi, t) = x(\xi) + \Delta x(\xi, t) = x(\xi, t-1) + \sum_{\xi_{seed}=1}^{N} (x(\xi, t-1) - x(\xi_{seed}, t-1)) \\ \cdot \exp\left[-\frac{\|x(\xi, t-1) - x(\xi_{seed}, t-1)\|^2}{s^2(x(\xi_{seed}, t-1))}\right] w(\xi_{seed}, t), \end{aligned} \tag{6.3.1}$$

where $x(\xi, t-1) = x(\xi) + \Delta x(\xi, t-1)$ with $x(\xi, t) = (x_1(\xi, t), x_2(\xi, t))$ and denoting

$$w(\xi_{seed}, t) = w_i \text{ for each } \xi_{seed} = i, i = 1, 2, \ldots, N \ , \tag{6.3.2}$$

the gradient of $E_{likelihood}$ with N components is given by

$$\begin{aligned} \frac{\partial}{\partial w_i} E_{likelihood}(w_1, w_2, \ldots, w_N) = -2 \sum_{\xi \in \Xi} \frac{1}{2\sigma_I^2} [I_2(x(\xi), T) - I_1(x(\xi, T))] \cdot J(x(\xi)) \\ \cdot \left[\frac{\partial I_1}{\partial x_1}\frac{\partial x_1}{\partial w_i} + \frac{\partial I_1}{\partial x_2}\frac{\partial x_2}{\partial w_i}\right], \end{aligned} \tag{6.3.3}$$

where $\left(\frac{\partial I_1}{\partial x_1}, \frac{\partial I_1}{\partial x_2}\right)$ is the gradient of the image $I_1(x)$ interpolated onto the Darcyan grid $x(\xi, t)$ and

$$\frac{\partial x_j}{\partial w_i} = (x_j(\xi, t-1) - x_j(i, t-1)) \exp - \frac{\|x(\xi, t-1) - x(i, t-1)\|^2}{s^2(x(i, t-1))} \tag{6.3.4}$$

for $j = 1, 2$ and seeds $i = 1, 2, \ldots, N$. Here, we use a simplified notation for seeds in the X-field $x(\xi_{seed}, t) = x(i, t)$.

The gradient of $x(\xi, t)$ evaluated at $w(\xi, t) = w_i$ is given by

$$\nabla_{w_i} x = \begin{pmatrix} (x_1(\xi, t-1) - x_1(i, t-1)) \exp\left[-\frac{\|x(\xi,t-1) - x(i,t-1)\|^2}{s^2(x(i,t-1))} \right] \\ (x_2(\xi, t-1) - x_2(i, t-1)) \exp\left[-\frac{\|x(\xi,t-1) - x(i,t-1)\|^2}{s^2(x(i,t-1))} \right] \end{pmatrix}. \tag{6.3.5}$$

Thus, the gradient of the likelihood energy can be represented as the dot product of the gradient of $E_{likelihood}$ with respect to $x = x(\xi, t)$ and the gradient of the transformation $x(\xi, t)$ with respect to $w(\xi, t)$

$$\nabla_w E_{likelihood}(\vec{w}) = \nabla_x E_{likelihood} \cdot \nabla_w x, \tag{6.3.6}$$

where $\vec{w} = (w_1(t), w_2(t), \ldots, w_N(t))$ defined at points of the Darcyan space $\xi_1, \xi_2, \ldots, \xi_N$ and w takes values of $\vec{w}$ components.

To compute the gradient of the penalty function $\Phi(w(\xi, t)) = \sum_{\xi \in \Xi} |\nabla w(\xi, t)|^2$ with respect to $w(\xi, t)$ we need an explicit expression for $\Phi(w(\xi, t))$ in terms of N components of $\vec{w}$. We use finite difference approximations to the partial derivatives of $w(\xi, t)$ with respect to ξ_1 and ξ_2. Since ξ_1 and ξ_2 span a finite range of integers $(\xi_1, \xi_2) \in \{1, 2, \ldots, n\} \times \{1, 2, \ldots, m\}$, enumerating radial and angular coordinate curves, we have

$$\frac{\partial w}{\partial \xi_1} = \frac{w(\xi_{1_i}, \xi_{2_j}) - w(\xi_{1_{i-1}}, \xi_{2_j})}{1}, \quad \frac{\partial w}{\partial \xi_2} = \frac{w(\xi_{1_i}, \xi_{2_j}) - w(\xi_{1_i}, \xi_{2_{j-1}})}{1}. \tag{6.3.7}$$

Substituting (6.3.7) for the components of $\nabla w(\xi, t)$ in the penalty function expression we obtain

$$\Phi(\vec{w}) = \sum_{\xi_{1_i}=1}^{n} \sum_{\xi_{2_j}=1}^{m} \left[(w(\xi_{1_i}, \xi_{2_j}) - w(\xi_{1_{i-1}}, \xi_{2_j}))^2 + (w(\xi_{1_i}, \xi_{2_j}) - w(\xi_{1_i}, \xi_{2_{j-1}}))^2 \right] \tag{6.3.8}$$

with $n \times m = N$ and components of vector $\vec{w}$ in the form $w(\xi_{1_i}, \xi_{2_j})$. Referring to ξ_{1_i} and ξ_{2_j} by i and j respectively for simplicity of notation we record $(i-1, j)$th, (i, j)th and $(i, j+1)$st additive terms in the sum given on the right-hand side of (6.3.8)

$$(i+1, j)\text{th term: } [(w(i+1, j) - w(i, j))^2 + (w(i+1, j) - w(i+1, j-1))^2], \tag{6.3.9}$$

$$(i, j)\text{th term: } [(w(i, j) - w(i-1, j))^2 + (w(i, j) - w(i, j-1))^2], \tag{6.3.10}$$

$$(i, j+1)\text{st term: } [(w(i, j+1) - w(i-1, j+1))^2 + (w(i, j+1) - w(i, j))^2]. \tag{6.3.11}$$

Note that the rest of the additive terms on the right-hand side of (6.3.8) do not contain $w(i, j)$. Thus, the gradient of Φ has N components defined by

$$\frac{\partial \Phi}{\partial w(i, j)} = 8w(i, j) - 2(w(i+1, j) + w(i-1, j) + w(i, j-1) + w(i, j+1)) \tag{6.3.12}$$

for $1 \leq i \leq n$, $1 \leq j \leq m$.

Remark 6.3.1. *For consistency with the notation for $a(\xi, t)$ introduced earlier in N-dimensional vector form, each seed (i, j) can be referred to as $l = (i-1) \cdot n + j$, where $1 \leq j \leq m$. In this way we alter the representation of Φ, where w-field is given by $\vec{w} = (w_1, w_2, \ldots, w_N)$, as opposed to the matrix $\{w(i, j)\}$ with $N = n \times m$ elements.*

We now present the Polak-Ribière conjugate gradient algorithm [51], written in Matlab scripts "inference.m" and "inference2.m" with the use of different prior energy models (see Appendix G).

Initialization.

0. Select the initial GRID growth parameter value $w(\xi, 0)$. Specify the initial Darcyan grid $x(\xi, 0) = x(\xi)$.

1. Compute the gradient of the cost function

$$\nabla E_{post}(w(\xi,0)) = \nabla E_{likelihood}(w(\xi,0)) + \nabla E_{prior}(w(\xi,0)) + \nabla \Phi(w(\xi,0)). \tag{6.3.13}$$

2. Set initial direction of search $g_0(x(\xi)) = h_0(x(\xi)) = -\nabla E_{post}(w(\xi, 0))$.

Main part.

3. **if** $g(\cdot, 0) = 0$ **then** stop,
else set $i = 0$ and go to step **4**.

4. Compute a scalar λ_i such that

$$E_{post}(w(\xi,i) + \lambda_i \cdot h_i(\cdot)) = min_{\lambda>0} E_{post}(w(\xi,i) + \lambda \cdot h_i(\cdot)).$$

5. Update the GRID parameter $w(\xi, i+1) = w(\xi, i) + \lambda_i h_i(\cdot)$.

6. Update the Darcyan grid $x(\xi, i+1)$ by solving the discretized macroscopic growth equation

$$x(\xi, i+1) = x(\xi, i) + \sum_{\xi_{seed}=1}^{N} (x(\xi, i) - x(\xi_{seed}, i)) \cdot e^{-\frac{\|x((\xi),i)-x(\xi_{seed},i)\|^2}{s^2(x(\xi_{seed},i))}} w(\xi_{seed}, i+1)$$

subject to $x(\xi, t = i) = x(\xi, i)$.

7. Compute gradient $\nabla E_{post}(w(\xi, i+1))$.

8. **if** $\nabla E_{post}(w(\xi, i+1)) = 0$ **then** stop,
else set

$$g_{i+1}(\cdot) = -\nabla E_{post}(w(\xi, i+1)),\ h_{i+1}(\cdot) = g_{i+1}(\cdot) + \gamma_i h_i(\cdot), \text{ where} \tag{6.3.14}$$

(Fletcher-Reeves algorithm) $\gamma_i = \frac{\|g_{i+1}(\cdot)\|^2}{\|g_i(\cdot)\|^2}$ or
(Polak-Ribière algorithm) $\gamma_i = \frac{\|(g_{i+1}(\cdot) - g_i(\cdot)) g_{i+1}(\cdot)\|^2}{\|g_i(\cdot)\|^2}$.
Go to line minimization step **4**.

The algorithm constructs two sequences in $\Re^N$, $g_0, g_1, \ldots$, and $h_0, h_1, h_2, \ldots$, such that

$$g_i \cdot g_j = 0 \text{ for all } i \neq j \text{ and } g_{i+1} \cdot h_i = 0, \tag{6.3.15}$$

where $(\cdot)$ designates a scalar product of two vectors and $\{h_0, h_1, \ldots, h_N\}$ is a *conjugate* set of vectors. It can be shown for a strictly convex cost function that the conjugate gradient algorithm described above constructs the $\hat{w}(\xi)$ that minimizes E_{post} over $\Re^N$ in a finite number of iterations $k \leq N$ (see Appendix B). In practice, the cost function is usually non-convex, and in this case Polak-Ribière conjugate gradient algorithm "with reinitialization" is applied. That is, after each $k \geq n+1$ iterations we set $h_{ik} = g_{ik}$, for $i = 0, 1, 2, \ldots$, rather than computing h_{ik} according to (6.3.14).

Ideally, we would like to stop iterating (the stopping time $t = T$) when the distance measure between images $I_2(x(\xi), T)$ and $I_1(x(\xi, T))$ becomes reasonably close to 0. However, as experimental results will show, due to imposed constraints on $w(\xi, t)$ that do not allow it to vary too much, the local minimum of the posterior energy settles at a non-zero value. If we omit constraints on $w(\xi, t)$ then we will not be able to iterate until full convergence since further calculations would destroy the Darcyan coordinate system of the growing disc.

6.3.3 Computational aspects of inference algorithm

According to Polak-Ribière procedure, at each iteration i we need to minimize the energy functional $E_{post}(\lambda(\xi, t))$ along the direction $h_i \in \Re^N$ conjugate to all previous directions. For this purpose we solve the one-dimensional line minimization problem in step 4 of the algorithm,

$$\lambda_i = \arg\min_{\lambda \geq 0} \{E_{post}(w(\xi, i) + \lambda \cdot h_i(\xi))\},$$

which appears to be non-trivial when the behavior of $E_{post}(\lambda)$ is unknown. Since it is impossible to calculate λ_i exactly an accumulation of computational errors can affect the convergence of the proposed algorithm towards the minimum. What is the "least error" one-dimensional minimization procedure solving optimization of the posterior energy that takes a high computational effort to evaluate?

It is tempting to approximate the energy functional as a function of λ by a high-order interpolating polynomial. Indeed, it is possible to construct it based on the information of the energy functional and its derivative values at the endpoints of the interval $[0, b]$ where unknown λ belongs. Choosing some value of b, say, $b = 1$ we compute

$$\begin{aligned} f(b, w(\xi, i)) &= E_{post}(w(\xi, i) + b \cdot h_i(\xi)) - E_{post}(w(\xi, i)) \text{ and} \\ f_\lambda(b, w(\xi, i)) &= \nabla E_{post}(w(\xi, i) + b \cdot h_i(\xi)) \cdot h_i, \end{aligned}$$

where $f_\lambda(b, w(\xi, i))$ is the derivative of $f(\lambda, w(\xi, i))$ with respect to λ evaluated at $\lambda = b$. Then we also evaluate $f(\lambda, w(\xi, i))$ and $f_\lambda(\lambda, w(\xi, i))$ at the left endpoint of the interval $[0, b]$ and use the four values to construct an interpolating cubic polynomial $g(\lambda)$ to the function $f(\lambda, w(\xi, i))$. We minimize the polynomial approximation $g(\lambda)$ to find the point of minimum λ' for $\lambda \geq 0$. If $f(\lambda', w(\xi, i)) < 0$ then we set $\lambda_i = \lambda'$. Otherwise, we set $\lambda = \beta\lambda$, where $\beta \in (0, 1)$ and repeat the procedure of constructing the polynomial. This procedure is performed by a Matlab code "linmin_simple.m" (see Appendix G).

Using this approximation allows us to avoid evaluations of the image function at each updated value of λ_i, thereby saving computational time. However, this approach yields an incorrect interpolation of $E_{post}(\lambda)$ at early stages of algorithm implementation due to its sharp features. Also, it is not clear how far we should go in search for the minimum, that is, what value of b we should choose.

Instead, we follow a slow but a reliable strategy of initially bracketing the point of minimum at all time iterations and then using the derivative information to choose new trial points within the bracket. This is a computationally intensive task since it involves a number of evaluations of the cost function and its derivative with respect to λ at each iteration i. However, we prefer at the expense of computational time a gain in the accuracy of λ_i estimation. For this purpose, we perform a one-dimensional minimization sub-algorithm that contains

(i) an initial routine for finding the optimal bracketing interval (a, b, c) using the *golden section* and inverse parabolic interpolation that brackets the local minimum [54],

(ii) a routine for a one-dimensional search of the point of minimum with first derivatives that isolates it using the signs of the posterior energy derivative on both sides of the golden mean point b of the bracket (a, b, c) [54].

The initial routine iteratively constructs the bracket (a, b, c) that has a middle point b a fractional distance 0.38197 from one end and 0.61803 from the other end. That is, the ratio of the longer fractional distance to the shorter one is equal to the golden mean $\frac{1+\sqrt{5}}{2}$. The basic idea is to fit a parabola through the three points (a, b, c) using Lagrangian polynomial interpolation and update the bracketing triplet to (a, x, b) or (b, x, c) computing a new trial point x as the minimum of the parabola. The value of the cost function at the golden section point x should be the least of $E_{post}(a), E_{post}(x)$, and $E_{post}(b)$.

We then isolate the minimum using the sign of the derivative of the cost function at the middle point of the bracket (a, b, c) that indicates uniquely whether the next test point should be taken in the interval (a, b) or in the interval (b, c). To calculate the size of the step towards the minimum we simply extrapolate the value of the derivative at b and at the point with the second least value of E_{post} to zero using the secant method. If the trial point is outside of the bracket then the interval of choice is bisected.

We now describe the proposed algorithm written in a Matlab script "linmin.m" (see Appendix G) in more detail.

Initialization: bracketing the minimum.

1. Choose a right endpoint b as an initial guess for an interval $(0, b)$ possibly containing λ_i and compute $E_{post}(0)$.
2. Construct a vector $w(\xi, i+1) = w(\xi, i) + bh_i$, update the Darcyan grid $x(\xi, i+1)$ by formula (6.3.5) and evaluate $E_{post}(b)$.
3. **if** $E_{post}(b) > E_{post}(0)$ **then** repeat Steps **1-2** for a maximum of 50 times.
   If maximum number of steps is achieved return $\lambda_i = 0$.
   else set $c = b(1 + GOLD)$, where $GOLD = 1.618034$.(This step locates the next point to be tried at a fractional golden section distance 0.61803 from b).
   Repeat Step **2** for the value of $\lambda = c$.
4. Given the bracketing triplet (a, b, c) and $E_{post}(a)$, $E_{post}(b)$, $E_{post}(c)$, where initially $a = 0$, compute a new point using parabolic extrapolation

$$x = b - \frac{1}{2}\frac{(b-a)^2[E_{post}(b) - E_{post}(c)] - (b-c)^2[E_{post}(b) - E_{post}(a)]}{(b-a)[E_{post}(b) - E_{post}(c)] - (b-c)[E_{post}(b) - E_{post}(a)]}.$$

5. **if** $E_{post}(b) < E_{post}(x)$ **then** set the new bracket to (a, b, x).
   else if $E_{post}(b) > E_{post}(x)$ set the new bracket to (b, x, c).
   Repeat Steps **4-5** until $|c - a| \le \epsilon$, where ϵ is a user-supplied precision. **else** reset $c = c + GOLD(c - b)$ and repeat Step **2** for the new value $\lambda = c$.
   Repeat Steps **4-5** until $|c - a| \le \epsilon$.

Main part: isolating the minimum.

6. Given the bracket (a, b, c), compute the derivative $E_{post_\lambda}(b)$ at the golden section point b

$$E_{post_\lambda}(b) = \nabla E_{post}(w(\xi, i) + b \cdot h_i(\xi)) \cdot h_i,$$

7. **if** $E_{post_\lambda}(b) < 0$ choose an interval (b, c). Go to Step **8**.
   else if $E_{post_\lambda}(b) > 0$ choose an interval (a, b). Go to Step **8**.
   else stop and return $\lambda_i = b$.

8. Compute the derivative $E_{post_\lambda}(z) = \nabla E_{post}(w(\xi, i) + z \cdot h_i(\xi)) \cdot h_i$ at the point z with the second least value of E_{post} (initially, $z = a$ or $z = c$).
Compute the size of the step d to move from the point b with the least value of E_{post} to the next trial point x using the secant method.

$$d = E_{post_\lambda}(b) \frac{(z - b)}{(E_{post_\lambda}(b) - E_{post_\lambda}(z))}$$

9. **if** $b + d$ is within the bracket (b, c) (or (a, b)) **then** set $x = b + d$.
else bisect the chosen interval and set $d = 0.5 \cdot (c - b)$ (or $d = 0.5 \cdot (b - a)$.)

10. Having obtained the triplet (a, x, b) (or (b, x, c)) repeat Steps **6-8**.
if $d \leq tol$, where *tol* is the precision specified by a user **then** set a new point $x_{new} = x + d$. Compute the derivative $E_{post_\lambda}(x_{new})$.

> **if** $E_{post_\lambda}(x_{new}) > E_{post_\lambda}(x)$ **then** return $\lambda_i = x$.
> **else** return $\lambda_i = x_{new}$.

else go to Step **9**.

The return of the zeroth value of λ by this code is used as a stopping criterion for the multidimensional minimization Matlab code “inference.m”. Indeed, in this case E_{post} attains its minimum at the previous value of λ_i. Implementing such 1D minimization routine we accurately point the way to the minimum $\hat{w}(\xi)$ of the posterior energy.

Chapter 7

GRID characterization of the Drosophila wing disc growth

7.1 Homogeneous Poisson process of cell decisions

In this section we consider larval growth of the Drosophila wing disc with uniform space-time probability distribution of cell divisions. According to (6.2.1) the GRID growth variable $w(\xi, t)$ represents a local rate of contraction/expansion throughout the domain of a growing organism. We apply an algorithm proposed in Chapter 6 and posed as an unconstrained optimal control problem, to image data from the larval development of the Drosophila wing disc and discuss inference results.

Taking consecutive pairs of images in a given sequence of micrographs (see Figure 6.1.6 on page 151) we estimate the GRID growth parameter $w(\xi, T)$ as an optimal control of the growth-induced transformation $x(\xi, T)$ that drives a source image $I_1(x(\xi, T))$ into a registration with a target image $I_2(x(\xi))$ [53]. Since cell divisions occur randomly and uniformly we set the Poisson intensity $\lambda(\xi, T)$ to be constant in the Darcyan space of seeds Ξ and in time. In what follows, we do not impose a prior probability distribution on $w(\xi, T)$ and specify the cost function in the form of the Gaussian log-likelihood of the relative rate of growth/decay. Such a cost function basically measures grey level mismatch between the target and deformed source images. Thus, we seek a solution $w(\xi, T) = k(\xi, T)$ to the unconstrained optimal control problem,

$$\hat{k}(\xi, T) = \arg\min_{k \in \Re^N \times [0,T]} \left[\sum_{\xi \in \Xi} \frac{1}{2\sigma_I^2} [I_2(x(\xi), T) - I_1(x(\xi, T))]^2 \cdot J(x(\xi)) \right], \tag{7.1.1}$$

subject to the discretized macroscopic growth equation,

$$x(\xi, T) - x(\xi, 0) = \sum_{j=1}^{T} \sum_{\xi_{seed} \in \Xi} \frac{\theta(x(\xi, (j-1)) - x(\xi_{seed}, (j-1)))}{J(x(\xi_{seed}, (j-1)))} \cdot k(\xi_{seed}, j), \tag{7.1.2}$$

with the initial conditions

$$x(\xi,0)=x(\xi),\;\; k(\xi)=0. \tag{7.1.3}$$

Recall that we cannot claim that the optimal growth amplitude found by the conjugate gradient-based estimation algorithm is the global minimizer of the energy functional E_{post} since E_{post} is not necessarily convex, and as a function of $80\times 120=9600$ variables it may well possess a few local minima. With the initial guess of the zeroth value for the growth amplitude we expect to find an estimate close to 0 throughout the whole domain of the wing disc. Small values of $\hat{k}(\xi,T)$ preserve the integrity of the Darcyan grid.

We apply our estimation algorithm on a Darcyan 120×80 grid $x(\xi)$ representing the wing disc at a certain age as seen in the source image. A comparison of the estimated target images in Figures 7.1.1.g-7.1.1.i and 7.1.2.n-7.1.2.o and the corresponding target images shown in Figures 7.1.1.d-7.1.1.f and 7.1.2.l-7.1.2.m shows that the estimated biological transformation $x(\xi,T)$ does not fully register images. It tends to flatten subregions of high contrast such as the dorsal part of the wing disc with a strip of a high concentration of Wingless protein observed in target images (see the right panel of Fig.6.1.6 for the wing disc subdivision into dorsal, ventral, anterior and posterior parts). In the estimated images of the wing disc in the late stage of larval development (Fig.7.1.2.n and 7.1.2.o) the boundaries of this strip appear blurry. However, the algorithm performs well in subregions with the highest mismatch of grey levels, such as the area near the tip of the anterior part of the wing disc, seen as a black band in the source image (Fig.7.1.1.a) and as a light gray band in the corresponding target image (Fig.7.1.1.d).

Full convergence of Polak-Ribière minimization algorithm (in about 10 iterations) has been achieved in the experiments registering images I_1 and I_2, I_2 and I_3, I_3 and I_4. For the problem of registering images of the wing disc at a later stage of larval development, the results of only three iterations of the algorithm have been presented in Figures 7.1.2.n-7.1.2.o. Additional iterations of Polak-Ribière procedure cause local overlaps of the cellular field presented by its Darcyan grid with locally intersecting radial grid lines. In the color-coded plots shown in Figures 7.1.3.d-7.1.3.e, we observe that the estimated k-function oscillates wildly throughout the interior of the wing disc. This is the consequence of unconstrained optimization.

Combination of regions of contraction and expansion shown in blue and red in Figures 7.1.3.a-7.1.3.e is biologically meaningful. This distribution can describe growth with regions in red designating cell division locations. It is possible that the dividing cells push out the neighboring cells causing local contractions of the cellular field. This growth mode is also captured by the Darcyan coordinate system deformed under the estimated growth-induced transformation, as shown in Figures 7.1.4.a-7.1.4.e.

The magnitude of the displacement field $\|\Delta x(\xi)\; \|=\|\; x(\xi,T)-x(\xi,0)\|$ shown in Figures 7.1.5.a-7.1.5.e reveals a spatial-temporal deformation pattern with displacements concentrated near the tip of the anterior (upper) part of the wing disc in the early larval stage. As time progresses it evolves into a deformation pattern

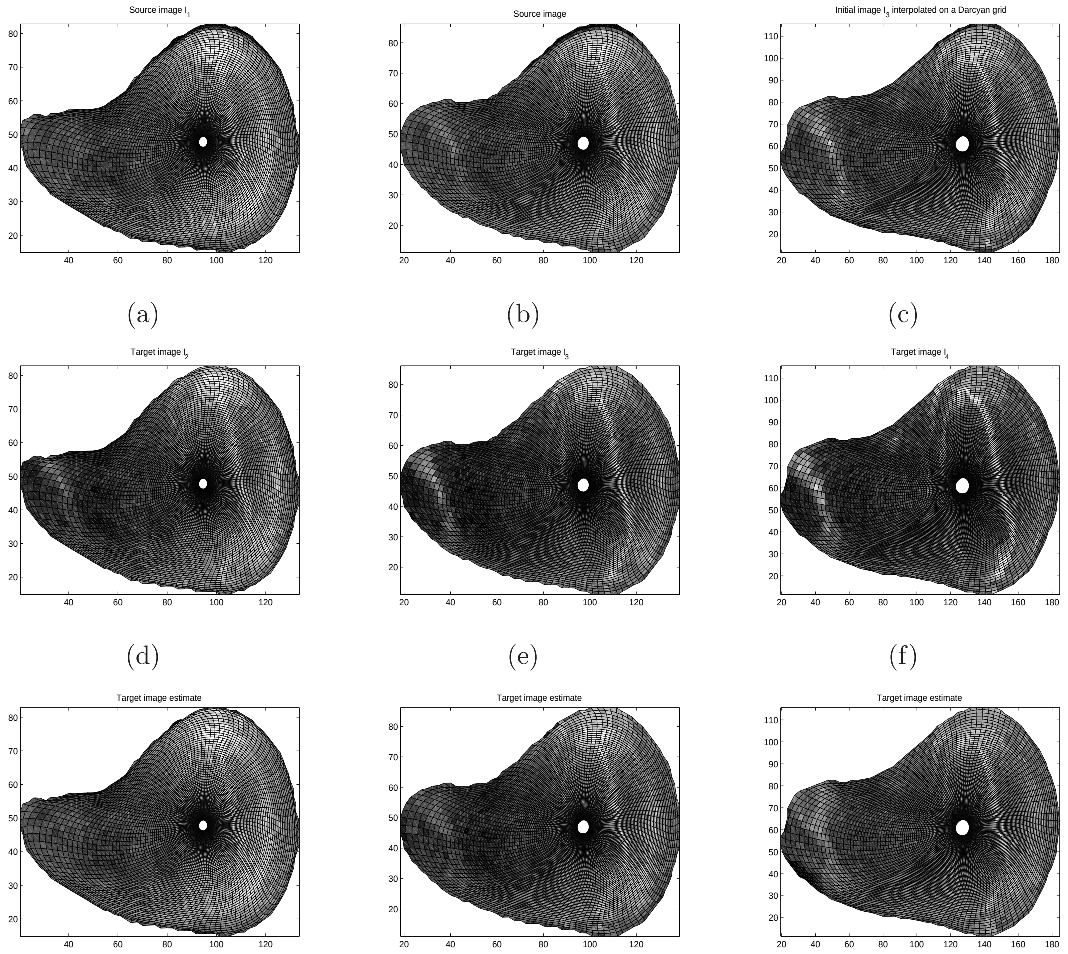

(a) (b) (c)

(d) (e) (f)

(g) (h) (i)

Figure 7.1.1: (a)-(c) Source images of the Drosophila wing disc $I_1,\ I_2,\ I_3$, (d)-(f) Target images of the wing disc $I_2,\ I_3,\ I_4$, (g)-(i) Estimates of target images $I_1,\ I_2,\ I_3$.

of high concentration in the dorsal region with the appearance of local deformation effects in the posterior part. This is consistent with the deformed Darcyan grid of the growing wing disc undergoing large expansions near the tip of the dorsal region. This suggests that the dorsal part of the wing disc grows faster during larval development.

In this section we have studied the performance of the direct estimation algorithm based on the cost function in the form of the Gaussian log-likelihood function only. The preliminary inference results suggest that an additional regularization term is needed to increase smoothness properties of the unknown w-field. This can be achieved by including a penalty term $E_{penalty} = 1/2{\sigma_w}^2 \parallel w(\xi) \parallel^2$ proposed in section 5.6.

Most importantly, we would like to increase the accuracy of our estimate that would yield more realistic growth patterns as driven by the cell activities such as

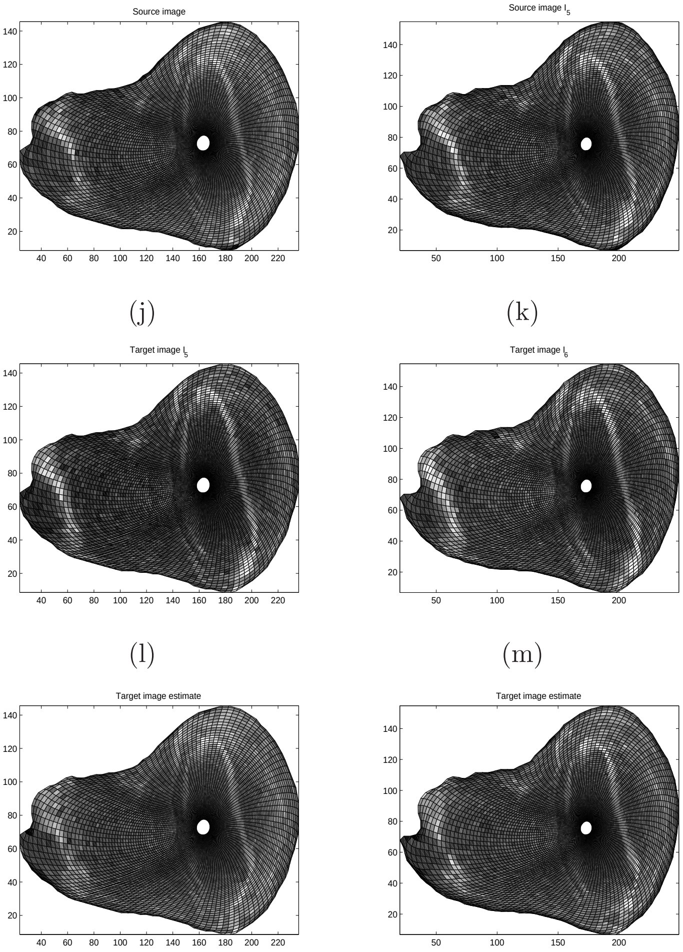

(j) (k)

(l) (m)

(n) (o)

Figure 7.1.2: (j)-(k) Source images of the Drosophila wing disc $I_4,\ I_5$, (l)-(m) Target images of the wing disc $I_5,\ I_6$, (n)-(o) Estimates of target images $I_4,\ I_5$.

cell divisions/deaths, cell enlargements, etc. Given that elementary cell decisions are random we can only measure such cell activities in terms of probability distributions. Since such biological events are naturally represented by the Poisson intensity parameter we define the absolute value of the unknown w-field as the Poisson intensity measure $|\lambda(\xi, t)|$ (by definition developed in section 5.3 on page 138) and seek a prior model for $|\lambda(\xi, t)|$. In what follows we develop the cost function model suitable for characterization of biological growth with the non-uniform probability distribution of cell decisions.

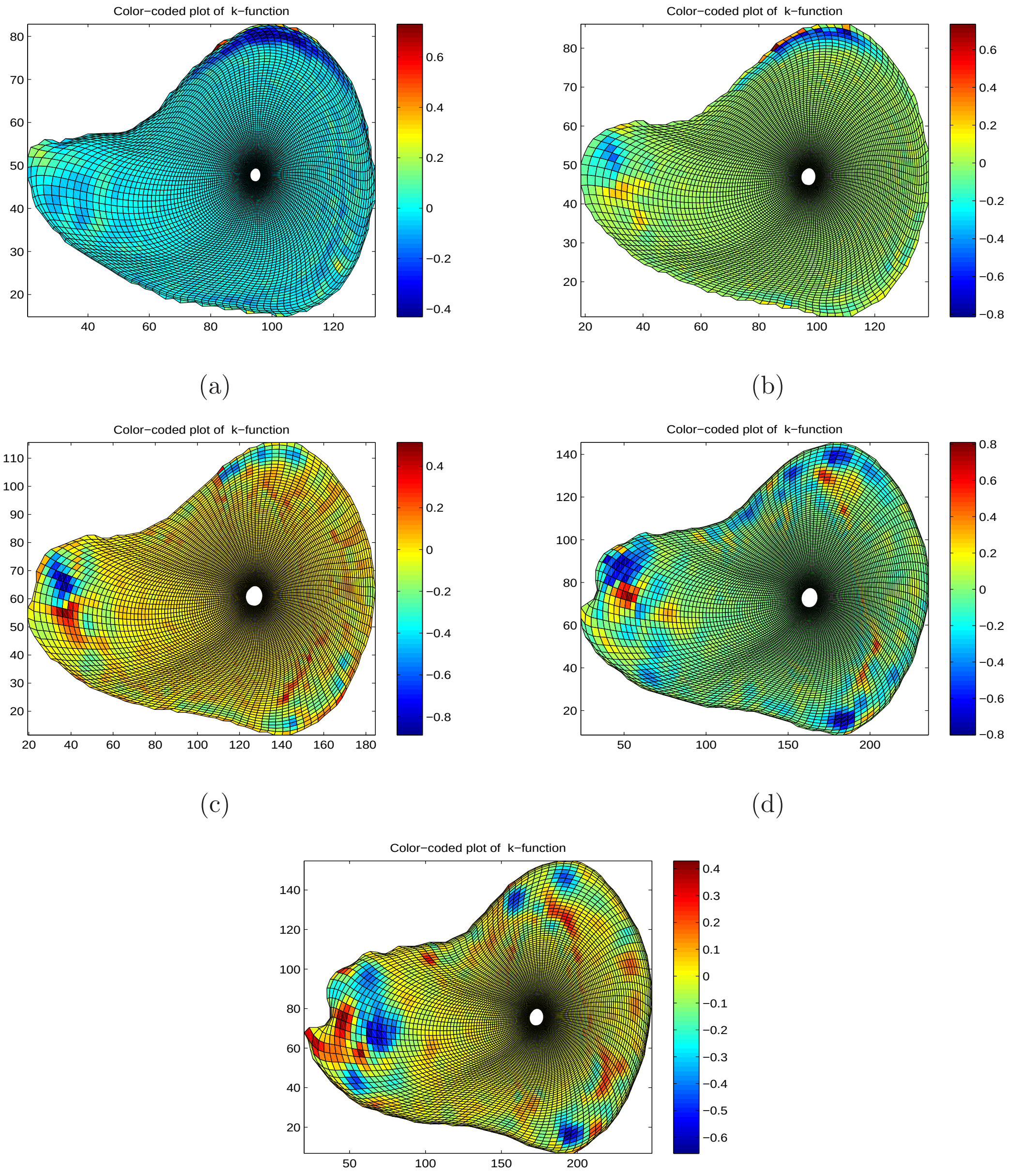

(a) (b)

(c) (d)

(e)

Figure 7.1.3: (a)-(e) Color-coded plot of the optimal local expansion/contraction rate $\hat{k}(\xi, T)$ for image pairs $(I_1,\ I_2)$, $(I_2,\ I_3)$, $(I_3,\ I_4)$, $(I_4,\ I_5)$ and $(I_5,\ I_6)$.

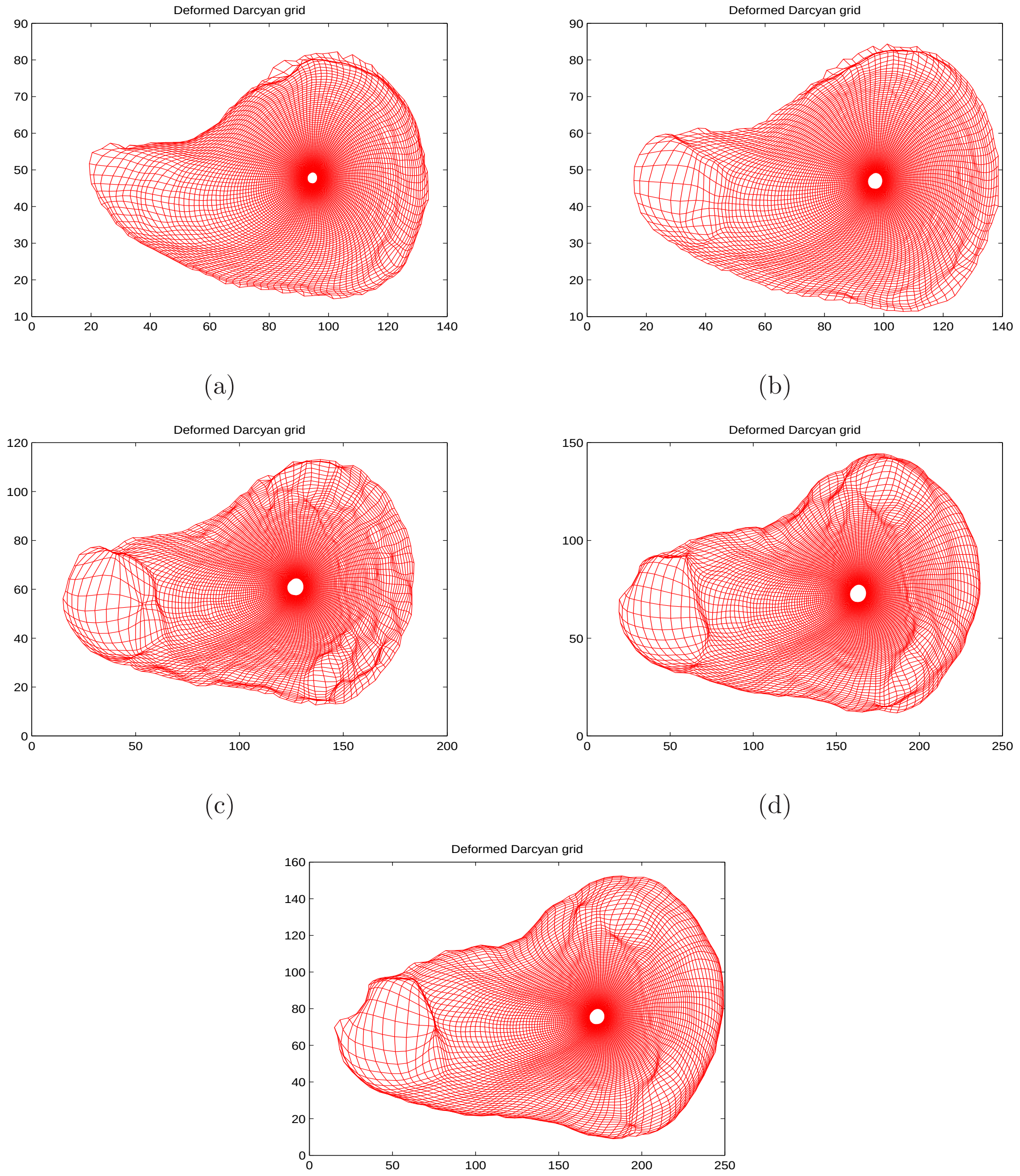

(a) (b) (c) (d) (e)

Figure 7.1.4: (a)-(e) Deformed Darcyan grid of the wing disc given, respectively, in $I_1,\ I_2,\ I_3,\ I_4,\ I_5$ generated by the estimated biological transformation $x(\xi, t)$, $0 \leq t \leq T$.

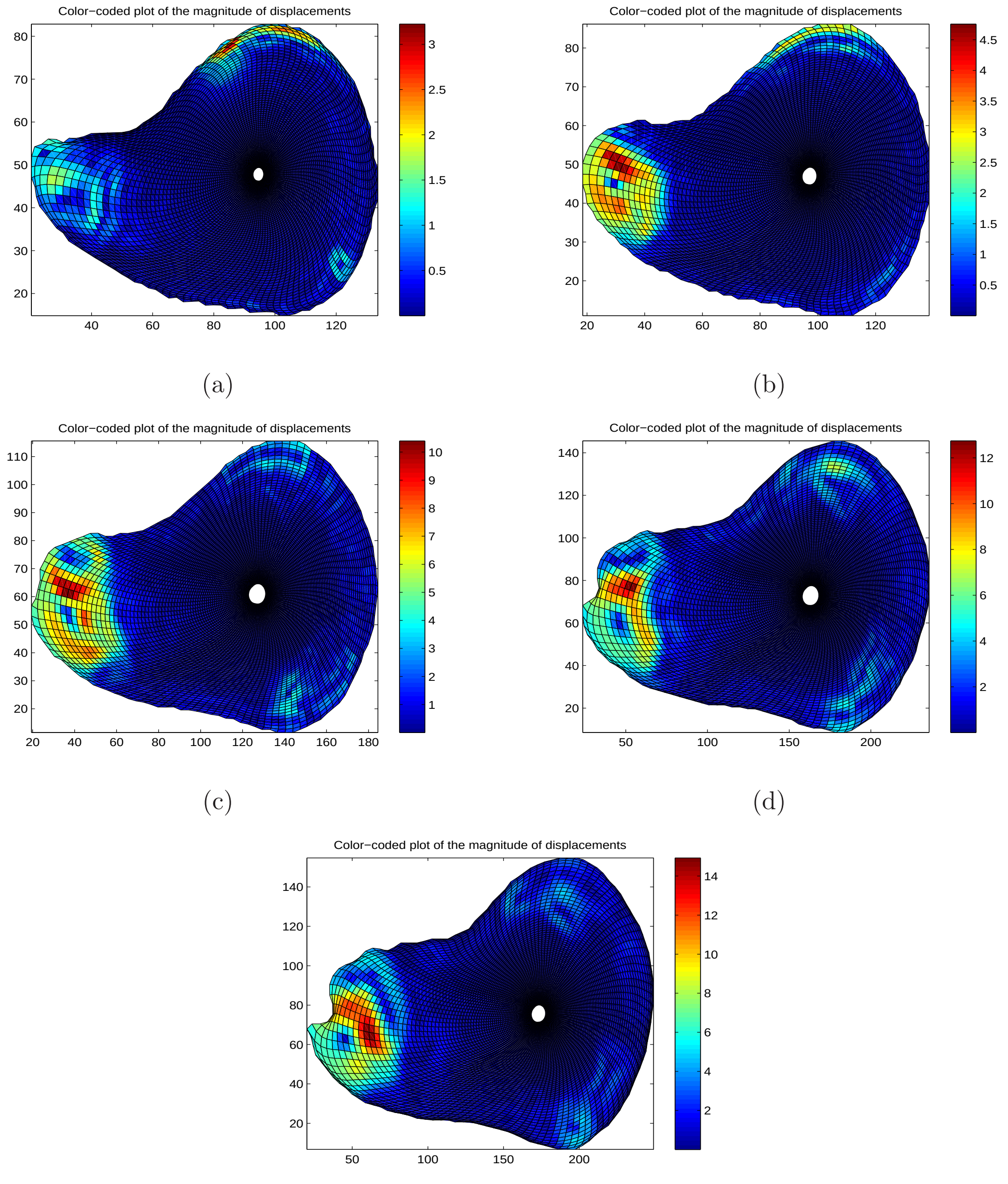

(a)

(b)

(c)

(d)

(e)

Figure 7.1.5: (a)-(e) Color-coded plot of the magnitude of the displacements for image pairs $(I_1,\ I_2)$, $(I_2,\ I_3)$, $(I_3,\ I_4)$, $(I_4,\ I_5)$ and $I_5,\ I_6$.

7.2 Inhomogeneous Poisson process of cell decisions

In this section we focus our efforts on the search for a prior model in the form of a probability measure of cell activities as represented by the Poisson intensity of elementary biological events. We discuss prior models for the unobserved intensity function as a Gaussian random field and as a random field governing a spatial Poisson point process. For the latter prior model we study the performance of the direct estimation algorithm depending on the value of the prior energy coefficient. Here, we also find experimentally the value that yields "best" inferences characterizing larval growth of Drosophila wing disc. We demonstrate inference results for the larval growth of the Drosophila wing disc assuming that the underlying biological process of cell divisions is inhomogeneous in space and time.

7.2.1 Poisson intensity as a Gaussian random field

In the Bayesian view the source of the growth-induced deformation is an unobserved space-time stochastic process

$$\{\lambda(\xi, t);\ \xi \in \Xi,\ 0 \leq t \leq T\}$$

defined on the planar lattice Ξ, called a *random field*. At a particular time instant we can consider such a process as a purely spatial process reflecting the fact that there is a large number of cell decisions (equal to the dimension of the problem N) occurring in the growing organism's domain according to the macroscopic growth law.

Assuming that on average cell decisions are equally likely to happen everywhere in the organism's domain we can define the mean intensity λ-field as

$$\langle \lambda(\xi, t) \rangle = \frac{1}{N} \text{ for } \forall t \in [0, T].$$

Note that this assumption is actually true for the larval development of the Drosophila wing disc. For simplicity we let all elements $\lambda(\xi_i, t)$, $i \in 1, 2, ..., N$ be stochastically independent. Then we can model each $\lambda(\xi_i, t)$ as a Gaussian distributed random variable with standard deviation σ_λ, that is $\lambda(\xi_i, t) \sim \mathcal{N}(\frac{1}{N}, \sigma_\lambda^2)$. So, at a time $t \geq 0$, $\lambda(\xi, t) = \Lambda(\xi)$ is a realization of the Gaussian random field with the probability measure

$$p(\Lambda(\xi)) = \frac{1}{(\sqrt{2\pi\sigma_\lambda^2})^N} \exp\left[-\frac{1}{2\sigma_\lambda^2} \cdot \sum_{\xi \in \Xi} (\Lambda(\xi) - \frac{1}{N})^2\right]. \qquad (7.2.1)$$

From (7.2.1) we define the prior energy

$$E_{prior}(\lambda(\xi, t)) = \frac{1}{2\sigma_\lambda^2} \cdot \sum_{\xi \in \Xi} \left(\lambda(\xi, t) - \frac{1}{N}\right)^2 \qquad (7.2.2)$$

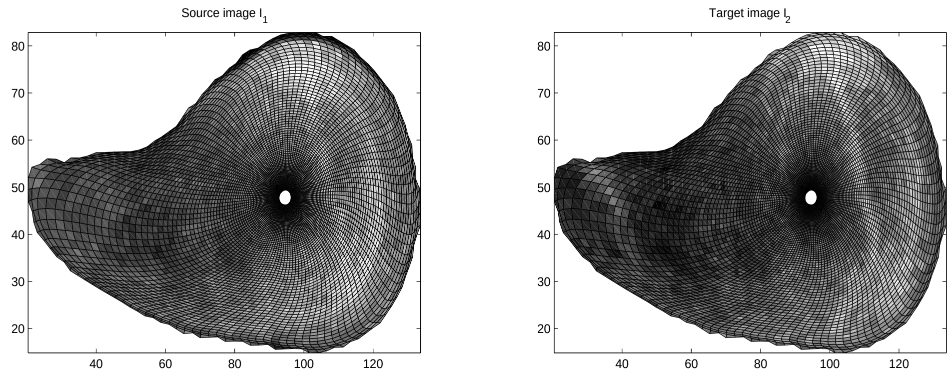

(a) (b)

Figure 7.2.1: (a) Source image $I_1(x(\xi),0)$ and (b) target image $I_2(x(\xi),T)$ interpolated on the Darcyan grid of the wing disc in I_1 obtained $T \approx 11$ hours later.

and formulate the resulting optimal control problem

$$\begin{aligned}\hat{\lambda}(\xi,T) =& \arg\min_{\lambda\in\Re^N\times[0,T]} \frac{1}{2\sigma_I^2}\cdot\sum_{\xi\in\Xi}[I_2(x(\xi),T)-I_1(x(\xi,T))]^2\cdot J(x(\xi))\\ &+\frac{1}{2\sigma_\lambda^2}\cdot\sum_{\xi\in\Xi}\left(\lambda(\xi,t)-\frac{1}{N}\right)^2,\end{aligned} \tag{7.2.3}$$

where $x(\xi,T)$ is subject to the macroscopic growth equation (6.2.2) (on page 153. Here, $J(x(\xi))$ denotes the Jacobian of the transformation $x = x(\xi)$ with respect to ξ. $x(\xi)$ refers to the initial Darcyan coordinate grid of the wing disc seen in the source image I_1. The optimization problem (7.2.3) is equivalent to

$$\begin{aligned}\hat{\lambda}(\xi) =& \arg\min_{\lambda\in\Re^N\times[0,T]} \sum_{\xi\in\Xi}(I_2(x(\xi),T)-I_1(x(\xi,T))^2\cdot J(x(\xi))\\ &+\left\|\Gamma\left[\lambda(\xi,t)-\frac{1}{N}\right]\right\|^2,\end{aligned} \tag{7.2.4}$$

where $\Gamma = \alpha I$ is a *Tikhonov matrix* with the *Tikhonov factor* $\alpha = \frac{\sigma_I}{\sigma_\lambda}$ and the identity matrix I. Thus, $\lambda(\xi,t)$ is a *Tikhonov-regularized solution* [20].

Observe that the larger the Tikhonov factor, the smaller the variation of $\lambda(\xi,t)$ throughout the organism's domain.

Using a 120×80 Darcyan grid for the initial Drosophila wing disc $I_1(x(\xi))$ as shown in Figure 7.2.1.a, with an initial guess on λ-field $\lambda(\xi,0) = \frac{1}{N}$, $N = 120 \times 80$, and $\alpha = 0.5$ or, equivalently, $\sigma_\lambda = 2\sigma_I$, we have implemented the direct estimation algorithm based on Polak-Ribière conjugate gradient method to solve the optimization problem (7.2.4). In Figures 7.2.2.a, 7.2.2.c, 7.2.2.e are shown, respectively, the estimates of the scalar λ-field, growth-induced transformation and the magnitude of the displacements obtained after 30 iterations.

As expected, $\lambda(\xi, T)$ is oscillating wildly throughout the domain causing local expansions of the initial Darcyan grid combined with local contractions as seen from Figures 7.2.2.a and 7.2.2.c. The magnitude of oscillations is small and the biological transformation $x(\xi, t)$ estimated from $\lambda(\xi, t)$, where $0 \leq t \leq T$, preserves the smoothness of the Darcyan grid curves, as seen from Figure 7.2.2.c. Such an estimate can describe biological growth with small regions in red designating cell division locations. It is possible that the dividing cells push out the neighboring cells causing local contractions of the cellular field (shown in blue). Regions of faster growth shown in dark red appear like isolated cell division cites distributed uniformly throughout the wing disc. This is the consequence of the stochastic independency and identical distribution of elements of the random field $\lambda(\xi, t)$.

The magnitudes of the displacements appear in a pattern of concentric circles that are spread out in the interior domain excluding the central part of the wing disc where there are no changes in Wingless protein concentration. The maximal magnitudes shown in red are achieved at the tips of anterior and dorsal parts of the wing disc (see Fig.7.2.2.e).

In order to obtain a smoother behavior of the optimal λ-field we increase the Tikhonov factor to 1. Minimization of the posterior energy (7.2.4) with $\alpha = 1$ leads to the desired smoothness of $\hat{\lambda}(\xi)$ resulting in a lesser overall deformation effect as seen from Figures 7.2.2.b and 7.2.2.d. The regions of high cell activity (cell divisions, cell shape change) appear restricted to the tip of the anterior part and the dorsal part of the wing disc. These are subregions of the wing disc where the highest Wingless protein concentration level mismatch is observed (see Fig.7.2.1) and where the estimated magnitudes of displacements are the largest (see Fig.7.2.2.f).

On the other hand, increasing the smoothness of $\lambda(\xi, t)$ leads to a less satisfactory estimate of the target image I_2 (see Fig.7.2.3.b). The image estimate shown in Figure 7.2.3.a is a better result in terms of contrast present in the dorsal part of the wing disc (see Fig.7.2.1.b) and full reconstruction of the area near the tip of the anterior part. In both cases the estimated biological transformation tends to blur edges such as boundaries of a band of high concentration of Wingless protein observed in the ventral part of the wing disc.

All in all, the prior Gaussian model of the λ-field considered above suggests a typical growth pattern in the form of isolated dividing cells. Such a growth mode can be suitable for particular organisms but, certainly, it is not a universal growth mode. Since our main goal is not achieving a perfect image registration but rather revealing qualitative picture of a biological growth via a natural measure of cell activities, namely, the Poisson intensity parameter $|\lambda(\xi, t)|$, we make an effort to find a more general prior model.

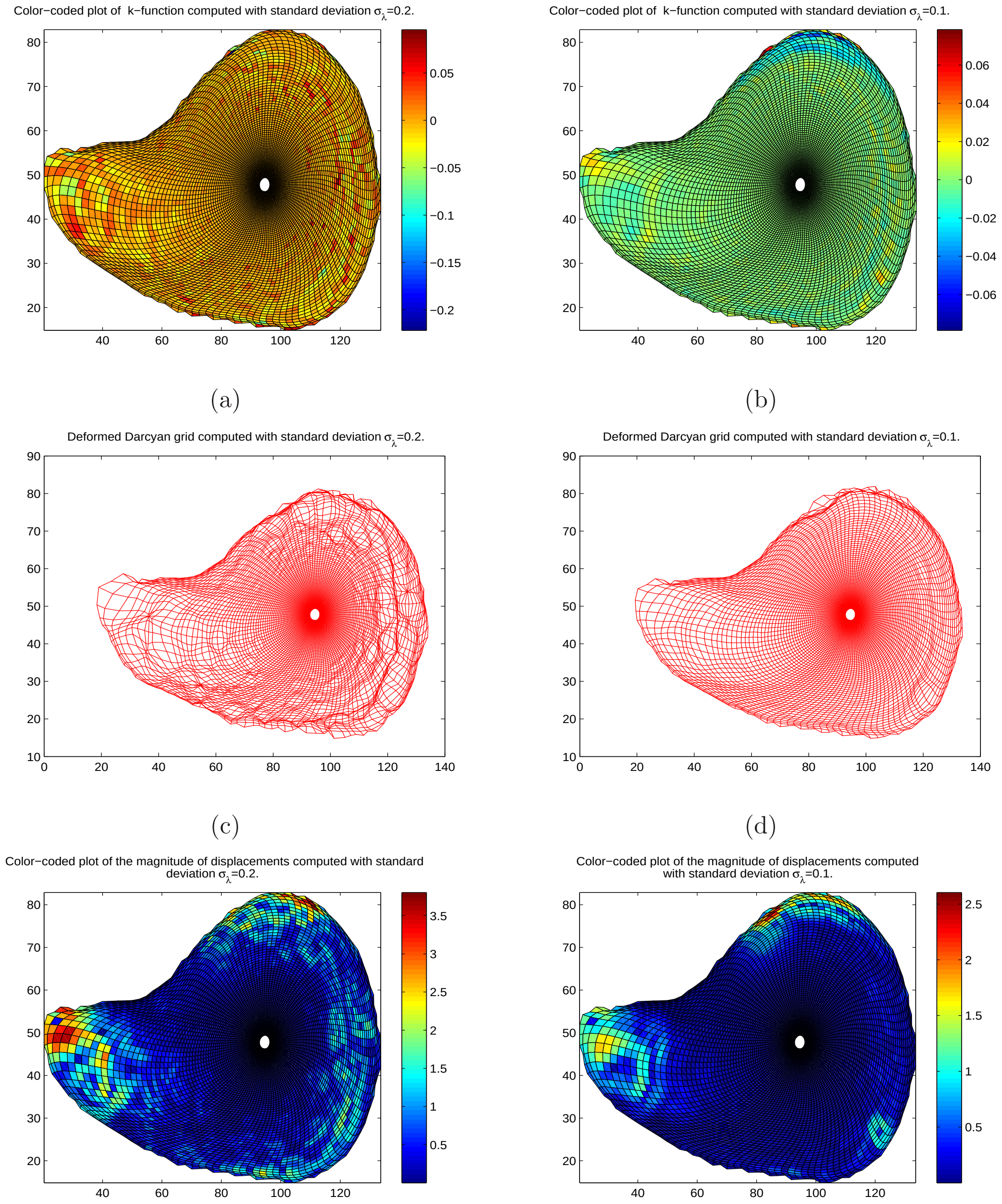

(a) (b)

(c) (d)

(e) (f)

Figure 7.2.2: Results of computations of optimal $\lambda(\xi, T)$ fields for the image pair $(I_1,\ I_2)$ (Fig.7.2.1) and for two values of the Tikhonov parameter α: (a), (c), (e) $\alpha = 0.5$ and (b), (d), (f) $\alpha = 1$. (a)-(b) The optimal $\lambda(\xi, T)$-field, (c)-(d) deformed Darcyan grid of the wing disc and (e)-(f) the magnitude of the displacements.

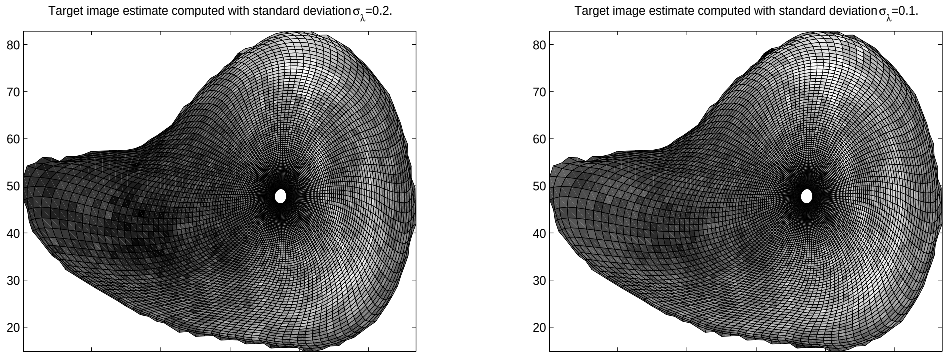

(a)

(b)

Figure 7.2.3: Estimates of target images $I_1(x(\xi, T))$ obtained with Tikhonov factor (a) $\alpha = 0.5$ and (b) $\alpha = 1$.

7.2.2 Poisson intensity as a random spatial field governing the Poisson process

We weaken the constraints on the λ-field and view it as a stochastic spatial process $\{|\lambda(\xi_{seed})\}|, \xi_{seed} \in \Xi\}$ defined in a planar continuous domain Ξ at each time t of a realization of the macroscopic growth equation. Its absolute value influences the occurrences of cell divisions modeled as points of a spatial Poisson process (seeds). That is, points in Ξ are distributed according to a stationary Poisson process in time with the Poisson intensity $|\lambda(\xi)|$. The process points occur in Ξ with the following probabilities,

$$Pr(N(\delta_{\xi_{seed}}) = 1|\xi_s \in \Xi \setminus \delta_{\xi_{seed}}, \xi_s \neq \xi_{seed}) = \int_{\delta_{\xi_{seed}}} |\lambda(\xi)|d\xi + o(|\delta_{\xi_{seed}}|), \quad (7.2.5)$$

where $\delta_{\xi_{seed}} \in \Xi$ is a small region centered at the Poisson point ξ_{seed}, N is a random number of seeds and ξ_s are all other seeds activated outside $\delta_{\xi_{seed}}$. To be more specific, for a fixed time t we define a doubly stochastic counting Poisson point process $\{N_\xi, \xi \in \Xi\}$ with intensity process $\{|\lambda(\xi_{seed})\}|, \xi_{seed} \in \Xi\}$ in the Darcyan space Ξ

$$Pr(N_A = n) = (n!)^{-1} \int_A |\lambda(\xi)|d\xi \cdot exp\{-\int_A |\lambda(\xi)|d\xi\}, \quad (7.2.6)$$

where $A \subset \Xi$ and n is the number of activated seeds.

Remark 7.2.1. *A spatial Poisson process is not totally separated from a temporal Poisson process. A stationary Poisson distribution in time is chosen as a model for a spatial Poisson process observed at a particular time instant* $t = j$*. That is, the optimal* $|\lambda(\xi_{seed}, j)| = |\hat{\lambda}(\xi_{seed})|$*, where* ξ_{seed} *are activated seeds in* Ξ*-space with their total number* N*. At different times we have different observations of gene expression patterns leading to different MAP estimates of the underlying Poisson intensity of cell decisions. Therefore, a divorce of the spatial process from the temporal process is rather artificial.*

Then at the time t, $\{x(\xi, t), \xi \in \Xi\}$ is a random two-dimensional vector field in the absolute space X influenced by the underlying doubly stochastic spatial Poisson point process. The Darcyan grid with n radial and m angular coordinate curves can be viewed as a result of the most likely realization of this process given observations in the form of images. It is the configuration of Darcyan nodes $\{x(\xi_{1_i}, \xi_{2_j}, t),\ 1 \leq i \leq n,\ 1 \leq j \leq m\}$ constructed from the path of the process $\{\xi; \xi \in \Xi\}$ yielding $N = n \times m$ Poisson points $\{\xi_{1_i}, \xi_{2_j}, t),\ 1 \leq i \leq n,\ 1 \leq j \leq m\}$ distributed with the optimal intensity parameter $|\hat{\lambda}(\xi_{seed})|$,

$$x(\xi, t) = x(\xi, 0) + \sum_{j=1}^{t} \sum_{\xi_{seed}=1}^{N} \frac{\theta(x(\xi, (j-1)) - x(\xi_{seed}, (j-1)))}{J(x(\xi_{seed}, (j-1)))} \cdot \hat{\lambda}(\xi_{seed}), \quad (7.2.7)$$

where $\xi \in \{1, 2, ..., N\}$.

For the doubly stochastic Poisson process $\{N_\xi, \xi \in \Xi\}$ the probability density of finding N points in small neighborhoods of $\xi_1, ..., \xi_N$ is

$$\begin{aligned} & p[\xi_1 \in \delta(\xi_1), \xi_2 \in \delta(\xi_2), ..., \xi_N \in \delta(\xi_N)] \\ & = \prod_{[i=1]}^{N} \int_{\delta(\xi_i)} |\lambda(\xi)| d\xi \cdot \exp\left[- \int_{\delta(\xi_i)} |\lambda(\xi)| d\xi \right], \end{aligned} \tag{7.2.8}$$

where the domain $\Xi = \bigcup_{[i=1]}^{N} \delta(\xi_i)$. Formula (7.2.8) defines the *sample-function density* for the spatial Poisson process with arbitrary ordering of position.

Since the number of events is large, it is reasonable to assume that $|\lambda(\xi)| = |\lambda(\xi_i)|$ in the small neighborhood of each Poisson point ξ_i of unit area, δ_{ξ_i}, with $1 \leq i \leq N$. Then the sample-function density simplifies to

$$\begin{aligned} p_\xi & = p[\xi_1 \in \delta(\xi_1), \xi_2 \in \delta(\xi_2), ..., \xi_N \in \delta(\xi_N] \\ & = \prod_{[i=1]}^{N} |\lambda(\xi_i)| \cdot \exp\{-|\lambda(\xi_i)|\}, \end{aligned} \tag{7.2.9}$$

The joint probability density for the doubly stochastic Poisson process appears to be a preferred representation of a prior knowledge about $|\lambda(\xi, t)|$ emphasizing not only its space and time varying nature (at each time t we have a different realization of the $|\lambda|$-field) but also its role in governing a biological process of cell decisions. It is a general prior model since no specific probability measure has been assigned to a random $|\lambda|$-field. Having generated the initial Darcyan grid with N nodes we view it as a result of a realization of a doubly stochastic Poisson spatial process. We find optimal measurements of the underlying Poisson intensity $\{|\lambda(\xi)|\}$ at N seed locations ξ_i that provide the shortest path $x(\xi, t)$ from the source image $I_1(x(\xi))$ to the target image $I_2(x(\xi), T)$.

Using the negative of the sample-function density logarithm for the prior energy term in the cost function

$$E_{prior}(\lambda(\xi, t)) = -\ln p_{\xi,t} = -\sum_{[i=1]}^{N} \ln |\lambda(\xi_i, t)| + \sum_{[i=1]}^{N} |\lambda(\xi_i, t)| \tag{7.2.10}$$

we formulate the following optimal control problem

$$\begin{aligned} \hat{\lambda}(\xi, T) = & \arg\min_{\lambda \in \Re^N \times [0,T]} \frac{1}{2\sigma_I^2} \sum_{\xi \in \Xi} (I_2(x(\xi), T) - I_1(x(\xi, T))^2 \cdot J(x(\xi)) \\ & - \sum_{[i=1]}^{N} \ln |\lambda(\xi_i, t)| + \sum_{[i=1]}^{N} |\lambda(\xi_i, t)|, \end{aligned} \tag{7.2.11}$$

where $x(\xi, t)$ is subject to the macroscopic growth equation (6.2.2)

Remark 7.2.2. *Since the cost function E_{post} depends on a high-dimensional intensity parameter $\lambda(\xi, t)$ it is not feasible to verify its convexity. It is possible that it* *possesses a few local minima and in this case a good initial guess on λ-field would ensure convergence of the conjugate gradient algorithm to the closest local minimum. A natural choice for $\lambda(\xi, 0)$ would be the uniform probability mass function assigned to N seeds in Ξ-space. This means that cell decisions are equally likely to occur anywhere in the organism's domain. We expect to obtain a perturbed version of the initially uniform distribution of seeds that would generate complex transformations reflecting inhomogeneous growth of the organism and bringing its source and target images into registration.*

We now examine $E_{prior}(\lambda(\xi, t)) : \Re^N \to \Re$ in more detail and drop time index t for the ease of notation. Its Hessian matrix, $H(E_{prior})$, is diagonal with entries

$$\frac{\partial^2 E_{prior}}{\partial^2 \lambda(\xi_i)} = \frac{1}{\lambda(\xi_i)^2}, \; \frac{\partial^2 E_{prior}}{\partial \lambda(\xi_i) \partial \lambda(\xi_j)} = 0, \; i \neq j \tag{7.2.12}$$

implying that it is positive-definite $\forall \lambda \in \Re \setminus \{0\}^n$

$$\lambda H(E_{prior}) \lambda^T \geq 0. \tag{7.2.13}$$

The prior energy possesses a global minimum attained at the stationary vectors in $\Re^N$ with components $\lambda_s(\xi_i) = -1$ or $\lambda_s(\xi_i) = 1$. Indeed,if $\lambda(\xi_i) > 0$

$$\frac{\partial E_{prior}}{\partial \lambda(\xi_i)} = -\frac{1}{\lambda(\xi_i)} + 1 = 0 \Rightarrow \lambda_s(\xi_i) = 1.$$

Similarly, if $\lambda(\xi_i) < 0$

$$\frac{\partial E_{prior}}{\partial \lambda(\xi_i)} = -\frac{1}{\lambda(\xi_i)} - 1 = 0 \Rightarrow \lambda_s(\xi_i) = -1.$$

Thus we obtain the critical value of the Poisson intensity $|\lambda_s(\xi)| = \vec{1}$ that maximizes the prior probability measure (7.2.9). The important implication of this result is that minimization of the prior energy term will force the Poisson intensity to stay close to the uniform probability distribution of seeds in Ξ-space at each time instant t and away from zero. This is consistent with the macroscopic growth law since it generates a growth deformation from a large number of seeds activated everywhere in the organism's domain. In the example of larval development of the Drosophila wing disc, such an optimal value of the Poisson intensity reflects biological evidence of the uniform division of cells throughout the whole cellular field.

The actual estimate of the growth parameter $\hat{\lambda}(\xi)$ that is most likely to occur in the presence of observations $(I_1(x(\xi)), I_2(x(\xi), T))$ provides more insight into organism's growth. Due to its varying sign it identifies contraction and expansion subregions in the organism's interior caused by growth. Clearly, the likelihood term plays a dominant role in finding $\hat{\lambda}(\xi)$ if there is a reason to believe that observed changes in pixel intensities are caused by a multitude of cell decisions such as cell division or death, for instance. In this case we would expect the estimated Poisson intensity $|\hat{\lambda}(\xi)|$ to disperse from the uniform probability density of seed placements and thus show subregions of higher level of cell activities.

Computational experiments using direct estimation algorithm suggest that the minimization of the proposed posterior energy yields an estimate of the λ-field that does not preserve the diffeomorphic property of the transformation $x(\xi, t)$, $0 \leq t \leq T$. We increase smoothness properties of $\lambda(\xi, t)$ by introducing an additional penalty term to our cost function in the form of the total variation integral,

$$\phi(\lambda) = \| \nabla\lambda \|_2^2 = \int_{\xi\in\Xi} |\nabla\lambda(\xi, t)|^2 d\xi,$$

as discussed in section 5.6. Including this term into the posterior energy and factoring out the coefficient $\frac{1}{\sigma_I^2}$ we arrive at the following optimal control problem at a time $t \geq 0$:

$$\begin{aligned}\hat{\lambda}(\xi, t) =& \arg\min_{\lambda\in\Re^N\times[0,T]} \sum_{\xi\in\Xi} \left[I_2(x(\xi), T) - I_1(x(\xi, t)^{-1})\right]^2 \cdot J(x(\xi)) \\ &+ \sigma_I^2 \cdot \left[\sum_{\xi_{seed}\in\Xi} [|\lambda(\xi, t)| - \ln|\lambda(\xi, t)|] + \sum_{\xi_{seed}\in\Xi} |\nabla\lambda(\xi, t)|^2 \right]\end{aligned} \tag{7.2.14}$$

subject to the discretized macroscopic growth equation

$$\begin{aligned}x(\xi, t) =& x(\xi, 0) + \sum_{j=1}^{t} \sum_{\xi_{seed}\in\Xi} [x(\xi, j-1) - x(\xi_{seed}, j-1)] \cdot \\ & exp\left(-\frac{\|x(\xi, j-1) - x(\xi_{seed}, j-1)\|^2}{step(x(\xi_{seed}, j-1))^2} \right) \cdot \frac{\lambda(\xi_{seed}, j)}{J(x(\xi_{seed}, j-1))}\end{aligned} \tag{7.2.15}$$

for all seeds $\xi = (\xi_1, \xi_2)$, $1 \leq \xi_1 \leq n$, $1 \leq \xi_2 \leq m$.

We now consider the variance σ_I^2 to be a constant. In the above setup σ_I^2 plays the role of the weighting coefficient that determines the dominant term in the cost function. Before we apply the inference algorithm to our image data we have to specify the value of σ_I^2. High values of σ_I^2 (of order $O(1)$) make the prior energy a dominating term. This is undesirable since information given in observations becomes ignored. So, we find the value of σ_I^2 experimentally, starting from 1 and then decreasing its value by a factor of 0.1. The idea is to choose the value at which the posterior energy reaches the absolute minimum as a function of σ_I^2.

7.2.3 The role of a prior energy coefficient

For a pair of images $(I_1(x(\xi)), I_2(x(\xi), T))$ we have performed 10 experiments with a number of values of σ_I^2. For each experiment i, $\sigma_I^2(i) = 0.1^{i-1}$. Shown in Figure 7.2.5 is the dynamics of $\hat{\lambda}(\xi)$ as a function dependent on the value of σ_I^2. For $\sigma_I^2 = 1$ the estimate $\hat{\lambda}(\xi)$ lies nearly at the bottom floor of the prior energy surface valley given by $\vec{1} \in \Re^N$ as seen from Figure 7.2.5.a. For the next value $\sigma_I^2 = 0.1$ the estimate of λ-field falls into another valley of E_{prior}, namely, $\overrightarrow{-1} \in \Re^N$ as seen from

Figure 7.2.5.b. This is due to the fact that both values of σ_I^2 make E_{prior} dominate over $E_{likelihood}$. Therefore, the obtained λ-estimates appear close to $\vec{1}$ and $-\vec{1}$, the points of minimum of E_{prior} in $\Re^N$.

$\hat{\lambda}(\xi)$ remains negative for σ_I^2 of order between $O(0.1^5)$ and $O(0.1)$ as shown in Figures 7.2.5.b-7.2.5.e. This is not a meaningful estimate since it implies a shrinking of the entire wing disc area. For σ_I^2 of order between $O(0.1^8)$ and $O(0.1^5)$ $\hat{\lambda}(\xi)$ becomes mostly positive with higher values at the top edge of the anterior part of the wing disc shown in red rapidly decreasing to negative values shown in blue (see Fig.7.2.5.f-7.2.5.i). This result suggests growth of the wing disc with a faster growing top edge causing contraction of the subregion lying next to it. Observe more complex behavior of $\hat{\lambda}(\xi)$ with the presence of occasional highly localized expansions and a band of expansions running across the ventral part of the wing disc for a particular choice of $\sigma_I^2 = 0.1^7$ (see Fig.7.2.5.h -7.2.7.h).

Shown in Figures 7.2.7.a-7.2.7.i are the deformed Darcyan grids generated by flows $x(\xi, t), 0 \leq t \leq T$ corresponding to λ-estimates given in Figures 7.2.5.a-7.2.5.i. As predicted by $\hat{\lambda}(\xi)$, the estimated transformation $x(\xi, T)$ reflects pure growth for $\sigma_I^2 = 1$ (see Fig.7.2.7.a), pure decay for σ_I^2 of order between $O(0.1^4)$ and $O(0.1)$ (see Fig.7.2.7.b-7.2.7.e) with contractions mostly concentrated near the dorsal boundary of the organism, mixed development for σ_I^2 of order between $O(0.1^8)$ and $O(0.1^5)$ (see Fig.7.2.7.f-7.2.7.i) with the combination of subregions of expansions and contractions mostly present near the top edge of the anterior part of the wing disc.

The magnitudes of the displacement $\| x(\xi, 0) - x(\xi, T) \|$ appear concentrated near the dorsal boundary of the wing disc that diffuses into the interior for the σ_I^2 of order decreasing from $O(1)$ to $O(0.1^4)$ as seen from Figures 7.2.9.a-7.2.9.e. For lower orders of σ_I^2 the concentration becomes higher at the top edge of the anterior part (see Fig.7.2.9.f-7.2.9.i) and more spread for $\sigma_I^2 = 0.1^7$ (see Fig.7.2.9.h).

All in all, the value of the prior energy weighting coefficient σ_I^2 influences qualitatively inference of the growth parameter $\lambda(\xi, t)$. As observed from Figure 7.2.5 meaningful estimates of λ-field are obtained for orders of σ_I^2 lower than $O(0.1^4)$.

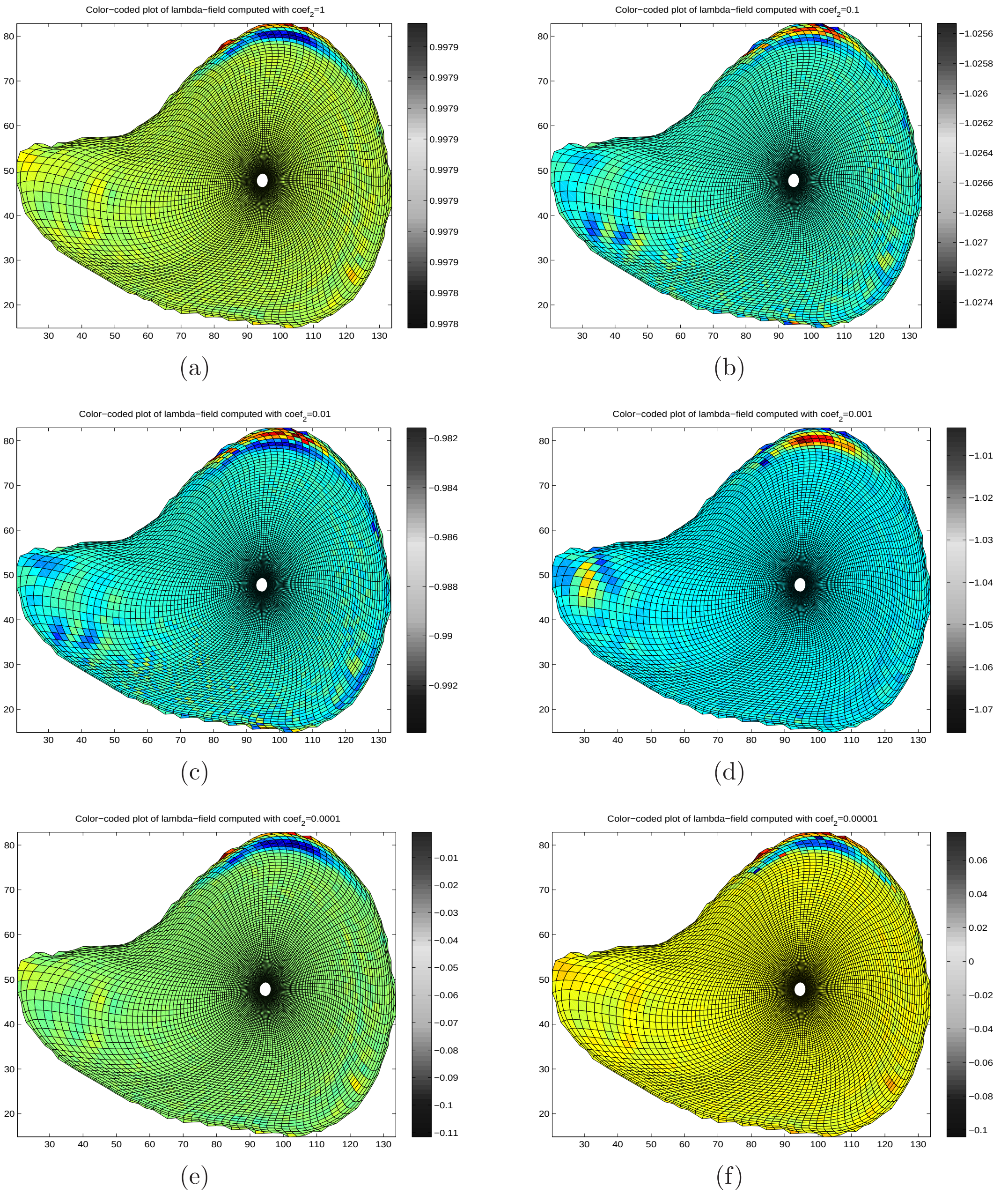

(a) (b)

(c) (d)

(e) (f)

Figure 7.2.4: (a)-(f) Color-coded plots of $\hat{\lambda}(\xi)$ for the image pair $(I_1,\ I_2)$ corresponding to the decreasing sequence of $\{\sigma_I^2(i)\}_{i=1}^{6}$.

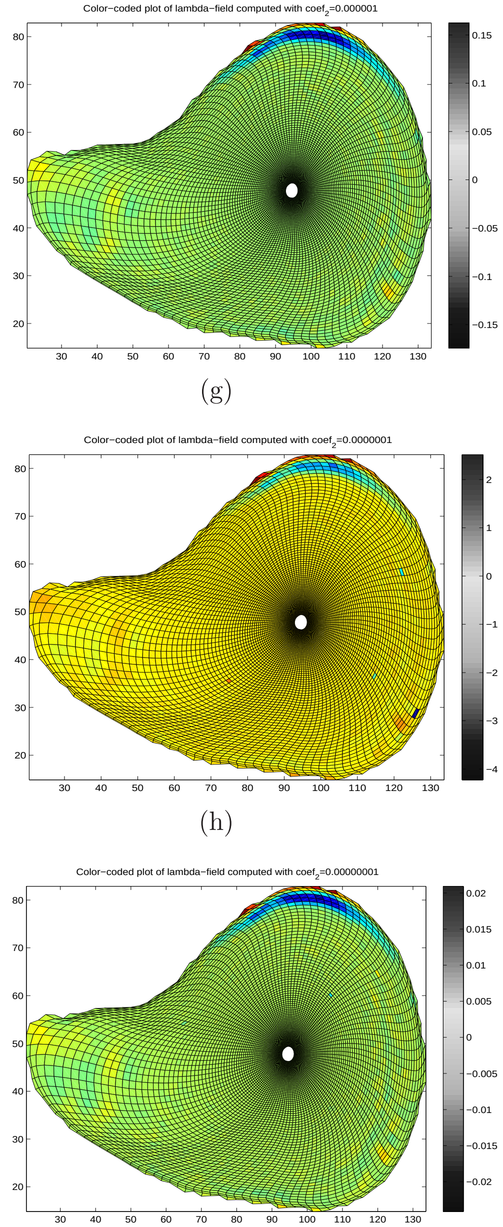
Color−coded plot of lambda−field computed with coef$_2$=0.000001

(g)

Color−coded plot of lambda−field computed with coef$_2$=0.0000001

(h)

Color−coded plot of lambda−field computed with coef$_2$=0.00000001

(i)

Figure 7.2.5: (g)-(i) Color-coded plots of $\hat{\lambda}(\xi)$ for the image pair (I_1, I_2) corresponding to the decreasing sequence of $\{\sigma_I^2(i)\}_{i=7}^{9}$.

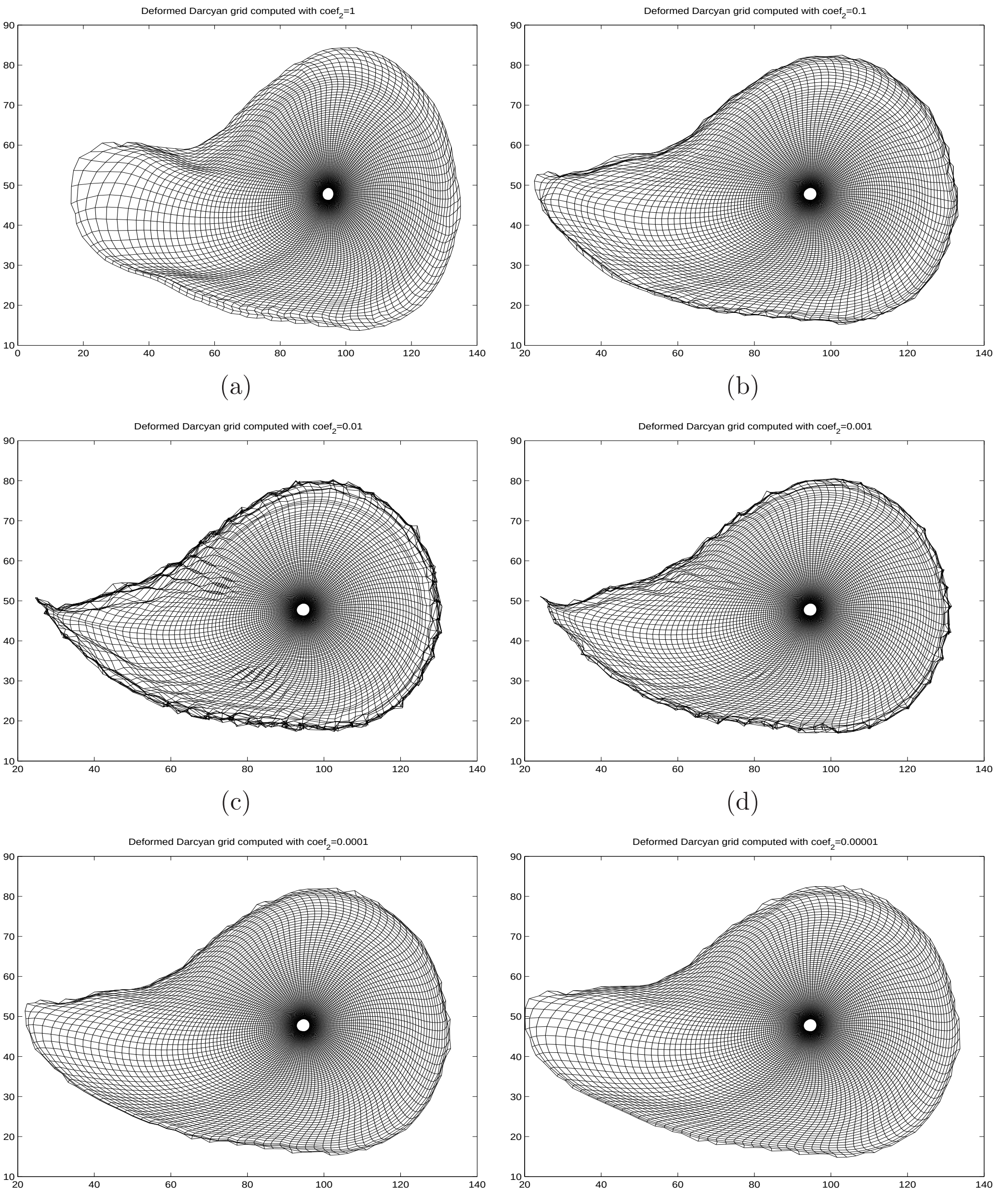

(a) (b)

(c) (d)

(e) (f)

Figure 7.2.6: (a)-(f) Deformed Darcyan grids of the wing disc generated by $x(\xi, t)$, $0 \leq t \leq T$ corresponding to the decreasing sequence of $\{\sigma_I^2(i)\}_{i=1}^6$.

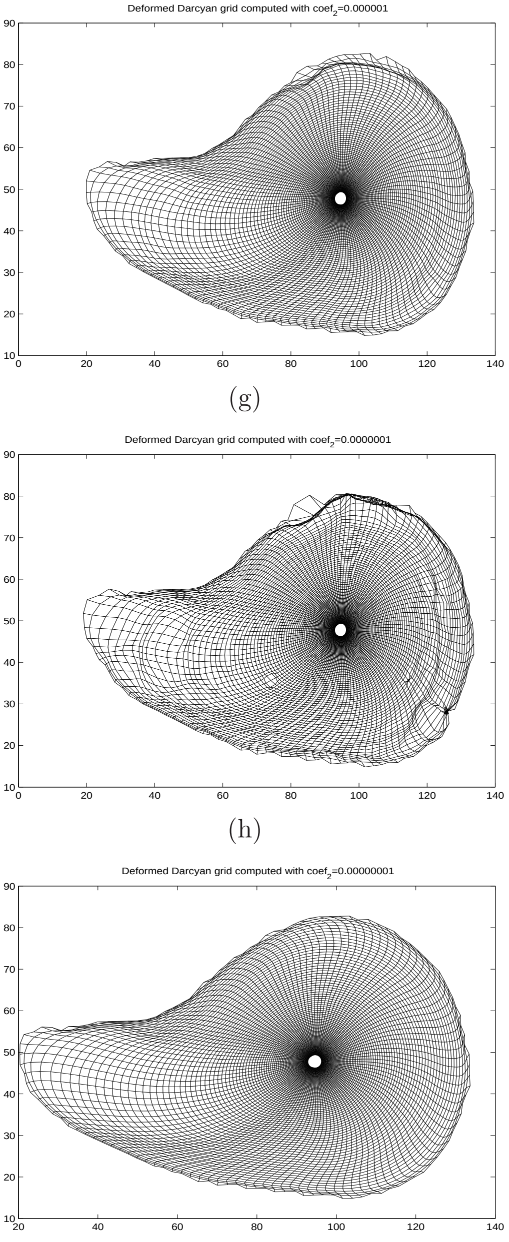

(g)

(h)

(i)

Figure 7.2.7: (g)-(i) Deformed Darcyan grids of the wing disc generated by $x(\xi, t)$, $0 \leq t \leq T$ corresponding to the decreasing sequence of $\{\sigma_I^2(i)\}_{i=7}^{9}$.

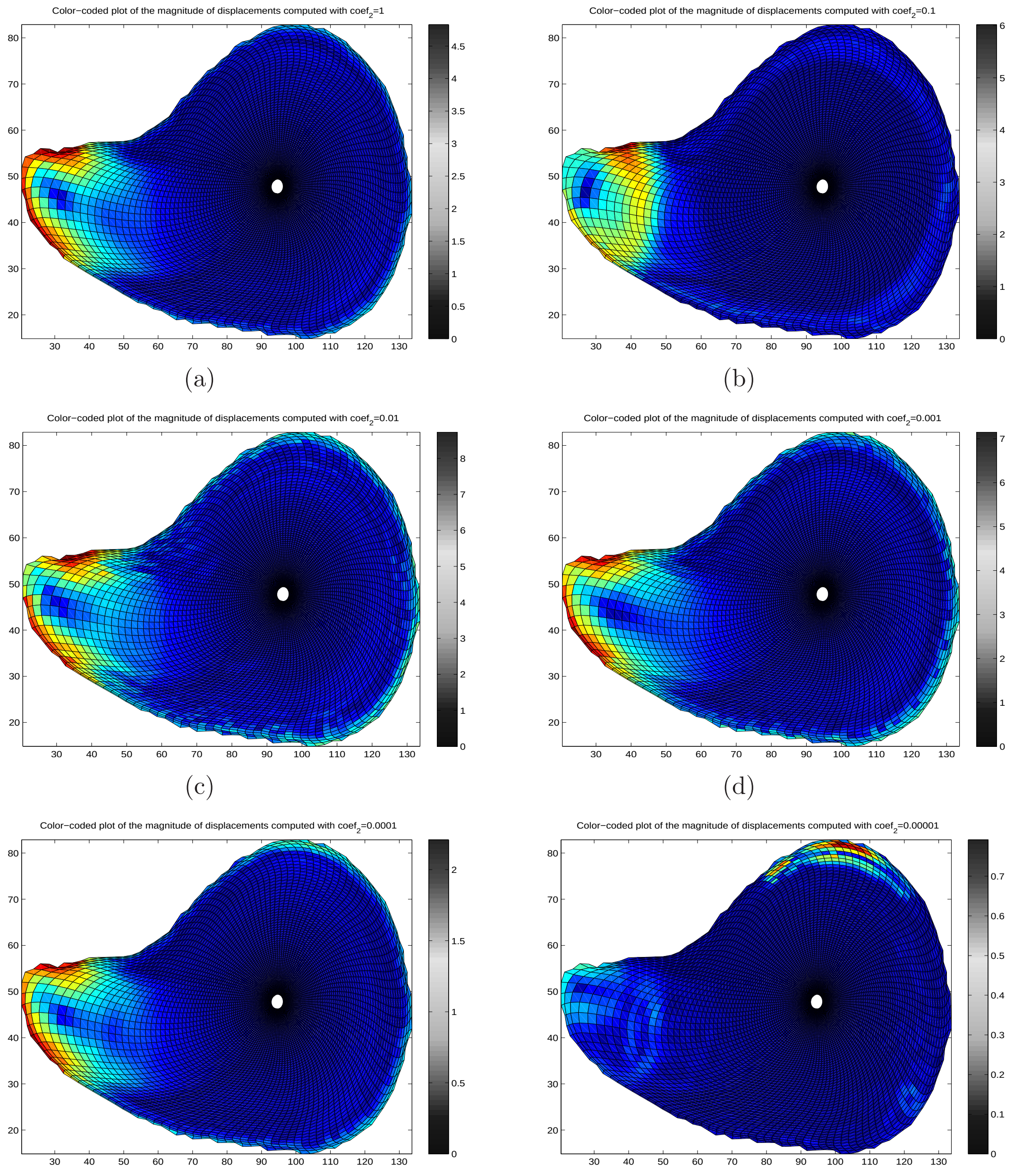

(a) (b) (c) (d) (e) (f)

Figure 7.2.8: (a)-(f) Magnitudes of the displacements corresponding to the decreasing sequence of $\{\sigma_I^2(i)\}_{i=1}^{6}$.

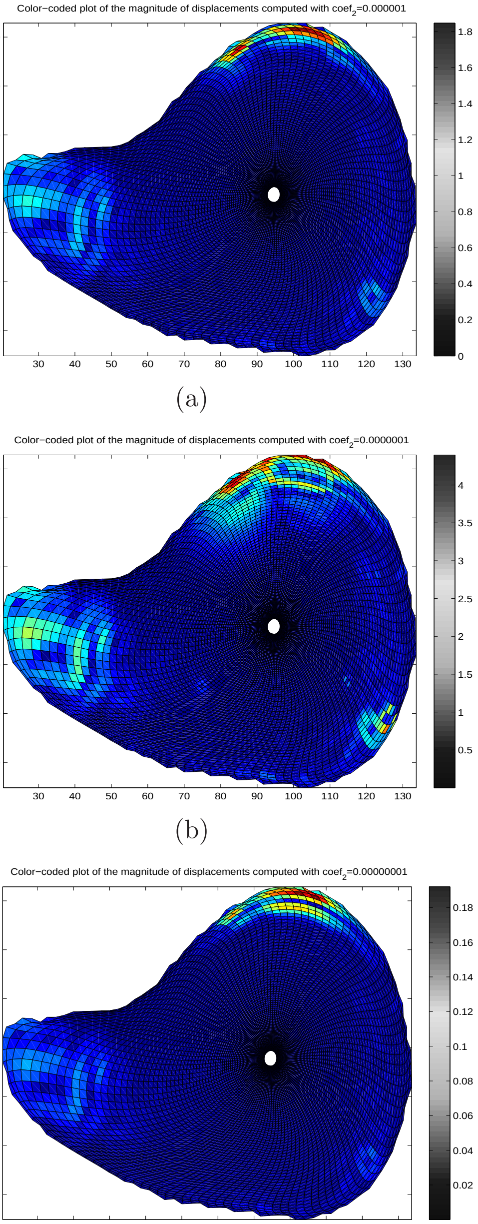

Color−coded plot of the magnitude of displacements computed with coef_2=0.000001

(a)

Color−coded plot of the magnitude of displacements computed with coef_2=0.0000001

(b)

Color−coded plot of the magnitude of displacements computed with coef_2=0.00000001

(c)

Figure 7.2.9: (g)-(i) Magnitudes of the displacements corresponding to the decreasing sequence of $\{\sigma_I^2(i)\}_{i=7}^{9}$.

As the next step in our search for the 'best' estimate of λ-field minimizing the posterior energy over the set $\{1, 0.1, 0.1^2.,,,, 0.1^9\}$ of possible σ_I^2 values, we examine the posterior, prior and likelihood energies as functions of σ_I^2. Recall that

$$E_{post}(\lambda, \sigma_I^2) = E_{likelihood}(\lambda) + \sigma_I^2 \cdot [E_{prior}(\lambda) + \|\nabla\lambda\|_2^2].$$

It appears that the second term $[E_{prior}(\lambda) + \|\nabla\lambda\|_2^2]$ dominates, i.e. it has values three orders of magnitude greater than the first term $E_{likelihood}(\lambda)$. The penalty function $\|\nabla\lambda\|_2^2$ is the smallest in magnitude term compared to $E_{prior}(\lambda)$ and $E_{likelihood}(\lambda)$. We expect that an order of magnitude of σ_I^2 be at most 10^{-4} to yield meaningful inference results.

Plots of these energies are presented in Figure 7.2.10 showing that the minimum is achieved at the value of $\sigma_I^2 = 0.1^7$. Since the energy functions have been evaluated at a discrete set of points we can state that $\sigma_I^2 = 0.1^7$ is approximately a local minimizer of E_{prior} and an absolute minimizer of $E_{likelihood}$ and E_{post}.

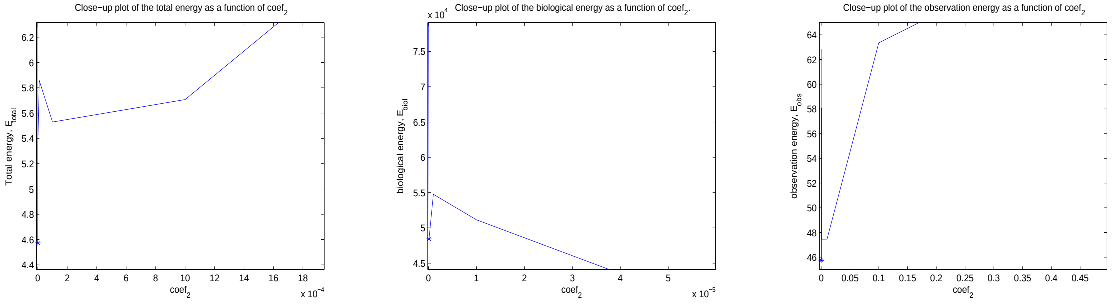

(a) (b) (c)

Figure 7.2.10: Close-up plots of (a) the posterior energy E_{post}, (b) the prior energy E_{prior} and (c) the likelihood energy $E_{likelihood}$ as a function of σ_I^2.

We conclude that with $\sigma_I^2 \sim O(0.1^7)$ we obtain a biologically meaningful estimate of λ-field and the best estimate of the target image (see Fig.7.2.11). As seen from Figure 7.2.5.h, the corresponding λ-field appears to be mostly positive throughout the domain of the wing disc except for a stripe-like subregion near the top edge of its anterior part shown in blue. Cell divisions have occurred everywhere with the peak of cell activities located near the top edge of the anterior part. This is a subregion with the highest mismatch of grey levels between source and target images $I_1(x(\xi))$ and $I_2(x(\xi), T)$ (see Fig.7.2.11.a-7.2.11.c). Also, the corresponding growth deformation $x(\xi, t)$ shown in Figure 7.2.7.h captures other changes in image pixel values such as a band of Wingless protein concentration near the ventral boundary seen in both images. It is possible that the rate of cell division is a bit higher in this subregion thus causing local contractions of its neighborhood.

The prior model of the λ-field implemented above suggests a typical growth pattern in the form of cells dividing in clusters with occasional appearance of isolated sites for the developing Drosophila wing disc. This result is qualitatively different from the one obtained using the prior Gaussian model. Elements of the estimated $\hat{\lambda}(\xi, T)$ appear correlated with their neighbors due to a more general view of $\lambda(\xi, t)$

as a random smooth field.

Having experimental evaluation of the weighting coefficient of E_{prior} built into our inference algorithm we now infer growth properties of the Drosophila wing disc from the sequence of micrographs of Wingless gene expression pattern at larval stage of its development.

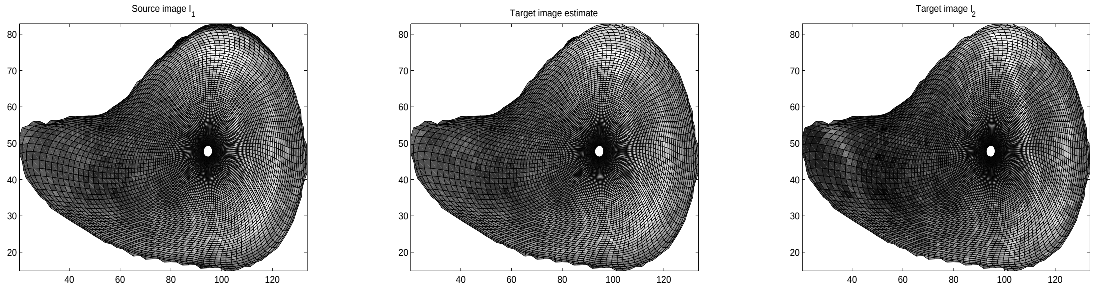

(a) (b) (c)

Figure 7.2.11: (a) Source image $I_1(x(\xi))$, (b) Target image estimate $I_1(x(\xi, T))$, (c) Target image $I_2(x(\xi), T)$.

7.2.4 Hidden patterns of growth in a sequence of micrographs

Taking into account the implicit dependency of the λ-field on the weighting coefficient of the prior energy term, σ_I^2, we modify our original direct estimation algorithm to yield the “best” estimate of $\lambda(\xi, t)$ that corresponds to the value of σ_I^2 minimizing the cost function. We apply it to the consecutive pairs of images given in the sequence of micrographs of Wingless expression pattern in Figure 7.2.12. As

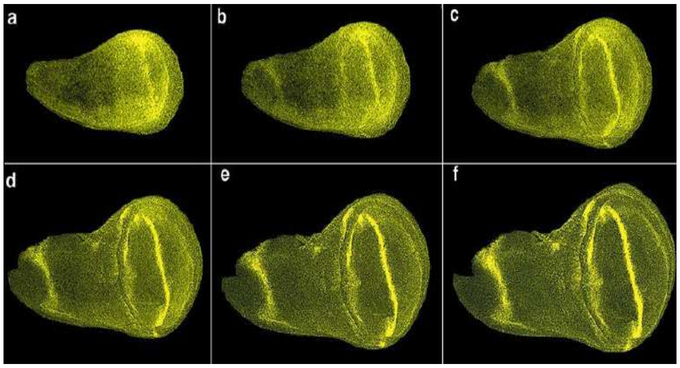

Figure 7.2.12: Dynamics of Wingless gene expression pattern $I(x, t)$ during the larval development of a wing disc from the second ($T \approx 48$ after egg laying) (a) through the third instar ($T \approx 120$ hours after egg laying) (f).

{Courtesy of S. Paddock and D. McDougal, University of Wisconsin, USA,[50]} a result, we reveal the underlying dynamics of λ-field controlling growth-induced deformation of the Darcyan grid of the Drosophila wing disc $x(\xi, t)$ as shown in Figures 7.2.15.a, 7.2.15.b, 7.2.15.g, 7.2.15.h, 7.2.15.n. At the early second instar of larval development (see Figures 7.2.15.a, 7.2.15.c, 7.2.15.e) the subregion of high cell activities stretches near the top edge of the anterior part where the organism undergoes large contractions next to the thin band of expansions. The magnitudes of displacement form patterns of oval rings with the largest values located at the top anterior edge.

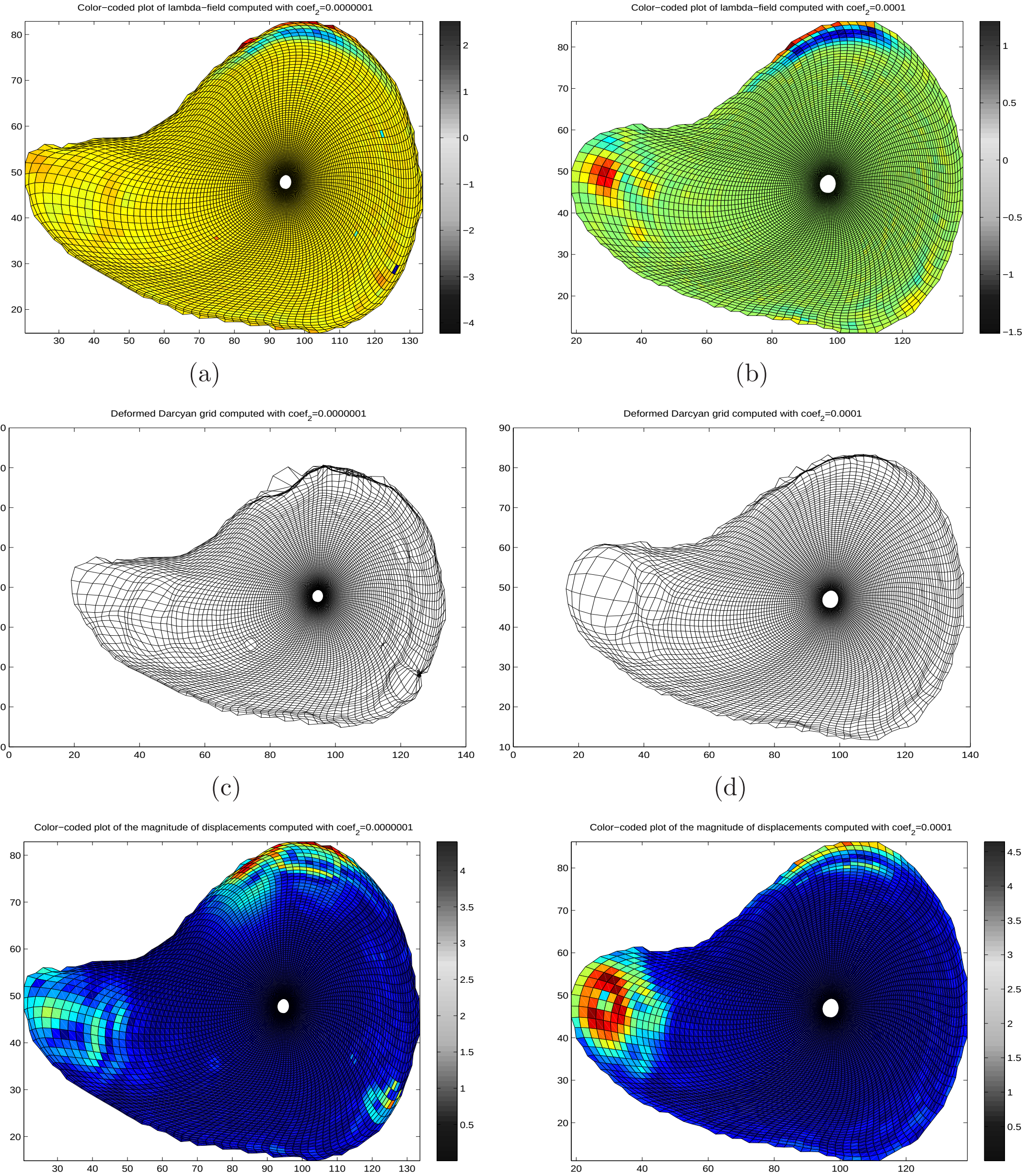

(e) (f)

Figure 7.2.13: The best estimates of $\lambda(\xi, T)$, $x(\xi, T)$ and $\|\Delta x(\xi, T)\|$ for an image pair (a), (c), (e) $(I_1,\ I_2)$, $\sigma_I^2 = 0.1^7$, (b), (d), (f) $(I_2,\ I_3)$, $\sigma_I^2 = 0.1^4$.

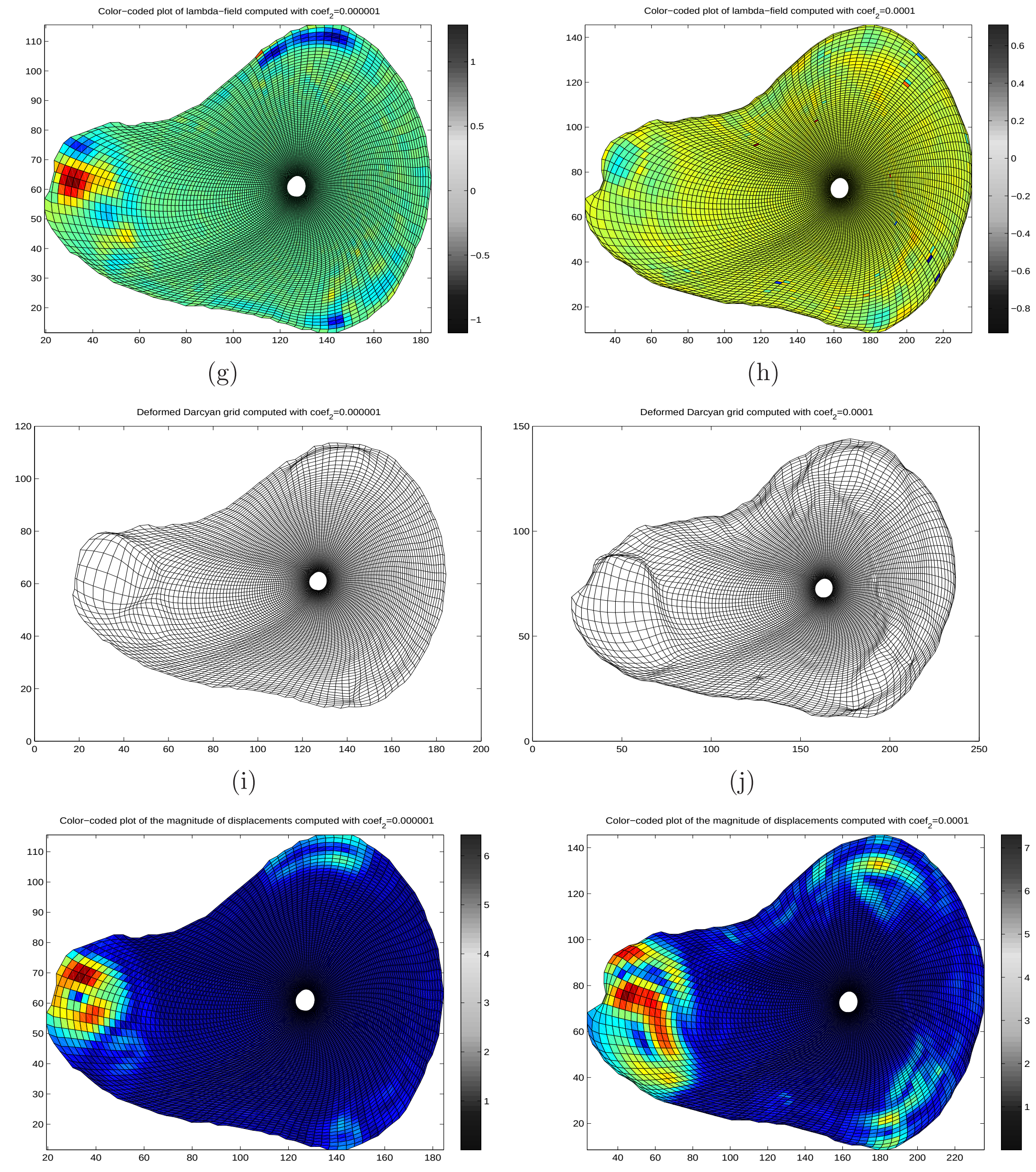

(g) (h)

(i) (j)

(k) (l)

Figure 7.2.14: The best estimates of $\lambda(\xi, T)$, $x(\xi, T)$ and $\|\Delta x(\xi, T)\|$ for an image pair (g), (i), (k) $(I_3,\ I_4)$, $\sigma_I^2 = 0.1^6$, (h), (j), (l) $(I_4,\ I_5)$, $\sigma_I^2 = 0.1^4$.

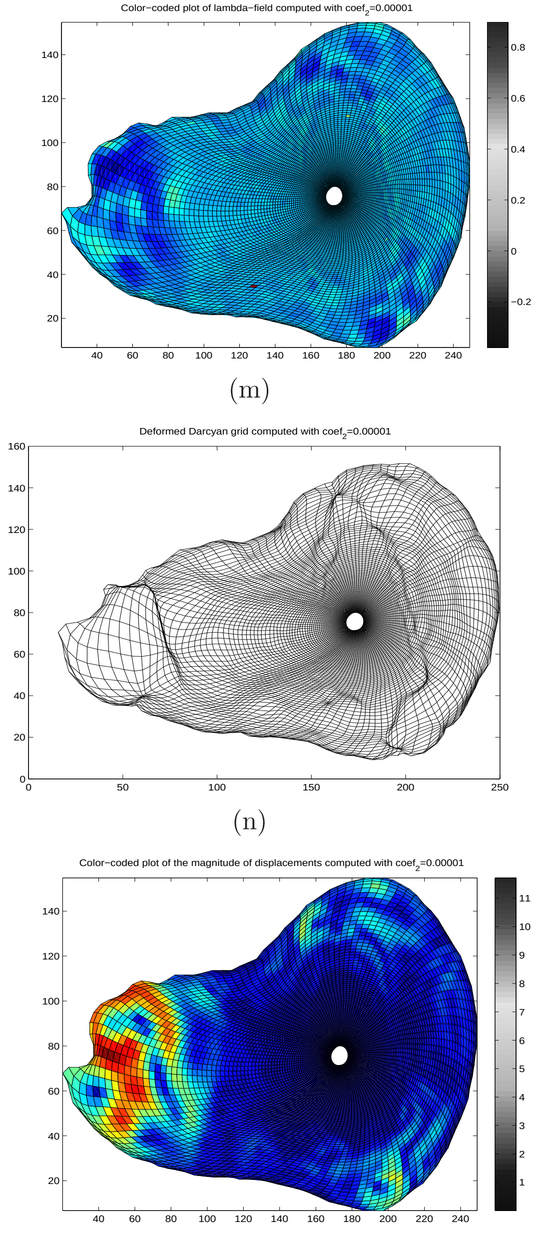

(m)

(n)

(o)

Figure 7.2.15: (m)-(o) The best growth estimates of $\lambda(\xi, T)$, $x(\xi, T)$ and $\|\Delta x(\xi, T)\|$ for an image pair $(I_5,\ I_6)$, $\sigma_I^2 = 0.1^5$.

There is also a visible concentration of lesser-magnitude deformations in the dorsal part of the wing disc. Mostly positive λ-values here suggest a faster growth of this region as compared to the central part of the disc.

As seen from Figures 7.2.15.b, 7.2.15.d, 7.2.15.f the peak of high cell activities moves to the dorsal part of the wing disc. Faster growth of the dorsal part occurs in a pattern of a large and two small discs with the largest magnitude of displacements forming a wide concentric ring. There is still a presence of large contractions close to the top edge of the anterior part, but the magnitudes of displacements pattern is changed to a couple of separate band-like subregions.

Figures 7.2.15.g, 7.2.15.i,7.2.15.k show a high concentration of cell divisions near the tip of the dorsal part causing contractions of larger/smaller magnitude in the anterior/posterior directions. The organism also undergoes contractions near the top anterior edge, but the magnitude of this deformation is significantly decreased.

In the following triplet of Figures 7.2.15.h, 7.2.15.j, 7.2.15.l, subregions of contraction appear larger in size and with smaller magnitudes of deformation in the anterior direction of dorsal and posterior parts and near the top anterior boundary. The intensity of cell divisions is relatively uniform throughout the wing disc. As a result, the magnitudes of deformation pattern evolves in the form of a larger disc in the dorsal part and band-like subregions in the posterior part and near the top anterior boundary.

At the late third instar of larval development seen in Figures 7.2.15.m-7.2.15.o subregions of contraction become more spread throughout the wing disc with the largest one arising as a wide band across the dorsal part. There is also a band-like subregion of expansions with contractions on both sides seen in the ventral part of the disc. Such deformations capture changes in the location of the highest concentration of Wingless protein. A combination of local contractions and expansions yields a complex growth deformation manifesting itself in a variety of forms throughout the wing disc.

The modified direct estimation algorithm based on the prior energy in the form of a sample-function density allows us to capture local deformations inside the domain of organism. As seen from Figures 7.2.16.a and 7.2.16.c, a band of the highest concentration of Wingless protein becomes slightly wider. One can imagine a series of cell divisions occurring in this narrow subdivision of the wing disc. The deformation effects of such cell activities are shown as the expansion band with contractions on both sides in the deformed Darcyan grid.

7.2.5 Summary

In this chapter we have derived the GRID macroscopic growth integro-differential equation from the microscopic properties of the Poisson driven Markov process of motion due to growth. Its solution is a diffeomorphic flow dependent on the GRID growth variables such as the Poisson intensity of cell decisions and the rate of contraction/expansion. It represents the growth pattern on a coarse time scale which underlies visible shape changes seen in images.

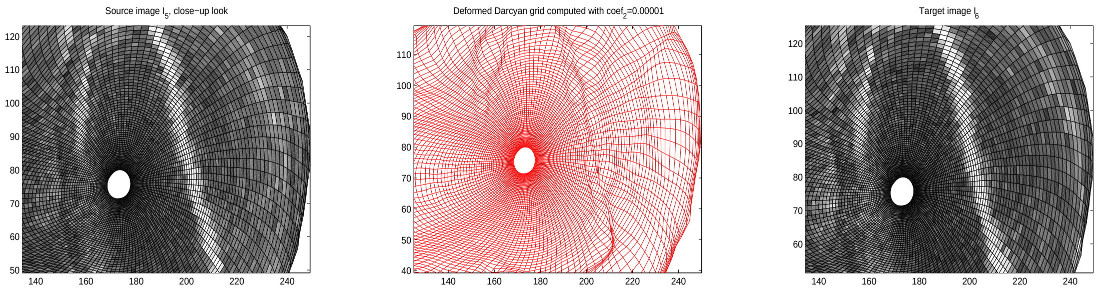

(a) (b) (c)

Figure 7.2.16: Close-up fragment of (a) the source image I_5, (b) the deformed Darcyan grid $x(\xi, T)$ and (c) the target image I_6.

One of the important properties discussed here is consistency of the macroscopic growth equation with the principle of biological invariance. We have shown that the inferred Poisson intensity parameter is invariant with respect to the Euclidean group of transformations of the Darcyan coordinate system of the organism.

We have introduced the discrete macroscopic growth operator and studied its regularity properties necessary for numerical stability of the inference. Since the inference problem is ill-posed a constraint on the intensity function that ensures its smoothness throughout the organism's domain is needed.

Following the methodology of computational anatomy in which a flow generates the shortest path from one specimen to another, we have formulated a *maximum a posteriori* estimation problem using the macroscopic growth law. Modeling the cost function as a Gibbs potential that is the sum of observation (or likelihood) and prior energies we have applied the Gaussian observation model that relates the image data with the unknown intensity parameter.

With the assumption of uniform space-time probability distribution of cell decisions, the unknown GRID growth variable represents a local rate of contraction/expansion throughout the domain of a growing organism. Based on the cost function in the form of the likelihood energy only the inference algorithm cannot generally be run to full convergence since the preservation of the organism's topology is not guaranteed.

With the assumption of non-uniform space-time probability distribution of cell decisions and constant rate of contraction/expansion we can increase the accuracy of our estimate to yield more realistic growth patterns as driven by the cell activities. For this purpose we have proposed and investigated prior models for the unobserved intensity function as a Gaussian random field and as a random field governing a spatial Poisson point process. The latter choice is biologically motivated and consistent with the discretized version of the macroscopic growth law.

For the latter prior model we have studied the performance of the direct estimation algorithm depending on the value of the prior energy coefficient. This weighting coefficient is a measure of independence between the observed dynamics of the gene expression pattern of interest and the growth process. Its values of order $O(1)$ suggest that the growth process does not drive changes in the initial pattern of protein concentration into a registration with the observed pattern in the grown Drosophila wing disc. Here, we also have found experimentally the value that yields “best” inferences characterizing larval growth of Drosophila wing disc.

We have estimated the Poisson intensity field and the biological transformation of the growing wing disc from the sequence of micrographs of Wingless gene expression patterns. We conclude that if there is experimental evidence that the observed dynamics of levels of a particular gene expression depends on an underlying biological process of cell decisions, then we can establish this hidden connection at least in principle via *maximum a posteriori* estimation of the intensity of cell decisions and the growth-related transformation.

Chapter 8

Conclusions

This thesis has shown that the GRID approach is well-suited for the modeling of biological growth in terms of gene expression patterns. However, the proposed GRID-based inference algorithm is not restricted to analysis of micrographs of gene expression patterns in a growing organism. It can also be applied for analysis of MRI growth images of a human anatomical structure, and, as a result, it can deform a growing anatomy in accordance with fundamental biological principles of growth. Since anatomical growth patterns are four-dimensional, extension of the inference method to three-dimensional organisms is needed and left to the future.

In this work, topology-preserving types of biological growth using the GRID model have been studied. Extending applications of the GRID model to heteromorphic growth is a future research direction leading to image recognition of heteromorphic pathology. This deformation type implies more drastic topological changes such as adding neoplasm (tumor growth) or eliminating structures (tissue decay). The GRID model appears to be appropriate for description of this type since it allows to capture such anomalies by introducing more seeds or eliminating them at random. The heteromorphic GRID model together with Neyman-Pearson hypothesis testing can then be used for recognition of an anomaly.

This research has resulted in a contribution to multiple fields of research:

1. A genetically-based model of a biological growth in quantitative biology. Experimental study and formalization of the isotropic 1D GRID model using theory of stochastic processes have formed a new general picture a growing organism as a force-free evolution of a discrete seed configuration in absolute space-time driven by the inhomogeneous Poisson point process of seed (gene site) activations. On the fine time scale, particle trajectories are realizations of the Poisson-driven Markov stochastic jump process. Since the Poisson-driven process represents the Langevin equation of particle motion under the influence of a random force only, the stochastic differential equation can be modified to model a growth pattern evolving in presence of external forces (such as a gravitational force, for instance). That is,

$$dx_t = a(x_t)dt + \int_{\Xi} y^{\xi_{seed}}(x_t)\mu(dt, d\xi_{seed}),$$

where $a(x_t)$ is an arbitrary function describing the effect of forces. This way, the connection with the second Newton's law of motion can be established.

The diffusive nature of seed trajectories has lead to an approximation of the jump process by the diffusion process. The Fokker-Planck equation derived in this thesis gives an insight into the statistical behavior of growth trajectories. Its coefficients reveal the microscopic properties of the stochastic flow such as the space-dependent average velocity and the diffusion rate. Its time-dependent and stationary numerical solutions reveal a bimodal distribution of a random seed trajectory in space-time. Future applications of the Fokker-Planck equation include computation of macroscopic properties of the stochastic flow such as the evolution of the mean and variance of seed trajectories in time. Direct extension of the Fokker-Planck equation to 2D growth leads to a possibility to compute the average motion of a 2D growing organism on the fine time scale provided that seeds move independently from one another.

A rigorous derivation of the "thermodynamic limit" equation presented in this thesis provides a deeper understanding of its meaning. The "thermodynamic limit" equation is basically the continuum mechanics equation of motion with the velocity resulting from an infinite number of seed activations in the hidden Darcyan space (not in the absolute space) at each time instant. It approximates a growth pattern on the coarse time scale by a diffeomorphic flow that depends on such GRID variables as the Poisson intensity of seed placements and the relative rate of expansion/contraction. The GRID variables represent the source of the macroscopic growth flow underlying shape changes of a growing organism seen in images. When the source is known this equation predicts a typical growth pattern in the average sense. When the source is unknown the GRID macroscopic growth equation is used for its direct inference from image data.

2. New computational methods in grid generation. A biological Darcyan coordinate system is a major "ingredient" of the GRID model that allows a biologically plausible, evolving coordinate representation of a growing organism and permits an analysis of complete shape changes including both its interior and its boundary. Mathematically, it is a curvilinear coordinate system of a bounded domain with no restrictions on the geometry of its boundary. Novel computational methods of its generation based on potential theory and the Level Set Method have been developed and implemented. The latter algorithm has been shown advantageous over the former one in terms of efficiency of Darcyan grid generation.

The Level Set-based algorithm of 2D Darcyan coordinate system generation needs further exploration with significantly oscillating 2D shapes (such as a dumbbell, for instance) and with 3D shapes. For 3D organisms the Eulerian formulation of the equations of front motion that views the front as the zeroth level set of a moving four-dimensional surface is needed.

3. Optimization methods in image analysis of growth. A novel GRID-based systematic approach to infer growth properties of the organism expressed in terms of the GRID variables directly from images has been developed. According to it, the estimated GRID parameters control the growth flow so that it continuously brings images of initial and grown organisms into the registration with minimal image matching costs. The distinguished features of the proposed inference algorithm are:

(i) Application of Darcyan curvilinear grids for an evolving coordinate representation of a growing organism and for image registration needed for removal of rigid transformations from images,

(ii) Implementation of the GRID macroscopic growth integro-differential equation that allows for automatic construction of the growth flow from the estimated GRID parameters.

(iii) High-dimensional optimization of the cost function in the form of the posterior probability density of the Poisson intensity field using Polak-Ribière conjugate gradient method.

Here, the cost function measures not only a mismatch in image functions of the initial and grown organisms but also cell activities that induce a series of deformations. Therefore, its design includes a prior model for the intensity of cell decisions based on the assumption that an organism grows locally isotropically. Two prior probability models of the intensity field have been proposed: These are a Gaussian random field and a sample-function density for a doubly stochastic Poisson point process.

Locally anisotropic growth patterns have to be addressed as well, and in this case a prior model in the form of a probabilistic catalog of elementary biological deformations can be used.

4. New application of image analysis to the field of confocal microscopy. The estimation algorithm has been implemented for inference of growth properties of the Drosophila wing disc from confocal micrographs of Wingless gene expression patterns. It has been shown that a prior model in the form of a sample-function density for a doubly stochastic Poisson process is more general yielding more realistic growth patterns.

The biologically meaningful cost function model is the most exciting result of this thesis. It allows *maximum a posteriori* estimation of the intensity of elementary biological events underlying observed dynamics of levels of gene expression. If there is experimental evidence that the observed dynamics of levels of a particular gene expression depends on an underlying biological process of cell decisions, then this hidden connection can be established at least in principle via *maximum a posteriori* estimation of the intensity of cell decisions and the growth-related transformation.

The cost function can be further modified to accommodate more biological data and thus to obtain more realistic estimates of the intensity parameter. For the GRID characterization of the Drosophila wing disc growth presented in this thesis only the micrographs of Wingless gene expression patterns that play a primary role in patterning of adult fly structures have been considered. But there are other key regulatory genes, namely, Vestigial and Apterous, required for the wing formation whose spatial-temporal patterns of expression may depend on cell division process. With image data of their expression patterns included into the cost function it would become

$$E_{post} = E^{Wingless}_{likelihood} + E^{Vestigial}_{likelihood} + E^{Apterous}_{likelihood} + {\sigma_I}^2 \cdot \left[E_{prior} + \parallel \nabla \lambda \parallel_2^2 \right] .$$

Such a biological adjustment of the cost function is a data-dependent task that can only be accomplished in collaboration with experimentalists in developmental biology.

Overall, the proposed cost function has new potential application in the analysis of micrographs of gene expression patterns in embryos. GRID-based analysis of dynamics of such gene expression patterns leads to the field of the genetics of geometry, the study of a link between gene expression patterns and generation of shape in embryos due to a growth process. It can assist in understanding the role that gene expression patterns play in the generation of a biological shape.

APPENDICES

Appendix A

Markov jump and diffusion processes

A.1 Typical jump processes

The following is intended to be a brief introduction to stochastic jump processes. For more details, a reader is referred to [16], [61].

A.1.1 Poisson point spatial-temporal process

Consider the process in which points occur randomly in a continuous connected space $\Xi \subset \Re^n$, $n \in \{1, 2, 3\}$ and time (t_0, ∞) shown in Figure A.1.1 [16].

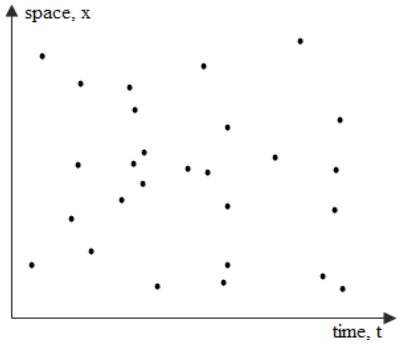

Figure A.1.1: Spatial-temporal Poisson point process with spatial coordinate x and time coordinate t.

Definition A.1.1. *Let $\mathcal{H}_t$ denote the history of the process at time t, i.e. specifications of all point positions in $\Xi \times [t_0, t]$ for some $t_0 \in \Re^+$. For a $\Delta t > 0$ let $\Delta\mu(A, t)$ be a random variable giving the number of points in $A \times \Delta t$, where $A \subset \Xi$.*

Then for a given intensity $\Lambda(x,t)$ *with dimensions* $[volume \times time]^{-1}$ *that admits the form*

$$\Lambda(x,t) = \lambda_t \cdot p_x, \tag{A.1.1}$$

where p_x *is the probability density of points in space* Ξ*, the spatial-temporal Poisson process* $\{\mu(A,t) : t \geq t_0, A \in \Xi\}$ *is defined by the requirements that for all* t*, as* $\Delta t \to 0^+$*,*

$$Pr\{\Delta\mu(A,t) = 1|\mathcal{H}_t\} = \lambda_t \Delta t \int_A p_x(x)dx + o(\Delta t), \tag{A.1.2}$$

$$Pr\{\Delta\mu(A,t) > 1|\mathcal{H}_t\} = o(\Delta t), \tag{A.1.3}$$

$$Pr\{\Delta\mu(A,t) = 0|\mathcal{H}_t\} = 1 - \lambda_t \Delta t \int_A p_x(x)dx + o(\Delta t), \tag{A.1.4}$$

where $\Delta\mu(A,t) = \mu(A,t+\Delta t) - \mu(A,t)$ *is the increment of the Poisson process.*

An important aspect of this definition is that the probability of finding a point in $[t, t+\Delta t]$ does not depend on history of events $\mathcal{H}_t$ before time t or on whether there is a point exactly at t. It means that the numbers of points in non-overlapping intervals are statistically independent. More precisely, if $\Delta t_i = [t_i, t_{i+1}), i = 1, ..., k$ are k disjoint intervals on $[t_0, \infty)$, then

$$Pr\{\mu(A,\Delta t_1) = n_1, \mu(A,\Delta t_2) = n_2, ..., \mu(A,\Delta t_k)\} = \prod_{i=1}^{k} \left[Pr\{N_{t_i} = n_i\} \int_A p_x(x)dx \right]. \tag{A.1.5}$$

The requirement (A.1.3) does not allow the possibility of multiple simultaneous point occurrences at the same time instant. The property (A.1.4) implies that $Pr\{\mu(A,t_0) = 0\} = 1$.

The counting Poisson process $\{\mu(A,t) : t \geq t_0, A \in \Xi\}$ is discrete since it takes only integer values $0, 1, 2, ..., j, ...$ It is a birth process since it can only increase as time progresses. Simulations of the homogeneous space-independent Poisson process with intensities $\lambda_t = 1$ per unit time and $\lambda_t = 4$ per unit time are shown in Figures A.1.1.a and A.1.1.b below. Observe that larger intensity value clearly implies more frequent point occurrences and smaller average interarrival time $\frac{1}{\lambda_t}$.

The Poisson probability distribution for a random number of points $\mu(A,\tau)$ occurring in a time interval $[t_1, t_2] \subset [t_0, \infty)$ of length $t_2 - t_1 = \tau$ and in the region $A \subset \Xi$ is derived using the definition of the Poisson process and Kolmogorov-Chapman equation for the discrete Markov process. For the Poisson counting process $\{\mu(A,t), t \geq t_0\}$ the Kolmogorov-Chapman equation is formulated as follows,

$$Pr_{ij}(t_0, t+\Delta t) = \sum_{k=1}^{\infty} Pr_{ik}(t_0,t) Pr_{kj}(t, t+\Delta t),\ t > t_0,\ \Delta t > 0, \tag{A.1.6}$$

where $Pr_{ij}(t_0,t) = Pr\{\mu(A,t) = j|\mu(A,t_0) = i\}$ are conditional probabilities of transition to a new state j at a time t given that at time t_0 the process was in a

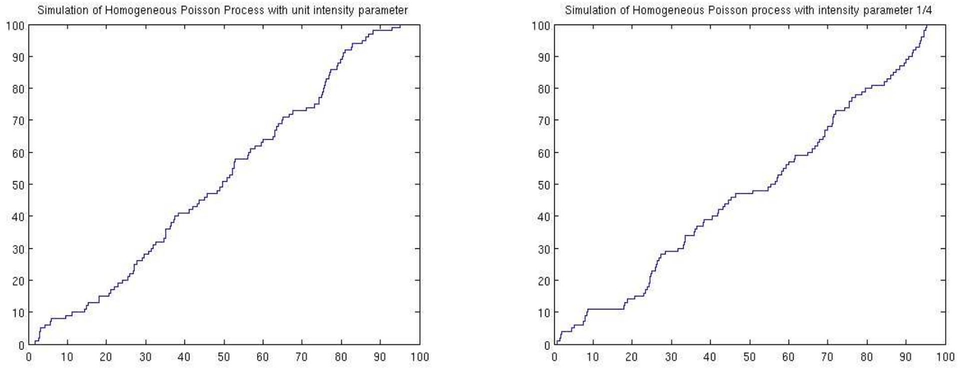

(a) (b)

Figure A.1.2: Homogeneous Poisson counting process with the intensity parameter (a) $\Lambda(x,t)=1$, (b) $\Lambda(x,t)=\frac{1}{4}$.

state i. Obviously, $\sum_{i=1}^{\infty} Pr_{ij}(t_0,t)=1$ and

$$Pr_{ij}(t_0,t_0)=\delta_{ij}=\begin{cases}1 & i=j,\\ 0 & i\neq j.\end{cases} \tag{A.1.7}$$

By the definition of the Poisson process, the probability that the state $\mu(A,t+\Delta t)$ does not change in a small time interval Δt is greater than the probability Pr_{ij} of a state change. Indeed,

$$\begin{aligned} Pr_{kk}(t,t+\Delta t) &= Pr\{\mu(A,t+\Delta t)=k|\mu(A,t)=k\} && \text{(A.1.8)}\\ &= 1-\lambda_t\left[\int_A p_x(x)dx\right]\cdot\Delta t+o(\Delta t), \\ Pr_{i_{i+1}}(t,t+\Delta t) &= Pr\{\mu(A,t+\Delta t)=i+1|\mu(A,t)=i\} && \text{(A.1.9)}\\ &= \lambda_t\left[\int_A p_x(x)dx\right]\cdot\Delta t+o(\Delta t), \\ Pr_{ij}(t,t+\Delta t) &= Pr\{\mu(A,t+\Delta t)=j|\mu(A,t)=i\} && \text{(A.1.10)}\\ &= o(\Delta t),\ \text{for all } j>i+1. \end{aligned}$$

Substituting equations (A.1.8), (A.1.9) and (A.1.10) into the Kolmogorov-Chapman equation and taking into account that $\mu(A,t)$ can only increase with time, implying that $Pr_{kj}(t,t+\Delta t)=0$ for $k>j$, the Kolmogorov-Chapman equation becomes

$$\begin{aligned} Pr_{ij}(t_0,t+\Delta t) &= \sum_{k=i}^{j} Pr_{ik}(t_0,t)Pr_{kj}(t,t+\Delta t)\\ &= \sum_{k=i}^{j-2} Pr_{ik}(t_0,t)o(\Delta t)+Pr_{i_{j-1}}(t_0,t)\cdot\left[\lambda_t\int_A p_x(x)dx+o(\Delta t)\right]\Delta t\\ &+ Pr_{ij}(t_0,t)\left[1-\lambda_t\int_A p_x(x)dx+o(\Delta t)\right]. \end{aligned} \tag{A.1.11}$$

After simple algebraic operations in equation (A.1.11) we take the limit as $\Delta t \to 0$ and arrive at the following differential equation for transition probabilities Pr_{ij} that holds for any pair $(i, j) : i \leq j$

$$\frac{\partial}{\partial t} Pr_{ij}(t_0, t) = \lambda_t \left[\int_A p_x(x) dx \right] Pr_{i,j-1}(t_0, t) - \lambda_t \left[\int_A p_x(x) dx \right] Pr_{ij}(t_0, t). \quad \text{(A.1.12)}$$

Since equation (A.1.12) holds for all i we can reset indices $i \Rightarrow 0$ and $j \Rightarrow j' = j - i$. Denoting $Pr_{0_j}(t_0, t) = Pr_j(t_0, t)$ and setting the initial conditions (by the property (A.1.4) of the Poisson process)

$$Pr_{0_j}(t_0, t_0) = Pr_j(t_0) = \begin{cases} 1 & j = 0, \\ 0 & j = 1, 2, \ldots, \end{cases} \quad \text{(A.1.13)}$$

we compute the probability of any state $j \in \{1, 2, \ldots\}$ at a time t that satisfies the following differential equation

$$\frac{d}{dt} Pr_j(t) = \lambda_t \left[\int_A p_x(x) dx \right] Pr_{j-1}(t) - \lambda_t \left[\int_A p_x(x) dx \right] Pr_j(t). \quad \text{(A.1.14)}$$

The solution to the initial value problem (A.1.13)-(A.1.14) for each $j \in \{1, 2, \ldots\}$ is given by

$$Pr_j(t) = \frac{1}{j!} \left[\int_{t_0}^{t} \lambda_{t'} dt' \int_A p_x(x) dx \right]^j \exp \left[- \int_{t_0}^{t} \lambda_{t'} dt' \int_A p_x(x) dx \right]. \quad \text{(A.1.15)}$$

For $j = 0$

$$Pr_0(t) = \exp\{- \left(\int_{t_0}^{t} \lambda_{t'} dt' \right) \int_A p_x(x) dx\}. \quad \text{(A.1.16)}$$

Thus, equation (A.1.15) determines the Poisson probability law for a random number of points $\mu(A, t)$ occurring at a time t in a specific region $A \subset \Xi$.

$$Pr\{\mu(A, t) = j\} = Pr_j(t). \quad \text{(A.1.17)}$$

From (A.1.15) it follows that the increment $\Delta\mu(A, \tau) = \mu(A, t + \tau) - \mu(A, t)$ of the Poisson process is distributed according to

$$Pr\{\Delta\mu(A, \tau) = j\} = \frac{1}{j!} \left[\int_{t}^{t+\tau} \lambda_{t'} dt' \int_A p_x dx \right]^j \exp \left[- \int_{t}^{t+\tau} \lambda_{t'} dt' \int_A p_x dx \right]. \quad \text{(A.1.18)}$$

The Poisson process $\{\mu(A, t) : t \geq t_0, A \subset \Xi\}$ is Markovian. For any collection of times $t_1 < t_2 < \ldots < t_k$ in $[t_0, \infty)$ and any collection of nonnegative integers $n_1, n_2, \ldots, n_k$, where $k = 1, 2, \ldots$, the joint probability is

$$\begin{aligned} & Pr\{\mu(A, t_1) = n_1, \mu(A, t_2) = n_2, \ldots, \mu(A, t_k) = n_k\} \\ &= Pr\{\Delta\mu(A, t_1 - t_0) = n_1, \Delta\mu(A, t_2 - t_1) = n_2 - n_1, \ldots, \Delta\mu(A, t_k - t_{k-1})\} \\ &= \prod_{i=1}^{k} Pr\{\Delta\mu(A, t_i - t_{i-1}) = n_i - n_{i-1}\} \end{aligned}$$

due to the fact that $\mu(A,t_1) = \mu(A,t_0) + \Delta\mu(A,t_1 - t_0)$ and independency of increments $\Delta\mu(A,t_i - t_{i-1})$. On the other hand, the joint probability can be written as

$$\begin{aligned}
&Pr\{\mu(A,t_1) = n_1, \mu(A,t_2) = n_2, \ldots, \mu(A,t_k) = n_k\} \\
&= Pr\{\mu(A,t_k) = n_k | \mu(A,t_{k-1}) = n_{k-1}, \mu(A,t_{k-2}) = n_{k-2}, \ldots, \mu(A,t_1) = n_1)\} \\
&\cdot Pr\{\mu(A,t_{k-1}) = n_{k-1}, \mu(A,t_{k-2}) = n_{k-2}, \ldots, \mu(A,t_1) = n_1)\},
\end{aligned}$$

where $Pr\{\mu(A,t_{k-1}) = n_{k-1}, \mu(A,t_{k-2}) = n_{k-2}, \ldots, \mu(A,t_1) = n_1)\}$ can be expanded further into a product of $k-1$ probabilities. Therefore, we find that

$$\begin{aligned}
Pr\{\mu(A,t_k) = n_k | \mu(A,t_{k-1}) = n_{k-1}, \mu(A,t_{k-2}) = n_{k-2}, \ldots, \mu(A,t_1) = n_1)\} \\
= Pr\{\Delta\mu(A, t_k - t_{k-1})\}
\end{aligned}$$

showing that the space-time Poisson process defined above is Markovian.

An important quantity that is applied to study problems of statistical inference for observed Poisson process is the *sample-function density* [61]. For the spatial-temporal Poisson process on a time interval $[t_0,t)$ and in a countable space $\Xi = \xi_1, \xi_2, \ldots, \xi_j, \ldots$ the sample-density function determines the probability of obtaining a particular realization of this process with $\mu(A,t) = n$ points occupying positions ξ_{σ_1}, ξ_{σ_2},…, ξ_{σ_n} at times $t_1 = T_1$, $t_2 = T_2$,…, $t_n = T_n$ respectively.

Definition A.1.2. *Let $\{\mu(\Xi,t) : t \geq t_0\}$ count points of the spatial-temporal Poisson process $\{\mu(A,t) : t \geq t_0\}$, where $A \subset \Xi$ and Ξ is a countable set, regardless of their position in space. The* ***sample-density function*** *for the process $\{\mu(A,t) : t \geq t_0\}$ on an interval $[t_0,t)$ is*

$$\begin{aligned}
&p\{t_1 = T_1, t_2 = T_2, \ldots, t_n = T_n; x_1 = \xi_{\sigma_1}, x_2 = \xi_{\sigma_2}, \ldots, x_n = \xi_{\sigma_n}; \mu(\Xi,t) = n\} \\
&= Pr\{\mu(\Xi,t) = n | \vec{t} = \vec{T}; x_1 = \xi_{\sigma_1}, x_2 = \xi_{\sigma_2}, \ldots, x_n = \xi_{\sigma_n}\} \\
&\times Pr\{x_1 = \xi_{\sigma_1}, x_2 = \xi_{\sigma_2}, \ldots, x_n = \xi_{\sigma_n} | \vec{t} = \vec{T}\} p_t\{\vec{t} = \vec{T}\} \text{ for } n \geq 1,
\end{aligned}$$

where $\vec{t}$ is a vector with n random time coordinates, $\{x_1, x_2, \ldots, x_n\}$ is a collection of random space coordinates and the corresponding $\vec{T}$ and $\{\xi_{\sigma_1}, \xi_{\sigma_2}, \ldots, \xi_{\sigma_n}\}$ are realizations of the Poisson point process in time-space.

The first factor on the right-hand side is the conditional probability that $\mu(\Xi,t) = n$ given the n occurrence time and space coordinates in $[t_0,t) \times \Xi$. The second factor is the conditional probability of n spatial locations given n occurrence times. The last factor is the joint probability density for the first n occurrence times.

Theorem A.1.3. *Let $\{\mu(A,t) : t \geq t_0\}$ be a space-time inhomogeneous Poisson counting process with intensity λ_t with respect to time and probability mass function*

$Pr(x)$ in a countable Ξ-space. Then the sample-function density for $\mu(A,t)$ is defined by

$$p\{\vec{t}=\vec{T}, x_1=\xi_{\sigma_1}, x_2=\xi_{\sigma_2},\dots,x_{\sigma_n}=\xi_n, \mu(\Xi,t)=n\} \\ = \left[\prod_{i=1}^{n}\lambda_{t_i}Pr(x_i=\xi_{\sigma_i})\right]\exp\left(-\int_{t_0}^{t}\lambda_{t'}dt'\right) \quad \textit{for } n\geq 1. \tag{A.1.19}$$

Proof. Since the spatial arrangement of points $\xi_{\sigma_1},\xi_{\sigma_2},\dots,\xi_{\sigma_n}$ is independent of their time occurrences $\vec{T}=(T_1,T_2,\dots,T_n)$ the sample-density function given by the definition above we have

$$p\{\vec{t}=\vec{T}, x_1=\xi_{\sigma_1}, x_2=\xi_{\sigma_2},\dots,x_n=\xi_{\sigma_n}, \mu(\Xi,t)=n\} \\ = Pr\{\mu(\xi,t)=n|\vec{t}=\vec{T}\}p(\vec{t}=\vec{T})\prod_{i=1}^{n}Pr(\xi_{\sigma_i}). \tag{A.1.20}$$

We first find the joint probability density for the first n occurrence times $t_0\leq t_1\leq \dots \leq t_n$ for the Poisson process $\{\mu(\Xi,t): t\geq t_0\}$. Let partition time interval into disjoint intervals $[t_0,T_1),[T_1,T_1+\Delta T_1),\dots,[T_n,T_n+\Delta T_n),[T_n+\Delta T_n,t)$. Consider the event $\{t_i\in[T_i,T_i+\Delta T_i); i=1,2,\dots,n\}$ that is identical to

$$\{\Delta\mu(\Xi,T_1-t_0)=0, \Delta\mu(\Xi,\Delta T_1)=1, \Delta\mu(\Xi,T_2-[T_1+\Delta T_1])=0, \\ \Delta\mu(\Xi,\Delta T_2)=1,\dots,\Delta\mu(\Xi,\Delta T_n)=1)\}.$$

Using independence of increments and the Poisson probability distribution (A.1.15), we compute the probability of the joint time occurrences

$$Pr\{t_i\in[T_i,T_i+\Delta T_i); i=1,2,\dots,n\} \\ = \left[\prod_{i=1}^{n}\int_{T_i}^{T_i+\Delta T_i}\lambda_{t'}dt'\right]\exp\left[-\int_{t_0}^{T_n+\Delta T_n}\lambda_{t'}dt'\right]. \tag{A.1.21}$$

Then the probability density becomes

$$p\{\vec{t}=\vec{T}\} = \lim_{\max\Delta T_i\to 0}\left[\prod_{i=1}^{n}\Delta T_i\right]^{-1} Pr\{t_i\in[T_i,T_i+\Delta T_i); i=1,2,\dots,n\} \\ = \prod_{i=1}^{n}\lambda_{T_i}\exp\left[-\int_{t_0}^{T_n}\lambda_{t'}dt'\right]. \tag{A.1.22}$$

Next, we find $Pr\{\mu(\Xi,t)=n|\vec{t}=\vec{T}\}$.

$$Pr\{\mu(\Xi,t)=n|\vec{t}=\vec{T}\} = Pr\{\mu(\Xi,t)=n|\mu(\Xi,T_n)=n\} \\ = Pr\{\mu(\Xi,t-T_n)=0\} = \exp\left[-\int_{T_n}^{t}\lambda_{t'}dt'\right]. \tag{A.1.23}$$

Substituting (A.1.22) and (A.1.23) for the factors in equation (A.1.20) we obtain the form of the sample-function density asserted in the Theorem statement. □

A.1.2 Poisson-driven Markov process

Definition A.1.4. *Let $\{\mu(d\xi, dt)\}$ be the space-time Poisson process introduced in subsection A.1.1, where $d\xi$ is an elementary unit volume and dt is a unit time. Then $\mu(A,t) = \int_{t_0}^{t}\int_A \mu(d\xi, dt)$, where $A \subset \Xi$ determines the number of incident points during $[t_0, t)$ A Poisson-driven Markov process $\{x_t : t \geq t_0\}$ satisfies an integral equation of the form*

$$x_t = x_0 + \int_{t_0}^{t} f_{t'}(x_{t'})dt' + \int_{t_0}^{t}\int_A g_{t'}(x_{t'}, \xi)\mu(d\xi, dt), \tag{A.1.24}$$

The integral term in (A.1.24) *has an evaluation given by*

$$\int_{t_0}^{t}\int_A g_{t'}(x_{t'}, \xi)\mu(d\xi, dt') = \begin{cases} 0 & \mu(\Xi, t) = 0, \\ \sum_{i=1}^{n} g_{T_i}(x_{T_i}, \xi_{\sigma_i}) & \mu(\Xi, t) = n \geq 1, \end{cases} \tag{A.1.25}$$

where T_i and ξ_{σ_i} are the time and space coordinates of occurrence of ith point.

Here, $f_t(x_t)$ is a deterministic function of random variables t and x_t, and $g_t(x_t, \xi)$ is a deterministic function of random variables t, ξ and x_t. This randomness enters through the influence of x which is random because of the influence of $\mu(d\xi, dt)$. $f_t(x_t)$ and $g_t(x_t, \xi)$ are continuous in time t. Suppressing dependency on x_t, $g_t(\xi)$ satisfies the following technical conditions.

1. The process $\{g_t(\xi) : t \geq t_0, \xi \in \Xi\}$ does not anticipate the underlying point process. $g_t(\xi)$ is statistically independent of $\int_{t_1}^{t_2}\int_A \mu(dt, d\xi)$ for any choice of $A \subset \Xi$ and collection of points $\{\xi_i, i = 1, 2, \ldots, n\}$ and for all triples $t \leq t_1 \leq t_2$.
2. Almost every realization of the process $g_t(\xi)$ is continuous in Ξ, left continuous in t, and bounded for $(\xi, t) \in A \times [t_1, t_2)$, where $[t_1, t_2)$ is a bounded interval in $[t_0, \infty)$ and A is any bounded set in Ξ.

These conditions ensure the existence of the integral term in the Poisson driven Markov process formulation. It is known in point processes literature as the *counting integral*

$$I_t(A) = \int_{t_0}^{t}\int_A g_{t'}(\xi)\mu(d\xi, dt). \tag{A.1.26}$$

Equation (A.1.24) for $\{x_t : t \leq t_0\}$ can be rewritten in differential form

$$dx_t = f_t(x_t)dt + \int_A g_t(x_t, \xi)\mu(d\xi, dt) \tag{A.1.27}$$

with the initial condition $x_{t_0} = x_0$. The differential $dx_t = x_{t+dt} - x_t$ denotes an infinitesimal increment in x that occurs during $[t, t + dt)$. If during this interval no points occur in the space-time process, $\mu(d\xi, dt) = 0$ and the increment in x is

$f_t(x_t)dt$. If a point occurs during $[t, t+dt)$ at the location ξ_{σ_i}, then the increment in x is $f_t(x_t)dt + g_t(x_t, \xi)$, which is dominated by $g_t(x_t, \xi)$. Clearly, x_t will have discontinuities at the occurrence times of the incident points and the size of the discontinuity for a point occurring at time t and location ξ_{σ_i} is $g_t(x_t, \xi)$.
x_t is called the *state* of the Poisson driven Markov process at time t. The state takes values in the state space $\mathcal{X}$ of the process, that is an n-dimensional Euclidean space.

An example of Poisson-driven Markov process is Brownian motion of a particle of mass m immersed in a fluid. We consider the one-dimensional case here, for simplicity. The Brownian particle moves chaotically due to random pushes of thermally agitated water molecules. The motion is damped to some extent depending upon the viscosity of the fluid. Let v_t denote the velocity of the particle at time $t \geq t_0$. Then the equation of motion first proposed by P. Langevin is

$$m\frac{dv_t}{dt} = -\alpha v_t + f_t, \tag{A.1.28}$$

where α is friction coefficient that depends on the viscosity of the fluid and f_t represents fluctuation forces due to molecular collisions. This equation is called *Langevin equation.* If the time of contact during collision is very short, the resulting force may be assumed impulsive. In this case, the velocity will not be differentiable and must be replaced by

$$m dv_t = -\alpha v_t dt + du_t, \tag{A.1.29}$$

where $\{u_t : t \geq t_0\}$ is a mark accumulator Poisson point process with a mark space U representing possible force values. The occurrence times t_i and the corresponding values u_i of this point process correspond to the collision instants and the forces induced on the particle, respectively.

The mark accumulator process is defined by

$$u_t = \sum_{i=0}^{\mu(A,t)} u_i, \text{where } u_0 = 0,\ A \subset U \text{ and} \tag{A.1.30}$$

1. $\{\mu(U,t) : t \geq t_0\}$ is an inhomogeneous Poisson process with intensity function λ_t counting time occurrences irrespective of their marks,
2. $\{u_i\}$ is a sequence of mutually independent, identically distributed random variables which are also independent of $\{\mu(U,t) : t \geq t_0\}$. If the marks are continuous random variables with probability density $p(u)$ then the intensity function for the marked Poisson process $\mu(A,t)$, $A \subset U$ is $\lambda_t p_u(u)$.

Therefore, u_t is the sum of the marks (forces) on all points (collision times) occurring in $[t_0, t)$. The mark accumulator process $\{u(t) : t \geq t_0\}$ can be represented as

$$u_t = \int_{t_0}^{t} \int_U u\mu(du, dt) \tag{A.1.31}$$

with the expected number of marked points $E(\mu(A,t)) = \int_{t_0}^{t}\int_A \lambda_{t'} p_{u'}(u')dt'du'$. From representation (A.1.31) follows the integral form of the increment du_t

$$du_t = \int_U u\mu(du, dt), \tag{A.1.32}$$

where u is a random variable taking force values from the space U in time interval dt and $\mu(du, dt)$ is a marked Poisson process. Thus, the Langevin equation becomes

$$dv_t = -m^{-1}\alpha v_t dt + \int_U m^{-1}u\mu(dt, du). \tag{A.1.33}$$

This is the form of the Poisson-driven Markov process with $f_t(v_t) = -m^{-1}\alpha v_t$ and $b_t(v_t, u) = m^{-1}u$ that models Brownian motion on the fine time-scale.

A.2 Diffusion process

Consider motion of a particle immersed in a fluid whose mass is significantly larger than the mass of fluid molecules. Ignoring the gravitational force the particle moves under the action of friction and fluctuating forces. If the mass of a heavy particle is m, then, neglecting effects of the friction force, the Langevin equation describing the particle motion for horizontal component of the velocity $W(t)$ is

$$m\frac{dW}{dt} = n(t), \tag{A.2.1}$$

where $n(t)$ is a component of the fluctuating force along the horizontal axis.

Assuming that pushes undergone by the given particle due to its collisions with fluid molecules are equally likely in negative and positive directions, the average value $\langle n(t)\rangle = 0$. The correlation time $W(t)$ is roughly equal to the average time length τ between pushes. The random force $n(t)$ represents the resulting effect of a large number of pushes. In time intervals $\Delta t \geq \tau$ the particle undergoes a large number of collisions with fluid molecules. That is why, according to the Central Limit Theorem, a random force $n(t)$ can be approximated by a normal δ-correlated process or *white noise*.

In reality, $n(t)$ has a finite, non-zero correlation time τ. Such an idealization of the fluctuating force by white noise is justified by the fact that we are interested not in microscopic but macroscopic properties of the particle motion. Also, the introduction of white noise significantly simplifies the mathematical calculations.

We now give a formal definition of the diffusion or Wiener process and state its basic properties.

Definition A.2.1. *The Wiener process $\{W(t) : t \geq 0\}$ satisfies the integral version of the differential equation $\frac{dW}{dt} = n(t), \quad W(0) = 0$,*

$$W(t) = \int_0^t n(t')dt', \tag{A.2.2}$$

where $n(t)$ is white noise, a normal stationary process with zero mean and δ-correlation function, i.e.,

$$\langle n(t)\rangle = 0,\ \ C(t_1,t_2) = \langle n(t_1)n(t_2)\rangle = \delta(t_2-t_1). \tag{A.2.3}$$

The integral (A.2.2) *exists in the mean-square sense.*

Since integration is a linear transformation of the normal process, the Wiener process is also normal. According to (A.2.2) the mean and variance of $W(t)$ are

$$\langle W(t)\rangle = 0,\ \ \sigma^2(t) = \int_0^t\int_0^t \langle n(\tau_1)n(\tau_2)\rangle\, d\tau_1 d\tau_2 = t. \tag{A.2.4}$$

Thus, the one-dimensional probability density of the Wiener process is

$$f(w,t) = \frac{1}{\sqrt{2\pi t}}e^{-\frac{w^2}{2t}},\ \ t\ge 0. \tag{A.2.5}$$

In other words, $W(t) = \mathcal{N}(0,t)$.

The Wiener process has stationary independent increments $W(t_2)-W(t_1)$ for any time pair $\{t_1,t_2\}$. Stationarity follows from the obvious relations $W(t_2)-W(t_1) = \int_{t_1}^{t_2} n(\tau)d\tau$ and $\langle[W(t_2)-W(t_1)]^2\rangle = (t_2-t_1)$ that imply the zero average value of increments and variance proportional to time difference. Using the autocorrelation function for the Wiener process

$$K(t_1,t_2) = \int_0^{t_1}\int_0^{t_2} \langle n(\tau_1)n(\tau_2)\rangle\, d\tau_1 d\tau_2 = min(t_1,t_2) \tag{A.2.6}$$

we compute the correlation function of increments $W(t_3)-W(t_2)$ and $W(t_2)-W(t_1)$ for any time triplet $t_1\le t_2\le t_3$

$$\langle[W(t_3)-W(t_2)][W(t_2)-W(t_1)]\rangle = K(t_3,t_2)-K(t_2,t_2)-K(t_3,t_1)+K(t_2,t_1) = 0. \tag{A.2.7}$$

This result implies the independency of increments of the Wiener process. It can also be shown that the Wiener process is Markovian, non-stationary and homogeneous in space and time.

The generalized form of Langevin equation for a stochastic Markov process $\{x(t) : t\ge t_0\}$ is

$$\frac{dx(t)}{dt} = \alpha_1(x(t),t) + \alpha_2(x(t),t)n(t),\ \ x(t_0) = x_0, \tag{A.2.8}$$

where the *drift* and *diffusion coefficients*, respectively, $\alpha_1(x(t),t)$ and $\alpha_2(x(t),t)$, are deterministic, continuously differentiable functions of x and t. $n(t)$ is *Gaussian white noise* with $\langle n(t)\rangle = 0$ and $\langle n(t_1)n(t_2)\rangle = \delta(t_1-t_2)$. Equations of type (A.2.8) containing Gaussian white noise are called *stochastic differential equations.*

An equivalent formulation of the stochastic differential equation is given in differential form as

$$dx = \alpha_1(x,t)dt + \alpha_2(x,t)dW(t),\ \ x(t_0) = x_0, \tag{A.2.9}$$

where $W(t)$ is Wiener process.

A.3 The Fokker-Planck equation and its relation to Langevin equation

Definition A.3.1. *The conditional probability density* $p(x,t|x_0,t_0), t > t_0$ *of a continuous Markov process of the Brownian motion* $\{x(t), t \geq t_0\}$ *satisfies the following parabolic partial differential equation:*

$$\begin{aligned}\frac{\partial}{\partial t}p(x,t|x_0,t_0) = &-\frac{\partial}{\partial x}[a(x,t)p(x,t|x_0,t_0)] \\ &+\frac{1}{2}\frac{\partial^2}{\partial x^2}[b(x,t)p(x,t|x_0,t_0)]\end{aligned} \tag{A.3.1}$$

with initial conditions $p(x,t_0|x_0,t_0) = \delta(x-x_0)$, *where* $\delta(x-x_0)$ *is the delta-Dirac function and the coefficients* $a(x,t)$ *and* $b(x,t)$ *are defined, respectively, by the first and the second jump moments of the process* $x(t)$

$$a(x,t) = \lim_{\Delta t \to 0} \frac{1}{\Delta t} \langle x(t+\Delta t) - x(t)|x(t)\rangle \tag{A.3.2}$$

$$b(x,t) = \lim_{\Delta t \to 0} \frac{1}{\Delta t} \left\langle [x(t+\Delta t) - x(t)]^2|x(t)\right\rangle. \tag{A.3.3}$$

Equation (A.3.1) *is called the Fokker-Planck equation (or forward Kolmogorov equation).*

It is possible to derive the Fokker-Planck equation starting from the Kolmogorov-Chapman equation by means of the Kramers-Moyal expansion [44]

$$\frac{\partial}{\partial t}p(x,t|x_0,t_0) = \sum_{n=1}^{\infty} \frac{(-1)^n}{n!}\frac{\partial^n}{\partial x^n}[\beta_n(x,t)p(x,t|x_0,t_0)], \tag{A.3.4}$$

for a stochastic process $x(t)$, where

$$\beta_n(x,t) = \lim_{\Delta t \to 0} \frac{1}{\Delta t} \langle [x(t+\Delta t) - x(t)]^n|x(t)\rangle \tag{A.3.5}$$

are jump moments of order n. It may happen that the jump moments β_n will be increasingly small, or identically zero, as the order n increases, allowing a truncation of the Kramers-Moyal expansion after a finite number of terms. For the time evolution of such diffusion processes as Wiener process (or Brownian motion) the Fokker-Planck equation is an *exact* equation since the jump moments $\beta_n = 0$ for the order $n \geq 3$.

The continuous Markov process $\{x(t) : t \geq t_0\}$ characterized by the probability density $p(x,t|x_0,t_0)$ in $x-t$ plane satisfies Langevin equation of motion. We consider the generalized differential form of Langevin equation

$$dx = \alpha_1(x,t)dt + \alpha_2(x,t)dW(t), \;\; x(t_0) = x_0, \tag{A.3.6}$$

where $W(t)$ is a Wiener process and $\alpha_1(x,t)$ and $\alpha_2(x,t)$ are drift and diffusion coefficients. Our goal is to find a link between the Fokker-Planck equation (A.3.1) and the Langevin equation of motion (A.3.6).

It follows from (A.3.6) that

$$x(t) = x(t_0) + \int_{t_0}^{t} \alpha_1(x(\tau),\tau)d\tau + \int_{t_0}^{t} \alpha_2(x(\tau),\tau)dW(t). \tag{A.3.7}$$

Note that the integral

$$\int_{t_0}^{t} \alpha_2(x(\tau),\tau)dW(\tau) \tag{A.3.8}$$

does not exist in Cauchy-Riemann or Stieltjes sense since $W(t)$ is a non-differentiable stochastic process.

Stratonovich has given the definition of the stochastic integral (A.3.8) in the symmetrized form that reflects symmetry of events with respect to the past and to the future.

Definition A.3.2. *Stochastic integral in Stratonovich sense is the mean square limit of converging integral sums*

$$\int_{t_0}^{t} \alpha_2(x(\tau),\tau)dW(t) = l.i.m._{n\to\infty} \sum_{i=0}^{n-1} \alpha_2\left(\frac{x(\tau_{i+1})+x(\tau_i)}{2},\tau_i\right)[W(\tau_{i+1})-W(\tau_i)], \tag{A.3.9}$$

where $t_0 = \tau_0 < \tau_1 < \tau_2 < \ldots < \tau_n < t$. *In other words,*

$$\lim_{n\to\infty} \left\langle \left(\sum_{i=0}^{n-1} \alpha_2\left(\frac{x(\tau_{i+1})+x(\tau_i)}{2},\tau_i\right)[W(\tau_{i+1})-W(\tau_i)] - \int_{t_0}^{t} \alpha_2(x(\tau),\tau)dW(t) \right)^2 \right\rangle = 0.$$

We now compute the averages of the jump $\Delta x(t) = x(t+\Delta t) - x(t)$ conditioned on $x(t) = x$ for the process $x(t)$ that satisfies (A.3.6)

$$\beta_n(x,t) = \lim_{\Delta t\to 0} \frac{1}{\Delta t} \left\langle [x(t+\Delta t) - x(t)]^n | x(t) = x \right\rangle, \tag{A.3.10}$$

where the average is taken over the ensemble of all realizations of the process $n(t)$. From the integral form of the Langevin equation (A.3.7) we obtain

$$x(t+\Delta t) - x(t_0) = \int_{t}^{t+\Delta t} \alpha_1(x(t'),t')dt' + \int_{t_0}^{t} \alpha_2(x(t'),t')dW(t'), \tag{A.3.11}$$

and iterate this equation by expanding the coefficients $\alpha_1(x(t'),t')$ and $\alpha_2(x(t'),t')$ as follows

$$\alpha_1(x(t'),t') = \alpha_1(x(t),t') + \frac{\partial}{\partial x}\alpha_1(x(t),t')[x(t') - x(t)] + \ldots, \tag{A.3.12}$$

$$\alpha_2(x(t'),t') = \alpha_2(x(t),t') + \frac{\partial}{\partial x}\alpha_2(x(t),t')[x(t') - x(t)] + \ldots. \tag{A.3.13}$$

In the first iteration, using continuity of $\alpha_1(x,t)$ and $\alpha_2(x,t)$ in time t, we obtain, from (A.3.11),

$$\begin{aligned} x(t+\Delta t) - x(t) &= \int_t^{t+\Delta t} \alpha_1(x(t),t')dt' + \int_t^{t+\Delta t} \alpha_2(x(t),t')dW(t') \\ &+ \alpha_1\left(x(t), t+\frac{\Delta t}{2}\right)\Delta t + \alpha_2\left(x(t), t+\frac{\Delta t}{2}\right)\int_t^{t+\Delta t} dW(t'), \end{aligned} \tag{A.3.14}$$

where $\int_t^{t+\Delta t} dW(t') = W(t+\Delta t) - W(t) = W(\Delta t)$. We now express the increment $[x(t') - x(t)]$ in (A.3.12) and (A.3.13) by means of the first iteration in (A.3.14),and insert so expanded $\alpha_1(x(t'),t')$ and $\alpha_2(x(t'),t')$ back into (A.3.11) to obtain the expansion for the jump in the second iteration, $\Delta x(t) = x(t+\Delta t) - x(t)$, conditioned on $x(t) = x$,

$$\begin{aligned} \Delta x(t)|_{x(t)=x} &= \alpha_1\left(x, t+\frac{\Delta t}{2}\right)\Delta t + \int_t^{t+\Delta t} \frac{\partial}{\partial x}\alpha_1(x,t')\alpha_1\left(x, t+\frac{\Delta t}{2}\right)(t'-t)dt' \\ &+ \alpha_2\left(x, t+\frac{\Delta t}{2}\right)W(\Delta t) + \int_t^{t+\Delta t} \frac{\partial}{\partial x}\alpha_1(x,t')\alpha_2\left(x, t+\frac{(t'-t)}{2}\right)[W(t'-t)]dt' \\ &+ \int_t^{t+\Delta t}\int_t^{t+\Delta t} \frac{\partial}{\partial x}\alpha_2(x,t')\alpha_1\left(x, t+\frac{\Delta t}{2}\right)(t'-t)dW(t') \\ &+ \int_t^{t+\Delta t} \frac{\partial}{\partial x}\alpha_2(x,t')\alpha_2\left(x, t+\frac{(t'-t)}{2}\right)[W(t'-t)]dW(t'). \end{aligned} \tag{A.3.15}$$

Here, $W(t'-t) = \int_t^{t'} dW(t'') = W(t') - W(t)$.

To evaluate the jump moment $a(x,t) = \lim_{\Delta t \to 0} \langle x(t+\Delta t) - x(t) | x(t) = x \rangle$ we take the average of (A.3.15) noting that the Wiener process increments

$$\langle W(\Delta t)\rangle = 0, \ \ \langle W(t'-t)\rangle = 0, \text{ and } \langle dW(t')\rangle = 0, \tag{A.3.16}$$

$$\begin{aligned} \langle \Delta x(t) | x(t) = x \rangle = \alpha_1\left(x, t+\frac{\Delta t}{2}\right)\Delta t + \frac{\partial}{\partial x}\alpha_2\left(x, t+\frac{\Delta t}{2}\right)\alpha_2\left(x, t+\frac{\Delta t}{2}\right) \\ \cdot \left\langle \int_t^{t+\Delta t} W(t'-t)dW(t') \right\rangle. \end{aligned} \tag{A.3.17}$$

Making a partition of an interval $[t_0, t+\Delta t)$ $t_0 < t_1 < \ldots < t_n = t+\Delta t$ we calculate the integral factor in (A.3.17) in Stieltjes sense and take the limit as $n \to \infty$ with

$\max(t_i - t_{i-1}) \to 0$,

$$\begin{aligned}
&\left\langle \int_t^{t+\Delta t} W(t'-t)dW(t') \right\rangle = \left\langle \int_t^{t+\Delta t} W(t')dW(t') \right\rangle - \int_t^{t+\Delta t} \langle W(t)dW(t') \rangle \\
&= \lim_{n\to\infty} \left\langle \sum_{i=1}^{n} W\left(\frac{t_i + t_{i-1}}{2}\right) [W(t_i) - W(t_{i-1})] \right\rangle \\
&= \lim_{n\to\infty} \sum_{i=1}^{n} \left\langle W\left(\frac{t_i + t_{i-1}}{2}\right) W(t_i) \right\rangle - \left\langle W\left(\frac{t_i + t_{i-1}}{2}\right) W(t_{i-1}) \right\rangle \\
&= \lim_{n\to\infty} \sum_{i=1}^{n} \frac{(t_i - t_{i-1})}{2} = \frac{1}{2}\Delta t.
\end{aligned}$$

We have used $\langle W(t)dW(t')\rangle = 0$ for $t' \geq t$, as well as the property of Wiener process that $\langle W(t')W(t'')\rangle = \min(t', t'')$. Therefore, we obtain the drift coefficient

$$a(x,t) = \alpha_1(x,t) + \frac{1}{2}\alpha_2(x,t)\frac{\partial}{\partial x}\alpha_2(x,t). \tag{A.3.18}$$

Starting from (A.3.15) evaluation of the jump moment for $n = 2$ gives the diffusion coefficient $b(x,t) = \alpha^2(x,t)$. Using (A.3.15) in the definition of conditional jump moments we find that $\beta_n = 0$ for $n \geq 3$. Thus, the Langevin equation (A.3.6) is equivalent to the Fokker-Planck equation with the appropriate relations between their respective coefficients.

Appendix B

Conjugate gradient methods in $\Re^N$

B.1 A concept of conjugate directions

Consider the problem

$$\min\{f(\vec{x}) : \vec{x} \in \Re^N\}$$

and suppose that $f(\vec{x})$ is strictly convex and twice continuously differentiable. Let some particular point $\vec{x}_0$ be our first guess at a minimum of $f(\vec{x})$. We approximate $f(\vec{x})$ in the neighborhood of $\vec{x}_0$ by its Taylor series,

$$\begin{aligned} f(\vec{x}) &= f(\vec{x}_0) + \sum_{i=1}^{N} \frac{\partial f}{\partial x_i} x_i + \frac{1}{2} \sum_{1 \le i,j \le N} \frac{\partial^2 f}{\partial x_i \partial x_j} x_i x_j + \dots \\ &\approx c - \vec{b} \cdot \vec{x} + \frac{1}{2} \vec{x} \cdot A \cdot \vec{x}, \end{aligned} \tag{B.1.1}$$

where

$$c \equiv f(\vec{x}_0) \quad b \equiv -\nabla f|_{\vec{x}_0} \quad [A_{ij}] \equiv \frac{\partial^2 f}{\partial x_i \partial x_j}|_{\vec{x}_0}. \tag{B.1.2}$$

The matrix A is the Hessian matrix of $f(\vec{x})$ evaluated at $\vec{x} = \vec{x}_0$.

Note that minimizing $f(\vec{x})$ along some direction $\vec{u}$ is equivalent to solving the one-dimensional minimization problem

$$\lambda_{min} = \min\{f(\vec{x} + \lambda \cdot \vec{u}) : \lambda \in \Re\}. \tag{B.1.3}$$

If λ_{min} is the point of minimum then the derivative of $f(\vec{x} + \lambda \cdot \vec{u})$ with respect to λ is

$$\frac{\partial f}{\partial \lambda} = \sum_{i=1}^{N} \frac{\partial f}{\partial z_i} \cdot \frac{\partial z_i}{\partial \lambda} = \nabla f \cdot \vec{u} = 0. \tag{B.1.4}$$

In other words, the gradient of $f(\vec{x})$ must be perpendicular to $\vec{u}$ at the line minimum $\vec{z}_{min} = \vec{x} + \lambda_{min} \cdot \vec{u}$. We can easily estimate the gradient of f from approximation (B.1.1)

$$\nabla f = A \cdot \vec{x} - \vec{b}. \tag{B.1.5}$$

It follows from (B.1.5) that a change in the gradient $\delta(\nabla f)$ as we move along some direction is given by

$$\delta(\nabla f) = A \cdot (\delta \vec{x}). \tag{B.1.6}$$

Suppose that we have moved along some direction $\vec{u}$ to a minimum $f(\vec{x}+\lambda_{min}\cdot\vec{u})$, and now we would like to follow some new direction $\vec{v}$ towards another minimum $f(\vec{x}_u + \lambda_{min_v} \cdot \vec{v})$, where $\vec{x}_u = \vec{x} + \lambda_{min} \cdot \vec{u}$. To ensure that motion along $\vec{v}$ does not spoil minimization along previous direction $\vec{u}$ we must require that the change in the gradient be perpendicular to $\vec{u}$. That is,

$$\vec{u} \cdot \delta(\nabla f) = \vec{u} \cdot A \cdot \vec{v} = 0. \tag{B.1.7}$$

When condition (B.1.7) holds for two vectors u and v, they are said to be *conjugate*. When (B.1.7) holds pairwise for all members of a set of N vectors, they are said to be a conjugate set. The question that naturally arises is how do we construct such a conjugate set of directions in a successive manner that would take us downhill?

B.2 Construction of a conjugate set of vectors

The conjugate gradient method was originally developed to solve the problem of minimizing a function $f : \Re^N \to \Re$ approximated by the quadratic form (B.1.1). In practice, the function to be minimized is usually not quadratic. Conjugate gradient methods have been successfully applied even for non-convex optimization if there is a reason to believe that $f(\vec{x})$ has local minima in the neighborhood of the initial guess $\vec{x}_0$ [51]. However, there is no mathematical theorem that guarantees the convergence of the conjugate gradient algorithm to the local minimum of the non-convex function. As such, we construct a conjugate set of vectors and show that successive conjugate directions point the way to the minimum of a strictly convex and twice continuously differentiable function $f(\vec{x})$.

We find a sequence of conjugate vectors $\{h_i\}_{i=1}^N$ following a *biorthogonalization* process. Such a process constructs two sequences in $\Re^N$, $\vec{g}_0, \vec{g}_1, \ldots,$ and $\vec{h}_0, \vec{h}_1, \ldots,$ such that their scalar products

$$\vec{g}_i \cdot \vec{g}_j = 0,\ \ \vec{h}_i \cdot A \cdot \vec{h}_j = 0 \text{ and } \vec{g}_i \cdot \vec{h}_j = 0 \text{ for all } j < i. \tag{B.2.1}$$

Let $\vec{g}_0 \in \Re^N$ be arbitrary. Set $\vec{h}_0 = \vec{g}_0$. Now set

$$\vec{g}_1 = \vec{g}_0 - \lambda_0 A \cdot \vec{h}_0,\ \text{ with } \lambda_0 = \frac{\vec{g}_0 \cdot \vec{g}_0}{\vec{g}_0 \cdot A \cdot \vec{h}_0}, \tag{B.2.2}$$

which ensures that $\vec{g}_0 \cdot \vec{g}_1 = 0$. Next, set

$$\vec{h}_1 = \vec{g}_1 + \gamma_0 \vec{h}_0, \text{ with } \gamma_0 = -\frac{A\vec{h}_0 \cdot \vec{g}_1}{A \cdot \vec{h}_0 \cdot \vec{h}_0} \tag{B.2.3}$$

which ensures that $\vec{h}_0 \cdot A\vec{h}_1 = 0$. In a successive manner, we can continue this process until for some $m \leq N$ $\vec{g}_m = \vec{h}_m = \vec{0}$. Thus, we obtain two sequences of vectors from the recurrence

$$\vec{g}_{i+1} = \vec{g}_i - \lambda_i A \cdot \vec{h}_i, \;\; \vec{h}_{i+1} = \vec{g}_{i+1} + \gamma_i \vec{h}_i \text{ for } i = 0, 1, 2, \ldots, \tag{B.2.4}$$

with the scalars λ_i and γ_i given by

$$\lambda_i = \frac{\vec{g}_i \cdot \vec{g}_i}{\vec{g}_i \cdot A \cdot \vec{h}_i}, \;\; \gamma_i = -\frac{A \cdot \vec{h}_i \cdot \vec{g}_{i+1}}{A \cdot \vec{h}_i \cdot \vec{h}_i}. \tag{B.2.5}$$

It can be shown [51] that

$$\lambda_i = \frac{\vec{g}_i \cdot \vec{g}_i}{\vec{g}_i \cdot A \cdot \vec{h}_i} = \frac{\vec{h}_i \cdot \vec{g}_i}{\vec{h}_i \cdot A \cdot \vec{h}_i}, \tag{B.2.6}$$

$$\gamma_i = -\frac{A \cdot \vec{h}_i \cdot \vec{g}_1}{A \cdot \vec{h}_i \cdot \vec{h}_i} = \frac{\vec{g}_{i+1} \cdot \vec{g}_{i+1}}{\vec{g}_i \cdot \vec{g}_i} \tag{B.2.7}$$

$$= \frac{\vec{g}_{i+1} \cdot \vec{g}_{i+1} \pm \vec{g}_{i+1} \cdot \vec{g}_i}{\vec{g}_i \cdot \vec{g}_i}. \tag{B.2.8}$$

Note that then expression for γ_i given in terms of g_i and g_{i+1} on the right-hand side of (B.2.7) is preferred since in practice the Hessian matrix A is usually unknown. If we knew the Hessian matrix A given in (B.1.1) then we could use the construction (B.2.4) to find successively conjugate directions $\{h_j\}$ along which to proceed towards the minimum. After a number of such constructions we would have arrived at $\vec{x}_{min}$. We state an important theorem that allows computation of the conjugate set of vectors without knowledge of the Hessian matrix A [54].

Theorem B.2.1. *Assume that at some point $\vec{x}_i$ a vector $\vec{g}_i = -\nabla f(\vec{x}_i)$, where $f(\vec{x}) \approx c - \vec{b} \cdot \vec{x} + \frac{1}{2}\vec{x} \cdot A \cdot \vec{x}$. Assume also then we proceed from $\vec{x}_i$ along the direction $\vec{h}_i = \vec{g}_i + \gamma_{i-1}\vec{h}_{i-1}$ conjugate to all previous directions h_j, $j < i$ to the local minimum of f located at some point $\vec{x}_{i+1}$ and set $\vec{g}_{i+1} = -\nabla f(\vec{x}_{i+1})$. Then*

$$\vec{g}_{i+1} = -\nabla f(\vec{x}_{i+1}) = \vec{g}_i - \lambda_i A \cdot \vec{h}_i, \text{ for } 1 \leq i \leq N-1. \tag{B.2.9}$$

Proof. By equation (B.1.5) and by the theorem assumption we have

$$\vec{g}_i = -\nabla f(\vec{x}_i) = \vec{b} - A \cdot \vec{x}_i, \tag{B.2.10}$$

$$\vec{g}_{i+1} = \vec{b} - A \cdot \vec{x}_{i+1} = \vec{b} - A \cdot (\vec{x}_i + \lambda \vec{h}_i) = \vec{g}_i - \lambda A \cdot \vec{h}_i, \tag{B.2.11}$$

where $\lambda = \lambda_i$ is chosen to take us to the line minimum. But along the direction $\vec{x}_i + \lambda_i \vec{h}_i$ at which $f(\vec{x}_i + \lambda \vec{h}_i)$ attains its minimum as a function of λ

$$\nabla f(\vec{x}_{i+1}) \cdot \vec{h}_i = -\vec{g}_{i+1} \cdot \vec{h}_i = 0. \tag{B.2.12}$$

Using the relation (B.2.12) we easily solve $(\vec{g}_i - \lambda A \cdot \vec{h}_i) \cdot \vec{h}_i = 0$ for λ. We arrive at the formula (B.2.6) for λ. But with this value of λ equation (B.2.11) for $\vec{g}_i$ is the same as (B.2.4). $\square$

Thus, we have obtained the basis for a conjugate gradient algorithm that would construct a sequence of conjugate vectors in the form $\vec{h}_{i+1} = -\nabla f(\vec{x}_{i+1}) + \gamma_i \vec{h}_i$ based on evaluation of the gradient vector, the latest auxiliary vector $\vec{g}_i$ for $i = 1, 2, \ldots, N-1$ and one-dimensional line minimization for estimation of λ_i. Setting a scalar $\gamma_i = \frac{\vec{g}_{i+1} \cdot \vec{g}_{i+1}}{\vec{g}_i \cdot \vec{g}_i}$ in the definition of a conjugate vector set h_i (B.2.4) we obtain the classical *Fletcher-Reeves algorithm*. The *Polak-Ribière algorithm* differs from the Fletcher-Reeves algorithm only in the formula for $\gamma_i = \frac{\vec{g}_{i+1} \cdot \vec{g}_{i+1} - \vec{g}_{i+1} \cdot \vec{g}_i}{\vec{g}_i \cdot \vec{g}_i}$. It can be shown that the γ_i are identical according to (B.2.7) for a symmetric, positive-definite matrix A of size $N \times N$. The following important theorem justifies application of the Polak-Ribière algorithm to minimization of a convex function in $\Re^N$ [51].

B.3 A major theorem for the Polak-Ribière algorithm in $\Re^N$

.

Theorem B.3.1. *Consider minimization problem*

$$\min\{f(\vec{x}) : \vec{x} \in \Re^N\}, \tag{B.3.1}$$

under the assumption that $f(\vec{x}) : \Re^N \to \Re$ *is a strictly convex, twice continuously differentiable function such that for all* $\vec{x} \in \{x | f(\vec{x}) \leq f(\vec{x}_0)\}$, *where* $\vec{x}_0$ *is an initial guess at a minimum of* $f(\vec{x})$ *and all* $\vec{y} \in \Re^N$,

$$0 \leq m \parallel \vec{y} \parallel^2 \leq \vec{y} \cdot A(\vec{x}) \cdot \vec{y} \leq M \parallel \vec{y} \parallel^2, \ 0 < m \leq M < \infty, \tag{B.3.2}$$

where $A(\vec{x}) = \left[\frac{\partial^2 f(\vec{x})}{\partial x_i \partial x_j}\right]$ *is the Hessian matrix. Then the Polak-Ribière algorithm constructs either a finite sequence* $\{x_i\}$ *whose last element,* $\vec{x}_k$, *satisfies* $\nabla f(\vec{x}_k) = 0$, *or an infinite sequence* $\{x_i\}$ *which converges to a point* $\hat{\vec{x}}$ *such that* $\nabla f(\hat{\vec{x}}) = 0$.

To prove this theorem we have to establish the following result.

Lemma B.3.2. *Given the problem* (B.3.1) *under the assumptions* (B.3.2) *and sequences* $\vec{x}_0, \vec{x}_1, \vec{x}_2, \ldots$ *and* $\vec{h}_0, \vec{h}_1, \vec{h}_2, \ldots$ *constructed by the Polak-Ribière algorithm*

$$\begin{aligned}
&\vec{x}_{i+1} = \vec{x}_i + \lambda_i \vec{h}_i, \\
&\vec{h}_{i+1} = \vec{g}_{i+1} + \gamma_i \vec{h}_i, \\
&\vec{g}_{i+1} = -\nabla f(\vec{x}_{i+1}), \;\; \textit{with } \gamma_i = \frac{(\vec{g}_{i+1} - \vec{g}_i) \cdot \vec{g}_{i+1}}{\vec{g}_i \cdot \vec{g}_i} \; \textit{for i=0,1,2,\ldots}
\end{aligned}$$

there exists a $\rho > 0$ *such that*

$$-\nabla f(\vec{x}_i) \cdot h_i \geq \rho \parallel \nabla f(\vec{x}_i) \parallel \parallel \vec{h}_i \parallel . \tag{B.3.3}$$

Proof. For every $\vec{x} \in \Re^N$, let $A(\vec{x}) = \left[\frac{\partial^2 f(\vec{x})}{\partial x_i \partial x_j}\right]$ and let $\vec{g}(\vec{x}) = -\nabla f(\vec{x})$. Then, making use of the Taylor formula for a continuous vector-function $q(\vec{x}) : \Re^N \to \Re^N$, $\vec{x}, \vec{h} \in \Re^N$ and any $\lambda \in \Re$,

$$q(\vec{x} + \lambda \vec{h}) = q(\vec{x}) + \lambda \left(\int_0^1 \nabla q_{\vec{x}}(\vec{x} + t\lambda \vec{h}) \cdot \vec{h} dt \right),$$

where $\nabla q(\vec{x})$ is an $N \times N$ Jacobian matrix, we obtain

$$-\vec{g}_{i+1} = -\vec{g}(\vec{x}_{i+1}) = -\vec{g}(\vec{x}_i + \lambda_i \vec{h}_i) = -\vec{g}_i + \lambda_i \left(\int_0^1 A(\vec{x}_i + t\lambda_i \vec{h}_i) \cdot \vec{h}_i dt \right). \tag{B.3.4}$$

Since by construction $\vec{h}_i \cdot \vec{g}_{i+1} = 0$ and by the fact that $\vec{h}_{i-1} \cdot \vec{g}_i = 0$ and $\vec{h}_i = \vec{g}_i + \gamma_i \vec{h}_{i-1}$ we obtain from (B.3.4)

$$\lambda_i = \frac{\vec{h}_i \cdot \vec{g}_i}{\vec{g}_i \cdot A_i \vec{h}_i} = \frac{\vec{g}_i \cdot \vec{g}_i}{\vec{h}_i, A_i \vec{h}_i}, \text{where} \tag{B.3.5}$$

$$A_i = \int_0^1 A(\vec{x}_i + t\lambda_i \vec{h}_i) dt. \tag{B.3.6}$$

Now, from (B.2.4) and (B.3.4) together with (B.3.5) we find that

$$\gamma_i = -\frac{\vec{g}_{i+1} \cdot A_i \cdot \vec{h}_i}{\vec{g}_i \vec{g}_i} \cdot \frac{\vec{g}_i \cdot \vec{g}_i}{\vec{h}_i \cdot A_i \cdot \vec{h}_i} - \frac{\vec{g}_{i+1} \cdot A_i \cdot \vec{h}_i}{\vec{h}_i \cdot A_i \cdot \vec{h}_i}. \tag{B.3.7}$$

But from assumption (B.3.2) we deduce that for all $\vec{h} \in \Re^N$ $m\|\vec{h}\|^2 \leq \vec{h}_i \cdot A_i \cdot \vec{h}_i \leq M\|\vec{h}\|^2$, and hence we must have

$$|\gamma_i| \leq \frac{\|\vec{g}_{i+1}\| \|A_i\| \|\vec{h}_i\|}{m\|h_i\|^2} \leq \frac{\|\vec{g}_{i+1}\|}{\|\vec{h}_i\|} \frac{M}{m}, \tag{B.3.8}$$

since $\|A_i\| \leq M$. Now, by the triangle inequality,

$$\|\vec{h}_{i+1}\| \leq \|\vec{g}_{i+1}\| + |\gamma_i| \, \|\vec{h}_i\|, \tag{B.3.9}$$

which becomes, because of (B.3.8),

$$\|\vec{h}_{i+1}\| \leq \|\vec{g}_{i+1}\| \left(1 + \frac{M}{m}\right). \tag{B.3.10}$$

Finally,

$$\vec{h}_{i+1 \cdot \vec{g}_{i+1}} = (\vec{g}_{i+1} + \gamma_i \vec{h}_i) \cdot \vec{g}_{i+1} = \vec{g}_{i+1} \cdot \vec{g}_{i+1}, \;\; i = 0, 1, 2, \ldots. \tag{B.3.11}$$

Consequently, for $i = 0, 1, 2, \ldots,$

$$\begin{aligned} \frac{\vec{h}_{i+1} \cdot \vec{g}_{i+1}}{\|\vec{h}_{i+1}\| \|\vec{g}_{i+1}\|} &= \frac{\|\vec{g}_{i+1}\|^2}{\|\vec{h}_{i+1}\| \|\vec{g}_{i+1}\|} = \frac{\|\vec{g}_{i+1}\|}{\|\vec{h}_{i+1}\|} \\ &\geq \frac{\|\vec{g}_{i+1}\|}{\|\vec{g}_{i+1}\|(1 + M/m)} = \frac{1}{1 + M/m}, \end{aligned} \tag{B.3.12}$$

which is the desired result. □

Having obtained a relation (B.3.3) by Lemma B.3.2 we use it in the proof of Theorem B.3.1. In what follows we only present the basic idea of the proof and its realization in a few major steps.

Proof. According to the Polak-Ribière algorithm we construct a sequence of points $\{\vec{x}_i = x_{i-1} + \lambda_{i-1}\vec{h}_{i-1}\}$, where $\lambda_{i-1} > 0$ is such that

$$f(\vec{x}_{i-1} + \lambda_{i-1}\vec{h}_{i-1}) = \min_{\lambda \geq 0}\{f(\vec{x}_{i-1} + \lambda\vec{h}_{i-1})\}. \tag{B.3.13}$$

The algorithm stops at the point $\vec{x}_k$ in a finite number of iterations k if and only if $\nabla f(\vec{x}_k) = 0$, and since by assumption, $f(\vec{x})$ is strictly convex, such a point is the solution to (B.3.1).

The infinite sequence of points $\{x_i\}$ converges to the point of global minimum $\hat{\vec{x}}$ if any accumulation point $\hat{\vec{x}}$ of the sequence $\{\vec{x}_i\}$ constructed by the Polak-Ribière algorithm satisfies $\nabla f(\hat{\vec{x}}) = 0$, and hence minimizes $f(\vec{x})$ over $\Re^N$. Thus, to prove the second part of the theorem we first have to show that the set $\{\vec{x}|f(\vec{x}) \leq f(\vec{x}_0)\}$ is compact. Second, we simply use the convexity of $f(\vec{x})$ to claim that there is only one minimizing accumulation point $\hat{\vec{x}}$ that satisfies $\nabla f(\hat{\vec{x}}) = 0$.

The set $\{\vec{x}|f(\vec{x}) \leq f(\vec{x}_0)\}$ is compact and contains the point of minimum if for all $\vec{x}' \in \{\vec{x}' : \|\vec{x} - \vec{x}'\| \leq \epsilon(\vec{x})\}$ and for all $\vec{y} = \vec{x} + \lambda\vec{h} \in \{\vec{x}' : \|\vec{x} - \vec{x}'\| \leq \epsilon(\vec{x})\}$, where $\vec{h}$ satisfies (B.2.4) for $i = 0, 1, 2, \ldots$

$$f(\vec{y}) - f(\vec{x}') \leq \delta(\vec{x}) < 0. \tag{B.3.14}$$

To validate (B.3.14) we find an upper bound $\delta(\vec{x})$ for the difference

$$f(\vec{x} + \lambda\vec{h}) - f(\vec{x})$$

using the Taylor expansion formula and inequality (B.3.3). That is, for every $\vec{h}$ constructed by the Polak-Ribière algorithm and for all $\lambda \geq 0$, we have

$$f(\vec{x}+\lambda\vec{h}) - f(\vec{x}) = \lambda\nabla f(\vec{x})\cdot\vec{h} + \lambda^2\int_0^1 (1-t)\vec{h}\cdot A(\vec{x}+t\lambda\vec{h})\cdot\vec{h}dt, \tag{B.3.15}$$

where A is the Hessian matrix. From (B.3.15) and assumption (B.3.2) it follows that

$$f(\vec{x}+\lambda\vec{h}) - f(\vec{x}) \leq -\lambda\rho\|\nabla f(\vec{x})\|\|\vec{h}\| + \frac{1}{2}\lambda^2 M\|\vec{h}\|^2. \tag{B.3.16}$$

To make sure that (B.3.16) is satisfied for all $\vec{y} = \vec{x}+\lambda\vec{h})$ we minimize the right-hand side of (B.3.16) with respect to λ to obtain

$$\delta(\vec{x}) = -\frac{\rho^2}{2M}\|\nabla f(\vec{x})\|^2 < 0 \tag{B.3.17}$$

as required by (B.3.14). □

Theorem B.3.1 guarantees convergence of the Polak-Ribière algorithm to the minimum of a quadratic function. When minimizing a non-convex function we usually arrive at the supposed minimum of the quadratic form in $k \leq N$ iterations and then start the conjugate gradient procedure anew resetting $\vec{h_k} = \vec{g_k}$ in the downhill local direction rather than computing $\vec{h}_k$ according to (B.2.4).

Appendix C

Matlab codes for generation of Darcyan coordinate systems

C.1 Elliptic method

```
%=====================================================================
Given an image this code subsequently calls subroutines ‘‘darcyan4.m’’
for computation of the Darcyan grid and ‘‘see_x_mod.m’’ for its display.
%=====================================================================
I=imread(’brain.jpg’);
I1=rgb2gray(I);
[bw,b,inside,u,x,tm]=darcyan4(I1);
see_x_mod(x);

%=====================================================================
%Generation of the Darcyan coordinate system in a compact, connected and
%simply connected domain "X" of an organism by elliptic method.
%=====================================================================
function [bw,b,inside,u,x,tm]=darcyan4(I1)

n_iter=2000;[l1,l2]=size(I1);
size(I1)
figure
%contour a polygonal region of interest
bw=roipoly(I1);
b=bwboundaries(bw,4);b=b{1,1};

%get interior pixel coordinates
inside=bw;
n_b=size(b);n_b=n_b(1);
for i=1:n_b
```

```
    inside(b(i,1),b(i,2))=0;
end

%enumerate interior
inside=inside(:);
indices=find(inside);n_indices=length(indices);
indices=indices-1;max(indices)

%start relaxation procedure for Poisson equation for solution "u" given "v"
%right hand side
[pole1,pole2]=ginput(1);
%get pole
pole1=round(pole1)
pole2=round(pole2)
tic
relax_coeff=0.8;u=zeros(l1,l2);v=u;v(pole2,pole1)=1;
1
for iter=1:n_iter

    for i=1:n_indices
       x=ceil(indices(i)/l1);
       y=indices(i)+1-(x-1)*l1;
       x1=x;x=y;y=x1;
       laplace=u(x+1,y)+u(x-1,y)+u(x,y+1)+u(x,y-1);
       u(x,y)=(1-relax_coeff)*u(x,y)+(relax_coeff/4)*(laplace-v(x,y));
    end

end
2
%normalize radial coordinate "xi1" increasing 0 -> 1 toward pole
u=1-exp(u);
u=u./max(max(u));%CHANGE VALUE IF POWER USED
u=sqrt(u);
%this is to make u-level curves more equally distributed
u=histeq(u,250);
[g1,g2]=gradient(u);
%discretizes boundary
%makes periodic boundary
b=[b;b(1,:)];
ds=diff(b,1,1);
%cumulated arc lengths
ls=ds.^2;ls=ls(:,1)+ls(:,2);ls=sqrt(ls);ls=cumsum(ls);

%discretize into "n_d" arcs
n_d=60;%NOTE!
```

```
%to improve, interpolate instead of "floor"
arcs=floor([1:n_d].*n_b./n_d);arcs=[1,arcs];
%darcyan coordinates
x=zeros(2,n_d,n_d);

%introduce angular coordinate xi_2 at boundary
for xi2=1:n_d
    x(1,1,xi2)=b(arcs(xi2),1);x(2,1,xi2)=b(arcs(xi2),2);
end
3
%increment  radial coordinate xi_1
for xi1=1:n_d-1
    for xi2=1:n_d
        x1=x(1,xi1,xi2);x2=x(2,xi1,xi2);
        x_set=u>xi1/n_d;%inside level curve of u
        [r,c]=find(x_set);
        dist2=(r-x1).^2+(c-x2).^2;
        [y,i]=min(dist2);x1_new=r(i);x2_new=c(i);
        x(1,xi1+1,xi2)=x1_new;x(2,xi1+1,xi2)=x2_new;
    end
end
toc
tm=toc;

%=================================================================
% Display the 2D Darcyan curvilinear coordinate system
%=================================================================
function see_x_mod(x)
%display Darcy coordinate system for x-field
l=length(x(1,:,1));
k=length(x(1,1,:));
for xi1=1:l
    plot([squeeze(x(1,xi1,:))',x(1,xi1,1)],[squeeze(x(2,xi1,:))',x(2,xi1,1)],'b')
    hold on
end

for xi2=1:k
    plot([squeeze(x(1,:,xi2))],[squeeze(x(2,:,xi2))],'b')
    hold on
end
```

C.2 Level Set Method

```
%=================================================================
% Automatic boundary extraction of an organism seen in image 'I'.
%=================================================================
function [b,x,y,s]=get_init_boundary_f(I);
I=rgb2gray(I);
h=fspecial('average', [11 11]);% removing noise from the boundary
Im=imfilter(I,h);

level=graythresh(Im);
BW=im2bw(Im,level);
figure, imshow(BW);
s=size(BW);

% find a point that belongs to the boundary
st=ceil(s(1)/2)-1;
row=st+1;
   for col=2:s(2)-1
      if BW(row,col), break,end
      end;

% trace the boundary of an organism in the clockwise direction
   cont = bwtraceboundary(BW, [row, col], 'W', 8, Inf,...
                                'clockwise');
   if(~isempty(cont))
      hold on;
      plot(cont(:,2),cont(:,1),'g','LineWidth',2);
      hold on;
      plot(col, row,'gx','LineWidth',2);
   else
      hold on; plot(col, row,'rx','LineWidth',2);
   end
  s_c=size(cont);

x=[1:s(2)];
y=[1:s(1)];

xv=cont(:,2);
yv=cont(:,1);

   figure, plot(xv,yv,'b');
   axis([1 s(2) 1 s(1)])
       hold on
```

```
       per=[2,1];%permutation

% form an array holding x- and y-coordinates of pixels
% comprising the boundary
    b=cont(:,per);


%====================================================================
%This script reads image data, extracts the boundary using
%the routine ’get_init_boundary_f.m’ and records the boundary info
%in fewer pixel coordinates ’coarseb’.
%’nodes’ is an array of Darcyan grid nodes returned by the
% Level Set Method code ’get_darcyan.m’.
%====================================================================
%I=im2double(imread(’sox9_1.jpg’));
[b,x,y,s]=get_init_boundary_f(I);
    X=x;
    Y=y;
    len=length(b);
%--------------------------------------------------------------------
% get a coarser grid to smoothen the boundary
    for k=1:floor(len/3)
        coarseb(k,:)=b(3*k-1,:);
    end
    figure, plot(coarseb(:,1),coarseb(:,2),’r*’)
    for i=1:floor(length(X)/3)
        x(i)=X(3*i-1);

    for j=1:floor(length(Y)/3)
        y(j)=Y(3*j-1);
       end;
    end;
 %  nodes=get_darcyan(coarseb, x,y,s);


%=================================================================
% Propagation of the extracted boundary of the organism inwards by
% means of curvature-dependent flow in order to generate the
% Darcyan coordinate system inside the organism’s domain.
%=================================================================
   function [current_nodes1,current_nodes2]=get_darcyan(b,x,y,s)

% computation of mean arclength between adjacent nodes
    ds=diff(b);
    lc=ds.^2;
    lc=lc(:,1)+lc(:,2);
```

```
    lc=sqrt(lc);
    len=length(lc)
    meanl=mean(lc);
    lcum=zeros(len,1);

% computation of the boundary length
    lcum(1)=lc(1);
    ssum=lcum(1);
    for l=2:len
    lcum(l)=ssum+lc(l);
    ssum=lcum(l);
    end;

% number of angular coordinate curves
    M=120;
% nodal equidistribution
    dist_eq=lcum(len)/M;
    newarcl=[1:M].*dist_eq;
    arcs=floor([1:M].*len./M);arcs=[1,arcs];

    xnode=b(arcs,1);
    ynode=b(arcs,2);

    figure,plot(xnode, ynode, 'b+');

    vector1=zeros(len,1);
    vector2=zeros(len,1);

    vector1=b(2:end,1);
    vector2=b(2:end,2);

    new_x=interp1(lcum,vector1,newarcl,'spline');
    new_y=interp1(lcum,vector2,newarcl,'spline');

    figure,plot (new_x,new_y,'r*');
    axis([1 s(2) 1 s(1)]);
    tic

     %solving parametric equations of motion
     %xt=F(k)*(ys/(xs^2+ys^2)^1/2)
     %yt=-F(k)*(xs/(xs^2+ys^2)^1/2)

%-----------------------------------------------------------
% initial nodal points  new_x, new_y
% finding central differences approximations
```

```
    meanl=dist_eq;
    lc=ones(M,1).*meanl;
% time step
    delta_t=0.8*dist_eq;

    nodes=zeros(length(new_x)+2,2);
    growth=zeros(length(new_x)+2,2);
    current_nodes1=zeros(length(new_x),5000);
    current_nodes2=zeros(length(new_x),5000);

% initial equidistant nodal distribution along the boundary
    nodes=[[new_x(end);new_x';new_x(1)],[new_y(end);new_y';new_y(1)]];
    iter=1;
    niter=60000;
    k=1;
    current_nodes1(:,k)=nodes(2:end-1,1);
    current_nodes2(:,k)=nodes(2:end-1,2);
    figure
    plot(nodes(:,1),nodes(:,2),'r');
    axis([1 s(2) 1 s(1)]);
    hold on

    for iter=1:niter
    total_l1=sum(lc);
% computing the right-had side of the equation of motion
    RHS=get_rhs(nodes);

    nodes0=nodes+delta_t*RHS;
    nodes0(1,:)=nodes0(end-1,:);
    nodes0(end,:)=nodes0(2,:);

% Heun's method
    RHS0=get_rhs(nodes0);
    growth=delta_t/2*(RHS+RHS0);
    nodes=nodes+growth;
    nodes(1,:)=nodes(end-1,:);
    nodes(end,:)=nodes(2,:);
    if (iter==1)
    distlist=sqrt(growth(:,1).^2+growth(:,2).^2);
    maxd=max(distlist);
    [j,l]=find(distlist==maxd);
    dist=maxd;
    else
    dist_j=sqrt(growth(j,1).^2+growth(j,2).^2);
    dist=dist+dist_j;
```

```
     end;

% update the locations of Darcyan nodal points
     vector1=nodes(1:end-1,1);
     vector2=nodes(1:end-1,2);
     b=[vector1,vector2];

% compute minimal arclength between new adjacent nodes
% and the length of a new radial coordinate curve
     [minl,lc1]=get_arclen(b);

     [nodes]=redistr(nodes,lc1,M);
     vector1=nodes(1:end-1,1);
     vector2=nodes(1:end-1,2);
     b=[vector1,vector2];

     [minl,lc]=get_arclen(b);

     total_l2=sum(lc);

     if(k>=80)
         iter
         break
     end;
% a criterion that the distance between consequent radial curves
% has to satisfy in order for the next radial curve to be plotted
     if (dist>=(0.6*(k/80)^2+0.8)*meanl) %record the radial curve
     dist=0;
     meanl=mean(lc);
     plot(nodes(:,1),nodes(:,2),'r');
     axis([1 s(2) 1 s(1)]);
     hold on
     k=k+1;
     current_nodes1(:,k)=nodes(2:end-1,1);
     current_nodes2(:,k)=nodes(2:end-1,2);
     end;
% set time step in accordance with the minimal arclength
     delta_t=0.1*minl;
     iter
     end;

        for m=1:length(new_x)
        plot(current_nodes1(m,:),current_nodes2(m,:),'b');
          axis([1 s(2) 1 s(1)]);
        hold on
```

```
        end;

      toc
      tm=toc

    xold(1,:,:)=current_nodes1(:,:);
    xold(2,:,:)=current_nodes2(:,:);

%=======================================================================
%Computation of the curvature-dependent speed of the boundary
%flow 'F(:,:)' and the gradient to the level curve 'grad(:,2)'.
%=======================================================================
function RHS=get_rhs(nodes)
     p=length(nodes);
% calculating the right-hand side
     nodes0=zeros(p,2);
     diff2=zeros(p,2);
     diff1=zeros(p,2);
     num=zeros(p,1);
     denum=zeros(p,1);
     absn=zeros(p,1);
     K=zeros(p,1);
     F=zeros(p,2);
     grad=zeros(p,2);
     RHS=zeros(p,2);

     i=[2:p-1];
     diff2(i,:)=nodes(i+1,:)-2*nodes(i,:)+nodes(i-1,:);
     diff1(i,:)=nodes(i+1,:)-nodes(i-1,:);
     num(i)=diff2(i,2).*diff1(i,1)-diff2(i,1).*diff1(i,2);
     absn(i)=(diff1(i,1).^2+diff1(i,2).^2);
     denum(i)=absn(i).^(3/2);
     indices=find(denum);

     K(indices)=num(indices)./denum(indices);
     K(~indices)=0.0;

     meanK=abs(mean(K));

     for j=2:p-1

        F(j,:)=min(-K(j),-meanK);
        end;

% calculate gradient to the level curve
```

```
     grad(indices,1)=diff1(indices,2)./(absn(indices).^(1/2));
     grad(indices,2)=-diff1(indices,1)./(absn(indices).^(1/2));
     grad(~indices,:)=0.0;

     RHS=F.*grad;

%===================================================================
% Nodal redistribution in accordance with equal arclength distance
% between adjacent nodes 'dist_eq'.
%===================================================================
function [nodes]=redistr(nodes,lc,M)
    p=size(nodes,1);

    len=length(lc);
    cum=zeros(len,1);
    newarcl=zeros(len,1);
    cum(1)=lc(1);
    ssum=cum(1);

    for l=2:len

    cum(l)=ssum+lc(l);
    ssum=cum(l);
    end;


    dist_eq=cum(len)/M;

    newarcl=[1:M].*dist_eq;
    newarcl(1)=newarcl(1)+0.0001;
    newarcl(M)=newarcl(M)-0.0001;

    vect1=zeros(len,1);
    vect2=zeros(len,1);

    vect1=nodes(2:p-1,1);
    vect2=nodes(2:p-1,2);
% new nodal coordinates
       node1=interp1(cum,vect1,newarcl,'spline');
       node2=interp1(cum,vect2,newarcl,'spline');

    nodes(2:p-1,1)=node1;
    nodes(2:p-1,2)=node2;

    nodes(1,:)=nodes(p-1,:);
```

```
    nodes(p,:)=nodes(2,:);

%======================================================================
% Computation of the boundary length 'lc1' and the minimum
% arclength distance 'minl'
%======================================================================
function [minl,lc1]=get_arclen(b);
    lc=zeros(size(b,1)-1,2);
    lc1=zeros(size(b,1)-1,1);
    ds=diff(b);
    lc=ds.^2;
    lc1=lc(:,1)+lc(:,2);
    lc1=lc1.^(1/2);
    len=length(lc1);
    minl=min(lc1);

%=======================================================================
%Display of the gene expression pattern 'F(:,2)' in Darcyan coordinates
%=======================================================================
% given Darcyan grid with nodal positions recorded by arrays
% 'current_nodes1(:,:)' and 'current_nodes1(:,:)'
function F=display_gs(current_nodes1, current_nodes2, I)
sz=size(current_nodes1);
k1=sz(1);
k2=sz(2)-1;

s=size(I);
x=[1:s(2)];
y=[1:s(1)];
st=ceil(s(1)/2)-1;
% display an image
iptsetpref('ImshowAxesVisible','on')
figure,imshow(I,'Xdata',x,'Ydata',y);
colormap(gray)
hold on;
% display the Darcyan grid over an organism under study
 for m=1:k2
     nodes1=[current_nodes1(:,m); current_nodes1(1,m)];
     nodes2=[current_nodes2(:,m); current_nodes2(1,m)];
         plot(nodes1,nodes2,'r');
         axis([1 s(2) 1 s(1)]);
        hold on
        end;
  for m=1:k1
```

```
        plot(current_nodes1(m,:),current_nodes2(m,:),'b');
          axis([1 s(2) 1 s(1)]);
          hold on
        end;
    n_sets=input(['how many gene sets in the phase \n']);
    genesets=cell(1,n_sets);
% input vertices of a polygonal area containing
% active gene cites that appear in dark color
    for i=1:n_sets
         [v1s,v2s]=ginput;
% get points inside polygon
    IN=inpolygon(current_nodes1,current_nodes2, v1s, v2s);
    inside=find(IN);
    n=length(inside);
% F represents a gene set
    F=[];
    for xi1=1:k1
        for xi2=1:k2
            if IN(xi1,xi2)==1
                F=[F;[current_nodes1(xi1,xi2), current_nodes2(xi1,xi2)]];
             end;
        end;
    end;
    plot(F(:,1), F(:,2),'*r')
    hold on
    genesets{1,i}=F;
    end;
```

Appendix D

Matlab codes for generation of 2D GRID growth patterns

D.1 Gene control structure

```
%======================================================================
%A code ’gene_contr.m’ for setting up initial conditions for the
%fundamental GRID equation of growth in the form of gene control
%algebraic structure.
%======================================================================
function gene_control = gene_contr(x)
%’x’ denotes polar Darcyan grid
%’x1,x2’ are absolute space coordinates
x1=squeeze(x(1,:,:));
x2=squeeze(x(2,:,:));
l1=size(x1,1);
l2=size(x1,2);

%defining a structure and field names
gene_control=struct(’phase’,[],’sets’,[],’durations’,[],’contrasts’,[],...
’k_values’,[],’directions’,[],’steps’,[]);

%loading a mat file containing a list of angular
%deformation functions ’k1, k2,...,k11’
load /home/nportman/Ulf/GRID_experiments/newk_values...
k1 k10 k11 k2 k3 k4 k5 k6 k7 k8 k9

n_phase=input([’how many phases \n’]);
dur=[];contrast=[];g1=[];step=[];

figure (’Units’, ’Normalized’, ’Position’, [0 0 1 1]);
```

```
for i_phase=1:n_phase
name=input(['name of a phase= \n'], 's');
gene_control(i_phase).phase=name;

%input a number of disjoint gene sets
n_sets=input(['how many gene sets in the phase \n']);

sets=cell(1, n_sets);
durations=cell(1, n_sets);
k_values=cell(1, n_sets);
contrasts=cell(1, n_sets);
steps=cell(1, n_sets);
%--------------------------------------------------------------

for i_sets=1:n_sets

[dur,contrast,g1]=inp_data(i_sets);

%determine the gene sets in the absolute space
sets{1,i_sets}=x_genesets(x,x1,x2,i_sets);
pause

%transform from X-field to xi-values
       xset=sets{1,i_sets};
       n_x_set=size(xset,1);
       xi_sets=[];

       for p=1:n_x_set
       xi_sets=[xi_sets;x2xi(x, xset(p,1), xset(p,2))] ;
       end;

sets{1,i_sets,:}=xi_sets
pause

durations{1,i_sets}=dur;
contrasts{1,i_sets}=contrast;
pause
m=menu('Choose k-function','uni-source-for','uni-source-mid',...
'uni-source-back','uni-sink-for','uni-sink-mid','uni-sink-back',...
        'bi-source-for-sink-back','bi-source-back-sink-for',...
        'multi-source-back-sink-mid-source-for',...
        'uni-source-skew-for','bulge')
eval(['k=k',num2str(m)]);
k=k';
```

```
%applying multiplicative operation to the k-values
k(2,:)=group(k(2,:),g1);
k_values{1,i_sets}=k;
pause

% determining the principal direction of growth/decay
direction=input(['direction in radians =\n']);
directions{1,i_sets}=direction;
pause

%determining the range of influence of each seed in 'gene_sets'
step=input(['step value =\n']);
steps{1,i_sets}=step;
pause
end;

 gene_control(i_phase).sets=sets;
 gene_control(i_phase).durations=durations;
 gene_control(i_phase).contrasts=contrasts;
 gene_control(i_phase).k_values=k_values;
 gene_control(i_phase).directions=directions;
 gene_control(i_phase).steps=steps;

end;

%=====================================================================
%This code inputs user data on phase duration, contrast and magnifying
%factor for k-values.
%=====================================================================
function [dur,contrast,g1]=inp_data(i_sets)
%input time interval
 dur=input(['duration 2_vector for set no. ',num2str(i_sets), '= \n']);
 pause
%input contrast value for the gene set
 contrast=input(['contrast value for set no. ',num2str(i_sets),'= \n']);
 pause
%input the multiplicative factor for k-values
 g1=input('Value of k-ampl group \n');
 pause

%=====================================================================
%This code determines a geometric form of gene sets and returns them
%in absolute space coordinates '(x1,x2)'.
```

```
%=====================================================================
function genesets = x_genesets(x,x1,x2,i_sets);
l1=size(x1,1);
l2=size(x1,2);

c=cell(1,3); c{1,1}=['point set']; c{1,2}=['line element'];
c{1,3}=['area set'];

%select a geometric form of a gene set
type=listdlg('PromptString', ['select type of gene set no. ', ...
num2str(i_sets)],'ListString',c);

    switch type
        case 3
%input polygon
    see_x_mod(x);

%polygon vertices
    [v1s,v2s]=ginput;

%get points inside polygon
    IN=inpolygon(x1,x2, v1s, v2s);
    inside=find(IN);
    n=length(inside);

%F represents a gene set in the Darcyan coordinate system 'X(xi1,xi2)'
    F=[];
    for xi1=1:l1
        for xi2=1:l2
            if IN(xi1,xi2)==1
                F=[F;[x1(xi1,xi2), x2(xi1,xi2)]];
             end;
        end;
    end;
    plot(F(:,1), F(:,2),'*g')
    hold on
    genesets=F;

        case 1
        % input point by point

        see_x_mod(x);
        [v1s,v2s]=ginput;
        n_v=length(v1s);%number of points
        plot (v1s,v2s, '*g');
```

```
        hold on
        genesets=[v1s';v2s']';

        case 2
        % define points on a line segment

        see_x_mod(x);
        [v1s,v2s]=ginput(2);
        d1=v1s(2)-v1s(1);
        d2=v2s(2)-v2s(1);
        % x1s and x2s are absolute space coordinates
        x1s=v1s(1)+(1:10)*d1/10;
        x2s=v2s(1)+(1:10)*d2/10;
        plot(x1s,x2s, '*g');
        hold on
        genesets=[x1s;x2s]';
        end;

%============================================================
%This code transforms absolute space coordinates of
%seeds in 'gene_sets' into Darcyan coordinates '(xi1,xi2)'
%============================================================
function xi_sets=x2xi(x, xp1, xp2)

l1=size(x(:,:,:),2); l2=size(x(:,:,:),3);
dist=zeros(l1,l2);
dist(1:l1,1:l2)=(x(1,1:l1,1:l2)-xp1).^2 + (x(2,1:l1,1:l2)-xp2).^2;
dist1=dist(:);
[minc,i]=min(dist1)
xi2=ceil(i/l1);
xi1=i-(xi2-1)*l1;
xi_sets=[xi1, xi2];
```

D.2 2D GRID growth pattern governed by the gene control structure

```
%=============================================================
%This code executes the genetic program of development
%specified by the 'gene_control' structure
%=============================================================
function [M,x_new]=execute_gene_control(gene_control,x)
%runs GRID for given gene control; results in movie "M" and
%new Darcyan grid "x_new"
```

```
t_iter=150;%INCREASE WHEN NEEDED
n_phase=length(gene_control);

%get duration n x 2 matrix "ts"
ts=[];set=[];
for nu=1:n_phase
g_c=gene_control(nu);d=g_c.durations;d=d{1};
d1=d(1);d2=d(2);ts=[ts;[d1,d2]];
end

%begin iterating GRID
for t=1:t_iter

%search for overlapping phases
%'w' is a vector with a number of components equal to 'n_phase'.
%If it contains two or more component values equal to 1,
%then the corresponding phases overlap.
    w=(t>=ts(:,1))&(t<=ts(:,2));
    w1=find(w); n_w=length(w1);
    if n_w==0
        return
    end

%Given 'n_w' phases enumerated by 'w1' values we choose
%one phase 'w1(s)' at random given that all of them are equally
%likely to occur at a time 't'
    s=select(ones(1,n_w)./n_w);s=w1(s);
    i_phase=s

%gene_control data for the chosen phase
    name=gene_control(i_phase).phase;
    ['build phase ',gene_control(i_phase).phase]
    pause(.5)
    k_values=gene_control(i_phase).k_values;
    durs=gene_control(i_phase).durations;
    sets=gene_control(i_phase).sets;n_sets=length(sets);
    steps=gene_control(i_phase).steps;

    for i_sets=1:n_sets
        dur=durs(1,i_sets);
        set=sets{1,i_sets};
        k_value=k_values{1,i_sets};
        step=steps{1,i_sets};
        xs=k_value(1,:);ys=k_value(2,:);
```

```
        n_set=size(set);n_set=n_set(1);

%Given 'n_set' uniformly distributed seeds in a
%current gene set activate one seed at random
        j=select(ones(1,n_set)./n_set);
        step=steps{1,i_sets};
        seed=set(j,:);

%update Darcyan grid 'x' to 'x_new' according
%to the GRID fundamental equation of growth
        [x_new,k]=get_new_x(x,seed,xs,ys,step);

            figure('Units','normalized','Position',[0 0 1 1])
            plot([-2 2 2 -2 -2],[-2 -2 3 3 -2],'b')
            hold on
            %axis manual
            see_x_mod(x_new);
            hold on
            title(name)
            xi_seed=x(:,seed(1),seed(2));
            plot(xi_seed(1),xi_seed(2),'b*')
            hold on
            for k=1:n_set
            x_set=x_new(:,set(k,1),set(k,2));
            plot(x_set(1),x_set(2),'g');
            hold on
            end;
            M(t)=getframe(gcf);
            image(M(t).cdata)
            colormap(M(t).colormap)
            hold off
            pause(.1)
            close
            x=x_new;
        end
end

function k_new=group(k_old,mult)
k_new=mult.*(k_old-1)+1;

%==================================================================
%This code deforms the Darcyan grid of a 2D organism in the
%neighborhood of the activated seed according to the specified
%'k'-function.
```

```
%====================================================================
function [x_new,k]=get_new_x(x,seed,xs,ys,step);
l1=length(x(1,:,1));
l2=length(x(1,1,:));
x_new=x;
step2=step^2;
vv1=x(:,seed(1)+1,seed(2))-x(:,seed(1),seed(2));
u1=vv1./(norm(vv1)+.0001);

%orthogonal unit vector:
u2=[u1(2),-u1(1)]';
k=zeros(l1,l2);

for xi1=1:l1
    for xi2=1:l2
        v=x(:,xi1,xi2)-x(:,seed(1),seed(2));u=v./(norm(v)+.0001);
        %compute cosine of an angle between unit vector 'v' and
        %the principal axis 'xi1';
        %interpolate to evaluate 'k'-function at 'kappa'
        kappa=u'*u1;k(xi1,xi2)=interp1(xs,ys,kappa);
    end;
end;

%apply phi-mapping to the current Darcyan grid 'x_new=x'.
    xx1=squeeze(x_new(1,:,:));
    xx2=squeeze(x_new(2,:,:));
          v1=xx1-xx1(seed(1),seed(2));
          v2=xx2-xx2(seed(1),seed(2));
    norm2=v1.^2+v2.^2;

    x_new(1,:,:)=xx1+(k-1).*v1.*exp(-norm2./(step2+0.0001));
    x_new(2,:,:)=xx2+(k-1).*v2.*exp(-norm2./(step2+0.0001));
```

D.3 Evolution of the Jacobian determinant in time

```
%=====================================================================
%This code is similar to the code 'execute_gene_control' but it also
%computes evolution of the Jacobian determinant in time.
%=====================================================================
function[F,x_new,J]=growth_rates(gene_control,x)
%_____________________________________________________________________
mov=avifile('growth_forward.avi');
mov.fps=1;
```

```
n_phase=length(gene_control);
%_____________________________________________________________________
for i_phase=1:n_phase
nsets(i_phase)=length(gene_control(i_phase).sets)
end;

%get duration n x 2 matrix "ts"
ts=cell(1,n_phase);
SET=[];
for nu=1:n_phase
    tt=[];
    for j=1:nsets(nu)
    g_c=gene_control(nu);d=g_c.durations{1,j};tt=[tt;d];
    end;
ts{1,nu}=tt;

%calculate total time of growth
l(nu)=max(max(tt));
end
t_iter=max(l);

%begin iterating GRID
%initialization

for t=1:t_iter
    arr=[];
    %determine a phase and a gene_set
    i_phase=1;

    while i_phase<=n_phase
    t_seq=ts{1,i_phase}
    w=(t>=t_seq(:,1))&(t<=t_seq(:,2));
    w1=find(w);
    n_w=length(w1);
    if n_w~=0
        for i=1:n_w
            arr=[arr;[i_phase,w1(i)]];
        end;
    end;
    i_phase=i_phase+1;
    end

    %select a phase
    l1=length(arr(:,1));
    s=select(ones(1,l1)./l1);
```

```
    i_phase=arr(s,1);
    %a number of a gene set associated with the phase
    i_sets=arr(s,2);

    %build a growth pattern
    name=gene_control(i_phase).phase;
    ['build phase ',gene_control(i_phase).phase]
    pause(.5)
    k_value=gene_control(i_phase).k_values{1,i_sets};
    dur=gene_control(i_phase).durations{1,i_sets};
    SET=gene_control(i_phase).sets{1,i_sets}
    n_set=size(SET,1);
    theta=gene_control(i_phase).directions{1,i_sets};
    step=gene_control(i_phase).steps{1,i_sets};

%'xs,ys' represent tabulated 'k'-function.
%'xs' refers to cos(tau) and 'ys' refers to 'k(cos(tau))'
    xs=k_value(1,:);ys=k_value(2,:);
%select a seed from a current gene set
    j=select(ones(1,n_set)./n_set);
    seed=SET(j,:);

       if(t==1)
       %initial value of the Jacobian determinant
           J_init=ones(size(x,2),size(x,3));
        else
           J_init=J;
       end;
       [J,x_new,k]=get_jacob(x,seed,xs,ys,step,theta,J_init);
       %plotting the Jacobian
       X_coord=squeeze(x(1,:,:));
       Y_coord=squeeze(x(2,:,:));
   %_____________________________________________
    fig=figure;
    set(fig,'Units','normalized');
    rec=[0.2 0.2 0.8 0.6];
    set(fig,'Renderer','painters','DoubleBuffer','on', 'Position',rec);
    set(gca, 'xlim',[-1.2 2],'ylim',[-1.2 1.2]);
    hold on
   %____________________________________________
   %color-coded plot of the Jacobian determinant over the Darcyan grid
    pcolor(X_coord,Y_coord,J);
    hold on;
    xi_seed=x(:,seed(1),seed(2));
```

```
    plot(xi_seed(1),xi_seed(2),'g*')
    hold on
    F(t)=getframe(gcf);
    L=F(t).cdata;
    mov=addframe(mov,L);
    pause(1.0);
    close all
    x=x_new;
 end
mov=close(mov);

%==================================================================
%A code for computation of the Jacobian determinant at all times 't'
%with respect to the initial Darcyan coordinate system 'X(xi)'
%==================================================================
function [J,x_new,k]=get_jacob(x,seed,xs,ys,step,theta,J_init);
l1=length(x(1,:,1));
l2=length(x(1,1,:));
x_new=x;
step2=step^2;

%k_values of the Darcyan coordinate system,
%k is a function of an angle k=k(cos %tau)
k=zeros(l1,l2);

theta1=acos(xs);
theta=theta+theta1;

%redefine the domain of 'k(tau)'
xs=cos(theta);
xs(1)=xs(1)-0.05;
xs(10)=xs(10)+0.05;
for xi1=1:l1
    for xi2=1:l2

        v=x(:,xi1,xi2)-x(:,seed(1),seed(2));
        r=norm(v);
        norm2=r^2;
        kappa=v(1)/(norm(v)+.0001);
        %compute 'k'-values for all Darcyan nodes 'x(xi1,xi2)'
        k(xi1,xi2)=interp1(xs,ys,kappa);
        K=k(xi1,xi2)-1;
J(xi1,xi2)=(1+K*exp(-norm2./(step2+0.0001)))*...
          (1+K*exp(-norm2./(step2+0.0001))*(1-2*r^2/step2));
    end;
```

```
end;
%update the Jacobian determinant of the cumulative transformation
    J=J_init.*J;

%update the Darcyan grid

    xx1=squeeze(x_new(1,:,:));
    xx2=squeeze(x_new(2,:,:));
          v1=xx1-xx1(seed(1),seed(2));
          v2=xx2-xx2(seed(1),seed(2));

    x_new(1,:,:)=xx1+(k-1).*v1.*exp(-norm2./(step2+0.0001));
    x_new(2,:,:)=xx2+(k-1).*v2.*exp(-norm2./(step2+0.0001));

%=======================================================================
%This is a very important auxiliary code that returns an integer labeling
%a seed to be activated in given 'gene_sets'.
%Here, 'probs' is a probability vector '(p1,p2,...,pn)' and a stochastic
%variable 'x' takes the integer value 'x=j' with probability 'pj'.
%=======================================================================
function number=select(probs)
%selects at random integer from 1 to length(probs) with
%probabilities in "probs"
r=length(probs);
number=1+sum(rand(1)>cumsum(probs));
```

Appendix E

Matlab codes for Chapter 4

E.1 “grid1d.m” for generation of long-time seed trajectories

```
% 1D GRID experimental study of growth
%=======================================================================
%Consider a 1D organism occupying (0,1) and seeds 'x_seed'
%uniformly distributed over (0,1). The organism's seed configuration
%is given by a chain of 'nseeds'=1000 seeds {x_1(x_seed),x_2(x_seed),
%...,x_nseeds(x_seed)}initially uniformly distributed with a spacing
%'delta_x'. The 'step'parameter is chosen by a user and the amplitude
%of growth 'k'=1.
%This code generates 'nexp'=30 various long-time
%(niter=20,000) trajectories for each of the four seeds starting at
%x(2), x(1000), x(floor(nseeds/3)), x(nseeds/2). Also, it computes the
%evolution of the whole seed configuration.This code can also be used
%for numerical estimation of the average length 'meanl'. For this purpose
%the number of experiments 'nexp' should be taken large.
%=========================================================================
%Initialization
nseeds=1000;
niter=20000;
delta_x=1/(nseeds+1);
x=0:delta_x:1;
nexp=30;
n=length(x(2:end-1));
seeds=zeros(n,1);
%s=zeros(nexp,n+2);
len=zeros(nexp,niter);
seeds0=x(2:end-1)';
k=1.0;
```

```
step=1*delta_x;
step2=step^2 ;
%============================================================
figure('Units','normalized','outerposition',[0 0 1 1])
axis xy
axis square
%============================================================
for j=1:nexp

seeds=seeds0;
x=0:delta_x:1;
% defining initial endpoints of the organism
a=x(1);
b=x(end);

            for i=1:niter
            q=a+(b-a)*rand; % random seed placement
            x_seed=q;
            v1=x-x_seed;
            norm2=v1.^2;
            %applying GRID transformation
            x=x+k.*v1.*exp(-norm2/step2);
            seeds=x(2:end-1)';
            %computing length increment
            len(j,i)=x(end)-x(1);
            %new seed positions
            x1(j,i)=x(2);
            x2(j,i)=x(end-1);
            x3(j,i)=x(floor(nseeds/3));
            xm(j,i)=x(nseeds/2);

            y1(i)=i;


            y=i*ones(n+2,1);
            %plotting the whole seed configuration
            plot(x, y, 'Marker', '.');
            hold on
            %plotting a particular seed trajectory
            plot(x1(niter),y1(niter),'r*')
            plot (x_seed ,i, 'r*')
            hold on
            %updating endpoints
            a=x(1);
            b=x(end);
```

```
            end;
end;
%=============================================================
figure
%plotting all four seed trajectories
plot(x1,y1,'g',x2,y1,'g',x3,y1,'c',xm,y1,'b')
hold on
%plotting initial seed positions
plot(x1(1,1),y1(1),'g*',x2(1,1),y1(1),'g*', x3(1,1),y1(1),'c*',...
xm(1,1),y1(1),'b*')

%computing mean length as a function of time
meanl=mean(len);
%mean seed trajectories
meanx1=mean(x1);
meanx2=mean(x2);
meanxm=mean(xm);
plot(meanx1,y1,'r',meanx2,y1,'r',meanxm,y1,'r')

%plotting average length
figure
for j=1:niter
y=j*ones(1,nexp);
plot(y',len(:,j)','r')
hold on
end;
%plotting exact length
for j=1:niter
    y0(j)=j;
    L_exact(j)=1/2+1/2*sqrt(1+4*y0(j)*step2);
end;
hold on
plot(y0,meanl','b',y0,L_exact,'c');
```

E.2 "FPE_sol.m" for solving 1D Fokker-Planck equation

```
%=========================================================================
%An algorithm for numerical solution of the Fokker-Planck Equation using
%forward Euler's method.
%Given (1)'nseeds'=1000 seeds marking active gene sites 'xi' uniformly
%distributed over (0,1), (2) a large range of seed influence 'step'=0.05,
%(3)initial seed position at 'xi_0' chosen by a user, (4)a seed
```

```
%configuration representing 1D organism {x_1(xi),x_2(xi),...,x_100(xi)}
%that changes in space-time due to activation of seeds 'xi' this code
%computes the probability density 'f(x,t)' of finding a seed at the
%space coordinate 'x' and at a time 't' in a finite time interval.
%========================================================================
%Initialization
%define rectangular mesh of points
delta_x=1/100;
x=0:delta_x:1;
delta_t=0.00005;
t=0:delta_t:10;
step=0.05;
step2=step^2;
K=1.0;
xi_0=0.5;
n2=length(t);
n1=length(x);
f=zeros(n1,n2);
%==============================================================
%initial and absorbing boundary conditions
eps=0.001;
%normalizing constant
N=sqrt(eps)/(atan((1-xi_0)(sqrt(eps)))-atan(-xi_0/sqrt(eps)));
f(:,1)=0;
f(51,1)=1;
%f(n1,1)=0;% 11*delta_x is the initial position
f(1,:)=0;
f(n1,:)=0;
%==============================================================
% calculate the FPE coefficients
[a,b,d1b,d2b,d1a]=get_FPEcoef2(x,N,K,step2);
% calculate ratios
r1=delta_t/(2*(delta_x ^2));
r2=delta_t/(2*delta_x);
if (2*r1>min(1./b))
delta_t=input('Choose a smaller time interval\n')
end;
%calculate the coefficients of the difference equation
alpha=r1*b+r2*(d1b-a);
beta=1-r1*b+delta_t *(1/2*d2b-d1a);
gamma=r1*b-r2*(d1b-a);

for l=2:n2
    for i=2:n1-1
   f(i,l)=alpha(i)*f(i+1,l-1)+beta(i)*f(i,l-1)+gamma(i)*f(i-1,l-1);
```

```
    end;
    C=delta_x*sum(f(:,l));
%normalization of the probability density f(x,t)
    f(:,l)=f(:,l)/C;
end;
 en=(n2-1)/1000;
 for l=2:en
 ft(:,l)=f(:,1000*l);
 end;
 ft(:,1)=0;
 ft(:,en+1)=0;
 tt=0:delta_t *1000:6;
% play a movie of the evolution of f(x,t) in time-space
 figure
 axis tight
 for j=1:en
 plot (x,ft(:,j))
     R(j)=getframe;
 end;
 movie(R,2)
%================================================================
%numerical computation of the Fokker-Planck coefficients for the
%initial position xi_0=0.5
%================================================================
function [a,b,d1b,d2b,d1a]=get_FPEcoef2(x,N,K,step2);
delta_xi=0.001;
xi=0:delta_xi:1;
k=K;
n=length(x);

for j=1:n
a(j)=k*N*delta_xi *sum((x(j)-xi).*exp(-1/step2 *(x(j)-xi).^2). ...
/(0.001+(xi-0.5).^2));
b(j)=k^2 *N*delta_xi*sum( ((x(j)-xi).^2) .*exp(-2/step2 *(x(j)-xi).^2). ...
/(0.001+(xi-0.5).^2));
d1b(j)=2*k^2*N*delta_xi*sum( (x(j)-xi).*exp(-2/step2 *(x(j)-xi).^2). ...
/(0.001+(xi-0.5).^2).*(1-2/step2 *(x(j)-xi).^2));
d2b(j)=2*k^2 *N*delta_xi*sum(exp(-2/step2 *(x(j)-xi).^2)./(0.001+(xi-0.5).^2). ...
*(1-10/step2 *(x(j)-xi).^2 +8/(step2^2) *(x(j)-xi).^4));
d1a(j)=k*N*delta_xi*sum(exp(-1/step2 *(x(j)-xi).^2)./(0.001+(xi-0.5).^2). ...
*(1-2/step2 *(x(j)-xi).^2));
end;
```

Appendix F

Matlab code for 2D macroscopic growth patterns

```
%====================================================================
function x=disk
%an auxiliary code that computes initial x-field for an unit disk with
%a polar xi_field with 150 radial and 150 angular coordinate curves.
%====================================================================
l=150;
radii=(1:l)/l;
%angles=(0:l)./l;angles=2*pi.*angles;
angles=(1:l)./l;angles=2*pi.*angles;
for xi1=1:l
  %  for xi2=1:l+1
      for xi2=1:l
        x(1,xi1,xi2)=radii(xi1)*cos(angles(xi2));
        x(2,xi1,xi2)=radii(xi1)*sin(angles(xi2));
    end
end

%===========================================================================
function [x_new,F]=macroscopic(x)
%computes thermodynamic growth with preassigned Poisson intensities and
%special "a"-array. Here, the magnitude of growth 'a_val'=const.
%suppose a single alpha-value and an initial organism comprised of seeds
%distributed according to the Poisson intensities throughout the whole
%organism domain. Here, the Poisson intensity is normalized and given by
%the probability mass function 'weight' radially decaying from the center
%of the disk.
%===========================================================================
x_1=squeeze(x(1,:,:));x_2=squeeze(x(2,:,:));a_val=2;
[n1,n2]=size(x_1);x_new=x;
```

```
step=0.2;
step2=step^2;
% defining Poisson intensity parameters:
weight=ones(n1,n2);
for i=1:10
    for j=1:n2
        weight(i,j)=4*(10-i+1);
    end;
end;
z=sum(sum(weight));
P=weight./z;
for T=1:10

for m=1:n1
    for n=1:n2
x=x_new(1,m,n);
y=x_new(2,m,n);

        v1=x_new(1,:,:)-x;v2=x_new(2,:,:)-y;norm2=v1.^2+v2.^2;
        x_new(1,:,:)=x_new(1,:,:)+a_val.*v1.*exp(-norm2/step2)*P(m,n);
        x_new(2,:,:)=x_new(2,:,:)+a_val.*v2.*exp(-norm2/step2)*P(m,n);
         end;
end;

figure('Units','Normalized','Position',[0 0 1 1])
see_x_mod(x_new);
pause(1);
print('-djpeg95', sprintf('macrosc1%03d.jpg',T));
F(T)=getframe;
close
end;
pause
movie(F);
```

Appendix G

Matlab codes for image inference

```
%=================================================================
% image preprocessing algorithm that aligns source image I_1
% with the target image I_2 about the origin of the Darcyan
% coordinate system of the wing disc seen in I_2.
% 'xold' is the Darcyan grid of the wing disc in I_1.
% 'xnew' is the Darcyan grid of the wing disc in I_2.
%=================================================================
function [I1new,xupdate,xold1,X,Y]=im_preproc(I1,I2,xold,xnew)
s=size(squeeze(xold(1,:,:)));
sz=size(I1);
x=[1:sz(2)];
y=[1:sz(1)];
N=s(1)*s(2);
x1_old=squeeze(xold(1,:,:));
x2_old=squeeze(xold(2,:,:));
x1_new=squeeze(xnew(1,:,:));
x2_new=squeeze(xnew(2,:,:));

%find the centre of mass of the cloud of points of the Darcyan coordinate
%system of both images
dis1=zeros(s(1),s(1));
dis2=zeros(s(1),s(1));
    for i=1:s(1)
        x_i=x1_old(i,end);
        y_i=x2_old(i,end);

        x2_i=x1_new(i,end);
        y2_i=x2_new(i,end);
           for j=1:s(1)
               x_j=x1_old(j,end);
               y_j=x2_old(j,end);
```

```
        x2_j=x1_new(j,end);
        y2_j=x2_new(j,end);

               dis1(i,j)=sqrt((x_i-x_j)^2 +(y_i-y_j)^2);
               dis2(i,j)=sqrt((x2_i-x2_j)^2 +(y2_i-y2_j)^2);
           end;
    end;
    [C,J]=max(max(dis1));%column number of a maximum distance
    col=dis1(:,J)';
    [C,I]=max(col);% row number of a maximum distance
    x1=x1_old(I,end);
    y1=x2_old(I,end);
    x2=x1_old(J,end);
    y2=x2_old(J,end);
    %find the middle point
    xm=(x1+x2)/2;
    ym=(y1+y2)/2;
    c1_x=xm;
    c1_y=ym;
%column number of a maximum distance
    [C,J]=max(max(dis2));
    col=dis2(:,J)';
% row number of a maximum distance
    [C,I]=max(col);
    x1=x1_new(I,end);
    y1=x2_new(I,end);
    x2=x1_new(J,end);
    y2=x2_new(J,end);
    %find the middle point
    xm=(x1+x2)/2;
    ym=(y1+y2)/2;
    c2_x=xm;
    c2_y=ym;
x1_seq=x1_old(:);
x2_seq=x2_old(:);

x1_seq_n=x1_new(:);
x2_seq_n=x2_new(:);
Xold(1,:)=x1_seq-c1_x;
Xold(2,:)=x2_seq-c1_y;
Xnew(1,:)=x1_seq_n-c2_x;
Xnew(2,:)=x2_seq_n-c2_y;

% calculate covariance matrices of both images
```

```
Cov1=Xold*Xold'/N;
Cov2=Xnew*Xnew'/N;

%singular value matrix decomposition
[U1,S1,V1]=svd(Cov1);
[U2,S2,V2]=svd(Cov2);

%rotation matrix p2=R*p1+t
R=U2*inv(U1);
%translation vector
t=[c2_x;c2_y]-R*[c1_x;c1_y];
for i=1:s(1)
   for j=1:s(2)
xold1(:,i,j)=R*xold(:,i,j)+t;
    end;
end;

%pixel coordinate transformation
[X,Y]=meshgrid(x,y);
for i=1:sz(1)
    for j=1:sz(2)
        vec=[X(i,j);Y(i,j)];
xupdate(:,i,j)=R*vec+t;
    end;
end;
I1new=griddata(squeeze(xupdate(1,:,:)),squeeze(xupdate(2,:,:)),I1,X,Y,...
'nearest',{'qhull d QJ'});
figure, imshow(I1new);
xx1=squeeze(xold1(1,:,:));
xx2=squeeze(xold1(2,:,:));
xx11=[xx1(:,:);xx1(1,:)];
xx21=[xx2(:,:);xx2(1,:)];
xx12=[x1_new(:,:);x1_new(1,:)];
xx22=[x2_new(:,:);x2_new(1,:)];

I1interp=interp2(X,Y,I1new,xx1,xx2,'linear',0)
I2interp=interp2(X,Y,I2,x1_new,x2_new,'linear',0)

I1_interp=[I1interp(:,:); I1interp(1,:)];
I2_interp=[I2interp(:,:); I2interp(1,:)];
%display source and target images interpolated onto the Darcyan grid xold1
figure, pcolor(xx11,xx21,I1_interp); axis tight; colormap(gray);
figure, pcolor(xx12,xx22,I2_interp); axis tight; colormap(gray);

%============================================================
```

```
%this script uses Polak-Ribiere method to find a minimizing
%sequence {a(xi,t)}_[t=1] ^N that converges to a(\xi), an
%estimate of the Poisson intensity.
%a(\xi,t) is assumed to be a sample from the Gaussian multivariate
%distribution 1/sigma_a^2 *||a(\xi,t)-a_mean||^2, where
%a_mean is an N-dimensional vector whose components a_mean_i=1/N,
%where N is the total number of seeds.
%=========================================================
function[I1interp,I2interp,a,x_new,F,F0]=inference(I1new,I2,xold1,X,Y)

[k1,k2]=size(squeeze(xold1(1,:,:)));
% the Darcyan coordinate system of the image I1 registered with the image I2;
xfix=xold1;
x_update=xold1;
%interpolation of I2 on the Darcyan grid;
I2interp=interp2(X,Y,I2,squeeze(xfix(1,:,:)),squeeze(xfix(2,:,:)),'linear',0);
I1interp=interp2(X,Y,I1new,squeeze(xfix(1,:,:)),squeeze(xfix(2,:,:)),...
'linear',0);
mu=abs(jacob(xfix));

%initialization
% assumption of the uniform intensity measure
a=ones(k1,k2)/(k1*k2);
a_mean=a;
% max number of updates of Polak-Ribiere algorithm solution
ITMAX=30;
step2=mu.^2;
sigma_I=0.1;
sigma_a=0.1;
coef_2=(sigma_I/sigma_a)^2;

%initial distance between interpolated source and target images plus
%a prior term derived from the assumption that the a-field is Gaussian;
F0=0.5/(sigma_I^2)*sum(sum(mu.*(I2interp-I1interp).^2+coef_2*(a-a_mean).^2))

%computing gradient of the energy functional F(a) at time t=0;
% F(a)= int {over all xi_seeds} (I2(xfix)-I1(xfix+dx(a)))^2
% mu(xi)d xi +1/sigma_a^2 int {over all xi_seeds} a(xi)d xi
jac=mu;
[I1_x,I1_y]=gradient(I1new);
F_a=gradF_Ebiol(x_update,I1_x,I1_y,I1new,I2interp,step2,mu,jac,a_mean,a,...
coef_2,sigma_I,X,Y,k1,k2);
g_a=-F_a;
h_a=g_a;
lambda=0.05;
```

```
for iter=1:ITMAX

   g_a0=g_a;
   num_g0=sum(sum(g_a0.^2));
   h_a0=h_a;
   x_init=x_update;
   jac=abs(jacob(x_init));
   step2=jac.^2;
    if (abs(g_a0)<=0.00001)
        break
    end

%one-dimensional minimization to find lambda
[lambda,W]=linmin_simple(lambda,x_init,a_mean,a,h_a,k1,k2,step2,mu,...
jac,I1new,I2interp,coef_2,sigma_I,X,Y,I1_x,I1_y)
   if (W==0)
       break
   end;

%update the Poisson intensity
 a=a+lambda*h_a;
   disp1=zeros(k1,k2);
   disp2=zeros(k1,k2);
  x_1=squeeze(x_init(1,:,:));
  x_2=squeeze(x_init(2,:,:));

%updating the Darcyan grid
   for xi_1=1:k1
          for xi_2=1:k2

          u1=x_1(:,:)-x_1(xi_1,xi_2);
          u2=x_2(:,:)-x_2(xi_1,xi_2);
          def_x=u1.*exp(-1/step2(xi_1,xi_2) *(u1.^2+u2.^2));
          def_y=u2.*exp(-1/step2(xi_1,xi_2) *(u1.^2+u2.^2));
           disp1=disp1+def_x.*a(xi_1,xi_2)./jac(xi_1,xi_2);
           disp2=disp2+def_y.*a(xi_1,xi_2)./jac(xi_1,xi_2);
            end;
     end;
     x_update(1,:,:)=x_1+disp1;
     x_update(2,:,:)=x_2+disp2;

%computing the gradient of the posterior energy
 F_a=gradF_Ebiol(x_update,I1_x,I1_y,I1new,I2interp,step2,mu,jac,...
 a_mean,a,coef_2,sigma_I,X,Y,k1,k2);
 F=func_Ebiol(mu,I1new,I2interp,x_update,a_mean,a,coef_2,sigma_I,X,Y)
```

```
 g_a=-F_a;

%calculating gamma according to Polak-Ribiere algorithm
 num_g=sum(sum((g_a-g_a0).*g_a0));
 gamma=num_g/num_g0;
 h_a=g_a+gamma*h_a0;
 end;
 x_new=x_update;

%auxiliary subroutines called by the Matlab code 'inference.m'
%=================================================================
%subprogram that computes the gradient of the posterior energy F_a
%with respect to the GRID variable 'a'.
%Here, 'a' is k1*k2-dimensional vector.
%=================================================================
function F_a=gradF_Ebiol(x_new,I1_x,I1_y,I1new,I2interp,step2,mu,jac,...
a_mean,a,coef_2,sigma_I,X,Y,k1,k2)

I1x=interp2(X,Y,I1_x,squeeze(x_new(1,:,:)),squeeze(x_new(2,:,:)),'linear',0);
I1y=interp2(X,Y,I1_y,squeeze(x_new(1,:,:)),squeeze(x_new(2,:,:)),'linear',0);

I1interp=interp2(X,Y,I1new,squeeze(x_new(1,:,:)),squeeze(x_new(2,:,:)),...
         'linear',0);
for xi_1=1:k1
          for xi_2=1:k2

          u1=squeeze(x_new(1,:,:)-x_new(1,xi_1,xi_2));
          u2=squeeze(x_new(2,:,:)-x_new(2,xi_1,xi_2));
          def_x=u1.*exp(-1/step2(xi_1,xi_2) *(u1.^2+u2.^2))./jac(xi_1,xi_2);
          def_y=u2.*exp(-1/step2(xi_1,xi_2) *(u1.^2+u2.^2))./jac(xi_1,xi_2);
F_a(xi_1,xi_2)=-1/(sigma_I^2)*sum(sum(mu.*(I2interp-I1interp).*...
               (I1x.*def_x+I1y.*def_y)));

         end;
      end;
Ebiol=coef_2/(sigma_I^2)*(a-a_mean);
F_a=F_a+Ebiol;
%=================================================================
%subprogram that evaluates the posterior energy at the current value
%of the Poisson intensity 'a' using interpolation of the image
%function on the updated Darcyan grid 'x_new'.
%=================================================================
function F=func_Ebiol(mu,I1new,I2interp,x_new,a_mean,a,coef_2,sigma_I,X,Y)
I1interp=interp2(X,Y,I1new,squeeze(x_new(1,:,:)),squeeze(x_new(2,:,:)),...
'linear',0);
```

```
F=0.5/(sigma_I^2)*sum(sum(mu.*(I2interp-I1interp).^2+coef_2*(a-a_mean).^2));

%=================================================================
%this script uses Polak-Ribiere method to find a minimizing
%sequence {a(xi,t)}_[t=1] ^N that converges to a(\xi), an
%estimate of the Poisson intensity.
%a(\xi,t) is assumed to be a Poisson intensity, a random field
%governing the Poisson process of cell decisions. The prior energy
%is given in the form -log(abs(a))+abs(a)+phi, where 'phi' is the
%penalty function sum_{i=1}^N |grad phi(i)|^2.
%=================================================================
function[S,x_update,I2interp]=inference2(I1new,I2,xold1,X,Y)
[k1,k2]=size(squeeze(xold1(1,:,:)));
% the Darcyan coordinate system of I1 registered with I2;
xfix=xold1;
xx1=squeeze(xfix(1,:,:));
xx2=squeeze(xfix(2,:,:));
xx11=[xx1(:,:);xx1(1,:)];
xx21=[xx2(:,:);xx2(1,:)];
mu=abs(jacob(xfix));
step2=mu.^2;
S=cell(4,10);
%interpolation of I2 on the Darcyan grid;
I2interp=interp2(X,Y,I2,squeeze(xfix(1,:,:)),squeeze(xfix(2,:,:)),...
         'linear',0);
a=1/(k1*k2)*ones(k1,k2);% initial Poisson measure
coef2=1;

% calculating the initial Darcyan grid corresponding to this a-value
 disp1=zeros(k1,k2);
 disp2=zeros(k1,k2);

  x_1=squeeze(xfix(1,:,:));
  x_2=squeeze(xfix(2,:,:));
 %updating the Darcyan grid
   for xi_1=1:k1
         for xi_2=1:k2
         u1=x_1(:,:)-x_1(xi_1,xi_2);
         u2=x_2(:,:)-x_2(xi_1,xi_2);
         def_x=u1.*exp(-1/step2(xi_1,xi_2) *(u1.^2+u2.^2));
         def_y=u2.*exp(-1/step2(xi_1,xi_2) *(u1.^2+u2.^2));
          disp1=disp1+def_x.*a(xi_1,xi_2)./mu(xi_1,xi_2);
          disp2=disp2+def_y.*a(xi_1,xi_2)./mu(xi_1,xi_2);
            end;
    end;
```

```
    x_new(1,:,:)=x_1+disp1;
    x_new(2,:,:)=x_2+disp2;
I1interp=interp2(X,Y,I1new,squeeze(x_new(1,:,:)),squeeze(x_new(2,:,:)),...
         'linear',0);
x_update=x_new;
jac=abs(jacob(x_update));
step2=jac.^2;

%initialization
coef=0.1;
sigma_obs=1/sqrt(2);

% max number of updates of Polak-Ribiere algorithm solution
ITMAX=10;
[phi,phia]=penalty(a);

for it=1:10
coef2=coef2*(0.1)^(it-1);

%initial distance between interpolated source and target images
% + the prior energy + the penalty
F0=coef*(sum(sum(1/(2*sigma_obs^2)*mu.*(I2interp-I1interp).^2-...
   coef2*(log(abs(a))-abs(a))))+coef2*phi)

%computing gradient of the energy functional F(a) at time t=0;
% F(a)= int {over all xi_seeds} (I2(xfix)-I1(xfix+dx(a)))^2
% mu(xi)dxi +1/sigma_a^2 int {over all xi_seeds} a(xi)dxi
[I1_x,I1_y]=gradient(I1new);
F_a=gradF_Ebiol2(x_update,I1_x,I1_y,I1new,I2interp,step2,mu,a,jac,...
                coef,coef2,X,Y);
g_a=-F_a;
h_a=g_a;

for iter=1:ITMAX

   lambda=0.01;
   g_a0=g_a;
   num_g0=sum(sum(g_a0.^2));
   h_a0=h_a;
   x_init=x_update;
   jac=abs(jacob(x_init));
   step2=jac.^2;

    if (abs(g_a0)<=0.0001)
        break
```

```
    end
[F,lambda,W]=linmin(lambda,x_init,a,jac,coef,coef2,h_a,step2,mu,I1new,...
                   I2interp,X,Y,I1_x,I1_y)
   if (W==0)
       break
   end;
 a=a+lambda*h_a;
% int_a=sum(sum(abs(a)))
% a=a/int_a;
   disp1=zeros(k1,k2);
   disp2=zeros(k1,k2);

  x_1=squeeze(x_init(1,:,:));
  x_2=squeeze(x_init(2,:,:));
 %updating the Darcyan grid
   for xi_1=1:k1
          for xi_2=1:k2

          u1=x_1(:,:)-x_1(xi_1,xi_2);
          u2=x_2(:,:)-x_2(xi_1,xi_2);
          def_x=u1.*exp(-1/step2(xi_1,xi_2) *(u1.^2+u2.^2));
          def_y=u2.*exp(-1/step2(xi_1,xi_2) *(u1.^2+u2.^2));
           disp1=disp1+def_x.*a(xi_1,xi_2)./jac(xi_1,xi_2);
           disp2=disp2+def_y.*a(xi_1,xi_2)./jac(xi_1,xi_2);
            end;
     end;
    x_update(1,:,:)=x_1+disp1;
    x_update(2,:,:)=x_2+disp2;
% reinitialization
F_a=gradF_Ebiol2(x_update,I1_x,I1_y,I1new,I2interp,step2,mu,...
                 a,jac,coef,coef2,X,Y);
[F,E_obs,E_biol]=func_Ebiol2(mu,I1new,I2interp,x_update,a,...
                 coef,coef2,X,Y);
g_a=-F_a;

 num_g=sum(sum((g_a-g_a0).*g_a0));
 gamma=num_g/num_g0;
 h_a=g_a+gamma*h_a0;
 end

x_new=x_update;
S{1,it}=a;
S{2,it}=x_new;
S{3,it}=F0;
S{4,it}=[F,E_obs,E_biol];
```

```
end

%auxiliary subroutines called by the Matlab code 'inference2.m'
%================================================================
%subprogram that computes the gradient of the posterior energy F_a
%with respect to the GRID variable 'a'.
%Here, 'a' is k1*k2-dimensional vector.
%================================================================
function F_a=gradF_Ebiol2(x_new,I1_x,I1_y,I1new,I2interp,step2,...
                         mu,a,jac,coef2,X,Y)
[k1,k2]=size(squeeze(x_new(1,:,:)));

%interpolate gradient of the image function I_1 onto the updated
%Darcyan grid 'x_new'
I1x=interp2(X,Y,I1_x,squeeze(x_new(1,:,:)),squeeze(x_new(2,:,:)),...
            'linear',0);
I1y=interp2(X,Y,I1_y,squeeze(x_new(1,:,:)),squeeze(x_new(2,:,:)),...
            'linear',0);
I1interp=interp2(X,Y,I1new,squeeze(x_new(1,:,:)),squeeze(x_new(2,:,:)),...
            'linear',0);
  for xi_1=1:k1
          for xi_2=1:k2
          u1=squeeze(x_new(1,:,:)-x_new(1,xi_1,xi_2));
          u2=squeeze(x_new(2,:,:)-x_new(2,xi_1,xi_2));
  def_x=u1.*exp(-1/step2(xi_1,xi_2) *(u1.^2+u2.^2))./jac(xi_1,xi_2);
  def_y=u2.*exp(-1/step2(xi_1,xi_2) *(u1.^2+u2.^2))./jac(xi_1,xi_2);
  coef=1/sum(sum(mu.*(I2interp-I1interp).^2));
F_a(xi_1,xi_2)=-2*coef*sum(sum(mu.*(I2interp-I1interp).*...
               (I1x.*def_x+I1y.*def_y)));
         end;
      end;

%compute the gradient of the prior energy
for i=1:k1
    for j=1:k2
        if(a(i,j)>=0)
Ebiol2(i,j)=-1/max(a(i,j),0.00000001)+1;
           else
Ebiol2(i,j)=-1/(a(i,j))-1;
    end;
end;

end;
```

```
[phi,phia]=penalty(a);
%'phia' is the derivative of the penalty function with respect to 'a'
F_a=F_a+coef2*(Ebiol2+phia);
%==============================================================
%subprogram that evaluates the posterior energy at the current
%value of the intensity field 'a'.
%==============================================================
function [F,E_obs,E_biol]=func_Ebiol2(mu,I1new,I2interp,x_new,...
                                     a,coef2,X,Y)

%interpolation of the image function 'I1new' onto the update Darcyan grid
I1interp=interp2(X,Y,I1new,squeeze(x_new(1,:,:)),squeeze(x_new(2,:,:)),...
               'linear',0);

%'phi' is the penalty function
[phi,phia]=penalty(a);
E_obs=log(sum(sum(mu.*(I2interp-I1interp).^2)));
E_biol=sum(sum(-log(abs(a))+abs(a)))+phi;
F=E_obs+coef2*E_biol;
%=============================================================
%subprogram that computes the penalty function
%'phi'=sum_{i=1}^N |grad phi(a_i)|^2 and its gradient.
%=============================================================
function [phi,phia]=penalty(a)
[k1,k2]=size(a);
lambda=zeros(k1+2,k2+2);
%define ghost points
lambda(k1+2,2:k2+1)=a(1,:);
lambda(1,2:k2+1)=a(k1,:);
lambda(2:k1+1,2:k2+1)=a(1:k1,1:k2);
%linear extrapolation to find lambda(k1+2,i) and lambda(1,i)
%calculating the slope
m1=lambda(:,k2+1)-lambda(:,k2);
m2=lambda(:,3)-lambda(:,2);
lambda(:,k2+2)=lambda(:,k2+1)+m1(:,1);
lambda(:,1)=lambda(:,2)-m2(:,1);

%calculate first derivatives
for i=1:k2+2
a_xi_1(:,i)=lambda(2:end,i)-lambda(1:end-1,i);
end;
for j=1:k1+2
a_xi_2(j,:)=lambda(j,2:end)-lambda(j,1:end-1);
end;
kern=(a_xi_1(1:k1,1:k2)).^2+(a_xi_2(1:k1,1:k2)).^2;
```

```
phi=sum(sum(kern));

%calculating the derivative of phi
%phi_a=zeros(k1+1,k2+1);
a1=zeros(k1+1,k2+1);
phi_a=zeros(k1+1,k2+1);
for i=2:k1+1
    for j=2:k2+1
    a1(i-1,j-1)=2*(a_xi_1(i-1,j-1)+a_xi_2(i-1,j-1));
    a1(i,j-1)=-2*a_xi_2(i,j-1);
    a1(i-1,j)=-2*a_xi_1(i-1,j);
    phi_a=phi_a+a1;
    end;
end;
phia=phi_a(1:k1,1:k2);

%===============================================================
%one-dimensional line minimization algorithm based on a
%cubic polynomial approximation to the difference
%E_{post}(lambda)-E_{post}(0). Here, the notation 'F' is
%referred to the posterior energy 'E_{post}'.
%===============================================================
function [lambda,x_update,W]=linmin_simple(lambda,x_new,a,k,coef,h_a,...
         k1,k2,step2,mu,I1new,I2interp,X,Y,I1_x,I1_y)
%initial guess for lambda
x_init=x_new;
x_update=x_init;
iter=1;
    lambd(iter)=lambda;
    while(iter<=10)
        lambda=lambd(iter);

%forming a new function theta(lambda, a) =F(a+lambda*h)-F(a)
    a_d=a+lambd(iter)*h_a;

    x_1=squeeze(x_init(1,:,:));
    x_2=squeeze(x_init(2,:,:));
    disp1=zeros(k1,k2);
    disp2=zeros(k1,k2);

%update Darcyan grid with new a
     for xi_1=1:k1
          for xi_2=1:k2
          u1=x_1(:,:)-x_1(xi_1,xi_2);
          u2=x_2(:,:)-x_2(xi_1,xi_2);
```

```
          def_x=u1.*exp(-1/step2(xi_1,xi_2) *(u1.^2+u2.^2));
          def_y=u2.*exp(-1/step2(xi_1,xi_2) *(u1.^2+u2.^2));
          disp1=disp1+def_x.*a_d(xi_1,xi_2);
          disp2=disp2+def_y.*a_d(xi_1,xi_2);
            end;
     end;
     x_update(1,:,:)=x_1+disp1;
     x_update(2,:,:)=x_2+disp2;

%evaluate the energy functional F at the value of a_d
     jac=abs(jacob(x_update));
     step22=jac.^2;
     F2=func_Ebiol2(mu,I1new,I2interp,x_update,a_d,k_d,coef,X,Y)
     F1=func_Ebiol2(mu,I1new,I2interp,x_init,a,k,coef,X,Y);
     theta1=F2-F1;

%calculate theta_lambda (lambda, a),
%the derivative of theta w.r.t lambda
F_a_d=gradF_Ebiol2(x_update,I1_x,I1_y,I1new,I2interp,step22,...
                   mu,a_d,k_d,coef,X,Y,k1,k2);
     theta_lambda1=sum(sum(F_a_d .*h_a));

%evaluate theta and theta_lambda at 0
     theta0=0;
F_a=gradF_Ebiol2(x_init,I1_x,I1_y,I1new,I2interp,step2,...
                 mu,a,k,coef,X,Y,k1,k2);
     theta_lambda0=sum(sum(F_a .*h_a));

%construct a cubic polynomial approximation to theta(lambda)
%theta(lambda=alambda^3 +b lambda^2+c lambda+d
%since theta(0)=0 d=0;
     c=theta_lambda0;
     q1=theta1;
     q2=theta_lambda1;

%find unknown coefficients a and b
     A=[lambd(iter)^3 lambd(iter)^2;3*lambd(iter)^2 2*lambd(iter)];
     B=[q1-c*lambd(iter);q2-c];
     sol=A\B;
     aa=sol(1);
     b=sol(2);

%compute lambda that minimizes theta(lambda);
     d=4*b^2-12*aa*c;
     theta_out(iter)=aa*lambd(iter)^3+b*lambd(iter)^2+c*lambd(iter)
```

```
if (iter>=2)&&(theta_out(iter)>theta_out(iter-1))
   lambda=lambd(iter-1);
   break
end;
if (d>=0)
    lambda1=(-2*b+sqrt(d))/(6*aa)
    lambda2=(-2*b-sqrt(d))/(6*aa)
    lambdas=[lambda1;lambda2];
   w=[lambda1<lambda&lambda1>0;lambda2<lambda&lambda2>0]
    I=find(w==1);
    if isempty(I)
        switch(theta_out(iter)<0)
            case 0
                if (theta1<0)
                    break
                else
                lambd(iter+1)=lambd(iter)/2;
                iter=iter+1;
                end;
            case 1
               break
        end
    elseif (length(I)==2)
        for i=1:2
         theta_pin(i)=aa*lambdas(i)^3+b*lambdas(i)^2+c*lambdas(i);
        end
         if (theta_pin(1)>theta_pin(2))
           theta_pin=theta_pin(2);
           lambda_upd=lambdas(2);
         else
           theta_pin=theta_pin(1);
           lambda_upd=lambdas(1);
         end
            switch (theta_pin<theta_out(iter))
                case 0
                    if (theta_out(iter)<0)
                        lambda=lambd(iter);
                        break
                    else
                        lambd(iter+1)=lambda_upd/2;
                        iter=iter+1;
                    end;
                case 1
                    if (theta_pin<0)
                        lambd(iter+1)=lambda_upd;
```

```
                             iter=iter+1;
                         else
                             lambd(iter+1)=lambda_upd/2;
                             iter=iter+1;
                         end
                 end
         else
             theta_pin=aa*lambdas(I)^3+b*lambdas(I)^2+c*lambdas(I);
               lambda_upd=lambdas(I);
               switch (theta_pin<theta_out(iter))
                     case 0
                         if (theta_out(iter)<0)
                             lambda=lambd(iter);
                             break
                         else
                             lambd(iter+1)=lambda_upd/2;
                             iter=iter+1;
                         end;
                     case 1
                         if (theta_pin<0)
                             lambd(iter+1)=lambda_upd;
                             iter=iter+1;
                         else
                             lambd(iter+1)=lambda_upd/2;
                             iter=iter+1;
                         end
                 end
         end
     else
         switch(theta_out(iter)<0)
                 case 0
                     lambd(iter+1)=lambd(iter)/2;
                     iter=iter+1;
                 case 1
                     lambda=lambd(iter);
                    break
         end
     end
% compute the value of the polynomial at the estimate of lambda
   ts=aa*lambda^3+b*lambda^2+c*lambda
   W=[ts<0];
   end

%=============================================================
%one-dimensional line minimization based on initial
```

```
%procedure of bracketing the minimum and isolating it
%using first derivatives of the posterior energy 'E_{post}'
%with respect to 'lambda'.
%==============================================================
function [F,lambda,W]=linmin(lambda,x_new,a,jac,coef2,h_a,step2,mu,I1new,...
I2interp,X,Y,I1_x,I1_y)
 [k1,k2]=size(squeeze(x_new(1,:,:)));
%--------------------------------------------------------------
%initial bracketing a minimum lambda_min
%golden mean ratio
    GOLD=1.618034;
%precision of estimation
    TINY=10^(-7);
%maximum number of iterations
    GLIMIT=50;
    x_init=x_new;
    lambda1=0;
%initial guess set by a user
    lambda2=lambda;
    [x_update,a_d]=darc_update(lambda2,x_init,step2,jac,a,h_a);

%evaluate the energy functional F at the value of (a_dx,a_dy)
     F2=func_Ebiol2(mu,I1new,I2interp,x_update,a_d,coef2,X,Y);
     F1=func_Ebiol2(mu,I1new,I2interp,x_init,a,coef2,X,Y);

     while((F2>F1)&&(lambda2<=GLIMIT*lambda))
         lambda2=lambda2+lambda;
         [x_update,a_d]=darc_update(lambda2,x_init,step2,jac,a,h_a);

%evaluate the energy functional F at the value of a_d
     F2=func_Ebiol2(mu,I1new,I2interp,x_update,a_d,coef2,X,Y);
     end
     if (F2>F1)
        lambda=0;
        F=F1;
        W=0;
        return
     end

%first guess for the right end point
     lambda3=lambda2+GOLD*(lambda2-lambda1);
     [x_update,a_d]=darc_update(lambda3,x_init,step2,jac,a,h_a);
     F3=func_Ebiol2(mu,I1new,I2interp,x_update,a_d,coef2,X,Y)
     while(F2>F3)
         r=(lambda2-lambda1)*(F2-F3);
```

```
         q=(lambda2-lambda3)*(F2-F1);
         const=sign(q-r);
         if(max(abs(q-r),TINY)==TINY)
             lambda=lambda3;
             F=F3;
             W=1;
             return
         end
u=lambda2-((lambda2-lambda3)*q-(lambda2-lambda1)*r)/(2*const*(abs(q-r)))
         ulim=lambda2+GLIMIT*(lambda3-lambda2);

%test various possibilities
      if((lambda2-u)*(u-lambda3)>0)
          [x_update,a_d]=darc_update(u,x_init,step2,jac,a,h_a);
          Fu=func_Ebiol2(mu,I1new,I2interp,x_update,a_d,coef2,X,Y);
          if (Fu<F3)%got a minimum between lambda2 and lambda3
              lambda1=lambda2;
              lambda2=u;
              F1=F2;
              F2=Fu;
              break
          elseif(Fu>F2)%got a minimum between lambda1 and u
              lambda3=u;
              F3=Fu;
              break
          end

%parabolic fit was of no use
      u=lambda3+GOLD*(lambda3-lambda2);
      [x_update,a_d]=darc_update(u,x_init,step2,jac,a,h_a);
      Fu=func_Ebiol2(mu,I1new,I2interp,x_update,a_d,coef2,X,Y);

%parabolic fit between lambda3 and its allowed limit
      elseif ((lambda3-u)*(u-ulim)>0)
       [x_update,a_d]=darc_update(u,x_init,step2,jac,a,h_a);
      Fu=func_Ebiol2(mu,I1new,I2interp,x_update,a_d,coef2,X,Y);
      if(Fu<F3)
          lambda2=lambda3;
          lambda3=u;
          u=lambda3+GOLD*(lambda3-lambda2);
          F2=F3;
          [x_update,a_d]=darc_update(u,x_init,step2,jac,a,h_a);
          Fu=func_Ebiol2(mu,I1new,I2interp,x_update,a_d,coef2,X,Y);
          F3=Fu;
      end
```

```
%limit parabolic u to maximum allowed value
      elseif((u-ulim)*(ulim-lambda3)>=0)
          u=ulim;
          [x_update,a_d]=darc_update(u,x_init,step2,jac,a,h_a);
          Fu=func_Ebiol2(mu,I1new,I2interp,x_update,a_d,coef2,X,Y);
      else
reject parabolic u, use default magnification
          u=lambda3+GOLD*(lambda3-lambda2);
          [x_update,a_d]=darc_update(u,x_init,step2,jac,a,h_a);
           Fu=func_Ebiol2(mu,I1new,I2interp,x_update,a_d,coef2,X,Y);
      end;
      lambda1=lambda2;
      lambda2=lambda3;
      lambda3=u;
      F1=F2;
      F2=F3;
      F3=Fu;
     end;
%-------------------------------------------------------------
%one-dimensional search for the minimum using derivatives
  e=0.0; W=1;
  ZEPS=10^(-10);
%precision of the estimate of lambda
  tol=0.001;
%maximum number of iterations
  ITMAX=100;
  if(lambda1<lambda3)
      a_1=lambda1;
      b_1=lambda3;
  else
      a_1=lambda3;
      b_1=lambda1;
  end;
  x=lambda2;
  w=x; v=x;
  [x_update,a_d]=darc_update(x,x_init,step2,jac,a,h_a);
F_a_d=gradF_Ebiol2(x_update,I1_x,I1_y,I1new,I2interp,step2,mu,a_d,jac,coef2,X,Y);
F_dx=sum(sum(F_a_d .*h_a))
F_x=func_Ebiol2(mu,I1new,I2interp,x_update,a_d,coef2,X,Y)
  F=F_x;
  lambda=x;
  F_w=F_x;F_v=F_x;
  F_dw=F_dx;F_dv=F_dx;
  for iter=1:ITMAX
```

```
      xm=0.5*(a_1+b_1);
      tol1=tol*abs(x)+ZEPS;
      tol2=2*tol1;
      if(abs(x-xm)<=(tol2-0.5*(b_1-a_1)))
% if the required precision is achieved return lambda=x
          xmin=x;
          F=F_x;
          lambda=xmin;
          break
      end;
   if(abs(e)>tol1)
       d1=2*(b_1-a_1);%the size of the step
       d2=d1;
       if(F_dw ~= F_dx)
           d1=(w-x)*F_dx/(F_dx-F_dw);%secant method with one point
       end
       if (F_dv~=F_dx)
           d2=(v-x)*F_dx/(F_dx-F_dv);
       end
   u1=x+d1;
   u2=x+d2;
%verify if u1 or u2 belong to the bracket
   ok1=((a_1-u1)*(u1-b_1)>0)&&(F_dx*d1<=0)
   ok2=((a_1-u2)*(u2-b_1)>0)&&(F_dx*d2<=0)
   olde=e;
   e=d;
   if (ok1 || ok2)
       if (ok1 && ok2)
% if both steps take a current point x to new locations within the bracket
% then take a smaller step to advance to the minimum
           if (abs(d1)<abs(d2))
               d=d1;
           else
              d=d2;
           end;
       elseif (ok1)
           d=d1;
       else
           d=d2;
       end;
           if (abs(d)<=abs(0.5*olde))
% set a new trial point u
               u=x+d;
               if(u-a_1<tol2 || b_1-u<tol2)
               d=sign(xm-x)*tol1;
```

```
               end
           else
% bisect the interval of choice
                 if(F_dx>=0)
                  e=(a_1-x);
                 else
                  e=(b_1-x);
                 end
               d=0.5*e;
           end
   else
     if(F_dx>=0)
     e=(a_1-x);
     else
     e=(b_1-x);
     end
     d=0.5*e;
   end
else
     if(F_dx>=0)
     e=(a_1-x);
     else
     e=(b_1-x);
     end
  d=0.5*e;
   end
  sprintf('d=%7.4f',d)
  if(abs(d)>=tol1)
      u=x+d;
      [x_update,a_d]=darc_update(u,x_init,step2,jac,a,h_a);
      F_u=func_Ebiol2(mu,I1new,I2interp,x_update,a_d,coef2,X,Y);
  else
      u=x+sign(d)*tol1;
      [x_update,a_d]=darc_update(u,x_init,step2,jac,a,h_a);
      F_u=func_Ebiol2(mu,I1new,I2interp,x_update,a_d,coef2,X,Y);
      if(F_u>F_x)
% f the minimum step moves a current point x uphill then return lambda=x
          xmin=x;
          F=F_x;
          lambda=xmin;
          break
      end
  end
F_a_d=gradF_Ebiol2(x_update,I1_x,I1_y,I1new,I2interp,step2,mu,a_d,...
jac,coef2,X,Y);
```

```
F_du=sum(sum(F_a_d .*h_a))
  if(F_u<=F_x)
          if(u>=x)
            a_1=x;
          else
            b_1=x;
          end
    v=w;
    F_v=F_w;
    F_dv=F_dw;
    w=x;
    F_w=F_x;
    F_dw=F_dx;
    x=u;
    F_x=F_u;
    F_dx=F_du;
  else
     if(u<x)
         a_1=u;
     else
         b_1=u;
     end
        if ((F_u<=F_w)||w==x)
            v=w;
            F_v=F_w;
            F_dv=F_dw;
            w=u;
            F_w=F_u;
            F_dw=F_du;
        elseif((F_u<F_v)||v==x||v==w)
            v=u;
            F_v=F_u;
            F_dv=F_du;
        end
  end
%keep track of x, the point with the least value of the cost function F,
%w, the point with the second least value of F,
%v, the previous value of w,
%u, the point at which F was evaluated most recently,
%(a1,b1), the bracket for the minimum
sprintf(['x=%7.4f','w=%7.4f','v=%7.4f','u=%7.4f','a_1=%7.4f','b_1=%7.4f'],...
[x,w,v,u,a_1,b_1])
 end
 W=1;
```

References

[1] Y. Amit, U. Grenander, and M. Piccioni. Structural image restoration through deformable templates. *J. American Statistical Association*, 86(414):376–387, 1991. 10

[2] D. E. Bentil and J. D. Murray. Pattern selection in biological pattern formation mechanisms. *Appl. Maths. Letters*, pages 4–15, 1991. 5

[3] F. L. Bookstein. *Lecture Notes in Biomathematics.24. The Measurement of Biological Shape and Shape Change.* Springer-Verlag, Berlin, 1978. 13

[4] F. L. Bookstein. *Morphometric Tools for Landmark Data: Geometry and Biology.* Cambridge University Press, 1991. 13

[5] F. L. Bookstein. Biometrics, biomathematics and the morphometric synthesis. *Bulletin of Mathematical Biology*, 58(2):313–365, 1996. 13

[6] S. B. Carroll. *Endless Forms Most Beautiful. The New Science of Evo Devo and the Making of Animal Kingdom.* W. W. Norton. 34, 145

[7] K. N. Chaudhury and K. R. Ramakrishnan. Stability and convergence of the level set method in computer vision. *Pattern Recognition Letters*, 28:884–893, 2007. 24

[8] J. Chimal-Monroy, J. Rodriguez-Leon, J. A. Montero, Y. Ganan, D. Macias, R. Merino, and J. M. Hurle. Analysis of the molecular cascade responsible for mesodermal limb chondrogenesis: Sox genes and bmp signaling. *Developmental Biology*, 257:292–301, 2003. 29, 30, 34, 35

[9] G. E. Christensen, S. C. Joshi, and M. I. Miller. Volumeric transformation of brain anatomy. *IEEE Transactions on Medical Imaging*, 16(6):864–877, 1997. 13

[10] G. E. Christensen, R. D. Rabbitt, and M. I. Miller. A deformable neuroanatomy textbook based on viscous fluid mechanics. In *Proc. of the Twenty Seventh Annual Conference on Information Sciences and Systems, Baltimore, Maryland*, volume 36, pages 211–216, 1993. 10, 13

[11] G. E. Christensen, R. D. Rabbitt, and M. I. Miller. 3d brain mapping using a deformable neuroanatomy. *Physics in Medicine and Biology*, 39:609–618, 1994. 10, 13

[12] G. E. Christensen, R. D. Rabbitt, and M. I. Miller. Deformable templates using large deformation kinematics. *IEEE Transactions on Image Processing*, 5(10):1435–1447, 1996. 10, 11, 13

[13] G. E. Christensen, R. D. Rabbitt, M. I. Miller, S. C. Joshi, U. Grenander, and T.A. Coogan. *Topological Properties of Smooth Anatomic Maps.* Kluwer Academic Publishers, 1995. 10, 13

[14] E. Coen. *The Art of Genes.* Oxford University Press, Oxford, 2000. 7

[15] E. Coen, A-G. Rolland-Lagan, M. Matthews, J.A. Bangham, and P. Prusinkiewicz. The genetics of geometry. *PNAS*, 101(14):4728–4735, 2003. 6, 7, 146

[16] D. R. Cox and V. Isham. *Point Processes.* Chapman & Hall, Boca Raton, Florida, 1980. 132, 202

[17] G. C. Cruywagen. *Tissue Interaction and Spatial Pattern Formation, Ph.D. Thesis.* University of Oxford, Oxford, 1992. 5

[18] C. Davatzikos. Spatial transformation and registration of brain images using elastically deformable models. *Comput.Vision Image Understanding*, 66(2):207–222. 10

[19] D. Davidson, J. Bard, M. Kaufman, and R.A. Baldock. The mouse atlas database: A community resource for mouse development. *Trends in Genetics*, 17:49–51, 2001. 28

[20] José Bioucas Dias. Course material: Svd-based regularization. `http://www.lx.it.pt/~bioucas/IP/`, 2007. 173

[21] P. Dupuis, U. Grenander, and M. I. Miller. Variational problems on flows of diffeomorphisms for image matching. *Quart. Appl. Math.*, 56:587–600, 1998. 13

[22] S. Geman and D. Geman. Stochastic relaxation, gibbs distributions, and the bayesian restoraiton of images. *IEEE Trans. on Pattern Analysis and Machine Intelligence*, PAMI-6(6):721–741, 1984. 153

[23] I. I. Gihman and A. V. Skorohod. *Stochastic differential equations.* Naukova Dumka, Kyiv, 1968. 112

[24] M. Grayson. The heat equation shrinks embedded plane curves to round points. *Journal of Diferential Geometry*, 26:285–314, 1987. 23

[25] P. B. Green, C. S. Steele, and S. C. Rennich. Phyllotactic patterns: A biophysical mechanism for their origin. *Annals of Botany*, 77:515–527, 1996. 6, 7, 146

[26] U. Grenander. *General Pattern Theory: A Mathematical Study of Regular Structures.* Clarendon Press-Oxford, New York, 1993. 9, 52

[27] U. Grenander. *Elements of Pattern Theory.* Johns Hopkins University Press, Baltimore and London, 1996. 7

[28] U. Grenander. Mathematical representation of biological laws. *Unpublished manuscript*, 2006. 51

[29] U. Grenander. On the mathematics of growth. *Quart. Appl. Math.*, 65:205–257, 2007. 14, 15, 18, 20, 22, 32, 33, 130, 131, 137

[30] U. Grenander and M. Miller. *Pattern Theory: From Representation to Inference.* Oxford University Press Inc., New York, 2007. 144, 150

[31] U. Grenander and M. I. Miller. Representation of knowledge in complex systems. *J. of the Royal Statistical Society B*, 56(3):549–603, 1994. 11

[32] U. Grenander and M. I. Miller. Computational anatomy: An emerging discipline. *Quart. Appl. Math.*, 56(4):617–694, 1998. 9, 10, 17, 154

[33] U. Grenander, A. Srivastava, and S. Saini. A pattern-theoretic characterization of biological growth. *IEEE Trans. Med. Imaging*, 26(5):648–659, 2007. 33, 39, 49, 54

[34] H. Haken. *Synergetics: an introduction.* Springer-Verlag, Berlin, 1978. 96

[35] S. Joshi. *Large Deformation Diffeomorphisms and Gaussian Random Fields for Statistical Characterization of Brain Submanifolds, Ph. D. Thesis.* Department of Electrical Engineering, Sever Institute of Technology, Washington University, St. Louis, Mo., 1997. 13

[36] S. Joshi, M. I. Miller, G. E. Christensen, A. Banerjee, T. A. Coogan, and U. Grenander. Hierarhical brain mapping via a generalized dirichlet solution for mapping brain manifolds. In *Proc. of the SPIE's 1995 International Symposium on Optical Science, Engineering and Instrumentation*, volume 2573, pages 278–289, 1995. 13

[37] P. Knupp and A. Steinberg. *Fundamentals of grid generation.* CRC Press Inc., Boca Raton, 1993. 20

[38] S. K. Kyriacou, C. Davatzikos, S. J. Zinreich, and R. N. Bryan. Nonlinear elastic registration of brain images with tumor pathology using biomechanical model. *IEEE Trans. Med. Imaging*, 18(7):580–592, 1999.

[39] S.M. Lee, P.S. Danielian, B. Fritzch, and A.P. McMahon. Evidence that fgf8 signaling from the midbrain-hindbrain junction regulates growth and polarity in the developing midbrain. *Development*, 124(5):959–969, 1997. 18

[40] Jr Lewis I. Held. *Imaginal Discs: The Genetic and Cellular Logic of Pattern Formation.* Cambridge University Press, New York, 2002. 147, 151

[41] L. Matejic. *Group Cascades for Representing Biological Variability, Ph. D. Thesis.* Brown University, Providence, RI, 1997. 13

[42] J. H. Mathews and K. K. Fink. *Numerical Methods Using Matlab, 4th Edition.* Prentice-Hall, Inc., Upper Saddle River, New Jersey, 2004. 24

[43] M. L. Miller, G. E. Christensen, Y. Amit, and U. Grenander. Mathematical textbook of deformable neuroanatomies. In *Proc. Natl. Acad. Sci.*, volume 90, pages 11944–11948, 1993. 13

[44] Z. Miskovic. *AMATH777 Lecture Notes on Stochastic Processes.* Department of Applied Mathematics, University of Waterloo, Ontario, 2007. 212

[45] J. D. Murray. *Mathematical Biology.* Springer-Verlag, Berlin, 1989. 4

[46] J. D. Murray and P. K. Maini. A new approach to the generation of pattern and form in embryology. *Sci.Prog.*, 70:539–553, 1986. 5

[47] S. A. Newman and H. L. Frisch. Dynamics of sceletal pattern formation in developing chicken limb. *Science*, 228:885–889, 1979. 4

[48] S. Osher and J.A. Sethian. Fronts propagating with curvature-dependent speed: Algorithms based on hamilton-jacobi formulation. *Journal of Computational Physics*, 79:12–49, 1988. 22

[49] G. F. Oster and J. D. Murray. Pattern formation models and developmental constraints. *J.Exp.Zool.*, 251:186–202, 1989. 5

[50] S. Paddock and D. McDougal. Making movies on a weekend. *Bioimaging*, 29(5):997–1004, 2000. 151, 189

[51] E. Polak. *Mathematics in Science and Engineering.77. Computational Methods in Optimization: a Unified Approach.* Academic Press, New York, 1971. 160, 217, 218, 219

[52] N. Portman, U. Grenander, and E. R. Vrscay. New computational methods of construction of darcyan biological coordinate systems. In *Proceedings of the 4th International Conference on Image Analysis and Recognition (ICIAR), Montreal, Ontario, August 22–24, 2007*, volume 4633, Berlin / Heidelberg, 2007. 23, 155

[53] N. Portman, U. Grenander, and E. R. Vrscay. Direct estimation of biological growth properties from image data using the "grid" model. In *Proceedings of the 6th International Conference on Image Analysis and Recognition (ICIAR), Halifax, Nova Scotia, July 6–8, 2009*, Berlin / Heidelberg, 2009. 165

[54] W. H. Press, B. P. Flannery, S. A. Teukolsky, and W. T. Vetterling. *Numerical Recipes in C: The Art of Scientific Computing.* Cambridge University Press, New York, 2 edition, 1992. 20, 162, 218

[55] D. Reinhardt and E. R. Pesce. Regulation of phyllotaxis by polar auxin transport. *Nature*, 426:255–260, 2003. 6, 7, 39, 41

[56] A.-G. Rolland-Lagan, J.A. Bangham, and E. Coen. Growth dynamics underlying petal shape and asymmetry. *Letters to Nature*, 422:161–163, 2003. 27, 28, 66

[57] J. Sethian. *Ph.D. dissertation: An Analysis of Frame Propagation.* Department of Mathematics, University of California, Berkeley, 1982. 23

[58] J. Sethian. Curvature flow and entropy conditions applied to grid generation. *Journal of Computaitonal Physics*, 115:440–454, 1994. 22, 23, 25, 27

[59] J. Sethian. *Level Set Methods: Evolving Interfaces in Geometry, Fluid Mechanics, Computer Vision and Materials Science.* Cambridge University Press, New York, 1996. 22, 23

[60] P. D. Shipman and A. C. Newell. Plant patterns. *manuscript*, 2004. 6

[61] D. L. Snyder. *Random point processes.* John Wiley & Sons, Inc., New York, 1975. 78, 202, 206

[62] A. Srivastava, S. Saini, Z. Ding, and U. Grenander. Maximum-likelihood estimation of biological growth variables. In *Energy Minimization Methods in Computer Vision and Pattern Recognition, LNCS*, volume 3757, pages 107–118, 2005. 14

[63] A. Srivastava, S. Saini, Z. Ding, and U. Grenander. Maximum-likelihood estimation of biological growth variables. *Energy Minimization Methods in Computer Vision and Pattern Recognition, LNCS*, 3757:107–118, 2005. 14

[64] C. R. Steele. Shell stability related to pattern formation in plants. 6

[65] D'Arcy Thompson. *On Growth and Form.* Cambridge University Press, Cambridge, 1961. 15, 18

[66] V. I. Tikhonov and M. A. Mironov. *Markov Processes.* Soviet Radio:in Russian, Moscow, 1977. 102

[67] A. Turing. The chemical basis of morphogenesis. *Phil. Trans. R. Soc. Lond. B*, 237:37–72, 1952. 4

[68] I. R. Wang, W. L. Wan, and G. V. G. Baranovski. Physically based simulation of plant leaf growth. *Comp. Anim. Virtual Worlds*, 15:237–244, 2004. 5

[69] J. A. Williams, S. W. Paddock, and S. B. Carroll. Pattern formation in a secondary field: a hierarchy of regulatory genes subdivides the developing drosophila wing disc into discrete subregions. *Development*, 117:571–584, 1993. 147, 148, 149, 150

[70] L. Wolpert, J. Brockes, T. Jessell, P. Lawrence, and E. Meyerowitz. *Principles of Development*. University Press, Oxford, 1998. 7

[71] Weng Yu-Xiang. Growth and form in biology: Generation of the plant morphology by spontaneous symmetry breaking based on a pressure field. *Chin.Phys.Lett.*, 21(1):211–214, 2004. 4